Universidade de Brasília
Instituto de Geociências
Programa de Pós-graduação em Geologia

DATAÇÃO U-PB DE ROCHAS CARBONÁTICAS DO PRÉ-SAL: IMPLICAÇÕES PARA A HISTÓRIA GEOLÓGICA DA BACIA DE SANTOS

U-Pb Dating of Pre-salt Carbonate Rocks: Implications for the Geological History of the Santos Basin

João Pedro Santos de Brito

Dissertação de mestrado n° 514

Orientador

Prof. Dr. Roberto Ventura Santos

BRASÍLIA-DF

2023

Universidade de Brasília
Instituto de Geociências
Programa de Pós-graduação em Geologia

DATAÇÃO U-PB DE ROCHAS CARBONÁTICAS DO PRÉ-SAL: IMPLICAÇÕES PARA A HISTÓRIA GEOLÓGICA DA BACIA DE SANTOS

U-Pb Dating of Pre-salt Carbonate Rocks: Implications for the Geological History of the Santos Basin

João Pedro Santos de Brito

Dissertação apresentada ao Programa de Pós-Graduação em Geologia – Instituto de Geociências – IG da Universidade de Brasília – UnB como requisito parcial obrigatório para a obtenção do título de Mestre em Geologia.

Área de concentração: Geoquímica

Orientador: Prof. Dr. Roberto Ventura Santos

Comissão Examinadora:

Prof. Dr. Márcio Vinicius Santana Dantas (IG/UnB);
Prof. Dr. Cristiano Carvalho Lana (DEGEO-UFOP)

BRASÍLIA-DF

2023

Ficha catalográfica elaborada automaticamente,
com os dados fornecidos pelo(a) autor(a)

Sd

Santos de Brito, João Pedro
Datação U-Pb de Rochas Carbonáticas do Pré-sal: Implicações para a História Geológica da Bacia de Santos / João Pedro Santos de Brito; orientador Roberto Ventura Santos. -- Brasília, 2023.
141 p.

Dissertação(Mestrado em Geologia) -- Universidade de Brasília, 2023.

1. Substituição do sistema U-Pb. 2. Datação de carbonatos. 3. Formação Barra Velha. 4. Interação rocha-fluido. I. Ventura Santos, Roberto, orient. II. Título.

“And in me too the wave rises”.

Virginia Woolf

AGRADECIMENTOS

Acima de tudo, agradeço aos meus pais, especialmente à minha mãe, por todo o amor, por todo o apoio. Isso nunca me faltou da parte de vocês.

Agradeço às minhas avós por todo o carinho e por fazerem de mim o baiano mais mimado e bem alimentado do mundo quando viajava à Bahia.

Agradeço ao prof. Roberto por aceitar me orientar, por acreditar em mim, e por me incentivar durante todo o percurso, sempre me instigando em diversos temas.

Agradeço ao prof. Abreu por todo o apoio, pela confiança no meu trabalho, pela amizade e pelos inúmeros almoços. Não seria exagero comentar que o senhor foi meio que uma figura paterna durante este mestrado.

Agradeço à Equinor por tornar esta pesquisa possível através do projeto de P&D intitulado "Geologia e geoquímica dos reservatórios das seções sag e topo do rifte das áreas de Sapinhoá e Lapa na bacia de Santos", projeto do qual fui bolsista, e do projeto de Infra de melhoria de instalações que serão usadas no Projeto de PD&I – LAPA e em demais futuros projetos.

Agradeço aos profissionais da Equinor, especialmente à Juliana, ao Jorge, e ao David, pelas discussões e pelo incentivo durante esta pesquisa.

Agradeço ao prof. Guilherme e à Paulinha pela paciência e ajuda durante e após as análises isotópicas.

Agradeço à profa. Paola, à mestra Maria Masella, e ao graduando Lucas, pelas análises de QEMSCAN.

Agradeço à Alaninha, a minha pessoa preferida do mundo! Estar com você torna tudo mais fácil. À Dona Ires, agradeço todo o carinho e acolhimento.

Agradeço ao Felipinho pelo companheirismo, pela amizade. Estaremos sempre juntos, amigo!

Agradeço aos colegas do Laboratório de Geocronologia pela convivência e pela ajuda.

Agradeço à UnB, ao Instituto de Geociências, e ao Programa de Pós-Graduação em Geologia da UnB.

Agradeço à FINATEC por todo o auxílio durante a pesquisa.

O presente trabalho foi realizado com apoio da Coordenação de Aperfeiçoamento de Pessoal de Nível Superior – Brasil (CAPES) – Código de Financiamento 001

RESUMO

Os carbonatos do pré-sal e suas características únicas representam um desafio para a compreensão dos processos deposicionais e diagenéticos relacionados a essas rochas. Também a geocronologia da Formação Barra Velha é controversa. Por exemplo, há controvérsias se os carbonatos dessa formação foram depositados durante o Barremiano ou durante o Aptiano. Para se obter a cronologia dos processos deposicionais e diagenéticos relacionados aos carbonatos da porção superior da Formação Barra Velha e também entender como funciona o sistema isotópico U-Pb em minerais carbonáticos, este estudo integrou petrografia convencional, imageamento por QEMSCAN, e datação U-Pb in situ de carbonatos. As amostras são de três testemunhos (3-BRSA-923A-SPS, 9-BRSA-928-SPS, e 7-SPH-6-SPS) do campo de Sapinhoá, localizado na porção central da Bacia de Santos. As idades obtidas neste estudo coincidiram com eventos tectônicos e termais regionais que afetaram a Bacia de Santos. Esses eventos têm idades de ~ 127/125 Ma, ~ 116/114 Ma, e ~ 105/100 Ma. Uma influência local nas idades obtidas também foi observada, já que os padrões de idades foram diferentes entre os testemunhos. Por exemplo, as partículas primárias de calcita dos testemunhos 9-BRSA-928-SPS e 3-BRSA-923A-SPS foram afetadas por uma substituição pós-deposicional do sistema U-Pb, o que resultou em idades entre ~ 105 Ma e ~ 82 Ma para essas partículas. No entanto, as partículas primárias do testemunho 7-SPH-6-SPS preservaram idades mais antigas de ~ 115 Ma. Tal comportamento contrastante das idades pode ser explicado por diferentes contextos magmáticos, hidrotermais, estruturais e estratigráficos atuando em diferentes áreas do campo de Sapinhoá. As dolomitas, por sua vez, demonstraram que a substituição do sistema U-Pb dos constituintes pode não ser um efeito pervasivo, mas que depende mais da interação rocha-fluido e das propriedades físicas das partículas, como porosidade e permeabilidade. Isso foi observado em consequência das camadas não-porosas e não-permeáveis de dolomita não terem sido afetadas por uma substituição geocronológica do sistema U-Pb. Na verdade, dolomita microcristalina e finos romboedros de dolomita registraram as primeiras datações diretas de idades barremianas para os carbonatos da Formação Barra Velha Superior. Em relação às idades das dolomitas, estas foram separadas em dolomitas pré-silicificação e em dolomitas pós-silicificação. As dolomitas pré-sílica ocorrem como dolomitas microcristalinas e como finos romboedros de idades barremiana-aptiana por volta de 124 Ma; como dolomita lamelar e como cristais finos de dolomita romboédrica pervasiva de ~117 – 110 Ma; e como dolomitas microcristalinas pseudomórficas que sofreram substituição do sistema isotópico U-Pb relacionado a um evento de silicificação do Albiano-Cenomaniano. Dolomitas pós-sílica têm idades por volta de ~100 Ma e são representadas por cimentos diagenéticos tardios como dolomita blocosa e dolomita em sela. A dolomita em sela limita temporalmente um evento de silicificação como mais velho que 100 Ma.

Palavras-Chave: Substituição do sistema U-Pb; Datação de carbonatos; Formação Barra Velha; Interação rocha-fluido

ABSTRACT

The Pre-salt carbonates and their unique characteristics represent a challenge for understanding depositional and diagenetic processes related to these rocks. The Barra Velha Formation's chronology is also controversial, whether it was deposited during Barremian and Aptian times. To constrain the chronology of depositional and diagenetic processes related to the Upper Barra Velha carbonates and also to understand how the U-Pb isotopic system works in carbonate minerals, this study presents an integrated study of conventional petrography, QEMSCAN imaging, and in situ U-Pb dating of carbonate samples from three wells (3-BRSA-923A-SPS, 9-BRSA-928-SPS, and 7-SPH-6-SPS) of the Sapinhoá field, located in the central part of the Santos Basin. Ages obtained in this study coincide with regional tectonic and thermal events that affected the Santos Basin. These events have geochronological ages of ~ 127/125 Ma, ~ 116/114 Ma, and ~ 105/100 Ma. A local influence of the geological and structural contexts of the analyzed particles was also detected, since the pattern of ages obtained in each well was different from the other. For instance, the calcite primary particles from the well 9-BRSA-928-SPS underwent U-Pb post-depositional replacement, which resulted in younger post-depositional ages of ~ 105 Ma for these particles. Instead, the calcite primary particles from the 7-SPH-6-SPS well preserved older ages of ~115 Ma. This different age behavior may be explained by different magmatic, hydrothermal, structural, or stratigraphic contexts acting on the studied wells. The dolomites, compared to calcite particles, showed that the geochronological replacement of the particles may not be a pervasive effect but may depend more on fluid-rock interaction and physical properties of the particles, such as porosity and permeability. This was observed hence the non-porous and non-permeable dolomitic aggregates were not affected by U-Pb geochronological replacement. Indeed, primary microcrystalline and fine dolomite rhombs recorded the first direct barremian ages for the Barra Velha carbonates. Otherwise, microcrystalline pseudomorphic dolomites and calcite particles underwent U-Pb replacement caused probably by fluid-rock interactions and thermal effects. Concerning dolomite ages, they were separated in pre-silicification and post-silicification dolomites. Pre-silicification dolomites occur as ~124 Barremian-Aptian microcrystalline to very fine laminated dolomite rhombs; as ~117 – 110 Ma lamellar and pervasive fine rhombohedral dolomite crystals; and as pseudomorphic microcrystalline dolomites that underwent U-Pb replacement related to an Albian-Cenomanian silicification event. Post-silicification dolomites have ages of ~ 100 Ma and are represented by later diagenetic cements such as blocky dolomite and saddle dolomite. The saddle dolomite temporally limits a silicification event as older than 100 Ma.

Keywords: U-Pb replacement; Carbonate dating; Barra Velha Formation; Fluid-rock interaction

SUMÁRIO

CAPÍTULO 1.....14

1.1 INTRODUÇÃO.....14

1.2 OBJETIVOS DA DISSERTAÇÃO.....17

1.3 ESTRUTURA DA DISSERTAÇÃO.....17

CAPÍTULO 2.....18

2.1 CONCEITUAÇÃO TEÓRICA.....18

2.1.1 Geocronômetro U-Pb.....18

2.1.2 Geocronologia de Carbonatos e Incorporação de U e Pb.....20

2.2 CONTEXTO GEOLÓGICO.....25

2.2.1 Localização da Área de Estudo.....25

2.2.2 O Pré-sal da Bacia de Santos.....26

2.2.3 Idades de Magmatismo na Bacia de Santos e de Hidrotermalismo no Sistema Pré-sal.....28

2.2.4 Idades de Deposição de Carbonatos e de Diagênese nas Bacias do Pré-sal.....29

CAPÍTULO 3.....31

3.1 MATERIAIS E MÉTODOS.....31

3.1.1 Correlação por Perfis de Raios Gama.....31

3.1.2 Petrografia.....31

3.1.3 Imageamento por QEMSCAN.....31

3.1.4 Geocronologia U-Pb em Carbonatos.....31

CAPÍTULO 4 U-Pb Dating of Pre-salt Carbonate Rocks: Implications for the Geological History of the Santos Basin.....36

4.1 INTRODUCTION.....37

4.2 GEOLOGICAL SETTING.....40

4.2.1 Ages of Magmatism in the Santos Basin and Hydrothermalism in the Pre-salt System.....41

4.2.2 Ages of Carbonate Deposition and Diagenesis in the Pre-salt Basins.....42

4.3 DATA AND METHODS….....45

4.3.1 Well Correlation.....45

4.3.2 Petrography.....45

4.3.3 QEMSCAN Imaging.....45

4.3.4 U-Pb Carbonate Geochronology.....45

4.4 RESULTS.....47

4.4.1 Petrography.....47
4.4.1.1 Facies.....48
4.4.1.2 Diagenetic Features.....51
4.4.2 U-Pb Carbonate Geochronology.....53
4.5 DISCUSSION.....59
4.5.1 Ages of Primary Carbonate Constituents.....61
4.5.2 Secondary Dolomites Ages, Morphologies and Their Geologic Contexts...65
4.6 CONCLUSIONS.....68
4.7 AKNOWLEDGEMENTS.....70
CAPÍTULO 5.....71
5.1 CONCLUSÕES E RECOMENDAÇÕES.....71
CAPÍTULO 6.....72
6.1 REFERÊNCIAS BIBLIOGRÁFICAS.....72
ANEXO A
ANEXO B
ANEXO C

ÍNDICE DE FIGURAS

Figura 1: Esquema do processo de decaimento radiogênico dos isótopos ^{238}U e ^{235}U em ^{206}Pb e ^{207}Pb, respectivamente, de acordo com suas respectivas cadeias de decaimento e meia-vida. O tempo de meia-vida é o tempo necessário para que metade dos radionuclídeos de U se transformem em Pb. A taxa de decaimento é exponencial**.....18**

Figura 2: Geocronologia U-Pb em carbonatos e diagrama da concórdia de Tera-Wasserburg associado. À esquerda: imagem petrográfica de um oóide. Os quadrados roxos representam os pontos de análise. À direita: diagrama da concórdia de Tera-Wasserburg. Cada elipse roxa representa uma única análise e os respectivos valores das razões $^{238}U/^{206}Pb$ e $^{207}Pb/^{206}Pb$. O eixo maior e o eixo menor das elipses indicam as incertezas de cada uma das duas razões medidas. Em condições ideais, no momento da cristalização, as razões isotópicas U/Pb são heterogêneas e a razão Pb/Pb é homogênea, resultando em uma linha de regressão horizontal (a isócrona, marcada pela linha azul pontilhada). Conforme o tempo passa e o U decai para Pb radiogênico, a linha de regressão inclina-se e corta a curva da concórdia em uma posição que indica a idade da amostra (o intercepto inferior). O intercepto superior entre a regressão e o eixo y representa a composição inicial de $^{207}Pb/^{206}Pb$ do mineral (Montano, 2021)**.....22**

Figura 3. (A) Área de estudo localizada na região sudeste da margem continental brasileira, mais especificamente na Bacia de Santos. O campo de Sapinhoá (em lilás) está na porção central da Bacia de Santos. O polígono amarelo representa o polígono do pré-sal. Em magenta, estão os demais campos de petróleo. No norte, a Bacia de Santos é separada da Bacia de Campos pelo Alto de Cabo Frio. Ao sul, é o Alto de Florianópolis que separa a Bacia de Santos da Bacia de Pelotas. (B) Detalhe do campo de Sapinhoá, mostrando a distribuição dos três poços estudados ao longo do campo**.....26**

Figura 4: (A) Seção estratigráfica do Cretáceo Inferior da Bacia de Santos (adaptado de Moreira et al., 2007). (B) Histograma de idades de eventos magmáticos na Bacia de Santos. (C) Histograma das idades de eventos de hidrotermalismo no pré-sal (dados das bacias de Santos, Campos, Namíbia e Kwanza). (D) Histograma de idades deposicionais e de diagênese registradas no pré-sal (dados das bacias de Santos, Namíbia e Kwanza). Os dados utilizados para a construção dos histogramas estão disponíveis nos anexos e são das seguintes referências: Rochelle-Bates et al. (2021); Godeau et al. (2021); Rochelle-Bates et al. (2022); Lawson et al. (2022); Moreira et al. (2007); Szatmari & Milani, (2016); Trittla et al. (2018); Loma et al. (2018); Rancan et al. (2018); Louback et al. (2021); Godeau et al. (2021); Rochelle-Bates et al. (2021); Louback et al. (2023); Gordon et al. (2023); Oliveira et al. (2023)**.....30**

Figura 5: (A) Correlação estratigráfica entre os poços estudados, por meio de perfil de raios-gama. O polígono roxo tracejado representa a porção amostrada do poço 923A. O polígono Vermelho tracejado representa a porção amostrada do poço 928. O polígono azul tracejado representa a porção amostrada do poço SPH-6. A linha tracejada laranja representa a base do sal. A linha azul tracejada marca a Discordância Intra-Alagoas. O polígono lilás marca a correlação entre a porção amostrada do poço 923A, que corresponde aos 15 metros imediatamente abaixo do marco Lula, com os 30 metros superiores da porção amostrada do poço 928, que provavelmente engloba o mesmo ou nível estratigráfico semelhante que o amostrado pelo testemunho 923A. O polígono azul marca a correlação entre a parte amostrada do poço SPH-6, que corresponde entre cerca de 100 m a 140 m de profundidade abaixo da base do sal, com a porção intermediária amostrada do poço 928 que provavelmente compreende um intervalo estratigráfico semelhante àquele compreendido pelo testemunho SPH-6. (B) Perfis estratigráficos da porção superior da Formação Barra Velha, amostrada pelos três poços estudados. A linha tracejada vermelha marca a divisão do testemunho 928 em duas partes: (1) a seção superior, localizada dentro de ~ 20 metros logo abaixo da base do sal, que provavelmente está em uma posição estratigráfica similar a do testemunho 923A; e (2) uma seção intermediária do testemunho 928, localizada entre 100 m e 150 m abaixo da base da Fm. Ariri, e que provavelmente corresponde a uma posição estratigráfica semelhante àquela na qual o testemunho SPH-6 foi amostrado. Os polígonos vermelhos marcam locais de houve amostragem para análises de U-Pb em carbonatos.**.....34**

Figure 1: (A) Location of the Zeta field in the central portion of the Santos Basin. The yellow polygon represents the Pre-salt polygon, with the oil fields illustrated in magenta. In the northern part, the Santos

Basin is separated by the Campos Basin through the Cabo Frio High. In the south, the Florianópolis High separates the Santos Basin from the Pelotas Basin. (B) Detail of the Zeta field, showing the distribution of the three wells studied along the area. (C) Lower Cretaceous stratigraphic section of the Santos Basin (adapted from Moreira et al., 2007). (D) Histogram of magmatism ages in the Santos Basin. (E) Histogram of hydrothermal events ages in the Pre-salt system. (F) Histogram of depositional and diagenetic ages recorded in the Pre-salt system. The data compiled from other studies are available in the supplementary material (Rochelle-Bates et al., 2021; Rochelle-Bates et al., 2022; Lawson et al., 2022; Moreira et al., 2007; Szatmari & Milani, 2016; Trittla et al., 2018; Loma et al., 2018; Rancan et al., 2018; Louback et al., 2021; Godeau et al., 2021; Rochelle-Bates et al., 2021; Louback et al., 2023; Gordon et al., 2023; Oliveira et al., 2023)**.....44**

Figure 2: Gamma ray well correlation between the three studied wells. The purple dashed polygon represents the sampled portion form the well A. The red dashed polygon represents the sampled portion from the well B. The blue dashed polygon represents the sampled portion from the well C. The orange dashed line marks the salt base. The light blue dashed line marks the Intra-Alagoas Unconfomity. The lilac polygon marks the correlation between the sampled part of the well A, which corresponds to ~15 m right under the Lula mark, with the uppermost ~ 30 m sampled from the well B, that encompasses the same portion. The blue polygon marks the correlation between the sampled part of the well C, which corresponds to ~100 m – 140 m under the salt base, with the middle sampled part of the well B that probably comprehends a similar interval. The red stars mark the stratigraphic position of the samples analyzed for U-Pb
dating**.....47**

Figure 3: (A) PPL photomicrograph of shrubstone with well-formed shrubs with the interparticle space occupied by dolomite rhombs. Sample is 5129.45 from well C. (B) PPL photomicrograph of spherulitestone with lamellar pseudomorphic microcrystalline dolomite and stratiform silicification. Sample is 5016.90 from well B. (C) PPL photomicrograph of grainstone with inteparticle porosity and formed by intraclasts of spherulites, composite ooids, basalt lithoclasts, and chert lithoclasts. Sample is 5014.75 from well B. (D) XP photomicrograph of laminated, soft-deformed and partially silicified dolostone formed by microcrystalline and rhombohedral dolomites. Sample is 5194.50 from well B. (E) PPL photomicrograph of dolomite-supported rock composed by fine dolomite rhombs occupying the interparticle space and replacing the framework constituents. Sample is 5124.60 from well C. (F) XP photomicrograph of a chert with carbonate particles preserved. Microcrystalline silica occupies the interparticle space and replaces particles. Macrocrystalline mosaic quartz fills vuggy pores. Sample is 5045.25 from well B. Bas: basalt; Ch: chert; CO: composite ooid; Dol: dolomite; IC: intraclast; MD: microcrystalline dolomite; MMQ: macrocrystalline mosaic quartz; MS: microcrystalline silica; LD: lamellar dolomite; Shr: shrub; Sph: spherulite**.....50**

Figure 4: Coupled conventional petrographic study-QEMSCAN imaging to a better understanding of diagenesis. (A-B) XP and QEMSCAM images of chert with carbonate particles preserved. It is possible to notice that the quartz crystals are replacing dolomite rhombs and calcite particles. Sample is 5020.10 from well B. (C-D) PPL and QEMSCAN images of dolomitized grainstone with rhombohedral dolomite filling pore spaces and replacing calcite paticles. Macrocrystalline mosaic calcite fills intraparticle-fracture porosity. Sample is 5100.75 from well A. Dol: dolomite; MC: macrocrystalline calcite; MS: microcrystalline silica; Qz: quartz; Shr: shrub**.....52**

Figure 5: Analyzed primary constituents and their respective Tera-Wasserbung concordia diagram ages. A) Tera-Wasserburg concordia diagram showing $^{238}U/^{206}Pb$ versus $^{207}Pb/^{206}Pb$ data of microcrystalline dolomite. (B) Tera-Wasserburg concordia plots showing $^{238}U/^{206}Pb$ versus $^{207}Pb/^{206}Pb$ data of rhombohedral dolomite. (C) PPL photomicrograph and QEMSCAN image of laminated dolostone formed by microcrystalline and rhombohedral dolomites. Sample is 5194.50 from well B. (D) Tera-Wasserburg concordia diagram showing $^{238}U/^{206}Pb$ versus $^{207}Pb/^{206}Pb$ data of a peloid. (E) XP photomicrograph of analyzed peloid particle in the midst of microcrystalline silica. Sample is 5132.50 from well C. (F) QEMSCAN image of figure in (E) highlighting the calcite peloid partially replaced by silica. (G) Tera-Wasserburg concordia diagram showing $^{238}U/^{206}Pb$ versus $^{207}Pb/^{206}Pb$ data of a particle of shrub. (H) PPL photomicrograph of a shrub particle in a silicified rudstone. Sample is 5127.90 from well C. (I) QEMSCAN image of figure in (H) highlighting calcite composition of shrub and the surrounding silica partially replacing the particle. (J) Tera-Wasserburg concordia diagram showing $^{238}U/^{206}Pb$ versus $^{207}Pb/^{206}Pb$ data of ostracod particles. (K) PPL photomicrograph of analyzed ostracod particles. Sample is 5113.00 from well C. (L) QEMSCAN image of figure in (K) highlighting the calcite composition of the ostracod. (M) Tera-Wasserburg concordia diagram showing $^{238}U/^{206}Pb$ versus $^{207}Pb/^{206}Pb$ data of a shrub particle (N) PPL

photomicrograph of a shrub particle in a dolomitized grainstone Sample is 5118.95 from well C. (O) QEMSCAN image of figure in (N) highlighting the calcite composition of the shrub particle, the surrounding dolomite cement and a few silica partially replacing calcite particles. (P) Tera-Wasseburg concordia diagram showing $^{238}U/^{206}Pb$ versus $^{207}Pb/^{206}Pb$ data of a shrub particle. (Q) XP photomicrograph of a silicified shrubstone. Sample is 5133.95 from well B. (R) QEMSCAN image of figure in (Q) highlighting the calcite composition of a shrub particle and the surrounding silica partially replacing particles of shrubs. (S) Tera-Wasserburg concordia diagram showing $^{238}U/^{206}Pb$ versus $^{207}Pb/^{206}Pb$ data of shrub particles. (T) PPL photomicrograph of a shrub particle in a silicified rudstone. Samples is 5099.05 from well A. (U) QEMSCAN image of figure in (T) highlighting the calcite shrub particle partially replaced by silica. Quoted age uncertainty includes propagated systematic uncertainties. Datapoint error ellipses are 2s. MSWD, mean squared weighted deviation. (Pb*)c is ($^{207}Pb/^{206}Pb$)c, known as common lead composition. Red circles represent analytical spots made on the particles. Dol: dolomite; MD: microcrystalline dolomite; MMQ: macrocrystalline mosaic quarz; MS: microcrystalline silica; Os: ostracod; Pel: peloid; SD: saddle dolomite; Shr: shrub**.....55**

Figure 6: (A) Tera-Wasserburg concordia plots showing $^{238}U/^{206}Pb$ versus $^{207}Pb/^{206}Pb$ data for microcrystalline lamellar dolomite. (B) PPL photomicrograph of microcrystalline lamellar dolomite contouring spherulite particles in a spherulitestone. Sample is 5016.90 from well B. (C) QEMSCAN image of figure in (B) highlighting silicification in the dolomite-rich sample. (D) Tera-Wasserburg concordia diagram showing $^{238}U/^{206}Pb$ versus $^{207}Pb/^{206}Pb$ data of rhombohedral dolomite. (E) PPL photomicrograph of grainstone affected by pervasive dolomitization, with rhombohedral dolomite crystals filling pores and partially replacing particles. Sample is 5020.10 from well B. (F) Tera-Wasserburg concordia diagram showing $^{238}U/^{206}Pb$ versus $^{207}Pb/^{206}Pb$ data of rhombohedral dolomite. (G) PPL photomicrograph of grainstone affected by pervasive dolomitization, with rhombohedral dolomite crystals filling pores and partially replacing particles. Sample is 5118.95 from well C. (H) Tera-Wasserburg concordia diagram showing $^{238}U/^{206}Pb$ versus $^{207}Pb/^{206}Pb$ data of blocky dolomite cement. (I) PPL photomicrograph of blocky dolomite cement filling vuggy and intraparticle porosities. Sample is 5113.00 from well C. (J) Tera-Wasserburg concordia diagram showing $^{238}U/^{206}Pb$ versus $^{207}Pb/^{206}Pb$ data of saddle dolomite cement. (K) PPL photomimcrograph of saddle dolomite filling intraparticle fracture porosity in a grainstone. Sample is 5124.60 from the well C. (L) Tera-Wasserburg concordia diagram showing $^{238}U/^{206}Pb$ versus $^{207}Pb/^{206}Pb$ data of rhombohedral dolomite. (M) PPL photomicrograph of grainstone affected by pervasive dolomitization, with rhombohedral dolomite crystals filling pores and partially replacing particles. Sample is 5124.60 from the well C. (N) Tera-Wasserburg concordia diagram showing $^{238}U/^{206}Pb$ versus $^{207}Pb/^{206}Pb$ data of saddle dolomite cement. (O) PPL photomicrograph of silicified and dolomitizes grainstone with saddle dolomite crystals filling the center of vuggy pores lined by quartz crystals. Sample is 5020.10 from the well B. Quoted age uncertainty includes propagated systematic uncertainties. Datapoint error ellipses are 2s. MSWD, mean squared weighted deviation. (Pb*)c is $(^{207}Pb/^{206}Pb)_c$, known as common lead composition. Red, green an white circles represent analytical spots made on the particles. BD: blocky dolomite; Dol: dolomite; LD: lamellar dolomite; MD: microcrystalline dolomite**.....58**

Figure 7: Microcrystalline pseudomorphic dolomites. (A) PPL photomicrograph of the sample where the microcrystalline pseudomorphic dolomites occur. Sample is 5049.95 from the well B. (B) QEMSCAN image from figure in (A). (C) Tera-Wasserburg concordia diagram showing $^{238}U/^{206}Pb$ versus $^{207}Pb/^{206}Pb$ data of microcrystalline pseudomorphic lamellar dolomite. (D). Tera-Wasserburg concordia diagram showing $^{238}U/^{206}Pb$ versus $^{207}Pb/^{206}Pb$ data of the microcrystalline pseudomorphic dolomite that replaced ostracod particles. (E) Tera-Wasserburg concordia plots showing $^{238}U/^{206}Pb$ versus $^{207}Pb/^{206}Pb$ data of the pooled data from these microcrystalline pseudomorphic dolomites, since they all occur in the same sample and have the same ($^{207}Pb/^{206}Pb$)c value. Datapoint error ellipses are 2s. MSWD, mean squared weighted deviation. (Pb*)c is ($^{207}Pb/^{206}Pb$)c, known as common lead composition. LD: lamellar dolomite; Os: ostracod**.....59**

Figure 8: (A) Kernel Density Estimation (KDE) curve and histogram ages of magmatic event in the Santos Basin. (B) KDE curve and histogram ages of hydrothermalism events recorded in Santos, Campos, Kwanza and Namibe basins. (C) KDE curve and histogram ages of depositional and diagenetic events in the pre-salt section of Santos, Kwanza and Namibe basins (literature data). (D) KDE curve and histogram ages of depositional and diagenetic events in the Upper Barra Velha Formation (our data). The histogram binwidth is 10 and the kernel bandwidth is 1.5 for figures A, B, C, D. (E) Summary chronology of the Upper Barra Velha Formation carbonates and related magmatic, hydrothermal, and sedimentary events in

the Santos Basin and other pre-salt basins (e.g., Campos, Kwanza and Namibe basins). The figure shows the relationship between the Barra Velha Formation carbonates ages with those of magmatic and hydrothermal events that affected the pre-salt. Kernel bandwidth is 5. Our data and compilation from other studies are available in the supplementary material (Rochelle-Bates et al., 2021; Rochelle-Bates et al., 2022; Lawson et al., 2022; Moreira et al., 2007; Szatmari & Milani, 2016; Trittla et al., 2018; Loma et al., 2018; Rancan et al., 2018; Louback et al., 2021; Godeau et al., 2021; Rochelle-Bates et al., 2021; Louback et al., 2023; Gordon et al., 2023; Oliveira et al., 2023)**.....61**

Figure 9: Dolomitic layers intercalated with shrubs and spherulites and their U-Pb ages. (A) Tera-Wasserburg concordia diagram showing $^{238}U/^{206}Pb$ versus $^{207}Pb/^{206}Pb$ data of fine rhombohedral dolomite crystals (B) Tera-Wasserburg concordia diagram showing $^{238}U/^{206}Pb$ versus $^{207}Pb/^{206}Pb$ data of spherulite particles. (C) PPL photomicrograph of dolomitic spherulitestone with fine rhombohedral dolomite crystals filling interparticle pores and partially replacing spherulite particles. Sample is 5090.95 from well A (D) QEMSCAN image of figure in (C) highlighting the calcite composition of the spherulites, the interstitial dolomite and silica partially replacing spherulites. (E) Tera-Wasserburg concordia diagram showing $^{238}U/^{206}Pb$ versus $^{207}Pb/^{206}Pb$ data of interstitial microcrystalline dolomite. (F) Tera-Wasserburg concordia diagram showing $^{238}U/^{206}Pb$ versus $^{207}Pb/^{206}Pb$ data of shrub particles. (G) PPL photomicrograph of dolomitic shrubstone with microcrystalline dolomite layers intercalated with layers of shrubs. Sample is 5015.10 from well B. (H) QEMSCAN image of figure in (G) highlighting the calcite composition of the shrubs, and the partial replacement of shrubs by the microcrystalline dolomite. (I) Tera-Wasserburg concordia diagram showing $^{238}U/^{206}Pb$ versus $^{207}Pb/^{206}Pb$ data of fine rhombohedral dolomite crystals. (J) Tera-Wasserburg concordia diagram showing $^{238}U/^{206}Pb$ versus $^{207}Pb/^{206}Pb$ data of spherulite particles. (K) PPL photomicrograph of dolomitic-silicified spherulitestone with fine rhombohedral dolomite crystals filling interparticle pores and partially replacing spherulite particles. Sample is 5144.00 from well B. (L) QEMSCAN image of figure in (K) highlighting the calcite composition of spherulite particles, the surrounding silica and the rhombohedral dolomite crystals between the particles. Quoted age uncertainty includes propagated systematic uncertainties. Datapoint error ellipses are 2s. MSWD, mean squared weighted deviation. (Pb*)c is $(^{207}Pb/^{206}Pb)_c$, known as common lead composition. Red circles represent analytical spots carried out at calcite particles. Blue circles represent analytical spots carried out at dolomite phases. Dol: dolomite; MD: microcrystalline dolomite; Shr: shrub; Sph: spherulite**.....67**

ÍNDICE DE TABELAS

Table 1: U-Pb age data acquired in the Upper Barra Velha Formation carbonates from the Santos Basin**.....54**

CAPÍTULO 1

1.1 INTRODUÇÃO

O interesse em compreender as condições ambientais que promoveram a deposição dos espessos carbonatos lacustres de idade Eocretácea do pré-sal, e a diagênese e hidrotermalismo associados a esses depósitos, teve um grande aumento durante os últimos dez anos (Wright e Barnett, 2015; Souza et. al., 2018; Farias et al., 2019; Lima et al., 2020; Carvalho e Fernandes; 2021; Rebelo et al., 2023). Tais depósitos compreendem principalmente carbonatos abióticos com assinaturas continentais de $^{87}Sr/^{86}Sr$ (0.7111–0.7141; Pietzsch et al., 2018, 2020; Farias et al., 2019; Lima et al., 2020; Lawson et al., 2022). O ambiente deposicional não-marinho desses carbonatos se dá em uma ampla variedade de fácies influenciadas por oscilações no nível do lago e pela configuração estrutural da bacia, responsável pelos paleo-altos e paleo-baixos (Wright & Barnett, 2015; De Paula Faria et al., 2017).

Shrubstones e grainstones são fácies formadas durante estágios de baixo nível do lago, possuem altas porosidade e permeabilidade, e compreendem as melhores rochas-reservatório de hidrocarbonetos da porção superior da Formação Barra Velha, na Bacia de Santos. Por outro lado, os mudstones, que não constituem as rochas-reservatório de hidrocarbonetos, são formadas em condições de lago com lâmina d'água profunda. A complexidade de fácies da Formação Barra Velha engloba também outras litologias como spherulitestones, rudstones, packstones, travertinos, dolostones, cherts e brechas (Wright & Barnett, 2015; Souza et al., 2018; Gomes et al., 2020; Carvalho & Fernandes; 2021; Rebelo et al., 2023). Porém, não são apenas as fácies que tornam esses carbonatos tão complexos: as modificações pós-deposicionais relacionadas a eventos de dissolução, silicificação e dolomitização, dentre outras alterações diagenéticas, são significativas. Elas ocorrem desde o momento da sua deposição e ao longo de vários ciclos de alterações durante o soterramento (Herlinger et al., 2017; Lima & De Ros, 2019; Lima et al., 2020). O ambiente deposicional, com suas características particulares de alta alcalinidade, altas concentrações de sílica e magnésio, e altas taxas de evaporação – junto com a ausência de bons análogos modernos para carbonatos lacustres – também contribuem para as dificuldades de entendimento da dinâmica sedimentar, das condições climáticas, do contexto tectônico, da química da água e da formulação de modelos deposicionais das fácies do pré-sal aptiano (Carvalho & Fernandes, 2021).

A cronologia da porção superior Formação Barra Velha também é um assunto controverso, já que Moreira et al. (2007) limitaram a porção superior Formação Barra Velha entre o intervalo de 117 – 113 Ma. Por outro lado, Lawson et al. (2022), baseando-se na datação isotópica de U-Pb de carbonatos da porção superior da Formação Barra Velha, sugerem uma idade deposicional de 115.83 ± 1.56 Ma para esta unidade. Porém, estudos bioestratigráficos e quimioestratigráficos (Tedeschi et al., 2017) situam o topo da Formação Barra Velha abaixo de ~120 Ma ou abaixo de ~125 Ma, de acordo com as diferentes calibrações de idade de Malinverno et al. (2010) ou Ogg et al. (2012) para o Evento de Anoxia Oceânica do Aptiano (OAE 1a). Em outro estudo, Pietzsch et al. (2020) propõe uma idade máxima Barremiano Superior para a deposição dos carbonatos da Formação Barra Velha. Como visto, a datação U-Pb dos constituintes da Formação Barra Velha é fundamental para estabelecer uma cronologia de eventos no sistema do pré-sal.

Minerais carbonáticos como calcita, dolomita, aragonita e magnesita podem se cristalizar por meio de processos diagenéticos, magmáticos, sedimentares, metamórficos e hidrotermais, podendo acumular urânio durante a sua formação, tornando-os úteis para a geocronologia U-Pb (Rasbury & Cole, 2009; Roberts et al., 2020). Em contraste com os carbonatos, o zircão é um mineral resistente a perturbações termais e é comumente utilizado como cronômetro U-Pb por incorporar teores de U no sítio do íon zircônio (Zr) e não incorporar nenhum Pb durante a sua cristalização. Desta forma, o Pb presente em zircões tem uma origem essencialmente radiogênica (Mezger & Krogstad, 1997; Montano, 2021). Por outro lado, os mecanismos de incorporação de U e Pb em carbonatos durante a cristalização e diagênese não são bem entendidos pois dependem de coeficientes de partição termodinamicamente determinados e de muitas variáveis. Por exemplo, dentre essas variáveis pode-se incluir a disponibilidade de elementos-traço, taxa de crescimento da calcita, temperatura, pH, Eh, pCO_2 e a razão $Ca^{2+}/CO_3{}^{2}$ em solução, raio iônico e complexação de U (Roberts et al., 2021). Além dessas variáveis, são importantes também as concentrações iniciais de U e Pb, alterações ou recristalizações a baixas temperaturas na presença de fluidos, difusão de Pb em temperaturas moderadas (Cherniak, 1997), além dos processos de formação de carbonatos serem complexos e duradouros (Rasbury & Cole, 2009). Então, uma das questões, quando se trata da datação de carbonatos, é sobre qual evento geológico está sendo representado pela idade (Rasbury & Cole, 2009; Drost et al., 2019; Roberts et al., 2020).

A datação de carbonatos tem sido realizada por meio de diluição isotópica por espectrometria de massas por ionização termal (ID-TIMS) ou por ablação a laser e espectrometria de massa com plasma indutivamente acoplado (ICP-MS) (Smith & Farquhar, 1989; DeWolf & Halliday, 1991; Brannon et al., 1996; Rasbury et al., 1997; Richards et al., 1998; Woodhead et al., 2006; Pickering et al., 2010).

Nos últimos anos, devido à vantagem em relação a alta resolução espacial e rápida aquisição de dados, a ablação a laser associada com um espectrômetro de massas com plasma indutivamente acoplado (LA-ICP-MS) tornou-se cada vez mais popular na datação U-Pb in situ de carbonatos. Estudos de eventos tectônicos e de fraturas (Hansman et al., 2018; Nuriel et al., 2019), de evolução termal de bacias sedimentares (Mangenot et al., 2018; MacDonald et al., 2019; Rochelle-Bates et al., 2022), e de interações rocha-fluido (Li et al., 2014; Godeau et al., 2018), são algumas das aplicações dessa técnica. No sistema do pré-sal, estudos foram realizados em carbonatos das bacias de Santos, Kwanza e da Namíbia (Rochelle-Bates et al., 2021; Godeau et al., 2021; Rochelle-Bates et al., 2022; Lawson et al., 2022), obtendo um amplo espectro de idades. As interpretações relacionadas a essas idades revelam que diferentes eventos deposicionais, diagenéticos, hidrotermais, tectônicos e magmáticos afetaram esses carbonatos.

As amostras analisadas foram obtidas de três poços do campo de Sapinhoá, localizado na parte central da Bacia de Santos. Um desses poços (9-BRSA-928-SPS) compreende um testemunho com cerca de 200 m de um intervalo quase contínuo amostrado da seção superior da Formação Barra Velha, no centro do campo. Neste testemunho é possível observar não apenas constituintes primários das rochas como shrubs, esferulitos, oncólitos e ostracodes, mas também a intensa diagênese que afeta esses carbonatos na forma de eventos de silicificação, dolomitização, carstificação, formação de brechas e fraturamento. Foram coletadas e analisadas também amostras de dois outros testemunhos: 7-SPH-6-SPS, localizado na parte norte do campo; e 9-BRSA-923A-SPS, localizado na porção sul e apesentando feições semelhantes às observadas no testemunho 928. O SPH-6 possui cerca de 30 m de intervalo contínuo da porção superior da Formação Barra Velha, enquanto o 923A possui aproximadamente 15 m de rochas testemunhadas, também da porção superior da Formação Barra Velha. A comparação das idades obtidas em amostras desses três testemunhos é importante para entender as variações mineralógicas e isotópicas em relação ao contexto diagenético, tectônico, estrutural, estratigráfico e magmático da bacia.

1.2 OJETIVOS DA DISSERTAÇÃO

O objetivo desta dissertação é a caracterização geocronológica de eventos deposicionais e diagenéticos nos carbonatos da porção superior da Formação Barra Velha. Para atingir esse objetivo, pretende-se:

- Identificar e caracterizar as fácies sedimentares que ocorrem nos testemunhos e nas lâminas petrográficas;
- Identificar principais produtos diagenéticos observados na petrografia, interpretando seu significado;
- Identificar a composição mineralógica, por meio de avaliação quantitativa de materiais por microscopia eletrônica de varredura (QEMSCAN), das fases observadas em petrografia;
- Relacionar as idades obtidas com a história geológica da Bacia de Santos e de outras bacias do Pré-sal, como as bacias de Campos, da Namíbia, e de Kwanza.

1.3 ESTRUTURA DA DISSERTAÇÃO

Esta dissertação de mestrado está organizada em cinco capítulos: Capítulo 1, que introduz o tema pesquisado e apresenta os objetivos deste trabalho; o Capítulo 2 apresenta a conceituação teórica sobre a geocronologia U-Pb, com foco na datação U-Pb em rochas carbonáticas, e aborda o contexto geológico do Pré-sal da Bacia de Santos; o capítulo 3, que apresenta os materiais e métodos utilizados no trabalho; o capítulo 4, no qual está o artigo intitulado "*U-Pb Dating of Carbonate Rocks From the Upper Barra Velha Formation: Implications for the Geological History of the Santos Basin*" a ser submetido ao periódico *Marine and Petroleum Geology*.; o capítulo 5, que constitui breves conclusões e recomendações deste trabalho sobre a utilização da geocronologia U-Pb nos carbonatos do pré-sal; e, por fim, o capítulo 6 apresenta o referencial bibliográfico.

CAPÍTULO 2

2.1 CONCEITUAÇÃO TEÓRICA

2.1.1 Geocronômetro U-Pb

O cronômetro isotópico U-Pb baseia-se nos processos de decaimento natural dos isótopos radioativos de U (os radionuclídeos) inicialmente incorporados no mineral a ser datado. Na natureza, os radionuclídeos mais comuns do U são o ^{238}U e o ^{235}U. Com o tempo, ^{238}U e o ^{235}U (os isótopos-mãe) decaem exponencialmente para os isótopos ^{206}Pb e ^{207}Pb (isótopos-filho) em uma taxa descrita por um parâmetro conhecido como meia-vida, que é de 4,47 bilhões de anos para a série de decaimento ^{238}U -> ^{206}Pb e de 0,703 bilhões de anos para a série de decaimento ^{235}U ->^{207}Pb. Depois de decorrida uma meia-vida, metade dos átomos do isótopo-mãe terá decaído para o isótopo-filho (Figura 1).

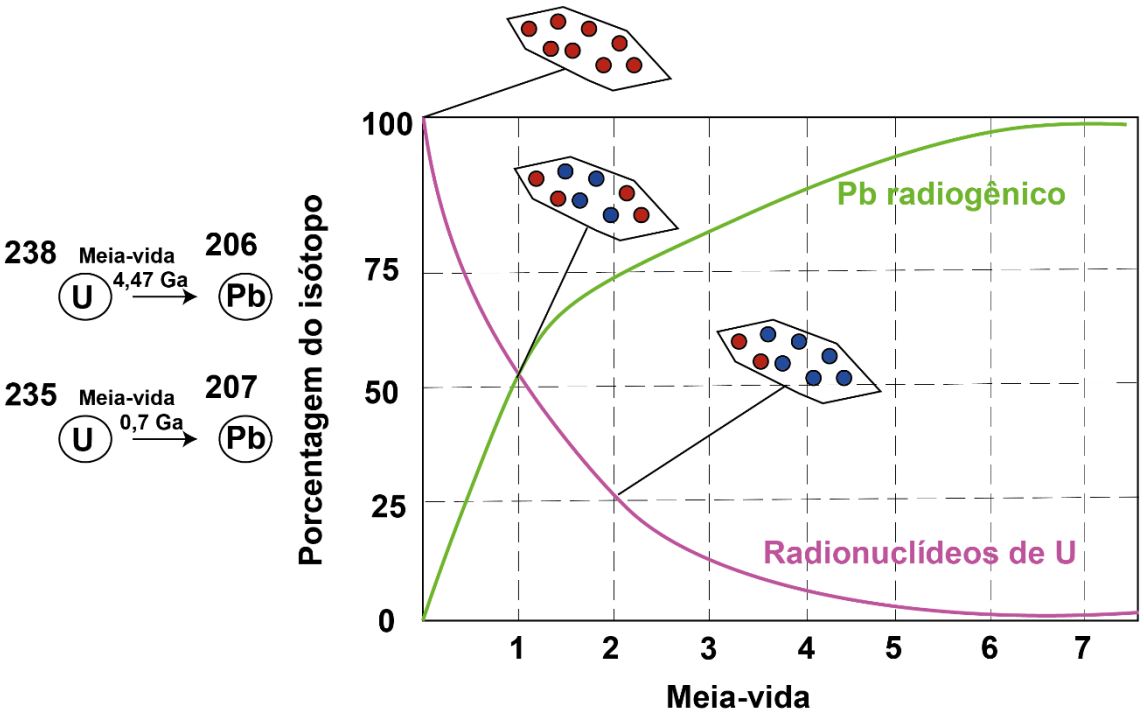

Figura 1. Esquema do processo de decaimento radiogênico dos isótopos ^{238}U e ^{235}U em ^{206}Pb e ^{207}Pb, respectivamente, de acordo com suas respectivas cadeias de decaimento e meia-vida. O tempo de meia-vida é o tempo necessário para que metade dos radionuclídeos de U se transformem em Pb. A taxa de decaimento é exponencial.

As duas series de decaimento são representadas pelas equações de Bateman (Bateman, 1910; Eqs 1.1 e 1.2):

$$^{206}Pb = {}^{206}Pb_0 + {}^{238}U\,(e^{\lambda 238t} - 1) \quad 1.1$$

$$^{207}Pb = {}^{207}Pb_0 + {}^{235}U\,(e^{\lambda 235t} - 1) \quad 1.2$$

onde o subscrito *0* se refere à concentração inicial do isótopo ou concentração de Pb não radiogênico (ou seja, Pb comum); λ é a constante de decaimento determinada com precisão; e t é o tempo decorrido desde o início da cristalização até o presente.

As técnicas de espectrometria de massa empregadas permitem coletar com mais precisão as razões isotópicas em vez da concentração individual de cada isótopo. Por isso, um isótopo estável tem que ser usado como referência para a normalização atuando como um denominador para as equações de decaimento. Como o ^{204}Pb não é radiogênico, e por ter a abundância constante desde o início da Terra, é utilizado como o isótopo de referência (Schoene, 2014). Normalizando as equações 1.1 e 1.2, resulta as seguintes equações:

$$^{206}Pb^*/^{204}Pb = (^{206}Pb/^{204}Pb)_0 + (^{238}U/^{204}Pb)\,(e^{\lambda 238t} - 1) \quad 1.3$$

$$^{207}Pb^*/^{204}Pb = (^{207}Pb/^{204}Pb)_0 + (^{235}U/^{204}Pb)\,(e^{\lambda 235t} - 1) \quad 1.4$$

Dividindo a equação 1.4 pela 1.3, chega-se na seguinte equação:

$$\frac{(^{235}U)(e^{\lambda 235t} - 1)}{(^{238}U)\,(e^{\lambda 238t} - 1)} = \frac{(^{207}Pb^* - {}^{207}Pb_0)}{(^{206}Pb^* - {}^{206}Pb_0)} \quad 1.5$$

*** refere-se à natureza radiogênica do Pb em questão**

A Equação 1.5 é muito útil porque permite evitar a medição da concentração do ^{235}U. Este isótopo tem uma menor abundância natural e uma meia-vida mais curta se comparado ao ^{238}U. Em relação ao ^{235}U, conclui-se que a maior parte do ^{235}U primordial da Terra já decaiu. Atualmente, a razão $^{238}U/^{235}U$ é considerada uma constante conhecida em sistemas terrestres e meteoríticos igual a 137,818 ± 0,045 (Hiess et al., 2012). Embora essa razão, juntamente com os valores das constantes de decaimento, ainda seja uma questão de debate na comunidade geocronológica (Craig et al., 2020), a única incógnita nesta equação continua sendo o Pb comum.

Existem diversas equações que permitem o cálculo da composição do Pb comum e diferentes diagramas têm sido usados como formas convenientes de exibir a composição

isotópica de Pb comum, como os diagramas da concórdia de Tera-Wasserburg e de Wetherill. A curva da concórdia (Wetherill, 1956) é uma curva paramétrica que define a evolução das razões de Pb radiogênico ao longo do tempo. Num sistema fechado, a composição de um mineral que inicialmente não incorpora nenhum Pb será plotada diretamente na curva da concórdia em uma posição que forneça a idade concordante da amostra. Em um modelo simplificado de decaimento das duas cadeias de decaimento U-Pb, sem Pb comum incorporado, as equações 1.1 e 1.2 seriam:

$$^{206}Pb^{*} = {}^{238}U\,(e^{\lambda 238 t} - 1) \quad 1.6$$

$$^{207}Pb^{*} = {}^{235}U\,(e^{\lambda 235 t} - 1) \quad 1.7$$

*** refere-se à natureza radiogênica do Pb em questão**

Como os dois sistemas de decaimento se desenvolvem em paralelo dentro de um determinado mineral, eles deveriam resultar na mesma idade (idade concordante). Assim, as equações 1.6 e 1.7 podem ser combinadas em um diagrama (diagrama da concórdia). Este diagrama coloca os resultados de $^{206}Pb/^{238}U$ versus $^{207}Pb/^{235}U$ de uma mesma análise. A curva concórdia não é linear, pois os isótopos de ^{238}U e ^{235}U possuem diferentes tempos de meia-vida. No diagrama da concórdia, todas as amostras que permaneceram como um sistema fechado desde o tempo de formação cairão sobre a curva (idade concordante). As que saem da curva são chamadas de discordantes e se comportaram como um sistema aberto (Dickin, 2005; Schoene, 2014)

Em minerais com alto teor de U, como zircão e monazita, a maior parte do Pb que ocorre é radiogênico e o eventual Pb comum pode ser negligenciado e ocasionalmente corrigido. Nesses minerais, o diagrama da concórdia geralmente utilizado é o de Wetheril (Wetherill, 1956), que utiliza as razões $^{206}Pb/^{238}U$ versus $^{207}Pb/^{235}U$. No entanto, para minerais como apatita ou carbonatos, que podem incorporar grande quantidade de Pb no momento da cristalização (Pb comum), a datação utiliza uma abordagem diferente: o diagrama da concórdia de Tera-Wasserburg (Tera & Wasserburg, 1972a,b).

2.1.2 Geocronologia de Carbonatos e Incorporação de U e Pb

Carbonatos são minerais com baixos a intermediários teores de U (10 ppb a 100 ppm; Weyer et al., 2008; Nuriel et al., 2021), que incorporam quantidades variáveis de Pb no momento da cristalização (Pb comum), resultando em uma alta variabilidade da razão

isotópica isótopo-mãe/isótopo-filho (por exemplo, $^{238}U/^{206}Pb$). Idades de carbonato obtidas através das duas cadeias de decaimento dificilmente serão concordantes e sua composição isotópica ficará fora da curva da concórdia.

O teor de Pb comum é avaliado pelo método da isócrona (Schoene, 2014), exigindo a realização de múltiplas análises na mesma fase carbonática. Se minerais carbonáticos coexistentes evoluíram a partir da mesma composição de Pb (isso é observável através de múltiplas análises no mesmo constituinte carbonático), os pontos formarão uma linha reta com significância de idade em um gráfico de $^{20x}Pb/^{204}Pb$ vs. $^{23x}U/^{204}Pb$ (Montano, 2021). É a isócrona. Porém, devido à dificuldade em medir o ^{204}Pb de forma precisa, pode-se fazer uso de isócronas alternativas como a de Tera-Wasserburg, que utiliza parâmetros normalmente bem detectados pelos coletores de Faraday como ^{238}U, ^{206}Pb, e ^{207}Pb (Ludwig, 1998; Woodhead et al., 2006). Portanto, a composição isotópica U-Pb de carbonatos é usualmente representada no diagrama da concórdia de Tera-Wasserburg que inclui ambas as cadeias de decaimento (^{238}U -> ^{206}Pb e ^{235}U ->^{207}Pb) e é o inverso do diagrama da concórdia de Wetherill. O diagrama da concórdia de Tera-Wasserburg apresenta a razão $^{238}U/^{206}Pb$ no eixo X e a razão $^{207}Pb/^{206}Pb$ no eixo Y.

Se $^{238}U/^{206}Pb^*$ e $^{207}Pb^*/^{206}Pb^*$ (* refere-se a Pb corrigido por Pb comum, como ocorre no diagrama da concórdia de Wetherill) forem plotados no diagrama da concórdia de Tera-Wasserburg, os dados concordantes e discordantes podem ser interpretados de forma idêntica ao diagrama da concórdia de Wetherill. No entanto, se um conjunto de amostras cogenéticas sair da concórdia por contaminação de Pb comum, então a regressão linear do conjunto de dados interceptará a concórdia no eixo X, correspondendo à idade, e interceptará o eixo Y ($^{207}Pb/^{206}Pb$) no valor de Pb comum. O diagrama da concórdia de Tera-Wasserburg, portanto, combina a eficácia da isócrona em obter uma composição de Pb comum com a eficácia de um diagrama da concórdia em testar se houve a abertura do sistema (Schoene, 2014). Um ponto de uma análise U-Pb será plotado com as seguintes coordenadas cartesianas:

$$\textbf{Eixo x: } \frac{(^{238}U)}{(^{206}Pb^*)} = \frac{1}{(e^{\lambda 238t} - 1)} \quad \textbf{1.8}$$

$$\textbf{Eixo y: } \frac{(^{207}Pb^*)}{(^{206}Pb^*)} = k\frac{(e^{\lambda 235t} - 1)}{(e^{\lambda 238t} - 1)} \quad \textbf{1.9}$$

*** refere-se à natureza radiogênica do Pb em questão**

onde k é a razão atual $^{235}U/^{238}U$ = 1/137,88 (Hiess e al., 2012). A curva da concordia é obtida considerando o mesmo t nas equações 1.8 e 1.9

A composição isotópica inicial de um carbonato (em t0) será plotada em um diagrama da concórdia de Tera-Wasserburg como um conjunto de pontos alinhados ao longo de uma linha de regressão horizontal. Com o tempo, os isótopos de U de cada ponto decaem para isótopos de Pb, resultando em um aumento progressivo da inclinação da linha de regressão. A idade da formação do carbonato é obtida pelo valor no qual a linha de regressão corta a curva da concórdia no intercepto inferior. Por esta razão, é chamada de "*Lower intercept age*" (Figura 2; Montano, 2021).

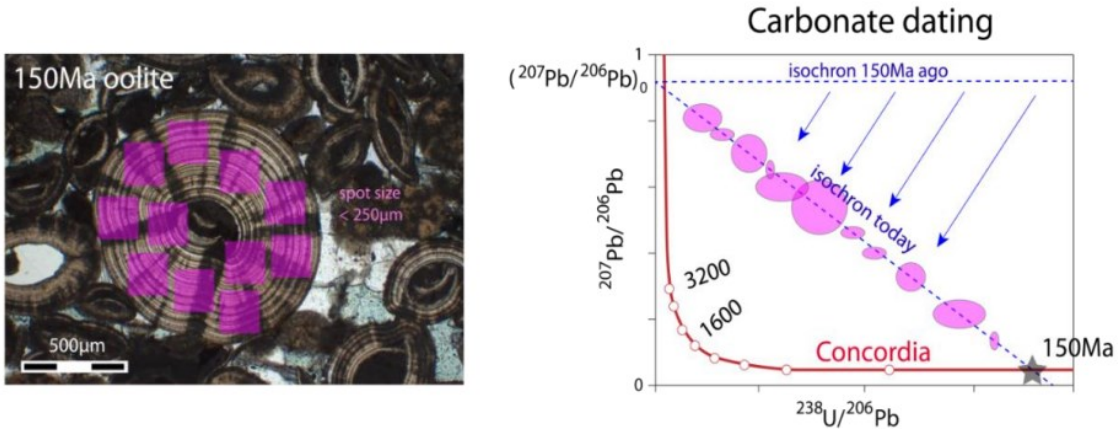

Figura 2. Geocronologia U-Pb em carbonatos e diagrama da concórdia de Tera-Wasserburg associado. À esquerda: imagem petrográfica de um oóide. Os quadrados roxos representam os pontos de análise. À direita: diagrama da concórdia de Tera-Wasserburg. Cada elipse roxa representa uma única análise e os respectivos valores das razões $^{238}U/^{206}Pb$ e $^{207}Pb/^{206}Pb$. O eixo maior e o eixo menor das elipses indicam as incertezas de cada uma das duas razões medidas. Em condições ideais, no momento da cristalização, as razões isotópicas U/Pb são heterogêneas e a razão Pb/Pb é homogênea, resultando em uma linha de regressão horizontal (a isócrona, marcada pela linha azul pontilhada). Conforme o tempo passa e o U decai para Pb radiogênico, a linha de regressão inclina-se e corta a curva da concórdia em uma posição que indica a idade da amostra (o intercepto inferior). O intercepto superior entre a regressão e o eixo y representa a composição inicial de $^{207}Pb/^{206}Pb$ do mineral (Montano, 2021).

Para obter uma robusta e significativa idade em uma amostra de carbonato, alguns pré-requisitos devem ser atendidos: 1) a composição inicial $^{207}Pb/^{206}Pb$ deve ser homogênea; 2) deve haver um espalhamento no valor da razão isotópica isótopo-mãe/isótopo-filho e é preferível que esta razão tenha valores altos; e 3) o sistema isotópico deve permanecer fechado. Os dois primeiros requisitos dizem respeito ao comportamento

do U e de seus isótopos-filho em sistemas aquosos e à captura deles pelos carbonatos. A complexidade dos sistemas carbonáticos pode facilmente resultar em heterogeneidade isotópica de Pb ou na homogeneidade da razão $^{238}U/^{206}Pb$. Atualmente, as circunstâncias para o sequestro heterogêneo de U e para a rejeição de Pb em carbonatos não são totalmente compreendidos, o que dificulta um bom resultado de datação. Outro fator fundamental a ser considerado é o impacto da diagênese que pode modificar a composição isotópica primitiva e, portanto, a idade (Rasbury et al., 2021; Montano, 2021).

Nos últimos anos, estudos focados na geocronologia de carbonatos e na incorporação de U e Pb em carbonatos têm aumentado (Rasbury & Cole, 2009; Kelly et al., 2003, Roberts et al., 2021; Miyajima et al., 2020).

Por exemplo, é sabido que o cátion Pb^{2+} é relativamente insolúvel e reativo a partículas, e em fluidos naturais este cátion é encontrado em baixas concentrações (ppt-ppb), possibilitando altas razões Ca/Pb (Rasbury & Cole, 2009). Apesar do raio iônico ligeiramente maior do Pb^{2+} em relação ao Ca^{2+} (Shannon, 1976; Rouff et al., 2004), ele possui afinidade pela calcita, substituindo o Ca^{2+} na rede cristalina, principalmente como um complexo de esfera interna (Rasbury & Cole, 2009).

A incorporação de U em carbonatos, por sua vez, é um processo mais complexo e menos compreendido do que a incorporação de Pb. A especiação de U no fluido está ligada às condições redox de baixa temperatura do fluido, enquanto a solubilidade do U depende principalmente de Eh e pH (Klinkhammer & Palmer, 1991; Seder-Colomina et al., 2018). O U tem dois estados de oxidação comumente identificados: U^{4+} (mais comum em condições redutoras) e U^{6+} (mais comum em ambientes oxidantes). U^{4+} tem um raio iônico semelhante ao do Ca^{2+} (0.89 Å, Shannon, 1976) e então poderia ser incorporado nos carbonatos. Contudo, U^{4+} é insolúvel em sistemas naturais e é usualmente capturado por outros minerais que precipitam em ambientes redutores, como a uraninita, por exemplo. Nenhum experimento laboratorial realizado em baixa temperatura demonstrou a incorporação de U^{4+} em carbonatos, porém: 1) elevadas concentrações de U ocorrem em carbonatos naturais com a forma reduzida do U (e.g. Klinkhammer & Palmer, 1991; Sturchio et al., 1998; Cole et al., 2004); 2) concentrações progressivamente altas de U foram detectadas em depósitos profundos nas Bahamas, onde outros parâmetros geoquímicos (Mo, V, Cr e Co) sugeriram condições fortemente redutoras (Wray et al., 2018); e 3) concentrações particularmente altas de U foram detectadas em cimentos precipitados a partir de águas subterrâneas anóxicas profundas (Drake et al., 2018).

Portanto, condições redutoras devem promover a concentração de U em carbonatos. Uma possível justificativa para a incorporação de U^{4+} em carbonatos foi proposta por Rasbury et al. (2021). Baseando-se nas altas concentrações de U encontradas nas tufas lacustres da Formação Barstow e nos carbonatos de Mono Lake, os autores sugeriram que o U^{4+} pode ser complexado com algum oxiânion (um fosfato ou bicarbonato, por exemplo) no fundo do lago e então incorporado ao carbonato durante a formação. Conclusivamente, parece que o U^{4+} é a espécie mais estável de U em carbonatos (Roberts et al., 2021).

Em condições oxidantes, o U^{6+} existe na forma do complexo uranila (UO_2^{2+}) (Langmuir, 1978) e é mais solúvel que o U^{4+}. O íon uranila é maior que os sítios do UO_2 e do Ca^{2+}. Assim, devido ao seu tamanho maior e a sua maior solubilidade em fluidos naturais, o entendimento da ocorrência do íon uranila em carbonatos é um desafio antigo. Kelly et al. (2003) e Reeder et al. (2001) demonstraram que o íon uranila pode ser singeneticamente incorporado em carbonatos no sítio do íon Ca^{2+}, sendo uma captura iônica duradoura e que promove uma distorção na estrutura cristalina do carbonato (Kelly et al., 2003; 2006).

Minerais ricos em uranila e em U (uraninita, por exemplo) formados em condições redutoras também podem ser adsorvidos pela superfície da rede cristalina (Carroll et al., 1992, Geipel et al., 1997, Elzinga et al., 2004, Rihs et al., 2004). Este processo de adsorção é influenciado pela especiação do U^{4+}, pela concentração de Ca no fluido, pelo pH e por processos biogeoquímicos. Em particular, quando o pH > 7, a porcentagem de U^{4+} adsorvido por complexos de esfera interna diminui fortemente, enquanto sob pH mais ácido a adsorção do U^{4+} aumenta (Elzinga et al., 2004).

Diferentes pseudomorfos de carbonato também são caracterizados por diferentes concentrações de U. Sabe-se que a incorporação de U é maior em aragonita > calcita com alto teor de Mg > calcita (Chung & Swart, 1990; Reeder et al., 2001). Isto é possivelmente devido a uma incompatibilidade de tamanho entre U e Mg que é maior do que aquela entre U e Ca (Rasbury & Cole, 2008). Em relação à dolomita, nenhum estudo experimental foi publicado sobre a incorporação de U em dolomitas. No entanto, devido às estruturas semelhantes, espera-se que a dolomita incorpore concentrações de U similares às das calcitas com alto teor de Mg (Rasbury et al., 2021).

Embora não esteja claro como a interação entre esses fatores afeta a captura de U em carbonatos, foi observado que tipos específicos de carbonatos são caracterizados por

elevadas e heterogêneas concentrações de U, e concentrações mais baixas e homogêneas de Pb, produzindo idades U-Pb robustas (Rasbury & Cole, 2009 e Roberts et al., 2021). Estes são espeleotemas (Woodhead et al., 2006; Woodhead & Petrus, 2019), *hardgrounds*, carbonatos aragoníticos ou geralmente carbonatos que possuem aragonita como precursor (Roberts et al., 2020a; Nuriel et al., 2021).

2.2 CONTEXTO GEOLÓGICO

2.2.1 Localização da Área de Estudo

A Bacia de Santos localiza-se na região sudeste da margem continental brasileira, entre os paralelos 23° e 28° Sul, abrangendo uma área de cerca de 350.000 km² até a cota batimétrica de 3.000 m (Moreira et al., 2007). A bacia se estende ao longo do litoral dos estados do Rio de Janeiro, São Paulo e Paraná, sendo separada da Bacia de Campos, a norte, pelo Alto de Cabo Frio. Seu limite Sul consiste no lineamento formado pelo Alto de Florianópolis, feição que a separa da Bacia de Pelotas (Figura 3).

A área de estudo está localizada na porção central da Bacia de Santos (Figura 3A), distante do litoral do estado de São Paulo por cerca de 310 km e ocupando uma área de aproximadamente 230 km² (Figura 3B). A estrutura do campo de Sapinhoá consiste em um *horst* alongado na direção NE-SW limitado por falhas normais de direção NNE que condicionaram o desenvolvimento de uma plataforma carbonática isolada (Sartorato, 2018).

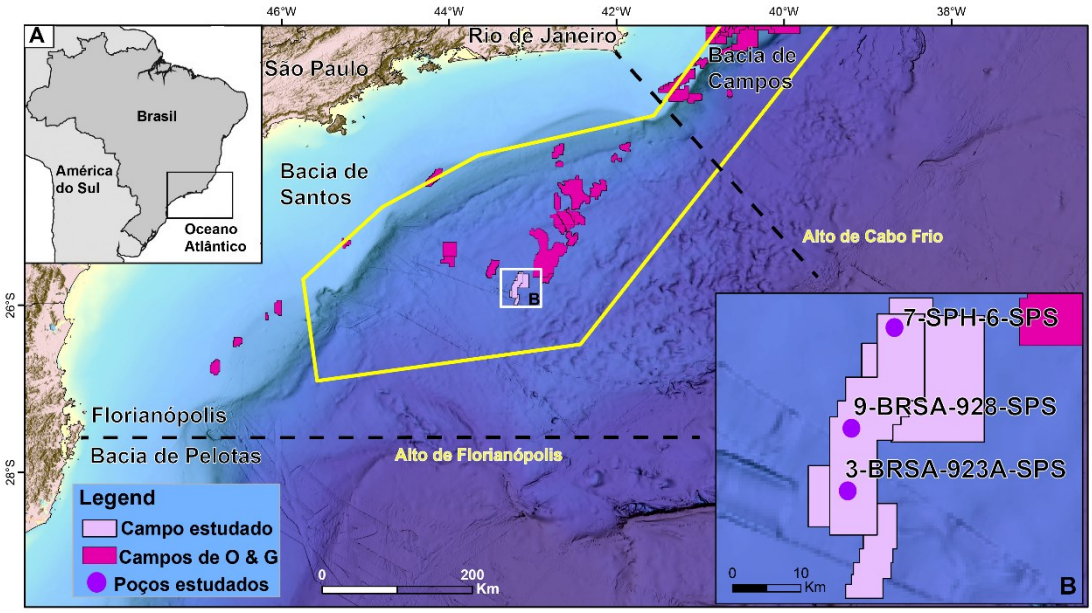

Figura 3. (A) Área de estudo localizada na região sudeste da margem continental brasileira, mais especificamente na Bacia de Santos. O campo de Sapinhoá (em lilás) está na porção central da Bacia de Santos. O polígono amarelo representa o polígono do pré-sal. Em magenta, estão os demais campos de petróleo. No norte, a Bacia de Santos é separada da Bacia de Campos pelo Alto de Cabo Frio. Ao sul, é o Alto de Florianópolis que separa a Bacia de Santos da Bacia de Pelotas. (B) Detalhe do campo de Sapinhoá, mostrando a distribuição dos três poços estudados ao longo do campo.

2.2.2 O Pré-sal da Bacia de Santos

A Bacia de Santos foi formada devido à quebra do supercontinente Gondwana durante o Cretáceo Inferior em torno de 135-140 Ma (Karner et al., 2021; Rangel et al., 1994). Esta bacia está localizada na porção sudeste da margem atlântica brasileira, limitada ao sul pela Bacia de Pelotas através do Alto de Florianópolis, e a sua parte norte é limitada pela Bacia de Campos através do Alto de Cabo Frio, cobrindo uma área de aproximadamente 350 mil km² (Ariza Ferreira et al., 2019).

A Bacia de Santos é classificada como uma bacia de margem passiva, que inclui o estágio sin-rifte (Hauteriviano ao Barremiano Superior), no qual os basaltos da Formação Camboriú marcam o início da fase rifte e representam o embasamento econômico da Bacia de Santos (Chang et al., 1992; Mohriak et al., 2008). Com a evolução gradual do rifteamento, a Fm. Camboriú foi sobreposta pelos depósitos flúvio-lacustres das formações Piçarras e Itapema, compostas por arenitos, siltitos e folhelhos de composição talco-estevensítica e por coquinas intercaladas com folhelhos, respectivamente (Moreira et al., 2007). A contração termal da crosta resultou em subsidência e colapso de domos

crustais, gerando bacias do tipo “sag” (Beasley et al., 2010). O intervalo pós-rifte/sag é composto por depósitos barremiano-aptianos da Formação Barra Velha, associados a águas lacustres saturadas e alcalinas (Wright & Barnett, 2015); e por evaporitos da Formação Ariri que foram depositados em um cenário paleogeográfico semelhante a um golfo com águas altamente salinas e sob um balanço hidrológico negativo (Chang et al., 1992). A sequência drifte compreende carbonatos plataformais e arenitos de águas rasas, e folhelhos e arenitos turbidíticos de águas profundas (Moreira et al., 2007; Gomes et al., 2012; Arienti et al., 2018; Neves et al., 2019).

A porção superior da Formação Barra Velha, que é o foco deste estudo, compreende três principais componentes e fácies relacionadas: (1) carbonatos laminados com granulometria de argila (os mudstones); (2) partículas milimétricas com formato esférico (esferulitos; spherulitestones) e (3) partículas milimétricas a centimétricas com formato semelhante ao de arbustos (shrubs; shrubstones). Esses constituintes frequentemente ocorrem retrabalhados, formando grainstones, packstones e rudstones. De acordo com Wright & Barnett (2015), a argila, os esferulitos e os shrubs (e as suas respectivas fácies relacionadas), ocorrem em intervalos de padrões cíclicos. Da base para o topo do ciclo, ocorrem argila e mudstones, esferulitos e spherulitestones (podendo ocorrer com argila intersticial), e shrubs e shrubstones (também podendo ocorrer com argila intersticial e com partículas de esferulitos). Basso et al. (2021) compilaram elementos de diversos estudos sobre os carbonatos do pré-sal e propuseram um novo modelo dos ciclos, semelhante ao ciclo proposto por Wright & Barnett (2015), mas considerando as fácies retrabalhadas: grainstones e packstones intraclásticos ocorrendo nas porções intermediárias dos ciclos; e com grainstones, rudstones e shrubstones marcando o topo dos ciclos.

A evolução tectono-sedimentar da Bacia de Santos, segundo Moreira et al. (2007), identifica seis principais discordâncias dentro da sequência do pré-sal (Figura 4A). As duas primeiras discordâncias são a base e o topo dos basaltos da Formação Camboriú. A seguinte, conhecida como Discordância Pré-Jiquiá (DPJ), limita a Formação Piçarras. Sobrejacente à DPJ, encontra-se a Formação Itapema cujo topo é limitado pela Discordância Pré-Alagoas (DPA). Esta última discordância marca a base da Formação Barra Velha, que é dividida em dois intervalos: Barra Velha Inferior e Barra Velha Superior; esses intervalos são separados pela Discordância Intra-Alagoas (DIA) de 117 Ma (Moreira et al., 2007) e correspondem às fases sin-rifte e sag, respectivamente

(Moreira et al., 2007; Wright e Barnett., 2015). A base do sal marca o limite superior da Formação Barra Velha, representando a discordância da base do sal (Moreira et al., 2007).

2.2.3 Idades de Magmatismo na Bacia de Santos e de Hidrotermalismo no Sistema Pré-sal.

Ao menos quatro eventos magmáticos foram identificados na Bacia de Santos (Moreira et al., 2007; Gomes et al., 2015; Oliveira et al., 2023). O evento mais antigo, Camboriú (~130 Ma, Moreira et al., 2007), é relacionado ao estágio rifte. Essas rochas são contemporâneas com o derrame basáltico continental Paraná-Etendeka e com o enxame de diques Serra do Mar, no sudeste do Brasil (134 – 132 Ma, idades $^{40}Ar/^{39}Ar$ em plagioclásio e em rocha total; Guedes et al., 2005; Thiede & Vasconcelos, 2010; Gomes & Vasconcelos, 2021).

Os basaltos toleíticos barremiano-aptianos do pós-rifte, datados de 125,5 ± 0,7 Ma por Rancan et al. (2018) são contemporâneos aos basaltos de idade Barremiana-Aptiana (127,4 ± 2,3 Ma) da Bacia de Kwanza (Trittla et al., 2018). Esse magmatismo Barremiano-Aptiano da Bacia de Santos está associado principalmente com a Formação Itapema (Rancan et al., 2018). Os eventos magmáticos do pós-rifte também incluem diabásios toleíticos e alcalinos de idade entre ~113 Ma e ~120 Ma (Moreira et al., 2007): os eventos Tupi (~120 Ma), Parati (~115 Ma), e Sul de Santos (~113 Ma). Esse magmatismo do Aptiano está associado com as formações Barra Velha e Itapema e, em escala regional, com a Discordância Intra-Alagoas (Ren et al., 2020). Recentemente, Hunt et al. (2021) mencionaram um magmatismo mais jovem que o Parati, denominado Pós-Parati Picinguaba, que ocorreu no campo de Bacalhau (Bacia de Santos). Louback et al. (2023) reportaram idades de basaltos toleíticos no campo de Bacalhau variando de 116 a 109 Ma (Figura 4B).

A atividade magmática foi acompanhada por uma ampla alteração hidrotermal que afetou os basaltos e a sucessão carbonática. Idades de alteração hidrotermal no pré-sal foram obtidas em rochas das bacias de Santos, Campos e Kwanza. Na Bacia de Santos, Rancan et al. (2018) obtiveram uma idade $^{40}Ar/^{39}Ar$ de 114,3 ± 1,1 Ma em alteração hidrotermal de um basalto toleítico. Uma idade $^{40}Ar/^{39}Ar$ mais jovem de 49,9 ± 0,45 Ma, do Eoceno, também foi obtida por Rancan et al. (2018) em uma alteração de rochas da suíte alcalina do Santoniano-Campaniano. Já na Bacia de Campos, atividade hidrotermal foi datada por meio de datação $^{40}Ar/^{39}Ar$ em adulária, obtendo idades de 107,0 ± 1,0 –

104,3 ± 0,8 Ma (Tritlla et al., 2018), enquanto na Bacia de Kwanza, duas idades de alterações hidrotermais em basaltos foram obtidas por Loma et al. (2018): uma idade $^{40}Ar/^{39}Ar$ mais velha do Aptiano Superior, de 114,5 ± 2,9 Ma; e uma idade albiana mais jovem, também por $^{40}Ar/^{39}Ar$, de 106,9 ± 1,6 Ma (Figura 4C).

A Bacia de Santos também foi afetada por um magmatismo mais jovem associado ao estágio drifte: os magmatismos Santoniano-Campaniano (~ 82 Ma; $^{40}Ar/^{39}Ar$; Oreiro, 2006; Rancan et al., 2018) e do Eoceno (~ 49 Ma; $^{40}Ar/^{39}Ar$; Dias et al., 1990; Rancan et al., 2018). As idades publicadas do magmatismo Santoniano-Campaniano são de 82 ± 1 Ma (Szatmari, 2001) e de 83,3 ± 0,66 Ma – 72,4 ± 4,9 Ma (Rancan et al., 2018). As idades do magmatismo do Eoceno, por sua vez, são de 48,9 Ma (Szatmari, 2001) e 41,06 ± 0,02 Ma a 38,62 ± 0,02 Ma (Louback et al., 2021). Esses magmatismos relacionados ao estágio drifte compreendem principalmente rochas alcalinas vulcânicas entre as sequências sedimentares do pré-sal, e rochas intrusivas que cortam as rochas sedimentares do pré-sal (Moreira et al., 2006).

2.2.4 Idades de Deposição de Carbonatos e de Diagênese nas Bacias do Pré-sal

Idades de carbonatos de constituintes do pré-sal foram obtidas por datação U-Pb através de técnicas como LA-ICP-MS e ID-TIMS (Goudeau et al., 2021; Rochelle-Bates et al., 2021; Lawson et al., 2022; Rochelle-Bates et al., 2022). Fases calcíticas da porção superior da Formação Barra Velha datadas por Rochelle-Bates et al. (2022) geraram idades de 107,0 ± 27,2 Ma e 113,0 ± 15,3 Ma para shrubs. Em esferulitos, as idades foram de 107,6 ± 5,1 Ma e 77,0 ± 11,2. Esses autores, então, reuniram os dados da população mais antiga de calcita primária, obtendo uma idade de 114,0 ± 13,4 Ma para os shrubs, e uma idade de 106,9 ± 4,3 Ma para todas as partículas de calcita (shrubs e esferulitos).

Fases de dolomita também foram analisadas por Rochelle-Bates et al. (2022), obtendo idades de 58,0 ± 4,6 Ma e 59,2 ± 5,3 Ma para "pontes" de dolomita e para dolomita romboédrica, respectivamente. Lawson et al. (2022) também publicou idades de U-Pb em carbonatos da porção superior da Formação Barra Velha, obtidas por LA-ICP-MS. Tais idades variaram de 114 ± 4,72 Ma a 58,85 ± 10,74 Ma, e uma análise por ID-TIMS produziu uma idade de 115,83 ± 1,56 Ma. Lawson et al. (2022) interpretaram essas idades como não deposicionais, exceto pelas idades de 115,83 ± 1,56 Ma, 114 ± 4,72 Ma e 109,73 ± 9,26 Ma. Rochelle-Bates et al. (2021) publicaram idades de veios de calcita (86,2 ± 2,4 Ma) e de veios de dolomita (56,8 ± 4,8 Ma) na Bacia da Namíbia. Já na Bacia

de Kwanza, Godeau et al. (2021) publicaram idades de 112-110 Ma para veios de calcita; de 115 – 90 para dolomita romboédrica pervasiva; 92 Ma para veios de calcedônia; e uma idade de 85,45 ± 9,5 Ma para cristais de calcita preenchendo porosidade vugular (Figura 4D). A tabela com os dados utilizados para os histogramas da figura 4 estão disponíveis nos anexos.

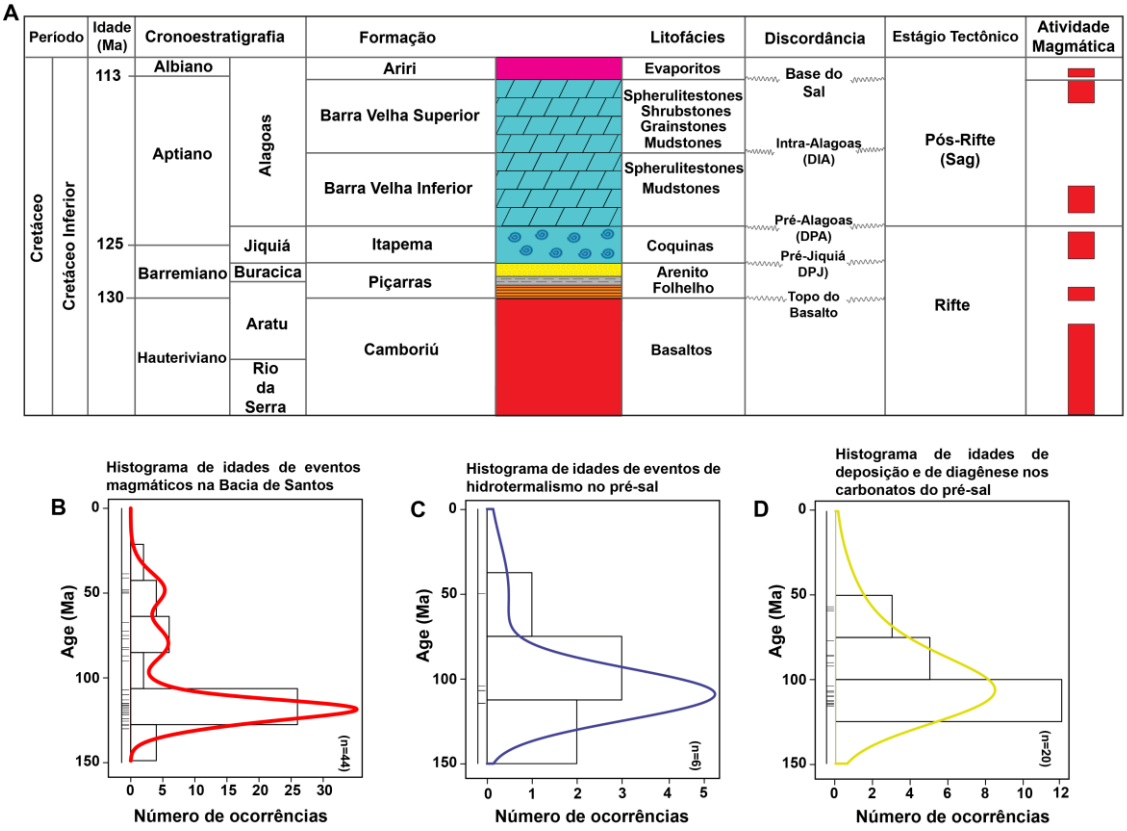

Figura 4. (A) Seção estratigráfica do Cretáceo Inferior da Bacia de Santos (adaptado de Moreira et al., 2007). (B) Histograma de idades de eventos magmáticos na Bacia de Santos. (C) Histograma das idades de eventos de hidrotermalismo no pré-sal (dados das bacias de Santos, Campos, Namíbia e Kwanza). (D) Histograma de idades deposicionais e de diagênese registradas no pré-sal (dados das bacias de Santos, Namíbia e Kwanza). Os dados utilizados para a construção dos histogramas estão disponíveis nos anexos e são das seguintes referências: Rochelle-Bates et al. (2021); Godeau et al. (2021); Rochelle-Bates et al. (2022); Lawson et al. (2022); Moreira et al. (2007); Szatmari & Milani, (2016); Trittla et al. (2018); Loma et al. (2018); Rancan et al. (2018); Louback et al. (2021); Godeau et al. (2021); Rochelle-Bates et al. (2021); Louback et al. (2023); Gordon et al. (2023); Oliveira et al. (2023).

CAPÍTULO 3

3.1 MATERIAIS E MÉTODOS

3.1.1 Correlação por Perfis de Raios Gama

A correlação dos poços foi realizada considerando o perfil de raios gama dos três poços estudados (3-BRSA-923A-SPS, 9-BRSA-928-SPS e 7-SPH-6-SPS; Figura 5A). A correlação é importante porque os testemunhos foram amostrados em diferentes partes da porção superior da Fm. Barra Velha. Por exemplo, no poço 928 foram amostrados ~ 200 m de um intervalo quase contínuo da parte superior da Formação Barra Velha; no poço 923A foram amostrados aproximadamente 15 metros; e no poço SPH-6 foram amostrados ~30 m. Portanto, para fins de comparação, deve-se saber se os intervalos amostrados são correlacionáveis.

3.1.2 Petrografia

Trinta e quatro amostras foram coletadas de 3 testemunhos descritos (3-BRSA-923A-SPS, 9-BRSA-928-SPS e 7-SPH-6-SPS) da porção superior da Formação Barra Velha (Figura 5B). Dessas amostras, foram observadas e descritas lâminas delgadas com espessura de 120 μm com o auxílio do microscópio *Axioscope 5*, da ZEISS. Das amostras de lâminas delgadas, 15 foram selecionadas para análise de U-Pb in situ por LA-ICP-MS.

3.1.3 Imageamento por QEMSCAN

Mapas mineralógicos detalhados foram obtidos usando um Quanta FEI 650F acoplado a um microscópio eletrônico de varredura com dois detectores de energia dispersiva. As lâminas delgadas foram revestidas com carbono e o equipamento foi configurado com uma corrente de 10 nA e uma voltagem de 15kV, para a geração de mapas com resolução de 10 μm. As análises foram realizadas no QEMLab da Universidade de Brasília. As imagens QEMSCAN ajudaram na distinção de características petrográficas e relações de substituição, incluindo alterações diagenéticas de constituintes primários e cimento.

3.1.4 Geocronologia U-Pb em Carbonatos

Dados de U-Pb foram obtidos no laboratório de geocronologia da Universidade de Brasília, utilizando o Espectrômetro de Massas Multicoletor de Alta Resolução (*Thermo Scientific Neptune XT*) acoplado a um sistema de ablação a laser *Analyte Excite*, da

Teledyne. As massas de interesse foram medidas em um espectrômetro de massa multi-coletor. O sistema de ablação a laser está equipado com uma câmara de volume dupla *HelEx II*. O espectrômetro de massa foi configurado para melhorar a sensibilidade dos sinais de U e de Pb enquanto minimiza a produção de óxidos antes de cada sessão analítica. Cada análise consistiu na medição de 10 s de sinal de fundo, seguida por 20 s de aquisição de sinal da amostra. As massas (202, 204, 206-208, 232, 238) foram medidas simultaneamente utilizando uma combinação dos seguintes detectores: copos de Faraday, multiplicadoras de elétrons secundários (SEM), e multiplicadores de elétrons de diodos discretos compactos (CDD). As condições do laser incluem um diâmetro do feixe de 85 μm, frequência de 10 Hz, e fluência de 4.0 J/cm^2. O dado bruto foi processado no *Iolite 4.0* (Paton et al., 2011) como sinal resolvido no tempo, e a inspeção individual do sinal foi feita com o auxílio da ferramenta *VizualAge* (Petrus & Kamber, 2012). A redução dos dados foi feita utilizando o esquema de redução de dados *UComPbine*, que leva em conta o Pb comum variável no material de referência (Chew et al., 2014), e as correções incluíram subtração de branco, correção de fracionamento à medida que ocorre a ablação usando um modelo exponencial + linear, e normalização pela calcita *Walnut Canyon* (Roberts et al., 2017). O valor de Pb comum usado para ancorar o dado foi de 0,85 ± 0,04 (Roberts et al., 2017). A calcita da Formação Barstow (Cole et al., 2005; Rasbury & Cole, 2009) foi usada como controle de qualidade. Excesso de variância do material de referência primário foi propagado em cada ponto analítico. Incerteza sistemática de cerca de 1% foi propagada em cada idade final. Nenhuma correção de Pb comum foi aplicada. As idades são cotadas em um intervalo de confiança de 95%.

Após a redução dos dados, o IsoplotR (Veermesch, 2018) foi utilizado para plotar dados U-Pb em diagramas da concórdia do tipo Tera – Wasserburg. Todas as idades são valores de onde a regressão linear corta o intercepto inferior (o eixo $^{238}U/^{206}Pb$) dos diagramas da concórdia Tera-Wasserburg, dentro de um intervalo de confiança de 2s, e a qualidade do ajuste da regressão linear é avaliada usando a estatística qui-quadrado reduzida, conhecida na geocronologia como *Mean Squared Weighted Deviation* (MSWD). Os valores claramente discrepantes são provavelmente uma consequência da análise de inclusões, fases diferentes ou misturas, e esses dados são rejeitados nas regressões para o cálculo da idade. Quando o diagrama da concórdia é traçado no IsoplotR, duas incertezas são calculadas para a idade obtida. Por exemplo, o resultado aparece assim: idade = x ± y (| z), onde x é a idade calculada na concórdia (em Ma); y é o erro padrão de x ou a

incerteza analítica de x (em 2s); e z é o erro padrão de x multiplicado por $\sqrt{}$MSWD para levar em conta qualquer sobredispersão. Na verdade, z só é medido e recomenda-se considerar z como a incerteza da idade se houver sobredispersão nos dados, ou seja, se o valor do MSWD diferir consideravelmente de 1,0 (Veermesch, 2018).

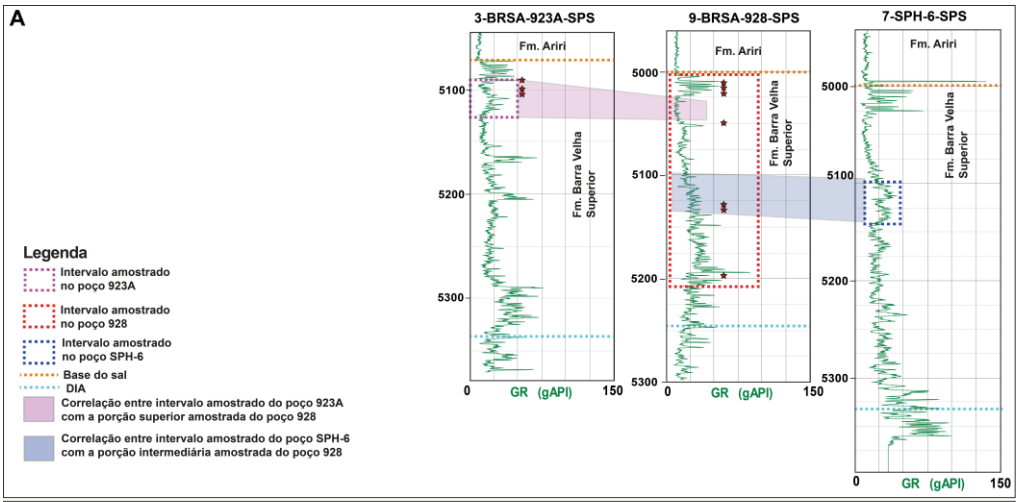
A
3-BRSA-923A-SPS
9-BRSA-928-SPS
7-SPH-6-SPS
Fm. Ariri
Fm. Barra Velha Superior
GR (gAPI)
Legenda
Intervalo amostrado no poço 923A
Intervalo amostrado no poço 928
Intervalo amostrado no poço SPH-6
Base do sal
DIA
Correlação entre intervalo amostrado do poço 923A com a porção superior amostrada do poço 928
Correlação entre intervalo amostrado do poço SPH-6 com a porção intermediária amostrada do poço 928

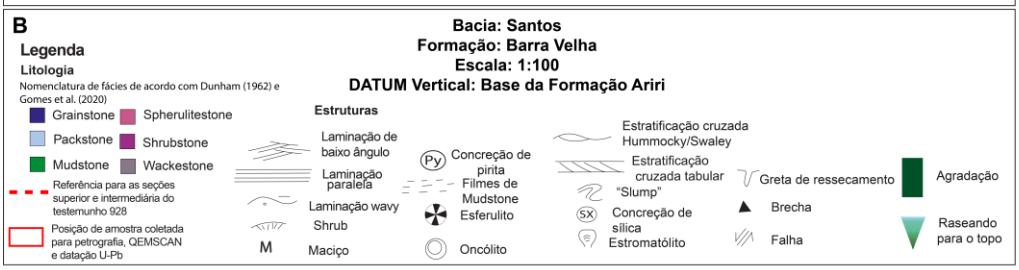
B
Bacia: Santos
Formação: Barra Velha
Escala: 1:100
DATUM Vertical: Base da Formação Ariri
Legenda
Litologia
Nomenclatura de fácies de acordo com Dunham (1962) e Gomes et al. (2020)
Grainstone
Spherulitestone
Packstone
Shrubstone
Mudstone
Wackestone
Referência para as seções superior e intermediária do testemunho 928
Posição de amostra coletada para petrografia, QEMSCAN e datação U-Pb
Estruturas
Laminação de baixo ângulo
Laminação paralela
Laminação wavy
Shrub
Maciço
Concreção de pirita
Filmes de Mudstone
Esferulito
Oncólito
Estratificação cruzada Hummocky/Swaley
Estratificação cruzada tabular
"Slump"
Concreção de sílica
Estromatólito
Greta de ressecamento
Brecha
Falha
Agradação
Raseando para o topo

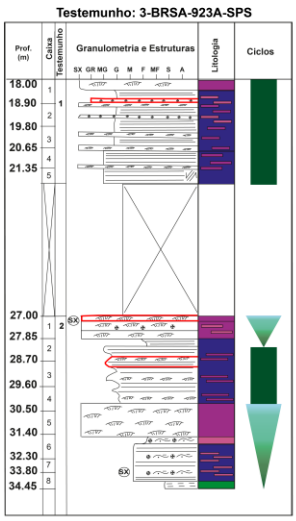
Testemunho: 3-BRSA-923A-SPS
Prof. (m)
Caixa Testemunho
Granulometria e Estruturas
Litologia
Ciclos

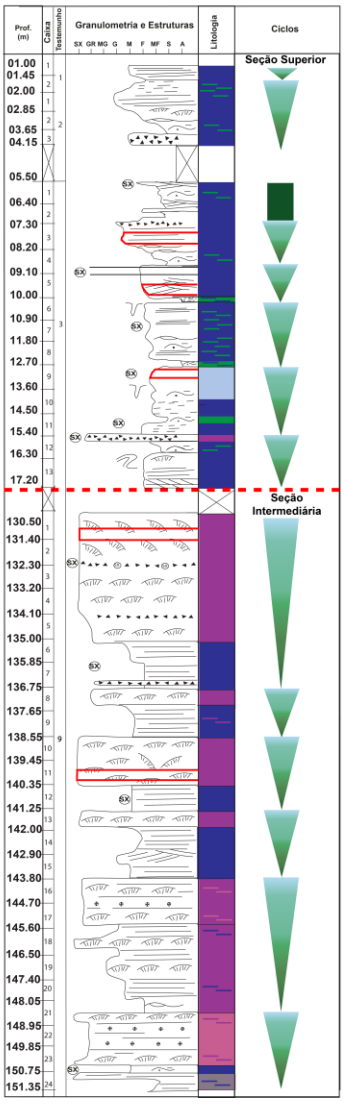
Testemunho: 9-BRSA-928-SPS
Prof. (m)
Caixa Testemunho
Granulometria e Estruturas
Litologia
Ciclos
Seção Superior
Seção Intermediária

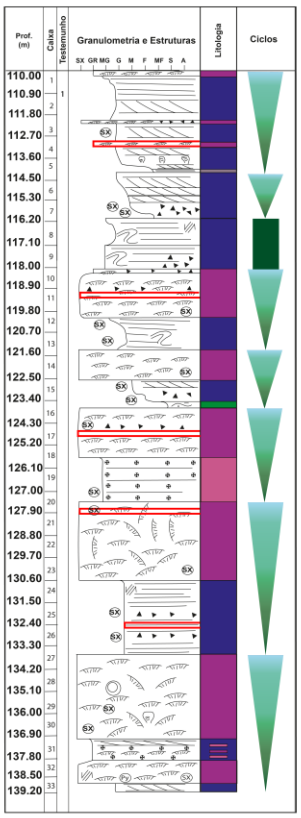
Testemunho: 7-SPH-6-SPS
Prof. (m)
Caixa Testemunho
Granulometria e Estruturas
Litologia
Ciclos

Figura 5. (A) Correlação estratigráfica entre os poços estudados, por meio de perfil de raios-gama. O polígono roxo tracejado representa a porção amostrada do poço 923A. O polígono Vermelho tracejado representa a porção amostrada do poço 928. O polígono azul tracejado representa a porção amostrada do poço SPH-6. A linha tracejada laranja representa a base do sal. A linha azul tracejada marca a Discordância Intra-Alagoas. O polígono lilás marca a correlação entre a porção amostrada do poço 923A, que corresponde aos 15 metros imediatamente abaixo do marco Lula, com os 30 metros superiores da porção amostrada do poço 928, que provavelmente engloba o mesmo ou nível estratigráfico semelhante que o amostrado pelo testemunho 923A. O polígono azul marca a correlação entre a parte amostrada do poço SPH-6, que corresponde entre cerca de 100 m a 140 m de profundidade abaixo da base do sal, com a porção intermediária amostrada do poço 928 que provavelmente compreende um intervalo estratigráfico semelhante àquele compreendido pelo testemunho SPH-6. (B) Perfis estratigráficos da porção superior da Formação Barra Velha, amostrada pelos três poços estudados. A linha tracejada vermelha marca a divisão do testemunho 928 em duas partes: (1) a seção superior, localizada dentro de ~ 20 metros logo abaixo da base do sal, que provavelmente está em uma posição estratigráfica similar a do testemunho 923A; e (2) uma seção intermediária do testemunho 928, localizada entre 100 m e 150 m abaixo da base da Fm. Ariri, e que provavelmente corresponde a uma posição estratigráfica semelhante àquela na qual o testemunho SPH-6 foi amostrado. Os polígonos vermelhos marcam locais de houve amostragem para análises de U-Pb em carbonatos.

CAPÍTULO 4

U-Pb Dating of Carbonate Rocks From the Upper Barra Velha Formation: Implications for the Geological History of the Santos Basin

J.P.S. Brito[a,*], R.V. Santos[a], C.J. Abreu[a], P.L. Barbosa[a] , G.O. Gonçalves[a] , C.E.S. Cruz[a], C.A. Ushirobira[a], V.S. Souza[a], F. Richter[a]

[a]University of Brasilia, Institute of Geosciences, Graduate Program in Geology.

*corresponding author: joao-brito.jb@aluno.unb.br

Highlights

• Primary calcite underwent U-Pb replacement;

• Microcrystalline and fine dolomite rhombs registered the first direct U-Pb Barremian ages of the Barra Velha Fomation carbonates;

• U-Pb carbonate ages are related to tectono-thermal events that affected the Santos Basin and other Pre-salt basins;

• An age spatial relation exists between the studied wells;

• The mineralogy of the particles and their physical properties, such as porosity and permeability, have a huge influence on the U-Pb ages.

Abstract: Deposition, diagenesis, and chronology of Upper Barra Velha carbonates are subjects of interest as these themes are still being properly understood. To elucidate the chronology of these events and to understand how the U-Pb isotopic system works in carbonate minerals, we present an integrated study of conventional petrography, QEMSCAN imaging, and in situ U-Pb dating of carbonate samples from wells A, B and C of the Zeta field, in the central part of Santos Basin. Our results span three main geochronological intervals: ~127/125 Ma, ~116/114 Ma, and ~105/100 Ma. Calcite primary particles from wells A and B underwent U-Pb replacement, resulting in ages of ~106 Ma. Otherwise, similar particles from well C exhibited ages around 115 Ma. Considering that the younger ages obtained in wells A and B overlap magmatic and hydrothermal events in the pre-salt, we suggest that a nearby heat source drove the hydrothermal system. However, this younger event not affected the ages of well C. Concerning dolomites, they showed that the geochronological replacement of particles may not be a pervasive effect, but may depend on fluid-rock interactions, mineralogy, porosity and permeability of geological materials. For instance, the non-porous, non-permeable, and less reactive dolomitic aggregates were not affected by U-Pb replacement. Indeed, primary microcrystalline and fine dolomite rhombs recorded the first direct Barremian ages of the Barra Velha carbonates. Regarding secondary dolomites, they were separated in pre and post-silicification dolomites. The former occurs as Barremian-Aptian ~124 Ma microcrystalline and fine dolomite rhombs; as ~117 – 108 Ma

lamellar and pervasive rhombohedral dolomites; and as pseudomorphic dolomites that underwent U-Pb replacement during the Albian-Cenomanian. Post-silicification dolomites have ages of ~ 100 Ma and are represented by later diagenetic cements like blocky and saddle dolomites. The latter temporally limits a silicification event as older than 100 Ma.

Keywords: U-Pb replacement; Carbonate dating; Barra Velha Formation; Fluid-rock interaction

4.1 INTRODUCTION

The origin, diagenesis, and hydrothermal processes of carbonate rocks that host the Brazilian pre-salt oil reservoirs have been debated by many recent studies (Wright and Barnett, 2015; Souza et al., 2018; Farias et al., 2019; Lima et al., 2020; Carvalho and Fernandes; 2021; Rebelo et al., 2023), as these reservoirs may be considered non-conventional deposits, with very few good modern analogs and unique characteristics. Therefore, tectonic, petrographic, sedimentological, stratigraphic and geochemical informations are helping to unravel the peculiarities of this complex geological system. For instance, the radiogenic $^{87}Sr/^{86}Sr$ ratio of these carbonates (0.7111–0.7141; Pietzsch et al., 2018; Farias et al., 2019; Lima et al., 2020; Lawson et al., 2022) points to a non-marine depositional environment in which the facies pattern was influenced by lake-level oscillations and by a substrate with paleo-highs and paleo-lows (Wright and Barnett, 2015; De Paula Faria et al., 2017).

Shrubstones and grainstones are facies formed during low-lake level conditions whose have porosity and high permeability, comprehending the best hydrocarbon reservoir rocks from the Upper Barra Velha Formation of the Santos Basin. Facies with low porosity and low permeability such as mudstones are not good hydrocarbon reservoirs and are supposed to be formed in high-lake level conditions (Wright & Barnett, 2015). The complexity of facies from the Barra Velha Formation comprises also another lithologies such as spherulitestones, rudstones, packstones, travertines, dolostones, cherts, and breccias (Wright and Barnett, 2015; Souza et al., 2018; Gomes et al., 2020; Carvalho and Fernandes; 2021; Rebelo et al., 2023). Nevertheless, it is not just the facies that make these carbonates so complex. The impacts of dissolution, silicification and dolomitization events, among other diagenetic effects, are very significative. They modify the Barra Velha carbonates from the moment of their deposition, going through several cycles of alteration during burial (Herlinger et al., 2017; Lima and De Ros, 2019; Lima et al., 2020). The depositional environment, with its unique characteristics of high alkalinity, high concentration of silica and magnesium, and high evaporative conditions — together with

the absence of good modern analogs for rift-to-sag lacustrine carbonates — also makes difficult to understand the sedimentary dynamics, climate conditions, tectonic context, water chemistry, and depositional predict ability of facies in the Aptian pre-salt (Carvalho and Fernandes, 2021).

The chronology of the Barra Velha Formation is also a controverse subject as Moreira et al. (2007) put the Upper Barra Velha Formation within the interval of 117 – 113 Ma and Lawson et al. (2022), based on direct U-Pb dating of carbonates from the Upper Barra Velha Formation, suggest a depositional age of 115.8 ± 1.6 (2s) Ma for this unit. On the other hand, biostratigraphic and chemostratigraphic studies such as the one from Tedeschi et al. (2017) place the top of the Barra Velha Formation below ~120 Ma or below ~125 Ma, according to different age calibrations of Malinverno et al. (2010) or Ogg et al. (2012) for the Aptian Ocean Anoxic Event (OAE 1a). Another study, from Pietzsch et al. (2020), proposes an older Late Barremian alternative maximum depositional age for the Barra Velha Formation carbonates. As such, the U-Pb dating of the Barra Velha Formation constituents is essential to establish a chronology of events in the pre-salt system.

Carbonate minerals such as calcite, dolomite, aragonite, and magnesite can be crystallized in diagenetic, magmatic, sedimentary, metamorphic, and hydrothermal processes. These minerals can accumulate uranium during their formation, making them useful for U–Pb geochronology (Rasbury and Cole, 2009; Roberts et al., 2020). Unlike carbonates, zircon is a mineral that is commonly used as a U-Pb chronometer because it incorporates amounts of U at the site of Zirconium ion (Zr) and virtually no Pb during its crystallization. This means that most of the Pb occurring in zircon crystals has a radiogenic origin (Mezger and Krogstad, 1997; Montano, 2021). On the other hand, the mechanisms for U and Pb incorporation and replacement in carbonates during deposition and diagenesis are not well understood because they do not rely on determined partition coefficients, but on a large number of phenomenological variables. These include trace element availability, calcite growth rate, temperature, pH, Eh, pCO_2 and the Ca^{2+}/CO_3^{2-} ratio in solution, ionic size, and U complexation (Roberts et al., 2021). Also, calcite is typically low in U and rich in initial Pb, it is susceptible to alteration or recrystallization at low temperatures in the presence of fluids, and allows Pb diffusion above moderate temperatures (Cherniak, 1997). Hence, the process of carbonate formation can be complex and long-lived (Rasbury & Cole, 2009). Then, the question, when it comes to

carbonate dating, arises as to which geological event is being dated (Rasbury & Cole, 2009; Drost et al., 2019; Roberts et al., 2020).

The dating of carbonates has been carried out using isotope dilution (ID) thermal ionization mass spectrometry (TIMS) or inductively coupled plasma mass spectrometry (ICP-MS) (Smith and Farquhar, 1989; DeWolf and Halliday, 1991; Brannon et al., 1996; Rasbury et al., 1997; Richards et al., 1998; Woodhead et al., 2006; Pickering et al., 2010). In recent years, due to the advantage in terms of high spatial resolution and rapid data acquisition, laser ablation inductively coupled plasma mass spectrometry (LA-ICP-MS) has become increasingly popular in carbonates in situ U–Pb dating, with a broad spectrum of applications within the geosciences. These applications include the assessment of tectonic events and fracturing (Hansman et al., 2018; Nuriel et al., 2019), the thermal evolution of sedimentary basins (Mangenot et al., 2018; MacDonald et al., 2019; Rochelle-Bates et al., 2022) and fluid-rock interactions (Li et al., 2014; Godeau et al., 2018). In the pre-salt system, U-Pb dating of carbonates from Santos, Kwanza and Namibe basins (Rochelle-Bates et al., 2021; Godeau et al., 2021; Rochelle-Bates et al., 2022; Lawson et al., 2022) indicate a wide range of ages that have been interpreted to different depositional, diagenetic, hydrothermal, tectonic and magmatic events.

The samples analyzed were from three wells of the Zeta field, located in the Santos Basin's central part (Figure 1A-B). In one of these wells (B), located in the center of the field, an almost continuous interval of ~ 200 m of the Upper Barra Velha Formation was sampled. In this well, it is possible to observe not only the primary features of the rocks as shrubs, spherulites, oncolites, and ostracods. Still, it is also possible to notice the intense diagenesis affected these carbonates as revealed by silicification, dolomitization, karstification, brecciation, and fracturing events. Another two wells were sampled and analyzed, one at the northern part and another at the southern of the field. Those comprehend smaller sampled intervals, with the northern well (C) comprehending ~ 30 m of a continuous interval of the Upper Barra Velha Formation, while the southern well (A) comprises ~ 15 m of cored rocks from the Barra Velha Formation.

This work presents an integrated study of petrography, quantitative evaluation of minerals by scanning electron microscopy (QEMSCAN) imaging, and in situ U-Pb carbonate dating on samples from three Zeta field wells. Primary and secondary carbonate constituents were dated after being identified and adequately characterized by petrographic-QEMSCAN imaging study. We relate the age and formation of these rocks

to the geological evolution of the Santos Basin, including syn-depositional and post-depositional processes related to diagenetic, tectonic, magmatic, or hydrothermal events.

4.2 GEOLOGICAL SETTING

The Santos Basin formed during the breakup and extension of the Gondwana supercontinent in the Early Cretaceous (~ 140-135 Ma) (Karner et al., 2021; Rangel et al., 1994). Placed in the southeastern portion of the Brazilian Atlantic margin, the basin covers an area of approximately 350,000 km². It is limited to the south by the Pelotas Basin through the Alto de Florianópolis and the northern part by the Campos Basin through the Alto de Cabo Frio (Ariza Ferreira et al., 2019) (Figure 1A).

The Santos Basin is classified as a passive margin basin. It includes three primary sequences: a synrift stage (Hauterivian to Late Barremian), in which the Camboriú Formation basalts mark the beginning of the rift phase and development of the economic basement of the Santos Basin (Chang et al., 1992; Mohriak et al., 2008). With the gradual evolution of the rift system, the Camboriú Formation was overlain by the fuvio-lacustrine deposits of the Piçarras and Itapema Formations, which are dominated by sandstones, siltstones and shales of talc-stevensitic composition and coquinas interlayered with shales, respectively (Moreira et al., 2007). The thermal contraction of the crust resulted in the subsidence and collapse of crustal domes, generating sag-type basins (Beasley et al., 2010). The post-rift/sag interval is composed of Barremian-Aptian deposits of the Barra Velha Formation, associated to highly saturated and alkaline lacustrine waters (Wright and Barnett, 2015), and evaporites of the Ariri Formation that were deposited in a paleogeographic scenario similar to a gulf with highly saline waters and negative hydrological balance (Chang et al.,1992). A drift sequence comprises shallow-water shelf carbonates and sandstones, and deep-water turbidites shales and sandstones (Moreira et al., 2007; Gomes et al., 2012; Arienti et al., 2018; Neves et al., 2019).

The Upper Barra Velha Formation, the focus of this study, comprises three main components and facies: (1) mud-grained laminated carbonates (mudstones); (2) millimetric spherulites (spherulitestones); and (3) millimetric to centimetric shrub-shaped particles (shrubstones). These constituents are often reworked, forming grainstones, packstones, and rudstones. According to Wright and Barnett (2015), the mud, spherulites, and shrubs occur in cyclic-pattern intervals with different thicknesses. The cycles, from base to top, are comprehended by mud and mudstones, spherulites and spherulitestones,

and shrubs and shrubstones. Basso et al. (2021) compiled elements from several studies on the pre-salt carbonates and proposed a new cycle model similar to that from Wright and Barnett (2015), but considering the reworked facies, with intraclastic grainstones and packstones occurring in the middle part of the cycle, and with grainstones, rudstones and shrubstones marking the top of the cycles.

The tectonic-sedimentary evolution of the Santos Basin pre-salt includes five sequences (i.e. Camboriú Formation, Piçarras Formation, Ipanema Formation, Lower Barra Velha Formation, and Upper Barra Velha Formation) separated by five unconformities (i.e. basalt top, Pre-Jiquiá (PJU), Pre-Alagoas (PAU), Intra-Alagoas (IAU), and Salt Base (Moreira et al., 2007) (Figure 1C). The Pre-Alagoas Unconformity separates the rift and post-rift-sag stages; the Intra-Alagoas Unconformity divides the Barra Velha Formation into two depositional episodes (the Lower Barra Velha and the Upper Bara Velha), whereas the salt base limits the top of the Upper Barra Velha Formation (Moreira et al., 2007; Wright and Barnett., 2015).

4.2.1 Ages of Magmatism in the Santos Basin and Hydrothermalism in the Pre-salt System

Magmatic events have been identified in the Santos Basin (Moreira et al., 2007; Gomes et al., 2015; Oliveira et al., 2023). An older event named Camboriú (~130 Ma, Moreira et al., 2007) is related to the rift stage. These rocks are contemporaneous with Paraná-Etendeka continental flood basalts and the Serra do Mar dike swarm in SE Brazil (ca. 134 – 132 Ma, plagioclase and whole-rock $^{40}Ar/^{39}Ar$ ages; Guedes et al., 2005; Thiede and Vasconcelos, 2010; Gomes and Vasconcelos, 2021). They are also coeval with the 134 ± 4 Ma Cabiúnas basalts from the Campos basin (whole-rock, K–Ar ages; Mizusaki et al., 1992).

The post-rift Barremian-Aptian tholeiitic basalts dated at 125.5 ± 0.7 Ma by Rancan et al. (2018) are contemporaneous to the Barremian-Aptian age (127.4 ± 2.3 Ma) basalts from the Kwanza Basin (Trittla et al., 2018). This Barremian-Aptian magmatism of the Santos Basin is mostly associated with the Itapema Formation (Rancan et al., 2018). The post-rift magmatism also includes alkaline and tholeiitic diabase dated between ~113 and ~120 Ma (Moreira et al., 2007): Tupi (~120 Ma), Parati (~115 Ma), and South of Santos (~113 Ma) events. This Early Aptian magmatism of the Santos Basin is associated with the Itapema and Barra Velha formations and, at a regional scale, with the Intra-

Alagoas Unconformity (Ren et al., 2020). Recently, Hunt et al. (2021) mentioned a younger magmatism than Parati, the post-Paraty Picinguaba Magmatic Event, occurring in the Bacalhau field (Santos Basin), and Louback et al. (2023) reported tholeiitic basalt ages varying from 116 to 109 Ma in the same area (Figure 1D).

The magmatic activity was accompanied by a widespread hydrothermal alteration that affected basalts and the carbonate succession. Ages of hydrothermal alteration in the pre-salt were dated in rocks from the Santos, Campos, and Kwanza basins. In the Santos Basin, Rancan et al. (2018) obtained an $^{40}Ar/^{39}Ar$ age of 114.3 ± 1.1 Ma in a hydrothermal alteration in a tholeiitic basalt. A younger $^{40}Ar/^{39}Ar$ Eocene age of 49.9 ± 0.45 Ma was also obtained by Rancan et al. (2018) for an alteration in rocks from the Santonian-Campanian alkaline suite. In the Campos Basin, hydrothermal (90–170°C) activity was dated with adularia $^{40}Ar/^{39}Ar$ ages of 107.0 ± 1.0 – 104.3 ± 0.8 Ma (Tritlla et al., 2018), while in the Kwanza Basin, two ages of hydrothermal (c. 140°C) alteration in basalts were obtained by Loma et al. (2018): an older $^{40}Ar/^{39}Ar$ Late Aptian age of 114.5 ± 2.9 Ma, and a younger, also by $^{40}Ar/^{39}Ar$, mid-Albian age of 106.9 ± 1.6 Ma (Figure 1E).

The Santos Basin has also been affected by a younger magmatism associated with the drift stage: the Santonian-Campanian (ca. 82 Ma; $^{40}Ar/^{39}Ar$; Oreiro, 2006; Rancan et al., 2018) and Eocene (ca. 49; $^{40}Ar/^{39}Ar$; Dias et al., 1990; Rancan et al., 2018) magmatisms. The Santonian-Campanian published ages of this magmatism are 82 ± 1 Ma (Szatmari, 2001) and 83.3 ± 0.66 Ma – 72.4 ± 4.9 Ma (Rancan et al., 2018). The Eocene magmatism ages are of 48.9 Ma (Szatmari, 2001) and 41.06 ± 0.02 Ma (1s) to 38.62 ± 0.02 Ma (1s) (Louback et al., 2021). These drift-related magmatism comprises mostly alkaline volcanic rocks within the post-salt sedimentary sequences and intrusive rocks that cut the pre-salt sedimentary rocks (Moreira et al., 2006).

4.2.2 Ages of Carbonate Deposition and Diagenesis in the Pre-salt Basins

Carbonate ages from the pre-salt constituents were carried out by U-Pb dating techniques such as LA-ICP-MS and ID-TIMS (Goudeau et al., 2021; Rochelle-Bates et al., 2021; Lawson et al., 2022; Rochelle-Bates et al., 2022). Carbonate primary phases from the Upper Barra Velha Formation dated by Rochelle-Bates et al. (2022) yielded ages of 107.0 ± 27.2 Ma (2s) and 113.0 ± 15.3 Ma (2s) for two samples of calcite shrubs. The spherulitic calcites yielded ages of 107.6 ± 5.1 (2s) Ma and 77.0 ± 11.2 Ma (2s). The authors pooled the data from the older calcite population, obtaining an age of 114.0 ±

13.4 Ma (2s) for all analyzed shrubs and 106.9 ± 4.3 Ma (2s) for all calcite analyses. Dolomite phases were also analyzed by Rochelle-Bates et al. (2022), obtaining ages of 58.0 ± 4.6 Ma (2s) and 59.2 ± 5.3 Ma (2s) for dolomite bridges and dolomite rhombs, respectively. Lawson et al. (2022) also reported LA-ICP-MS U-Pb ages in carbonates from the Upper Barra Velha Formation ranging from 114 ± 4.7 Ma (2s) to 58.8 ± 10.7 Ma (2s), and an ID-TIMS age of 115.83 ± 1.56 Ma (2s). They interpreted these ages as non-depositional, except for the 115.83 ± 1.56 Ma (2s), 114 ± 4.72 Ma (2s) and 109.73 ± 9.26 Ma (2s) ages. Rochelle-Bates et al. (2021) reported younger calcite (86.2 ± 2.4 Ma; 2s) and dolomite (56.8 ± 4.8 Ma; 2s) veins in the Namibe basin. In the Kwanza Basin, Godeau et al. (2021) reported ages of 112-110 Ma of calcite veins; 115 – 90 Ma for pervasive rhombohedral dolomites; 92 Ma for chalcedony-filling veins; and an age of 85.45 ± 9.5 Ma for vug calcites (Figure 1F). The data used for the Figure 1D-F is available as supplementary material.

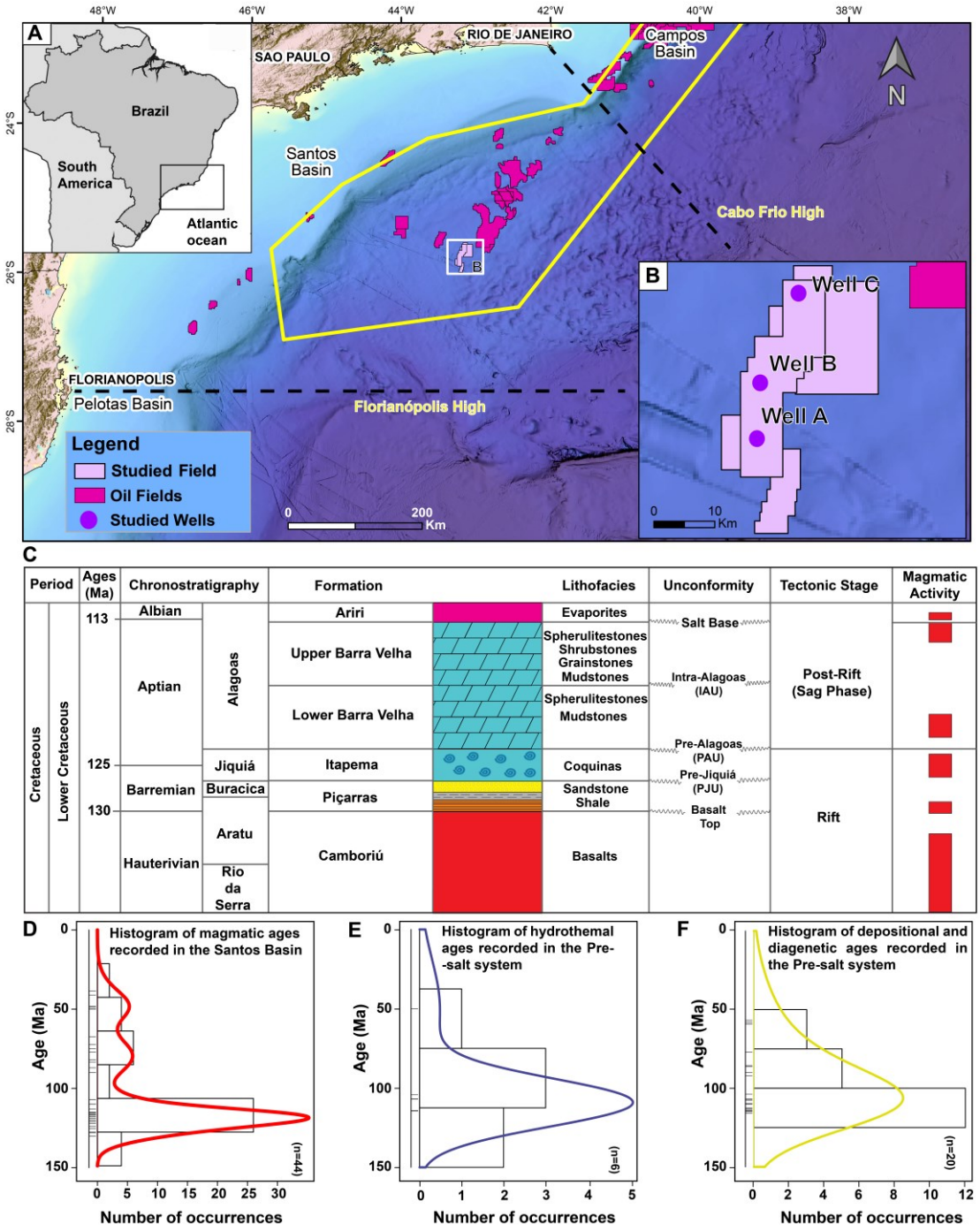

Figure 1. (A) Location of the Zeta field in the central portion of the Santos Basin. The yellow polygon represents the Pre-salt polygon, with the oil fields illustrated in magenta. In the northern part, the Santos Basin is separated by the Campos Basin through the Cabo Frio High. In the south, the Florianópolis High separates the Santos Basin from the Pelotas Basin. (B) Detail of the Zeta field, showing the distribution of the three wells studied along the area. (C) Lower Cretaceous stratigraphic section of the Santos Basin (adapted from Moreira et al., 2007). (D) Histogram of magmatism ages in the Santos Basin. (E) Histogram of hydrothermal events ages in the Pre-salt system. (F) Histogram of depositional and diagenetic ages recorded in the Pre-salt system. The data compiled from other studies are available in the supplementary material (Rochelle-Bates et al., 2021; Rochelle-Bates et al., 2022; Lawson et al., 2022; Moreira et al., 2007;

Szatmari & Milani, 2016; Trittla et al., 2018; Loma et al., 2018; Rancan et al., 2018; Louback et al., 2021; Godeau et al., 2021; Rochelle-Bates et al., 2021; Louback et al., 2023; Gordon et al., 2023; Oliveira et al., 2023).

4.3 DATA AND METHODS

4.3.1 Well Correlation

The well correlation was carried out considering the gamma ray log from the three wells studied (A, B, and C; Figure 2). The correlation is important because the cores were sampled at different parts of the Upper Barra Velha Formation For instance, in the well B, ~ 200 m of an almost continuous interval of the Upper Barra Velha Fm were sampled; in the well A, ~15 meters were sampled; and in the well C, ~ 30 m were sampled. So, for comparison purposes, we should know if the sampled intervals correlate with each other.

4.3.2 Petrography

Thirty-four samples were collected from the three described and studied cores (A, B and C). From these samples, thin sections with 120 μm thickness were observed and described using the microscope ZEISS Axioscope 5. Among these samples, fifteen were selected for carbonate in situ U-Pb LA-ICP-MS analyses.

4.3.3 QEMSCAN Imaging

Detailed mineralogical maps were obtained using a Quanta FEI 650F coupled to a scanning electron microscope with two energy-dispersive (EDS) detectors. We carbon-coated the thin sections to generate 10 μm resolution maps and set the instrument to a 10 nA current and a 15 kV voltage. Mineralogical data for each mineral were presented as a percentage of mass and surface area. Analyses were carried out at the QEMLab of the University of Brasilia. The QEMSCAN images were beneficial for distinguishing petrographic features and replacement relationships, including diagenetic changes of primary constituents and cement.

4.3.4 U-Pb Carbonate Geochronology

U-Pb data were obtained at the Geochronology Laboratory at the University of Brasília, Brazil, using a Thermo Scientific Neptune XT sector-field ICP-MS coupled to an 193 nm Teledyne Analyte Excite laser ablation system. The laser ablation system is equipped with a HelEx II dual-volume chamber. The mass spectrometer was tuned to improve U and Pb sensitivity while minimizing oxide production before each analytical

session. 20 spots of 85 μm were carried out in each analyzed phase. Each analysis consisted of 10 s of background measurement followed by 20 seconds of sample acquisition. Each mass (202, 204, 206-208, 232, 238) was measured simultaneously using a combination of Faraday cups, Secondary Electron Multipliers (SEM) and Compact Discrete Dynode Electron Multipliers (CDD) detectors. Laser conditions included a spot diameter of 85 μm, 10 Hz, and 4.0 J cm^{-2}. Raw data was processed on Iolite 4.0 (Paton et al., 2011) as time-resolved signal and individual signal inspection VizualAge tool (Petrus and Kamber, 2012). Data reduction using UComPbine data reduction scheme (DRS) accounts for variable initial lead on the primary calibrant (Chew et al., 2014). Corrections included blank subtraction, downhole using an exponential plus linear model, and normalization by the Walnut Canyon calcite (Roberts et al., 2017). The initial lead for anchoring the data was 0.85 ± 0.04 (Roberts et al., 2017). Barstow Formation calcite has an age range of 14.8 ± 0.3 to 16.2 ± 0.2 Ma (2s) (Cole et al., 2005; Rasbury and Cole, 2009) and was used for quality control. Excess variance on the primary calibrant was propagated on each analytical point. No common lead correction was applied.

After data reduction, IsoplotR (Veermesch, 2018) was used to plot U–Pb data on Tera–Wasserburg-type concordia plots. All ages are presented as lower intercept $^{238}U/^{206}Pb$ ages that were anchored using the common lead composition (the initial $^{207}Pb/^{206}Pb$ value) of the respective analyzed constituent (Chew et al., 2014). Ages are quoted at 2s absolute, and the goodness of fit is evaluated using the mean squared of weighted deviation (MSWD). When the Concordia diagram is plotted in the IsoplotR, two calculated uncertainties exist for the age result. For instance, the result appears this way: age = x ± y (| z), where x is the Concordia age (in Ma); y is the standard error of x or the analytical uncertainty of x (at 2s); and z is the standard error of x multiplied by $\sqrt{}$ MSWD to account for any overdispersion. We considered z as the uncertainty value that is included in the uncertainty propagation by quadratic addition. Excess variance and age uncertainty of reference material are propagated where appropriate.

Details about the methodology and dataset are available in the supplementary material.

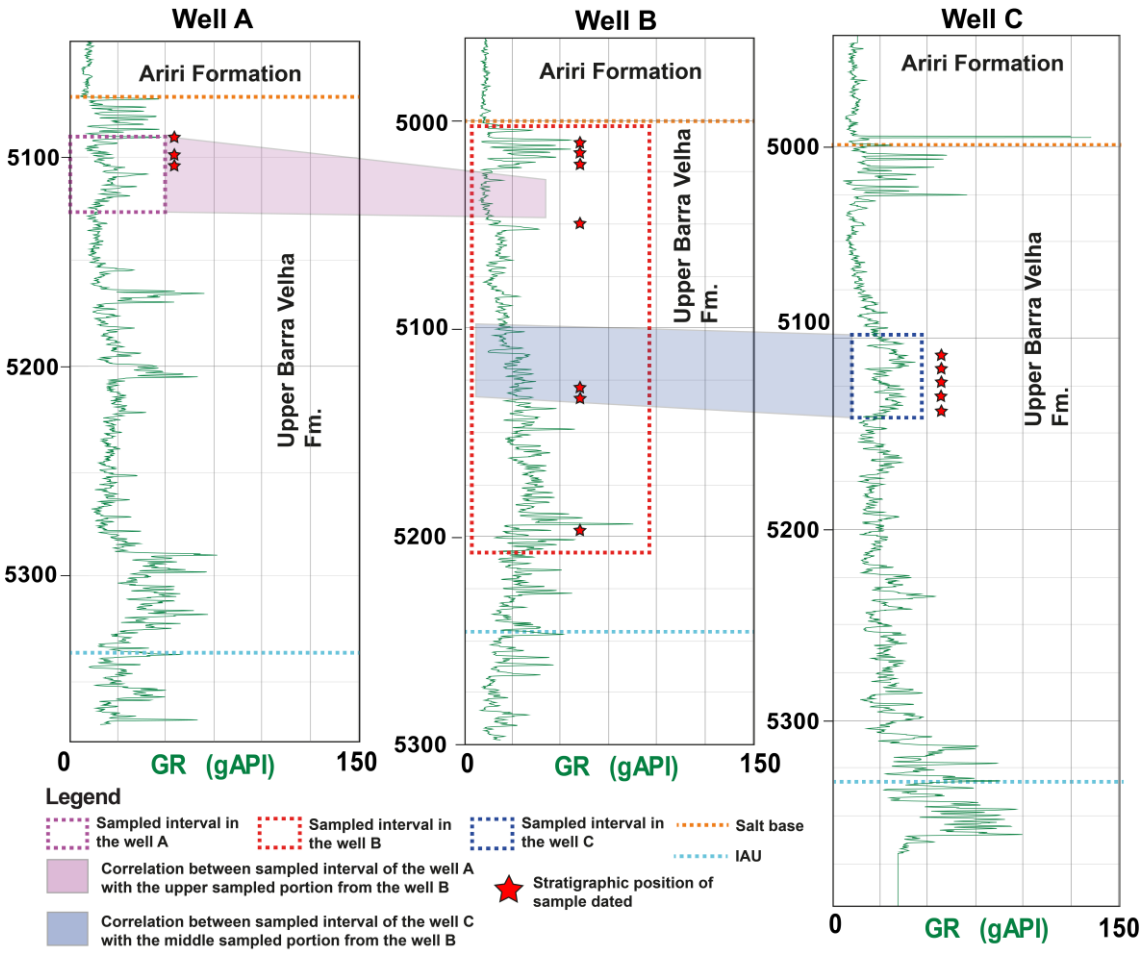

Figure 2. Gamma ray well correlation between the three studied wells. The purple dashed polygon represents the sampled portion form the well A. The red dashed polygon represents the sampled portion from the well B. The blue dashed polygon represents the sampled portion from the well C. The orange dashed line marks the salt base. The light blue dashed line marks the Intra-Alagoas Unconfomity. The lilac polygon marks the correlation between the sampled part of the well A, which corresponds to ~15 m right under the Lula mark, with the uppermost ~ 30 m sampled from the well B, that encompasses the same portion. The blue polygon marks the correlation between the sampled part of the well C, which corresponds to ~100 m – 140 m under the salt base, with the middle sampled part of the well B that probably comprehends a similar interval. The red stars mark the stratigraphic position of the samples analyzed for U-Pb dating.

4.4 RESULTS

4.4.1 Petrography

Samples from the Upper Barra Velha Formation (cores A, B and C) were described as shrubstones, spherulitestones, grainstones, rudstones, dolostones and cherts. Calcite primary constituents include particles of shrubs, spherulites, ostracods and peloids. These constituents may be partially replaced by dolomite or silica. Primary dolomites occur as laminae of microcrystalline and fine dolomite rhombs affected by silicification.

The interparticle space is occupied by dolomite and silica secondary constituents with different morphologies. We rarely observed calcite cements and remnants of the Mg-clay matrix. There are no major petrographic and mineralogic difference among samples from these wells. They all have well preserved constituents (e.g. shrubs and spherulites) and diagenetic features such as silicification and dolomitization.

4.4.1.1 Facies

Shrubs-related facies are made essentially by particles of shrubs measuring from a few millimeters to up to 3 cm long (Figure 3A). Shrubstones consist of layers dominated by shrubs, exhibiting interparticle, intercrystalline, vuggy, and intraparticle pores, often interlayered with laminated dolomitic layers. These rocks often display pervasive dolomitization and silicification features, with rhombohedral dolomite and microcrystalline silica partially replacing particles and filling pore spaces. Macrocrystalline quartz also may fill the interparticle space and partially replace the shrubs. Other diagenetic features include calcite and dolomite fringes coating the particles; and blocky calcite, blocky dolomite, chalcedony and quartz filling intraparticle, interparticle, and vuggy porosity.

The spherulite-related facies are dominated by spherulites particles. Dolomite and silica occur as microcrystalline dolomite, fine rhombohedral dolomite, microcrystalline silica, and chalcedony. Microcrystalline dolomite, also called bridge (Wright and Barnett, 2015) or lamellar (Sartorato, 2018), mimics the laminar habit of the Mg-clays and tend to contour the spherulite particles (Figure 3B). Dolomite rhombs occupy the interparticle space in this facies and may also replace the particles. Silica occurs as microcrystalline aggregates and quartz crystals replacing spherulites and microcrystalline dolomite, and may fill intraparticle and interparticle pores. Silicification and dolomitization also affects pervasively the spherulitic facies.

Reworked-related facies include grainstones, rudstones and packstones. They are formed by intraclasts of shrubs, spherulites, peloids, ostracods and chert, and may contain basalt lithoclasts. These rocks have a high interparticle porosity in the absence of cement (e.g. dolomite, silica, or calcite) (Figure 3C). Rhombohedral dolomite dominates as dolomite cement, but saddle dolomite crystals rarely also fill interparticle pores. Silica cement may occur as microcrystalline silica, chalcedony, microcrystalline, and macrocrystalline quartz, filling interparticle and vuggy pores. It may also replace

intraclasts. Calcite occurs as isopachous calcite cement and macrocrystalline mosaic calcite.

Dolomitic rocks are formed by intense dolomitization that replaces matrix and framework particles and fills pores, sometimes obliterating the original fabric of the rock. They also may be formed by precipitation of primary dolomites marking the rock-lamination (Figure 3D). The dolostones and rich-dolomite rocks consist of microcrystalline to fine rhombohedral dolomite crystals, mostly anhedral and subhedral, in which the intercrystalline space is low or absent. Dolomitic rocks often exhibit the Planar-s texture described by Sibbley and Gregg (1987), in which most dolomite crystals are subhedral to anhedral with straight, compromised boundaries and many crystal-face junctions (Figure 3E). This rock has, in general, low porosity, low permeability, and low intercrystalline matrix. Some dolomite-rich rocks are laminated, exhibiting soft-deformation (Figure 3D), while others are massive. They may occur as massive dolostone or as a rock supported by dolomite rhombs with remains of shrubs, spherulites, and ghosts of intraclasts.

Cherts are pervasively silicified rocks that are composed almost entirely of silica in different morphologies such as microcrystalline silica, microcrystalline quartz, chalcedony, macrocrystalline quartz, and by carbonate particles of shrubs, spherulites, peloids and dolomite phases that may be preserved. Silica minerals often obliterate the original fabric of the rock, filling pores and replacing constituents (Figure 3F).

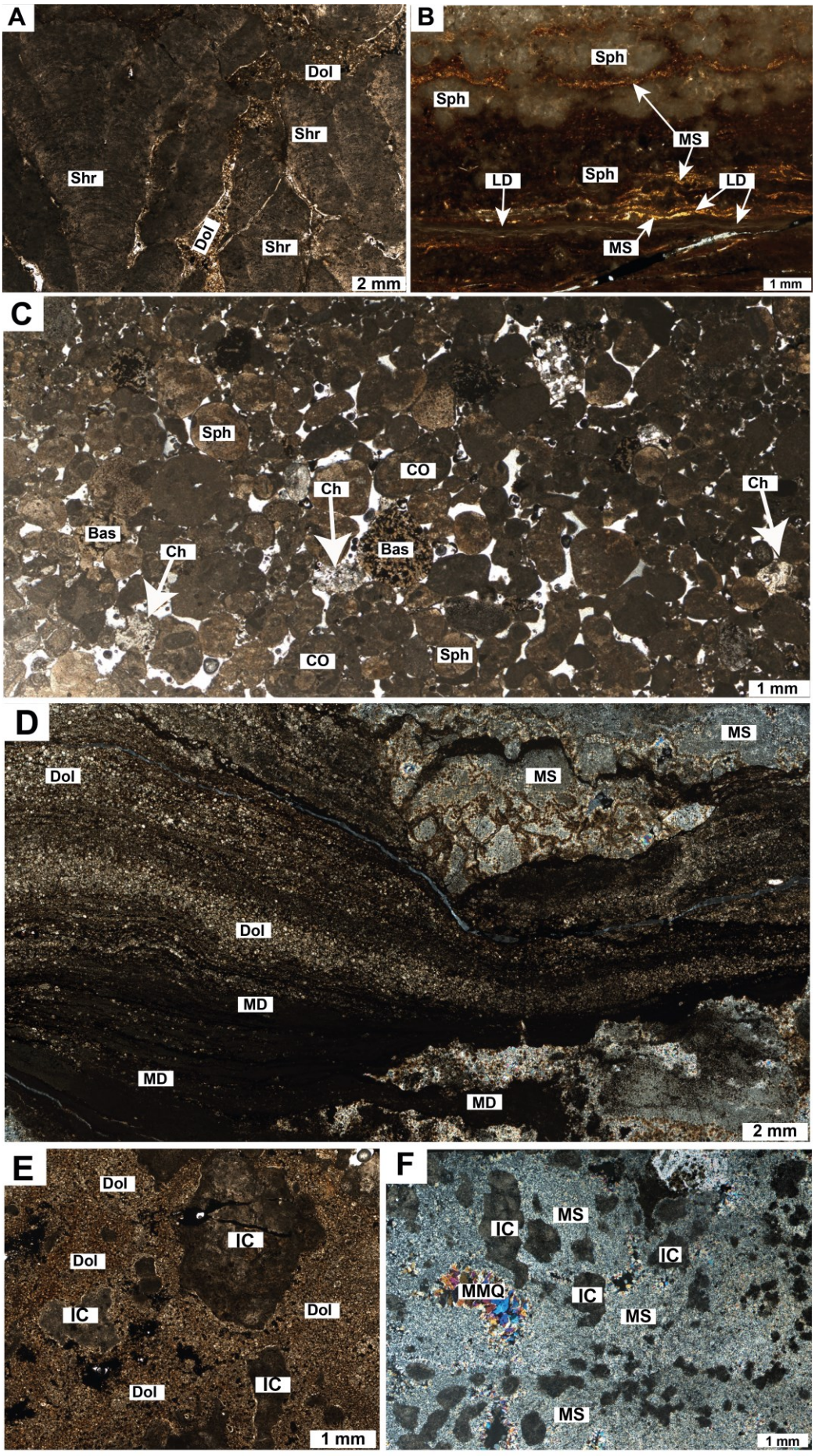
A
Dol
Shr
Shr
Dol
Shr
2 mm
B
Sph
Sph
MS
LD
Sph
LD
MS
1 mm
C
Sph
CO
Ch
Ch
Bas
Ch
Bas
CO
Sph
1 mm
D
MS
Dol
MS
Dol
MD
MD
MD
2 mm
E
Dol
IC
Dol
IC
Dol
Dol
IC
1 mm
F
IC
MS
IC
MMQ
IC
MS
MS
1 mm

Figure 3. (A) PPL photomicrograph of shrubstone with well-formed shrubs with the interparticle space occupied by dolomite rhombs. Sample is 5129.45 from well C. (B) PPL photomicrograph of spherulitestone with lamellar pseudomorphic microcrystalline dolomite and stratiform silicification. Sample is 5016.90 from well B. (C) PPL photomicrograph of grainstone with inteparticle porosity and formed by intraclasts of spherulites, composite ooids, basalt lithoclasts, and chert lithoclasts. Sample is 5014.75 from well B. (D) XP photomicrograph of laminated, soft-deformed and partially silicified dolostone formed by microcrystalline and rhombohedral dolomites. Sample is 5194.50 from well B. (E) PPL photomicrograph of dolomite-supported rock composed by fine dolomite rhombs occupying the interparticle space and replacing the framework constituents. Sample is 5124.60 from well C. (F) XP photomicrograph of a chert with carbonate particles preserved. Microcrystalline silica occupies the interparticle space and replaces particles. Macrocrystalline mosaic quartz fills vuggy pores. Sample is 5045.25 from well B. Bas: basalt; Ch: chert; CO: composite ooid; Dol: dolomite; IC: intraclast; MD: microcrystalline dolomite; MMQ: macrocrystalline mosaic quartz; MS: microcrystalline silica; LD: lamellar dolomite; Shr: shrub; Sph: spherulite.

4.4.1.2 Diagenetic Features

Diagenetic features vary according to the facies. In fine-grained and low-porosity facies, diagenetic modifications do not generate much porosity, but appear mostly as replacement features. These features include secondary microcrystalline dolomite that mimics the laminar habit of the Mg-clays, with this dolomite occurrence being frequently denominated as lamellar dolomite or dolomite bridges (Wright and Barnett, 2015; Tonietto et al., 2018). Fine to medium dolomite rhombs and microcrystalline silica replacing the original matrix also occur. In terms of coarse-grained rocks such as grainstones and shrubstones, they are porous, permeable rocks affected by dissolution, pervasive silicification and pervasive dolomitization events.

Coarse-grained facies are more frequent among the studied samples. They exhibit a variety of framework constituents, pore types, and diagenetic constituents. Eodiagenetic dolomite occurs as microcrystalline pseudomorphic dolomite that replaces constituents such as ostracods, composite ooid particles and Mg-clays, preserving the primary lamination. Early dolomite also occurs as fine to medium rhombohedral dolomite crystals that occupy the interparticle space by the replacement of a previous matrix or by the filling of interparticle pores, and this dolomite morphology also replaces framework particles. These early dolomites are partially replaced by microcrystalline silica and quartz (Figure 3B). Dolomitization often is pervasive, masking the original fabric of the rock by partially replacing the matrix and framework components (Figure 3E).

Eodiagenetic silicification also occurs as a pervasive phase. The earliest microcrystalline diagenetic silica hides the original fabric of the rock, fills pore spaces, and replaces constituents. Silicification also contributes on the formation of moldic pores that remain open or are filled by microcrystalline silica, microcrystalline quartz, chalcedony, and macrocrystalline quartz, with the microcrystalline silica to quartz gradation occurring towards the center of the pore space. The center of the pore space may be filled by later dolomite cements.

Later diagenetic phases are blocky dolomite, saddle dolomite, macrocrystalline calcite, and macrocrystalline quartz. Blocky dolomite replaces dolomite rhombs and fills intraparticle, vuggy, and interparticle pores. Saddle dolomite crystals are post-silicification since they fill vuggy pores lined by macrocrystalline quartz in silicified rocks. They may also fill intraparticle-fracture porosity. Macrocrystalline quartz is a late diagenetic phase that fills vuggy, intraparticle pores and fracture porosity. QEMSCAN images show that microcrystalline silica and quartz crystals replace diagenetic constituents such as dolomite rhombs. They also show rare macrocrystalline calcite filling vuggy and fracture-intraparticle pores (Figure 4A-D).

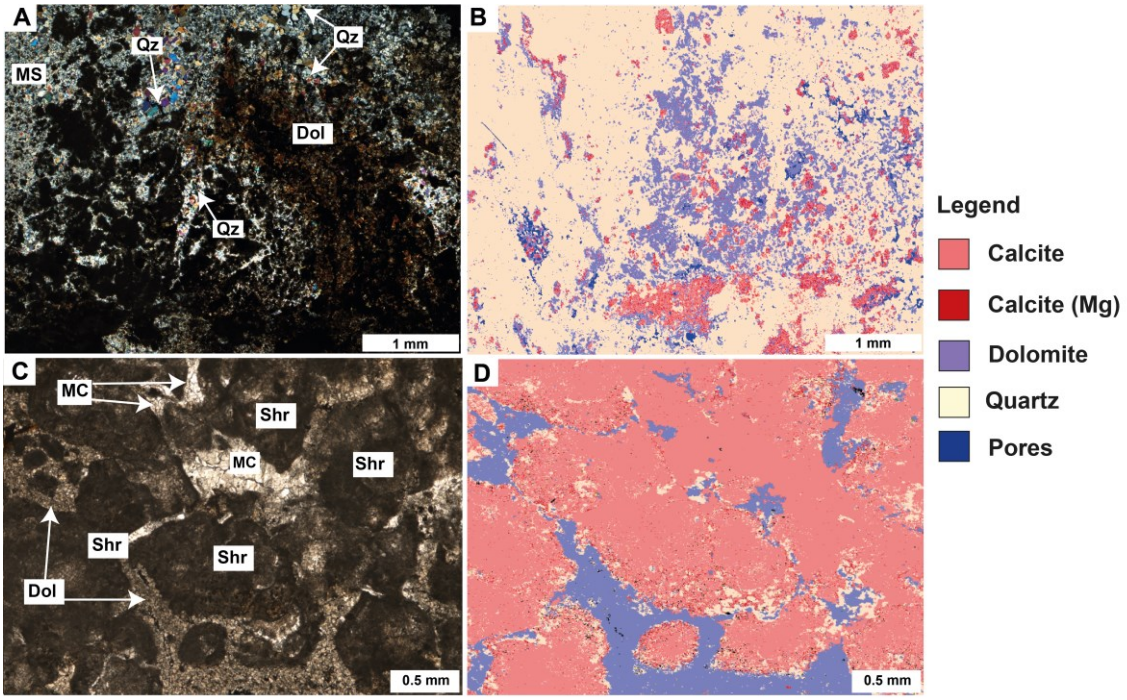

Figure 4. Coupled conventional petrographic study-QEMSCAN imaging to a better understanding of diagenesis. (A-B) XP and QEMSCAM images of chert with carbonate particles preserved. It is possible to notice that the quartz crystals are replacing dolomite rhombs and calcite particles. Sample is 5020.10 from well B. (C-D) PPL and QEMSCAN images of dolomitized grainstone with rhombohedral dolomite filling pore spaces and replacing calcite paticles. Macrocrystalline mosaic calcite fills intraparticle-fracture

porosity. Sample is 5100.75 from well A. Dol: dolomite; MC: macrocrystalline calcite; MS: microcrystalline silica; Qz: quartz; Shr: shrub.

4.4.2 U-Pb Carbonate Geochronology

Ages of carbonate constituents from the Upper Barra Velha Formation were determined in primary phases such as particles of shrubs, spherulites, peloids, ostracods, and microcrystalline to fine dolomite rhombs. Data were also obtained in diagenetic phases such as microcrystalline dolomite, rhombohedral dolomite, lamellar dolomite, blocky dolomite, and saddle dolomite. The ages of particles range from 124 ± 5 Ma to 82 ± 6 Ma, with the U content varying from 0.2 ppm to 16.1 ppm. The common lead composition ranges from 0.788 to 0.930 (Table 1). All Tera-Wasserburg concordia diagrams displaying U-Pb ages and common $^{207}Pb/^{206}Pb$ compositions are available in the supplementary material.

Most primary particles fall within different age intervals. There is an older interval with ages ranging between 124 ± 5 Ma and 122 ± 5 Ma. These are, respectively, a microcrystalline dolomite with a U average value of 7.9 ppm, and a common Pb composition of 0.788; and very fine dolomite rhombs with U average content of 3.7 ppm and with a common Pb value of 0.820. Indeed, the high U content (an average value of 7.9 ppm) of the 124 ± 5 Ma microcrystalline dolomite is an evidence of its primary nature. An intermediate age interval of calciferous primary particles varies from a 116 ± 4 Ma peloid to a 110 ± 4 Ma shrub. The highest U concentration (an average value of 16.9 ppm) of the particles within this intermediate age interval is from a 112 ± 3 Ma shrub with a commom Pb value of 0.810; while the lowest U average value (1.1 ppm) is recorded in the 110 ± 4 Ma shrub that has a common Pb composition of 0.850. A younger interval exhibit ages ranging from 105 ± 3 Ma to 82 ± 6 Ma. The former is a shrub with a U average value of 1.8 ppm and a common Pb composition of 0.870, while the youngest primary particle is a shrub that has an average U content of 0.6 ppm and a common Pb value of 0.858 (Table 1; Figure 5).

Regarding the ages, U values, and common Pb composition of other calciferous primary particles, there is the 116 ± 4 Ma peloid. It has an average U content of 3.4 ppm and a common Pb composition of 0.833. In turn, there is a low U (0.5 ppm) spherulite with an age of 100 ± 5 Ma and a common Pb value of 0.840. A high U (5.0 ppm) spherulite yielded an age of 100 ± 3 Ma and has a common Pb composition of 0.890. An ostracod

valve made of calcite with an age of 114 ± 3 Ma has an average U value of 2.1 ppm and a common Pb composition of 0.843 (Table 1).

There seems to exist a relationship between ages and the studied wells, i.e. a spatial relation of the ages. For example, U-Pb ages of calciferous primary constituents from well B fall between 105 ± 3 Ma and 99 ± 7 Ma. Otherwise, the ages of calciferous primary constituents from well C are older, varying between 116 ± 4 Ma and 110 ± 4 Ma. A majority of primary constituents from well A did not yield reliable results, except for a spherulite and a shrub that gave younger ages of 100 ± 5 Ma and 82 ± 6 Ma like occurs in the well B. When comparing similar particles in each core, it is also noticeable that constituents from core A display low U values (an average of 0.6 ppm) than constituents from cores B and C (average values of 2.3 ppm and 3.4 ppm, respectively) (Table 1).

Table 1. U-Pb age data acquired in the Upper Barra Velha Formation carbonates from the Santos Basin.

Well	Sample depth (m)	Depth from top BV (m)	Age (Ma)	±2s	$(^{207}Pb/^{206}Pb)_c$	Uppm (avg.)	Constituent
A	5090.95	18.95	123	4	0.840	1.0	Rhombohedral dolomite
A	5090.95	18.95	100	5	0.840	0.5	Spherulite
A	5099.05	27.05	82	6	0.858	0.6	Shrub
A	5100.75	28.75	108	5	0.852	0.2	Rhombohedral dolomite
B	5015.10	8.10	99	7	0.907	0.2	Shrub
B	5015.10	8.10	109	4	0.891	0.9	Microcrystalline dolomite
B	5016.90	9.90	117	3	0.880	1.5	Lamellar Dolomite
B	5020.10	13.10	112	7	0.870	1.1	Rhombohedral dolomite
B	5020.10	13.10	97	4	0.930	1.2	Saddle dolomite
B	5049.95	42.95	99	6	0.880	0.3	Pseudomorphic dolomite
B	5049.95	42.95	104	5	0.880	0.4	Lamellar Dolomite
B	5133.95	126.95	105	3	0.870	1.8	Shrub
B	5144.00	137.00	100	3	0.890	5.0	Spherulite
B	5144.00	137.00	109	3	0.880	4.0	Rhombohedral dolomite
B	5194.50	187.50	124	5	0.788	7.9	Microcrystalline dolomite
B	5194.50	187.50	122	5	0.820	3.7	Rhombohedral dolomite
C	5113.00	113.00	114	3	0.843	2.1	Ostracod
C	5113.00	113.00	113	3	0.850	2.7	Shrub
C	5113.00	113.00	99	4	0.870	0.3	Blocky dolomite
C	5118.95	118.95	110	4	0.850	1.1	Shrub
C	5118.95	118.95	100	3	0.840	2.3	Rhombohedral dolomite
C	5124.60	124.60	112	3	0.810	16.1	Shrub
C	5124.60	124.60	95	4	0.830	4.0	Rhombohedral dolomite
C	5124.60	124.60	97	5	0.850	0.6	Saddle dolomite
C	5127.90	127.90	115	5	0.850	1.3	Shrub
C	5132.50	132.50	116	4	0.833	3.4	Peloid

BV: Barra Velha; 2s: confidence interval; $(^{207}Pb/^{206}Pb)_c$: common lead composition; avg: average value

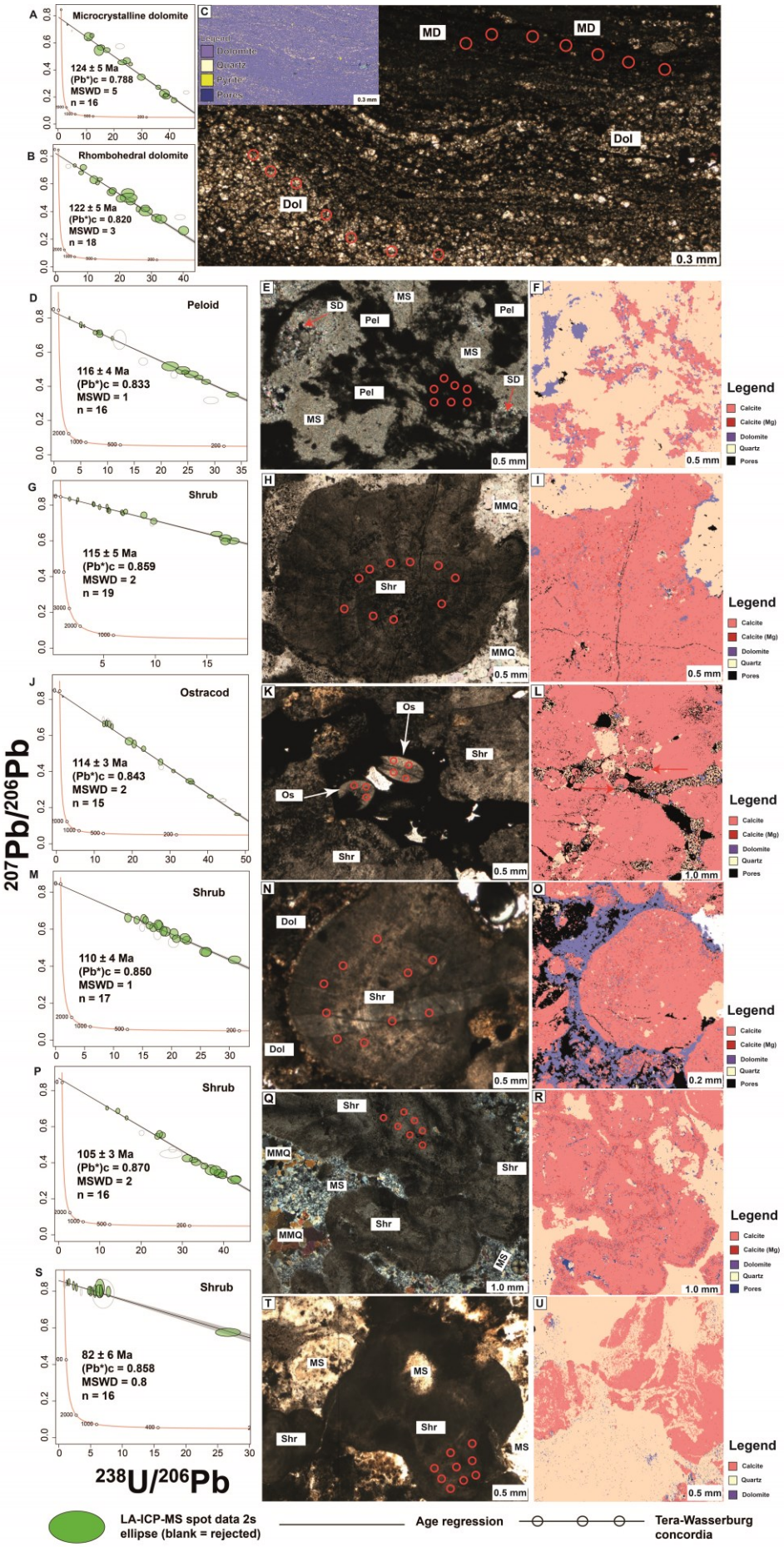
A
Microcrystalline dolomite
124 ± 5 Ma
(Pb*)c = 0.788
MSWD = 5
n = 16
B
Rhombohedral dolomite
122 ± 5 Ma
(Pb*)c = 0.820
MSWD = 3
n = 18
C
Legend
Dolomite
Quartz
Pyrite
Pores
0.3 mm
MD
MD
Dol
Dol
0.3 mm
D
Peloid
116 ± 4 Ma
(Pb*)c = 0.833
MSWD = 1
n = 16
E
SD
MS
Pel
Pel
MS
Pel
MS
SD
0.5 mm
F
0.5 mm
Legend
Calcite
Calcite (Mg)
Dolomite
Quartz
Pores
G
Shrub
115 ± 5 Ma
(Pb*)c = 0.859
MSWD = 2
n = 19
H
MMQ
Shr
MMQ
0.5 mm
I
0.5 mm
Legend
Calcite
Calcite (Mg)
Dolomite
Quartz
Pores
J
Ostracod
114 ± 3 Ma
(Pb*)c = 0.843
MSWD = 2
n = 15
K
Os
Shr
Os
Shr
0.5 mm
L
1.0 mm
Legend
Calcite
Calcite (Mg)
Dolomite
Quartz
Pores
M
Shrub
110 ± 4 Ma
(Pb*)c = 0.850
MSWD = 1
n = 17
N
Dol
Shr
Dol
0.5 mm
O
0.2 mm
Legend
Calcite
Calcite (Mg)
Dolomite
Quartz
Pores
P
Shrub
105 ± 3 Ma
(Pb*)c = 0.870
MSWD = 2
n = 16
Q
Shr
MMQ
Shr
MS
Shr
MMQ
MS
1.0 mm
R
1.0 mm
Legend
Calcite
Calcite (Mg)
Dolomite
Quartz
Pores
S
Shrub
82 ± 6 Ma
(Pb*)c = 0.858
MSWD = 0.8
n = 16
T
MS
MS
Shr
Shr
MS
0.5 mm
U
0.5 mm
Legend
Calcite
Quartz
Dolomite
207Pb/206Pb
238U/206Pb
LA-ICP-MS spot data 2s ellipse (blank = rejected)
Age regression
Tera-Wasserburg concordia

Figure 5. Analyzed primary constituents and their respective Tera-Wasserbung concordia diagram ages. A) Tera-Wasserburg concordia diagram showing $^{238}U/^{206}Pb$ versus $^{207}Pb/^{206}Pb$ data of microcrystalline dolomite. (B) Tera-Wasserburg concordia plots showing $^{238}U/^{206}Pb$ versus $^{207}Pb/^{206}Pb$ data of rhombohedral dolomite. (C) PPL photomicrograph and QEMSCAN image of laminated dolostone formed by microcrystalline and rhombohedral dolomites. Sample is 5194.50 from well B. (D) Tera-Wasserburg concordia diagram showing $^{238}U/^{206}Pb$ versus $^{207}Pb/^{206}Pb$ data of a peloid. (E) XP photomicrograph of analyzed peloid particle in the midst of microcrystalline silica. Sample is 5132.50 from well C. (F) QEMSCAN image of figure in (E) highlighting the calcite peloid partially replaced by silica. (G) Tera-Wasserburg concordia diagram showing $^{238}U/^{206}Pb$ versus $^{207}Pb/^{206}Pb$ data of a particle of shrub. (H) PPL photomicrograph of a shrub particle in a silicified rudstone. Sample is 5127.90 from well C. (I) QEMSCAN image of figure in (H) highlighting calcite composition of shrub and the surrounding silica partially replacing the particle. (J) Tera-Wasserburg concordia diagram showing $^{238}U/^{206}Pb$ versus $^{207}Pb/^{206}Pb$ data of ostracod particles. (K) PPL photomicrograph of analyzed ostracod particles. Sample is 5113.00 from well C. (L) QEMSCAN image of figure in (K) highlighting the calcite composition of the ostracod. (M) Tera-Wasserburg concordia diagram showing $^{238}U/^{206}Pb$ versus $^{207}Pb/^{206}Pb$ data of a shrub particle (N) PPL photomicrograph of a shrub particle in a dolomitized grainstone Sample is 5118.95 from well C. (O) QEMSCAN image of figure in (N) highlighting the calcite composition of the shrub particle, the surrounding dolomite cement and a few silica partially replacing calcite particles. (P) Tera-Wasseburg concordia diagram showing $^{238}U/^{206}Pb$ versus $^{207}Pb/^{206}Pb$ data of a shrub particle. (Q) XP photomicrograph of a silicified shrubstone. Sample is 5133.95 from well B. (R) QEMSCAN image of figure in (Q) highlighting the calcite composition of a shrub particle and the surrounding silica partially replacing particles of shrubs. (S) Tera-Wasserburg concordia diagram showing $^{238}U/^{206}Pb$ versus $^{207}Pb/^{206}Pb$ data of shrub particles. (T) PPL photomicrograph of a shrub particle in a silicified rudstone. Samples is 5099.05 from well A. (U) QEMSCAN image of figure in (T) highlighting the calcite shrub particle partially replaced by silica. Quoted age uncertainty includes propagated systematic uncertainties. Datapoint error ellipses are 2s. MSWD, mean squared weighted deviation. (Pb*)c is $(^{207}Pb/^{206}Pb)_c$, known as common lead composition. Red circles represent analytical spots made on the particles. Dol: dolomite; MD: microcrystalline dolomite; MMQ: macrocrystalline mosaic quarz; MS: microcrystalline silica; Os: ostracod; Pel: peloid; SD: saddle dolomite; Shr: shrub.

U-Pb dating revealed at least three main age intervals for secondary dolomites (Figure 6). The oldest secondary dolomites (123 ± 4 Ma) occur as fine dolomite rhombs occupying the interparticle space and partially replacing younger spherulites in a spherulitestone. It has an average U content of 1.0 ppm and a common Pb composition of 0.840. An intermediate dolomite generation has an age range of 117 ± 3 Ma to 108 ± 5 Ma. This generation of dolomites is formed by 117 ± 3 Ma pseudomorphic microcrystalline lamellar dolomite that replaced Mg-clays and outlines spherulite particles, being partially replaced by microcrystalline silica (Figure 6A-C). This lamellar dolomite has an average U content of 1.5 ppm and a common Pb value of 0.880. Fine

dolomite rhombs widely distributed in the sample, pervasively replacing constituents and filling pores mostly in grainstones and rudstones (6D-G) have ages from 112 ± 7 Ma to 108 ± 5 Ma. Their average U contents vary from 0.2 ppm to 4.0 ppm, and their common Pb values range from 0.852 to 0.880. Within this age interval (117 ± 3 Ma to 108 ± 5 Ma), there are stratiform dolomite occurrences intercalated with layers of younger shrubs and spherulites. These latter dolomites have ages of 109 ± 4 Ma and 109 ± 3 Ma. The former is a microcrystalline dolomite with an average U content of 0.9 ppm and a common Pb value of 0.891, while the latter has an average U value of 4.0 ppm and a common Pb composition of 0.880. It is worth mentioning that the 123 ± 4 Ma, 109 ± 4 Ma and 109 ± 3 Ma dolomites intercalated with younger spherulites and shrubs represent a curious feature and will be discussed in detail further (in the section 5.2; Figure 9).

A younger dolomite generation occurs in three main morphologies: (1) as blocky and saddle dolomites; (2) as pseudomorphic microcrystalline dolomites; and (3) as pervasive dolomite rhombs similar to those from the second dolomite generation (Figure 6).

Blocky and saddle dolomites fill vuggy, fracture and interparticle pores, showing ages from 99 ± 4 Ma – 97 ± 4 Ma. The 99 ± 4 Ma blocky dolomite has a U average value of 0.3 ppm and a common Pb value of 0.870. There are two occurrences of saddle dolomite. They exhibit ages of 97 ± 5 Ma and 97 ± 4 Ma, with average U values from 0.6 ppm to 1.2 ppm, and common Pb composition ranging from 0.850 to 0.930 (Figure 6H-J; 6N-O). The 97 ± 4 Ma is a post-silicification phase that places an age limit for a silicification event in the Upper Barra Velha Formation

Microcrystalline pseudomorphic dolomites from the same sample yielded ages from 104 ± 5 Ma to 99 ± 6 Ma. The 104 ± 5 Ma microcrystalline dolomite is a lamellar dolomite that mimics the lamination of previous Mg-clays. It has an average U value of 0.3 ppm and a common Pb composition of 0.880 (Figure 7A-C). The 99 ± 6 Ma microcrystalline pseudomorphic dolomite that replaces and mimics ostracod valves has an average U content of 0.3 ppm and a common Pb value of 0.880 (Figure 7A, B, D). As these pseudomorphic microcrystalline dolomites probably represent the same dolomitization event considering petrographic and geochemical criteria (for instance, these two dolomite occurrences have the same $^{207}Pb/^{206}Pb$ value of 0.880), an integration of their data was made, resulting in a pooled age of 103 ± 5 Ma. This pooled data exhibits an average U value of 0.3 ppm and a common Pb composition of 0.880 (Figure 7E).

The younger pervasive fine rhombohedral dolomites yielded ages of 100 ± 3 Ma and 95 ± 4 Ma (Figure 6L-M). Their average U value ranges from 2.3 ppm to 4.0 ppm, and their common Pb composition varies from 0.830 to 0.840.

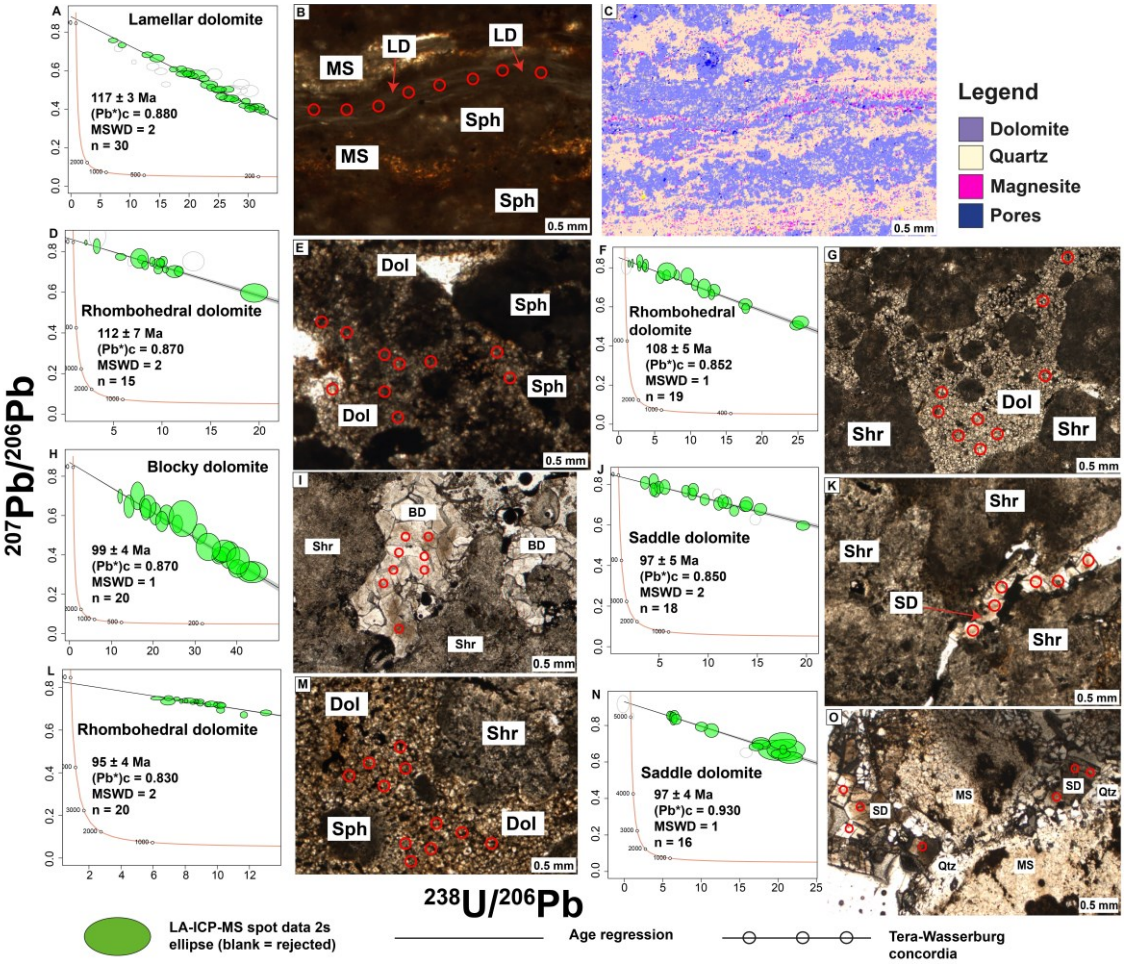

Figure 6. (A) Tera-Wasserburg concordia plots showing $^{238}U/^{206}Pb$ versus $^{207}Pb/^{206}Pb$ data for microcrystalline lamellar dolomite. (B) PPL photomicrograph of microcrystalline lamellar dolomite contouring spherulite particles in a spherulitestone. Sample is 5016.90 from well B. (C) QEMSCAN image of figure in (B) highlighting silicification in the dolomite-rich sample. (D) Tera-Wasserburg concordia diagram showing $^{238}U/^{206}Pb$ versus $^{207}Pb/^{206}Pb$ data of rhombohedral dolomite. (E) PPL photomicrograph of grainstone affected by pervasive dolomitization, with rhombohedral dolomite crystals filling pores and partially replacing particles. Sample is 5020.10 from well B. (F) Tera-Wasserburg concordia diagram showing $^{238}U/^{206}Pb$ versus $^{207}Pb/^{206}Pb$ data of rhombohedral dolomite. (G) PPL photomicrograph of grainstone affected by pervasive dolomitization, with rhombohedral dolomite crystals filling pores and partially replacing particles. Sample is 5100.75 from well A. (H) Tera-Wasserburg concordia diagram showing $^{238}U/^{206}Pb$ versus $^{207}Pb/^{206}Pb$ data of blocky dolomite cement. (I) PPL photomicrograph of blocky dolomite cement filling vuggy and intraparticle porosities. Sample is 5113.00 from well C. (J) Tera-Wasserburg concordia diagram showing $^{238}U/^{206}Pb$ versus $^{207}Pb/^{206}Pb$ data of saddle dolomite cement. (K) PPL photomimcrograph of saddle dolomite filling intraparticle fracture porosity in a grainstone. Sample is 5124.60 from the well C. (L) Tera-Wasserburg concordia diagram showing $^{238}U/^{206}Pb$ versus $^{207}Pb/^{206}Pb$

data of rhombohedral dolomite. (M) PPL photomicrograph of grainstone affected by pervasive dolomitization, with rhombohedral dolomite crystals filling pores and partially replacing particles. Sample is 5124.60 from the well C. (N) Tera-Wasserburg concordia diagram showing $^{238}U/^{206}Pb$ versus $^{207}Pb/^{206}Pb$ data of saddle dolomite cement. (O) PPL photomicrograph of silicified and dolomitizes grainstone with saddle dolomite crystals filling the center of vuggy pores lined by quartz crystals. Sample is 5020.10 from the well B. Quoted age uncertainty includes propagated systematic uncertainties. Datapoint error ellipses are 2s. MSWD, mean squared weighted deviation. (Pb*)c is $(^{207}Pb/^{206}Pb)_c$, known as common lead composition. Red, green an white circles represent analytical spots made on the particles. BD: blocky dolomite; Dol: dolomite; LD: lamellar dolomite; MD: microcrystalline dolomite.

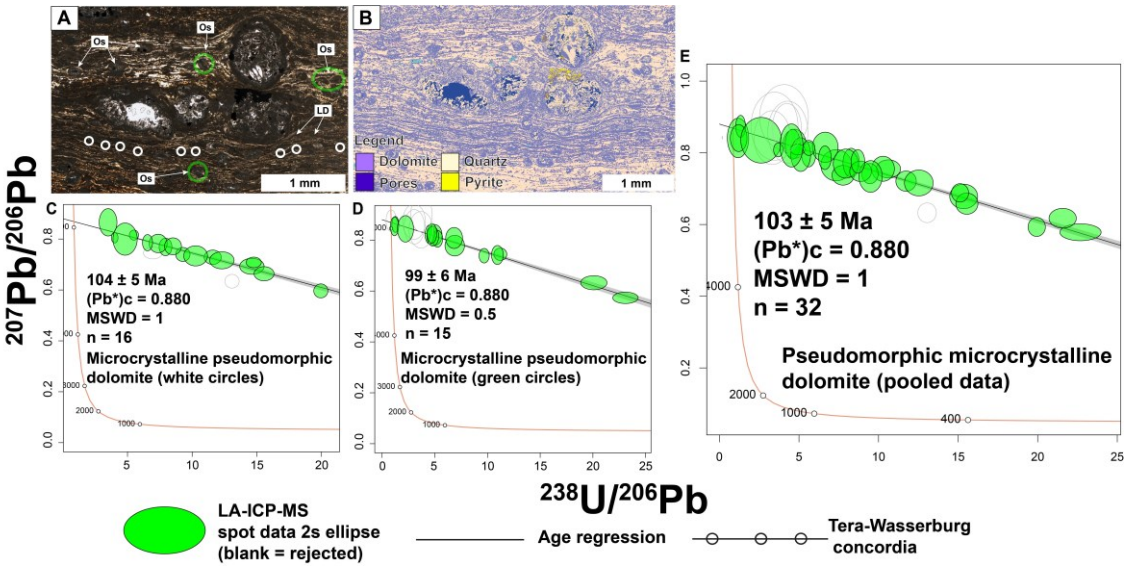

Figure 7. Microcrystalline pseudomorphic dolomites. (A) PPL photomicrograph of the sample where the microcrystalline pseudomorphic dolomites occur. Sample is 5049.95 from the well B. (B) QEMSCAN image from figure in (A). (C) Tera-Wasserburg concordia diagram showing $^{238}U/^{206}Pb$ versus $^{207}Pb/^{206}Pb$ data of microcrystalline pseudomorphic lamellar dolomite. (D). Tera-Wasserburg concordia diagram showing $^{238}U/^{206}Pb$ versus $^{207}Pb/^{206}Pb$ data of the microcrystalline pseudomorphic dolomite that replaced ostracod particles. (E) Tera-Wasserburg concordia plots showing $^{238}U/^{206}Pb$ versus $^{207}Pb/^{206}Pb$ data of the pooled data from these microcrystalline pseudomorphic dolomites, since they all occur in the same sample and have the same $(^{207}Pb/^{206}Pb)_c$ value. Datapoint error ellipses are 2s. MSWD, mean squared weighted deviation. (Pb*)c is $(^{207}Pb/^{206}Pb)_c$, known as common lead composition. LD: lamellar dolomite; Os: ostracod.

4.5 DISCUSSION

Reported U-Pb ages for the Upper Barra Velha Formation and its chrono-correlated Kwanza and Namibe pre-salt carbonates have a wide age range (between 115.83 ± 1.56 to 56.8 ± 4.8 Ma; 2s) (Rochelle-Bates et al., 2021; Godeau et al., 2021; Rochelle-Bates et al., 2022; Lawson et al., 2022). These ages may mark either depositional or post-depositional events. For instance, only a few age data of the Upper

Barra Velha Formation are interpreted as related to carbonate deposition (Lawson et al., 2022). Most age data are interpreted as related to post-sedimentary processes, such as magmatic and hydrothermal events that range in time from 116 Ma to 38 Ma (Moreira et al., 2007; Szatmari and Milani, 2016; Trittla et al., 2018; Loma et al., 2018; Rancan et al., 2018; Louback et al., 2021; Godeau et al., 2021; Rochelle-Bates et al., 2021; Louback et al., 2023; Gordon et al., 2023; Oliveira et al., 2023). Even well-preserved primary particles with no clear evidence of recrystallization or diagenetic imprints may yield a non-depositional age (Rochelle-Bates et al., 2022). Compared to U-Pb dating of silicate-bearing minerals such as zircons, carbonates are more susceptible to post-crystallization changes and may not record primary depositional ages (Jones et al., 1995; Kelly et al., 2003; Li et al., 2014; Roberts et al., 2020a).

Figure 8 compares U-Pb ages obtained in our study with published age data on primary carbonates, carbonates related to hydrothermal events, and igneous activity from the Santos (Moreira et al., 2007; Szatmari & Milani, 2016; Rancan et al., 2018; Louback et al., 2021; Rochelle-Bates et al., 2022; Lawson et al., 2022; Louback et al., 2023; Gordon et al., 2023; Oliveira et al., 2023), Campos (Trittla et al., 2018), Kwanza (Loma et al., 2018; Godeau et al., 2021), and Namibe (Rochelle-Bates et al., 2021) basins. It reveals that carbonate ages (Figure 8C-D) and magmatic and hydrothermal events (Figure 8 A-B) are related. It also reveals that the main magmatic age peak falls between 105 Ma and 130 Ma. It further shows that the ages of primary and hydrothermal carbonates, including our data, are contemporaneous or younger than the main peak of magmatism and contemporaneous with hydrothermal events. The ~124 Ma carbonates from our study also correlate with the 120-130 Ma magmatism peak. Figure 8E shows, with smoother KDE curves than the KDE curves from figures 8A-D, how the ages of carbonate precipitation and diagenesis are within the age range of magmatic and hydrothermal events. Compared to previously published age data, carbonates from our study are mostly Barremian to Albian in age and do not display ages younger than 70 Ma (Figure 8A-E). The wide age range of our data allows for raising questions regarding the preservation of primary age data. For instance, regarding the primary carbonate constituents, what explains their age differences? Is there any regional control on age distribution? What are the relationship among ages and hydrothermal alteration and sedimentary facies? Regarding secondary phases, what are their time constraint and what geological events they are related to?

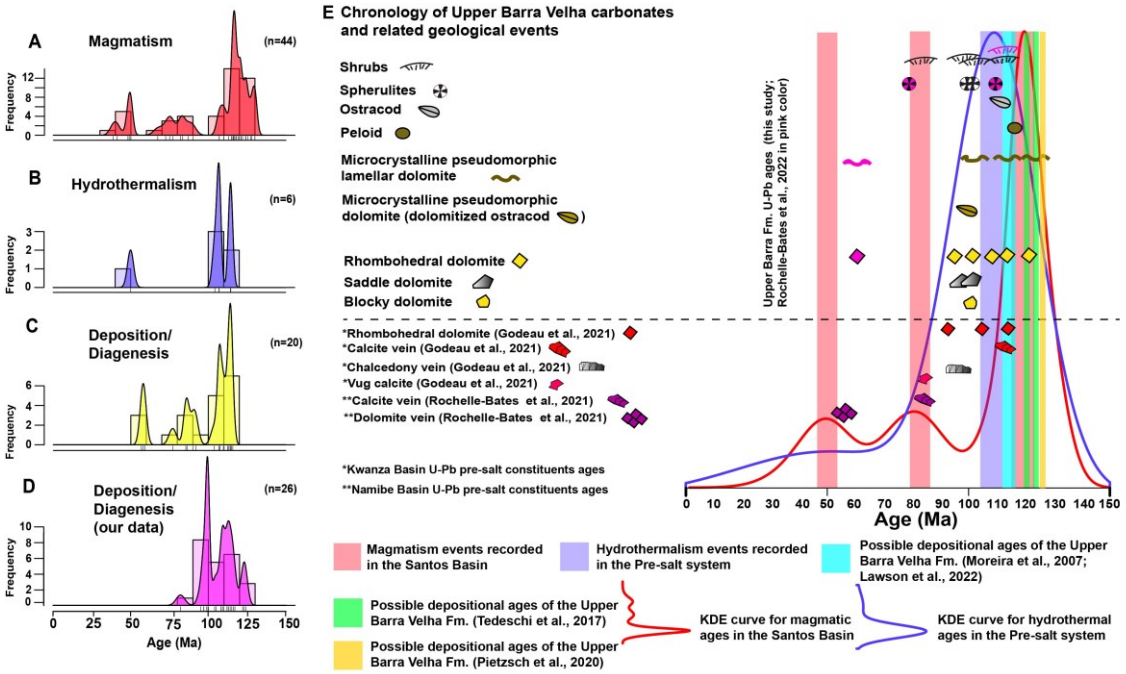

Figure 8. (A) Kernel Density Estimation (KDE) curve and histogram ages of magmatic event in the Santos Basin. (B) KDE curve and histogram ages of hydrothermalism events recorded in Santos, Campos, Kwanza and Namibe basins. (C) KDE curve and histogram ages of depositional and diagenetic events in the pre-salt section of Santos, Kwanza and Namibe basins (literature data). (D) KDE curve and histogram ages of depositional and diagenetic events in the Upper Barra Velha Formation (our data). The histogram binwidth is 10 and the kernel bandwidth is 1.5 for figures A, B, C, D. (E) Summary chronology of the Upper Barra Velha Formation carbonates and related magmatic, hydrothermal, and sedimentary events in the Santos Basin and other pre-salt basins (e.g., Campos, Kwanza and Namibe basins). The figure shows the relationship between the Barra Velha Formation carbonates ages with those of magmatic and hydrothermal events that affected the pre-salt. Kernel bandwidth is 5. Our data and compilation from other studies are available in the supplementary material (Rochelle-Bates et al., 2021; Rochelle-Bates et al., 2022; Lawson et al., 2022; Moreira et al., 2007; Szatmari & Milani, 2016; Trittla et al., 2018; Loma et al., 2018; Rancan et al., 2018; Louback et al., 2021; Godeau et al., 2021; Rochelle-Bates et al., 2021; Louback et al., 2023; Gordon et al., 2023; Oliveira et al., 2023).

4.5.1 Ages of Primary Carbonate Constituents

In our study, most preserved sedimentary rocks include shrubstones, spherulitestones, grainstones, and even laminated microcrystalline dolostones. Because of the superposed diagenetic and hydrothermal events, we may not have preserved a pristine carbonate rock. For instance, the coarse-grained facies like shrubstones, spherulitestones, grainstones occur at the upper part of depositional cycles (Wright & Barnett, 2015; Basso et al., 2021). These rocks are often porous and permeable, being the pore space occupied by dolomite and silica (Figure 3D-E, Figure 4C). Despite the

secondary mineralogy of the pore space, the framework particles made of calcite commonly display a good preservation under the microscope. In contrast, the laminated fine-grained dolostones made of microcrystalline dolomite and fine-grained dolomite rhombs usually occur at the base of sedimentary cycles, which are made of less porous and permeable rocks (Wright & Barnett, 2015; Basso et al., 2021). We contend that fluid-rock interaction was mainly controlled by fabric features, such as mineralogy, porosity, and permeability. For instance, we argue that the microcrystalline dolostone displays older age values because of its low permeability and porosity, thus preventing fluid-rock interaction. Furthermore, its dolomitic composition was less reactive with the percolating fluids than the calcite counterparts. In contrast, permeable and porous carbonate facies, like shrubstones and spherulitestones, were more susceptible to post-sedimentary processes, including interaction with early diagenetic fluids and hydrothermal events. These facies were more susceptible to post-depositional alteration such as the ~116 Ma basaltic magmatism intrusive in the pre-salt carbonates (Louback et al., 2023), the ~114 Ma hydrothermal alteration in the pre-salt rocks (Rancan et al., 2018), and the regional pervasive post-depositional hydrothermal alteration at ~105/100 Ma that significantly affected the pre-salt carbonate U-Pb system.

Our oldest ages in primary constituents were obtained in a microcrystalline dolomite (124 ± 5 Ma) and in fine dolomite rhombohedral crystals (122 ± 5 Ma). They occur in the same laminated fine-grained dolostone sample and are both related to primary dolomite precipitation or early diagenetic features that replace the previous Mg-clays, preserving the lamination of the rock. Indeed, since this dolostone exhibit no evidence of any precursor mineralogy or residual textures in petrographic and QEMSCAN observations, we suggest a primary origin rather than a diagenetic origin for these dolomites. In addition, their laminated texture and soft-deformation indicate syn-sedimentary precipitation instead of burial replacement (Figure 3D; Figure 5A-C).

These primary dolomites have ages close to the pre-Aptian sedimentation age (~ 120 Ma or ~ 125-128 Ma) of the Upper Barra Velha Formation as suggested by Tedeschi et al. (2017) and Pietzsch et al. (2020). The microcrystalline and fine-grained dolomite rhombs, due to their low porosity and permeability, may have prevented fluid percolation and fluid-rock interaction. Thus, these fine dolomites maintained their pristine U-Pb isotopic composition and ages, with well-regressed concordia diagrams that are typical of primary carbonates (Rasbury & Cole, 2009). Hence, they are the first direct U-Pb

Barremian ages of the Upper Barra Velha Formation carbonates. Primary dolomites, although infrequent, often form in lakes and lagoons (Mehmood et al., 2018). Yang et al. (2021), in turn, showed that primary dolomites can be precipitated rapidly in free suspension from hydrothermal fluids vented into the base of the lake. Also, other studies describe primary high-temperature dolomites formed within lacustrine basins during periods of very active volcanism associated with rifting during the Mesozoic (e.g., Jiuquan Basin; Wen et al., 2014). Likewise, the 124 ± 5 Ma and 122 ± 5 Ma primary dolomites from the Upper Barra Velha Formation may have their genesis related to the 125.5 ± 0.7 Ma age tholeiitic magmatic event dated by Rancan et al. (2018). This magmatism is associated with hydrothermal vents and fumaroles at the bottom of the lake, hence influencing the sedimentary deposition and the laminated pattern of dolomites (Rancan et al., 2018; Oliveira et al., 2019; Oliveira et al., 2023). Also, according to Moulin et al. (2012), the oldest oceanic spreading and plate rotation for the configuration of the Santos Basin happened at 127.5 Ma and 125 Ma, which formed open spaces for fluid circulation. In consequence, the combination of high heat flux and fluid circulation in a continental setting may have allowed Mg-rich brines to reach the lacustrine environment, inducing dolomite precipitation.

In our study, calcite primary particles like shrubs, spherulites, ostracods, and peloids, yielded ages ranging from 116 ± 4 Ma to 82 ± 6 Ma. When examined under the petrographic microscope, these particles seem to preserve their primary depositional features, including calcite mineralogy and the absence of diagenetic overprints. The older ages (ranging from 116 ± 4 Ma to 110 ± 4 Ma) were observed on samples collected from well C. Among the dated particles, an ostracod valve made of calcite in a coarse-grained and porous shrubstone provided a statistically robust (i.e., well-regressed) lower intercept U-Pb age of 114 ± 3 Ma (Figure 5J-L). This carbonate particle initially incorporated high and variable amounts of U and low, homogeneous levels of Pb, known as common Pb. Furthermore, it has no evidence of strong post-depositional diagenetic modifications, which commonly affects the age of carbonate rocks (Rasbury & Cole, 2009). Thus, based on petrography, mineralogy, and our U-Pb data, we contend that the age of these ostracods and similar calciferous particles represent an early diagenetic age of the Upper Barra Velha Formation carbonates. Despite the age range of these older calciferous primary constituents (116 ± 4 Ma - 110 ± 4 Ma) being within the depositional interval of primary particles proposed by Moreira et al. (2007) and Lawson et al. (2022), including an ID-

TIMS depositional age of 115.83 ± 1.56 Ma (2s) for the Upper Barra Velha Formation (Lawson et al., 2022), the studied particles occur in porous and permeable shrubstones, grainstones and rudstones (Figure 5) that had been modified by post-sedimentary fluids contemporaneous to the 116 Ma basaltic magmatism dated by Louback et al. (2023) and the 114 Ma hydrothermal alteration dated by Rancan et al. (2018).

In contrast to well C, calciferous primary particles from wells B and A display younger U-Pb ages. For instance, calcite samples from well B exhibit U-Pb ages ranging from 105 ± 3 Ma to 99 ± 7 Ma. Similarly, well A also displays U-Pb ages as young as 100 ± 5 Ma and 82 ± 6 Ma (Figure 5). As illustrated in Figure 2, the uppermost samples from cores B and A are within the same stratigraphic interval of the Upper Barra Velha Formation, thus reinforcing the similar age data. However, the middle section of the core B, despite being correlated with core C, exhibits younger U-Pb age data. The age of primary particles along core B is quite homogenous, suggesting that their ages were affected by a pervasive interaction with post-depositional fluids. Since both B and A cores exhibit younger ages that overlap magmatic and hydrothermal events in the pre-salt, we suggest that a heat source near these two cores was probably the main drive of the hydrothermal system that affected these cores at ~105/100 Ma. The core C, in turn, located in the north of the Zeta high, seemed not to be disturbed by this ~105/100 Ma hydrothermal event, preserving its older 116 ± 4 Ma to 110 ± 4 Ma ages.

Our primary age data for cores B and A are within the same range as those reported by Rochelle-Bates et al. (2022) for shrubs and spherulites in the Upper Barra Velha Formation (106.9 ± 4.3 Ma). These authors also interpreted this age as reflecting a diagenetic replacement of the U-Pb system. They attribute the recrystallization of particles to fluid-flow events and a spike in heat-flow during the onset–early stages of the post-rift. In another study, Tritlla et al. (2018) dated at 107.0 ± 1.0 to 104.3 ± 0.8 Ma by $^{40}Ar/^{39}Ar$ a hydrothermal adularia formed at 90–170°C from the Campos Basin pre-salt. In the pre-salt section of the Kwanza Basin, Loma et al. (2018) reported a hydrothermal basalt alteration at 106.9 ± 1.6 Ma ($^{40}Ar/^{39}Ar$). According to Godeau et al. (2021), a significant heat event occurred at ~ 104 Ma Kwanza Basin, possibly followed by a second event at ~85 Ma. These post-rift high thermal regimes drove hot fluid circulations associated with a significant transform fault corridor. Likewise, Lima et al. (2020) proposed a hydrothermal alteration model for the Macabu Formation, pre-salt of the Campos Basin. They suggested that the faults and horizontal permeability of the

carbonates contributed to the circulation of hydrothermal fluids. In most instances, these young primary particles lack evidence of recrystallization and diagenetic overprint, as revealed by petrographic observations. However, Zuddas et al. (2018) detected that a nanoscale stress-induced fluid-migration may occur in calcite crystals, affecting the physical properties of particle and rocks. These authors also noticed that the mobility of fluids at the micro-nano scale in calcite crystals is enhanced at higher temperatures, such as the burial diagenesis temperatures that the Upper Barra Velha Formation carbonates were subject to (45 ± 5 °C - 91 ± 8 °C; Lawson et al., 2022). Hosa et al. (2020), in turn, observed that shrubs morphologies may favor fluid flow because of their high porosity and permeability.

4.5.2 Secondary Dolomites Ages, Morphologies and Their Geologic Contexts

The secondary dolomites covered in this section exhibit ages between 123 ± 4 Ma and 95 ± 4 Ma. They occur as microcrystalline pseudomorphic lamellar dolomites, microcrystalline pseudomorphic dolomites, rhombohedral pervasive dolomites, blocky dolomite and saddle dolomites. They may be divided into pre-silicification dolomites and post-silicification dolomites.

Pre-silicification secondary dolomites exhibit an age range of 123 ± 4 Ma - 99 ± 6 Ma. The oldest of these dolomites appear as 123 ± 4 Ma fine rhombohedral dolomites that are intercalated with younger spherulites whose age is of 100 ± 5 Ma; and as a 117 ± 3 Ma microcrystalline pseudomorphic lamellar dolomite. These dolomites are interpreted as eodiagenetic replacement phases that substitute Mg-clays and spherulites in spherulitestones (Figure 6A-C; Figure 9A-C). Another pre-silicification secondary dolomites occur as pervasive rhombohedral dolomites that replace particles and fill pore spaces in shrubstones, grainstones and rudstones, with ages ranging from 112 ± 7 Ma to 108 ± 5 Ma. Also, there are microcrystalline and fine rhombohedral dolomites within laminated dolomitic layers that yielded ages of 109 ± 4 Ma, and 109 ± 3 Ma. These later ~109 Ma dolomitic layers are interlayered with younger spherulites and shrubs whose ages are of 99 ± 7 Ma and 100 ± 3 Ma, respectively (Figure 9D-F). The existence of dolomites with older ages than shrubs and spherulites ages is a curious result because, in these samples, dolomites are interpreted as early diagenetic phases formed later than the spherulites and shrubs, replacing them and filling pore spaces in the sample (Figure 9). Somehow, this is in accordance with the U-Pb post-depositional replacement observed in

primary calcite particles and the preservation of pristine ages in low-porous, low-permeable, and less reactive dolomitic aggregates. The youngest pre-silicification dolomites occur a pseudomorphic microcrystalline dolomites that replaced Mg-clays and ostracod particles. Since these dolomites show the same $^{207}Pb/^{206}Pb$ composition of 0.880, we integrate their U-Pb data, which resulted in a pooled age of 103 ± 5 Ma (Figure 7). These pre-silicification microcrystalline and rhombohedral dolomites are partially replaced by silica phases (Figure 6A-B; Figure 7A-B; Figure 9C-D; Figure 9K-L). We contend that the association of these dolomites with more porous and permeable facies can be related to the percolation of magnesium-rich fluids. For example, Lima et al. (2020) suggested that faults and the horizontal permeability of the carbonates contributed to the circulation of hydrothermal fluids in the Macabu Formation. This interpretation is supported by the age interval of these dolomites, falling within the age range (116 Ma – 109 Ma) of the Aptian magmatism dated by Louback et al. (2023), the tectonic activity related to the Helmut lineament (~115/114 Ma according to Dehler et al. 2016), and the hydrothermal alteration of tholeiitic basaltic rocks ($^{40}Ar/^{39}Ar$ 114.3 ± 1.1 Ma) reported by Rancan et al. (2018). These events documented in the Santos Basin suggest a correlation between dolomite precipitation, supply of thermal energy, and availability of Mg ions provided by basaltic magmatism and tectono-thermal events. Regarding the 103 ± 5 Ma pooled age of microcrystalline pseudomorphic dolomites, since their diagenetic occurrence is referred as early diagenetic (Wright and Barnett, 2015; Tonietto et al., 2018; Lima & De Ros, 2019; Carvalho & Fernandes, 2021; this study), we argue that their Albian-Cenomanian age is related to dolomite U-Pb replacement caused by the interaction with a silica-rich fluid and burial diagenesis (e.g. Sumner and Bowring, 1996; Gasparrini et al., 2023).

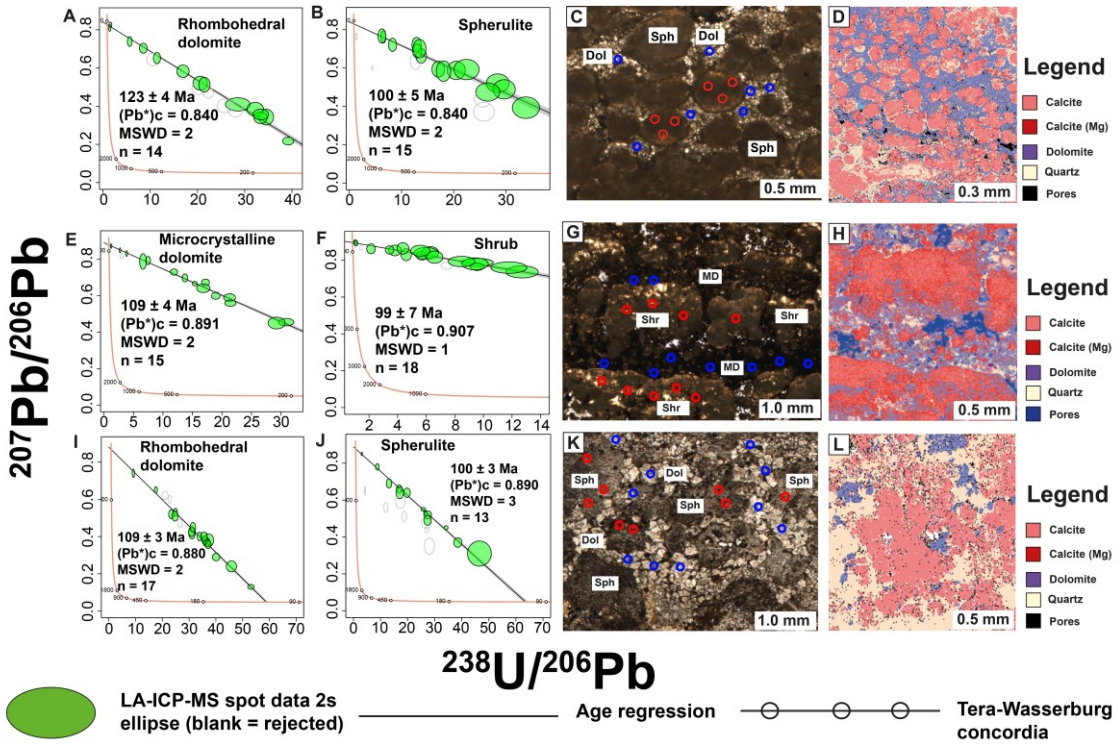

Figure 9. Dolomitic layers intercalated with shrubs and spherulites and their U-Pb ages. (A) Tera-Wasserburg concordia diagram showing $^{238}U/^{206}Pb$ versus $^{207}Pb/^{206}Pb$ data of fine rhombohedral dolomite crystals (B) Tera-Wasserburg concordia diagram showing $^{238}U/^{206}Pb$ versus $^{207}Pb/^{206}Pb$ data of spherulite particles. (C) PPL photomicrograph of dolomitic spherulitestone with fine rhombohedral dolomite crystals filling interparticle pores and partially replacing spherulite particles. Sample is 5090.95 from well A (D) QEMSCAN image of figure in (C) highlighting the calcite composition of the spherulites, the interstitial dolomite and silica partially replacing spherulites. (E) Tera-Wasserburg concordia diagram showing $^{238}U/^{206}Pb$ versus $^{207}Pb/^{206}Pb$ data of interstitial microcrystalline dolomite. (F) Tera-Wasserburg concordia diagram showing $^{238}U/^{206}Pb$ versus $^{207}Pb/^{206}Pb$ data of shrub particles. (G) PPL photomicrograph of dolomitic shrubstone with microcrystalline dolomite layers intercalated with layers of shrubs. Sample is 5015.10 from well B. (H) QEMSCAN image of figure in (G) highlighting the calcite composition of the shrubs, and the partial replacement of shrubs by the microcrystalline dolomite. (I) Tera-Wasserburg concordia diagram showing $^{238}U/^{206}Pb$ versus $^{207}Pb/^{206}Pb$ data of fine rhombohedral dolomite crystals. (J) Tera-Wasserburg concordia diagram showing $^{238}U/^{206}Pb$ versus $^{207}Pb/^{206}Pb$ data of spherulite particles. (K) PPL photomicrograph of dolomitic-silicified spherulitestone with fine rhombohedral dolomite crystals filling interparticle pores and partially replacing spherulite particles. Sample is 5144.00 from well B. (L) QEMSCAN image of figure in (K) highlighting the calcite composition of spherulite particles, the surrounding silica and the rhombohedral dolomite crystals between the particles. Quoted age uncertainty includes propagated systematic uncertainties. Datapoint error ellipses are 2s. MSWD, mean squared weighted deviation. (Pb*)c is $(^{207}Pb/^{206}Pb)_c$, known as common lead composition. Red circles represent analytical spots carried out at calcite particles. Blue circles represent analytical spots carried out at dolomite phases. Dol: dolomite; MD: microcrystalline dolomite; Shr: shrub; Sph: spherulite.

The post-silicification dolomites occur as later diagenetic cements such as (1) blocky dolomite cement filling vuggy and intraparticle fracture porosities in shrubstones, with an age of 99 ± 4 Ma (Figure 6H-I); (2) as saddle dolomite cements filling vuggy and fracture porosities lined by quartz crystals in cherts and grainstones, with the saddle dolomite crystals showing ages of 97 ± 5 Ma and 97 ± 4 Ma (Figure 6J-K; 6N-O); and (3) as 100 ± 3 Ma and 95 ± 4 Ma pervasive rhombohedral dolomite crystals in grainstones (Figure 6L-M). These dolomite occurrences are not affected by silicification features, thus being interpreted as post-silicification phases. Their ages are contemporaneous with the post-depositional hydrothermal alteration at ~ 105/100 Ma that significantly affected the pre-salt carbonate U-Pb system. Likewise, for the precipitation of saddle dolomite, a high temperature is required (> 60°C; Spötl & Pitman, 1998). The younger ~98 Ma pervasive rhombohedral dolomites seems to be contemporaneous to the ~ 90 Ma Cenomanian pervasive dolomitization event dated by Godeau et al. (2021) in the pre-salt of the Kwanza Basin, which was interpreted to have occurred at a relatively shallow burial, with the presence of hot fluids (ca. 150°C). Thus, these dolomite morphologies and timing are in concordance with the presence of an elevated thermal regime and sources of hydrothermal fluids affecting the Upper Barra Velha Formation and other basins of the pre-salt system at ~105 - 100 Ma (e.g. Trittla et al., 2018; Loma et al., 2018; Godeau et al., 2021; Rochelle-Bates et al., 2021; Rochelle-Bates et al., 2022). The 97 ± 4 Ma age saddle dolomite limits also a silicification event since the saddle dolomite is a post-silicification phase that fills vuggy pores lined by macrocrystalline quartz. This means that the silicification events observed in these samples are older than 100 Ma.

4.6 CONCLUSIONS

Carbonates from the Upper Barra Velha Formation exhibit a wide range of ages, indicating that the Santos Basin carbonates were affected by a superposition of geologic events. In contrast to U-Pb dating of zircons, which is a pretty stable mineral phase under low temperature processes, U-Pb dating in carbonates may be affected by post-depositional processes, such as diagenesis and hydrothermalism. Hence, as seen here, the interpretation of U-Pb dating of carbonate rocks requires the input of information about the geological evolution of the sedimentary rocks, including diagenesis, hydrothermal alteration, mineralogical transformations, tectonic events, among others.

The ages obtained in this study are comparable to tectonic and thermal events that affected the Santos Basin, including plate motion, oceanic spreading, and basaltic

magmatism. These events have geochronological ages of ~ 127/125 Ma; ~ 116/114 Ma; and ~ 105/100 Ma. Similar events are also reported for other pre-salt basins such as (1) the Campos Basin, in which a hydrothermal (90–170°C) activity was dated by adularia $^{40}Ar/^{39}Ar$ ages of 107.0 ± 1.0 – 104.3 ± 0.8 Ma (Tritlla et al., 2018); (2) the Kwanza Basin, in which a basalt alteration yielded $^{40}Ar/^{39}Ar$ ages of 114.5 ± 2.9 to 106.9 ± 1.6 Ma. Theses ages were used to constrain a hydrothermal (c. 140°C) pulse in the African pre-salt (Loma et al., 2018), where elevated thermal regimes were identified by Godeau et al. (2021) at ~104 Ma. These evidences imply that the tectonic-magmatic events identified here had a wide-reaching influence on carbonate deposition and diagenesis on a regional scale of the pre-salt system.

The geochronological replacement of the particles may not be a pervasive effect, but instead may depend more on fluid-rock interaction and physical properties of the particles such as porosity and permeability. This was observed on non-porous and non-permeable dolomitic layers formed by dolomite crystals arranged with a Planar-s texture, which were not affected by the U-Pb replacement. Ages of calcite primary particles, otherwise, recorded superposition of post-depositional events. As another example, carbonate particles from wells B and A have ages of ~ 105 Ma. In contrast, calcite particles from well C are older, displaying ages around ~ 115 Ma. We suggest that samples from cores B and A were affected by a nearby heat source at ~105/100 Ma, unlike carbonates from well C.

The first generation of dolomites occurs as pre-silicification Barremian-Aptian microcrystalline to very fine laminated primary dolomite rhombs. This is the first direct U-Pb Barremian age registered in the Upper Barra Velha Formation, in agreement with Tedeschi et al. (2017) and Pietzsch et al. (2020) that proposed an age of ~ 125/120 Ma for deposition of the Upper Barra Velha Formation. The second generation is formed essentially by ~ 117 – 108 Ma pre-silicification fine rhombohedral dolomite crystals that are the product of pervasive dolomitization. The third generation of dolomites have ages of ~ 100 Ma and are composed by pre-silicification pseudomorphic microcrystalline dolomites that likely underwent U-Pb replacement related to an Albian-Cenomanian silicification event, by pervasive dolomite rhombs, and by post-silicification later diagenetic cements such as blocky dolomite and saddle dolomite. The saddle dolomite temporally limits a silicification event as older than 100 Ma. Indeed, dolomite-silica

petrographic relations indicate a time constrain for silicification events between 112 Ma and 100 Ma in the studied rocks.

4.7 AKNOWLEDGEMENTS

This research was carried out in association with the ongoing R&D Project registered as ANP 21891-7, “Geologia e geoquímica dos reservatórios das seções “sag” e topo do rifte das áreas de Sapinhoá e Lapa na bacia de Santos” (UnB/IG/EQUINOR/ANP/FINATEC) – Geology and geochemistry of the “sag” and top of the rift reservoirs in the Sapinhoá and Lapa areas in the Santos Basin, sponsored by Equinor Brasil under the ANP R&D levy as “Compromisso de Investimentos com Pesquisa e Desenvolvimento”. This study was financed in part by the Coordenção de Aperfeiçoamento de Pessoal de Nível Superior – Brasil (CAPES) – Finance Code 001.

CAPÍTULO 5

5.1 CONCLUSÕES E RECOMENDAÇÕES

Este trabalho reforça a viabilidade da datação de carbonatos pelo sistema U-Pb e demonstra que a aplicação dessa técnica deve estar junta a estudos petrográficos, mineralógicos e geoquímicos. Isso permite a identificação não apenas da idade de deposição de carbonatos, mas também o reconhecimento temporal de eventos pós-deposicionais que afetaram as rochas carbonáticas estudadas, como a percolação de fluidos em rochas. Isso é relevante para o estabelecimento de uma cronologia da diagênese e para relacionar produtos diagenéticos ou perturbações no sistema isotópico U-Pb das partículas com a história geológica da bacia.

Este trabalho também mostra a influência de propriedades físicas das rochas sobre possíveis alterações pós-deposicionais. Por exemplo, fases de dolomita ocorrendo em arranjos mais fechados, com baixas porosidade e permeabilidade, dificultaram o efeito de rejuvenescimento geocronológico. Partículas primárias, por sua vez, com porosidade intrapartícula, frequentemente exibiram idades mais jovens do que o esperado. Isso ocorre provavelmente porque a substituição geocronológica do sistema U-Pb está relacionada a interações rocha-fluido.

Além disso, a geocronologia U-Pb de carbonatos, juntamente com análises petrográficas, pode ser considerada uma ferramenta adicional para detectar modificações diagenéticas em carbonatos. Como visto, o *a* substituição do sistema U-Pb pode ocorrer, o que indica uma modificação diagenética nos carbonatos estudados. Por outro lado, carbonatos com idades muito precisas, com razão isotópica U-Pb bem espalhada e com baixo Pb comum provavelmente mantiveram sua composição original. Tal implicação da geocronologia U-Pb de carbonatos pode ser relevante para estudos paleoambientais e paleoclimáticos que exigem amostras cuja composição geoquímica foi preservada.

Portanto, como recomendações para estudos de datação de carbonatos, deve-se ter atenção para a interpretação das idades obtidas por U-Pb em carbonatos, pois o sistema U-Pb pode se comportar de maneira heterogênea dentro de uma mesma lâmina delgada, podendo ocorrer de carbonatos exibirem idades mais jovens que o esperado. Então, demonstra-se necessário informações sobre eventos tectônicos, magmáticos e hidrotermais contemporâneos à evolução geológica da área estudada.

CAPÍTULO 6

6.1 REFERÊNCIAS BIBLIOGRÁFICAS

Arienti, L. M., R. S., Souza, S., Viana, M., Cuglieri, R., Silva Filho, F. V., Passos, S. N., Tonietto, L., Paula, and J. A. Gil. (2018), Sistemas deposicionais e modelos paleofisiográficos evolutivos da Formação Barra Velha: Pré-sal da Bacia de Santos: Resumo do 19 Congresso Brasileiro de Geologia, Rio de Janeiro, Brasil, Agosto 20–24, 1 p.

Ariza Ferreira, D. J., Lupinacci, W. M., Neves, I. A., Zambrini, J. P. R., Ferrari, A. L., Gamboa, L. A. P., Azul, M.A. (2019). Unsupervised seismic facies classification applied to a presalt carbonate reservoir, Santos Basin, offshore Brazil. *AAPG Bulletin* 2019;; 103 (4): 997–1012. doi: https://doi.org/10.1306/10261818055.

Basso, M., Belila, A.M.P., Chinelatto, G.F. et al., (2021). Sedimentology and petrophysical analysis of pre-salt lacustrine carbonate reservoir from the Santos Basin, southeast Brazil. Int J Earth Sci (Geol Rundsch) 110, 2573–2595 (2021). https://doi.org/10.1007/s00531-020-01932-7

Bateman, H. (1910). Solution of a system of differential equations occuring in the theory of radioactive transformations. Proceedings of the Cambridge Philosophical Society, 15:423–427.

Beasley, C. J., Fiduk, J. C., Bize, E., Boyd, A., Frydman, M., Zerilli, A., Dribus, J. R., Moreira, J. L. P., Capeleiro., Pinto, A. C. (2010). Brazil's presalt play. Oilfeld Rev 22(3):28–37.

Brannon, J. C., Cole, S. C., Podosek, F. A., Ragan, V. M., Coveney, R. M., Wallace, M. W., Bradley, A. J. (1996). Th-Pb and U-Pb dating of ore-stage calcite and Paleozoic fluid flow. Science, 271, 491-493, 1996.

Carroll, S.A., Bruno, J., Petit, J. C, Dran J.C. (1992). Interaction of U(VI), Nd, and Th(IV) at the calcite-solution interface. Radiochim. Acta, 58/59 (1992), pp. 245-252.

Carvalho, M.D., Fernandes, F.L. (2021). Pre-Salt Depositional System: Sedimentology, Diagenesis, and Reservoir Quality of the Barra Velha Formation, as a Result of the Santos Basin Tectono-Stratigraphic Development In: MELLO, M.R., YILMAZ, P.O., KATZ, B.J. (Eds.), Front Matter: The Supergiant Lower Cretaceous Pre-Salt Petroleum Systems of the Santos Basin, 124. AAPG Memoir, Brazil.

Chang, H. K., Kowsmann, R.O., Figueiredo, A. M. F., Bender, A. A. (1992). Tectonics and stratigraphy of the East Brazil Rift system: an overview. Tectonophysics 213:97–138

Cherniak, D.J. (1997). An experimental study of strontium and lead diffusion in calcite, and implications for carbonate diagenesis and metamorphism. Geochimica et Cosmochimica Acta, 61, 4173-4179, 1997.

Chew, D. M., Petrus, J. A., & Kamber, B. S. (2014). U–Pb LA–ICPMS dating using accessory mineral standards with variable common Pb. Chemical Geology, 363(Supplement C), 185– 199. DOI: 10.1016/j.chemgeo.2013.11.006.

Chung, G. S., & Swart, P. K. (1990). The concentration of uranium in freshwater vadose and phreatic cements in a Holocene ooid cay: a method of identifying ancient water tables. Journal of Sedimentary Research, 60(5).

Cole, J. M., Rasbury, E. T., Hanson, G. N, Montanez, I. P., and.Pedone, V. A. (2005). Using U-Pb ages of Miocene tufa for correlation in a terrestrial succession, Barstow Formation, California,Geol.Soc. Am. Bull.,117, 276–287, doi:10.1130/B25553.1.

Cole, J. M., Rasbury, E. T., Montañez, I. P., Pedone, V. A., Lanzirotti, A., and Hanson, G. N. (2004). Petrographic and trace element analysis of uranium-rich tufa calcite, middle Miocene Barstow Formation, California, USA: Uranium-rich tufa deposits, California, Sedimentology, 51, 433–453, DOI: 10.1111/j.1365-3091.2004.00631.x.

Craig, G., Horstwood, M. S. A., Reid, H. J., Sharp, B. L. (2020). 'Blind time' – current limitations on laser ablation multi-collector inductively coupled plasma mass spectrometry (LA-MC-ICP-MS) for ultra-transient signal isotope ratio analysis and application to individual sub-micron sized uranium particles. Journal of Analytical Atomic Spectrometry. 35, 1011-1021. DOI: 10.1039/D0JA00066C.

Dani, A. P. O., Remus, M. V. D., Dani, N., Lima, E. F. (2017) Magmatismo basáltico do Andar Alagoas (Bacia de Campos). Geol USP SerCient 17(2):269–287. https://doi.org/10.11606/issn.2316-9095.v17-373.

De Paula Faria, D. L., Dos Reis, A. T., and De Souza Jr, O. G. (2017). Three-dimensional stratigraphic-sedimentological forward modeling of an Aptian carbonate reservoir deposited during the sag stage in the Santos basin, Brazil. Marine and Petroleum Geology, 88, 676-695.

Dehler, N. M., Magnavita, L. P., Gomes, L. C., Rigoti, C. A., de Oliveira, J. A. B., Sant'Anna, M. V., & da Costa, F. G. D. (2016). The 'Helmut'geophysical anomaly: a regional left-lateral transtensional shear zone system connecting Santos and Campos basins, southeastern Brazil. Marine and Petroleum Geology, 72, 412-422.

DeWolf, C. P. and Halliday, A. N. (1991). U-Pb dating of a remagnetized Paleozoic limestone. Geophysical Research Letters, 18, 1445-1448, 1991.

Dias, J. L., Scarton, J. C., Esteves, F. R., Carminatti, M., & Guardado, L. R. (1990). Aspectos da evolução tectono-sedimentar e a ocorrência de hidrocarbonetos na Bacia de Campos. Origem e evolução de bacias sedimentares, 2, 333-360.

Dias, J. L., Sad, A.R.E., Fontana, R.L., and Feijó, F.J. (1994). Bacia de Pelotas: Boletim de Geociências da Petrobras, v. 8, p. 235–245.

Dickin, A. P., 2005. Rdiogenic Isotope Geology. Cambridge, School of Geography and Earth Sciences McMaster University, Hamilton, Ontario, 508p.

Drost, K., Chew, D., Petrus, J.A., Scholze, F., Woodhead, J. D., Schneider, J. W, Harper D. A. T. (2019). An image mapping approach to U-Pb LA-ICP-MS carbonate dating and applications to direct dating of carbonate sedimentation. Geochemistry, Geophysics, Geosystems 19, 4631–48

Dunham, R. J. (1962). Classification of carbonate rocks according to depositional texture. In: HAM, W.E. ed. Classification of carbonate rocks. Tulsa, AAPG Memoir 1. p. 108-121.

Elzinga, E.J., Tait, C.D., Reeder, R.J Rector, R.J. Donohoe, K.D. Morris, D.E. (2004). Spectroscopic investigation of U(VI) sorption at the calcite-water interface. Geochim. Cosmochim. Acta, 68. pp. 2437-2448

Farias, F., Szatmari, P., Bahniuk, A., França, A. B. (2019). Evaporitic carbonates in the pre-salt of Santos Basin—genesis and tectonic implications. Mar Pet Geol 105:251–272. https://doi.org/10.1016/j.marpetgeo.2019.04.020.

Fodor, R. V., Vetter, S. K. (1984). Rift-zone magmatism: Petrology of basaltic rocks transitional from CFB to MORB, southeastern Brazil margin. Contrib. Miner. Petrol. 88(4):307–321. https://doi.org/10.1007/BF00376755.

Gasparrini, M., Morad, D., Mangenot, X., Bonifacie, M., Morad, S., Nader, F. H., & Gerdes, A. (2023). Dolomite recrystallization revealed by Δ47/U-Pb thermochronometry in the Upper Jurassic Arab Formation, United Arab Emirates. Geology, 51(5), 471-475.

Geipel, G., Reich, T., Brandler, V., Bernhard, G. Nitsche, H. (1997). Laser and X-ray spectroscopic studies of uranium-calcite interface phenomena. J. Nucl. Mater., 248 pp. 408-411.

Godeau, N., Girard, J. P., Guihou, A., Hamelin, B., & Deschamps, P. (2021). U-Pb and Th-Pb dating of diagenetic/hydrothermal phases in the pre-salt series, Angola offshore: implication for the paleo-thermal history during South Atlantic rifting. Goldschmidt2021• Virtual• 4-9 July.

Gomes, A & Vasconcelos, P. (2021) Geochronology of the Paraná-Etendeka large igneous province. Earth Sci Rev 220:103716. https:// doi.org/10.1016/j.earscirev.2021.103716.

Gomes, J. P., Bunevich, R. B., Tedeschi, L. R., Tucker, M. E., & Whitaker, F. F. (2020). Facies classification and patterns of lacustrine carbonate deposition of the Barra Velha Formation, Santos Basin, Brazilian Pre-salt. Marine and Petroleum Geology, 113, 104176. https://doi.org/10.1016/j.marpetgeo.2019.104176

Gomes, L.C., Lima, F.M., Vieira, I.S., Lobo, J.T., et al., (2015). Magmatismo Jiquiá e Alagoas na Bacia de Santos. Petrobras Internal Report.

Gomes, P. O. B., Kilsdonk, T. Grow, J. Minken, and R. Barragan. (2012). Tectonic evolution of the outer high of Santos Basin, southern São Paulo Plateau, Brazil, and implications for hydrocarbon exploration, in D. Gao, ed., Tectonics and sedimentation: Implications for petroleum systems: AAPG Memoir 100, p. 1–14.

Gordon, A. C., Mohriak, W. U., Stanton, N., & Santos, A. C. (2023). Magmatic cycles in Santos Basin (SE Brazil): Tectonic control in the temporal-spatial distribution and geophysical signature. Journal of South American Earth Sciences, 121, 104111.

Guedes, E., Heilbron, M., Vasconcelos, P. M., de Morisson Valeriano, C., Almeida, J. C. H., Teixeira, W., Filho, A. T. (2005) K-Ar and $^{40}Ar/^{39}Ar$ ages of dikes emplaced in the onshore basement of the Santos Basin, Resende area, SE Brazil: Implications for the south Atlantic opening and Tertiary reactivation. J S Am Earth Sci 18(3–4):371–382. https://doi.org/10.1016/j.jsames.2004.11.008.

Hansman, R. J., Albert, R., Gerdes, A. and Ring, U. (2018). Absolute ages of multiple generations of brittle structures by U-Pb dating of calcite. Geology, 46, 207-210, 2018.

Herlinger, R.; Zambonato, E.E.; De Ros, L.F. Influence of diagenesis on the quality of lower cretaceous pre-salt lacustrine carbonate reservoirs from northern Campos Basin, Offshore Brazil. J. Sediment. Res. (2017). 87, 1285–1313.

Hiess, J., Condon, D. J., McLean, N., Noble, S.R. (2012). 238U/235U Systematics in Terrestrial Uranium-Bearing Minerals. Science 335, 1610. DOI: 10.1126/science.1215507.

Hosa, A., Wood, R. A., Corbett, P. W. M., de Souza, R. S., & Roemers, E. (2020). Modelling the impact of depositional and diagenetic processes on reservoir properties of the crystal-shrub limestones in the 'Pre-Salt'Barra Velha Formation, Santos Basin, Brazil. Marine and Petroleum Geology, 112, 104100.

Hunt, D. (2021). The Bacalhau Field: New Insights into Lacustrine Carbonate Platform Development, Santos Basin, Brazil. In Second EAGE Conference on Pre-Salt Reservoir (Vol. 2021, No. 1, pp. 1-5). European Association of Geoscientists & Engineers.

Jones, C. E., Halliday, A. N., and Lohmann, K. C. (1995) Theimpact of diagenesis on high-precision UPb dating ofancient carbonates: an example from the Late Permian ofNew Mexico.Earth Planet. Sci. Lett.,134(3–4), 409–423.

Karner, G., Johnson, C., Shoffner, J., Lawson, M., Sullivan, M., Sitgreaves, J., McHarge, J., Stewart, J., and Figueredo, P. (2021). Tectono-magmatic development of the Santos and Campos basins, offshore Brazil, in Mello, M.R., Yilmaz, P.O., and Katz, B.J., eds., The supergiant Lower Cretaceous pre-salt petroleum system of the Santos Basin, Brazil: AAPG Memoir 124, p. 215–256.

Kelly, S. D., Newville, M., Cheng, L. R., Kemner, K. M., Sutton, S. R., Fenter, P.,Sturchio, N.C., and Spotl, C. (2003). Uranyl incorporation in natural calcite..Environ.Sci. Technol.,37, 1284–1287

Klinkhammer, G. P. and Palmer, M. R (1991). Uranium in the Oceans: Where it goes and why. Geochim. Cosmochim. Acta 55, 1799-1806.

Langmuir, D. (1978), Uranium solution-mineral equilibria at low temperatures with applications to sedimentary ore deposits, Geochim. Cosmochim Acta, 42, 547– 569, doi:10.1016/0016- 7037(78)90001-7.

Lawson, M., Sitgreaves, J., Rasbury, T., Wooton, K., Esch, W., Marcon, V., ... & Eiler, J. (2022). New age and lake chemistry constraints on the Aptian pre-salt carbonates of the central South Atlantic. *Bulletin*, *135*(3-4), 595-607.

Li, Q., Parrish, R. R., Horstwood, M. S. A. and McArthur, J. M. (2014). U–Pb dating of cements in Mesozoic ammonites. Chemical Geology, 376, 76-83, 2014.

Lima, B. E. & De Ros, L. F. (2019). Deposition, diagenetic and hydrothermal processes in Aptian Pre-Salt lacustrine carbonate reservoirs of the northern Campos Basin, offshore Brazil. Sedimentary Geology 383, 55–81.

Lima, B. E., Tedeschi, L. R., Pestilho, A. L. S., Santos, R.V., Vazquez, J. C., Guzzo, J. V. P., De Ros, L. F. (2020). Deep-burial hydrothermal alteration of the Pre-Salt carbonate reservoirs from northern Campos Basin, offshore Brazil: Evidence from petrography, fluid inclusions, Sr, C and O isotopes, Marine and Petroleum Geology (2020), doi: https:// doi.org/10.1016/j.marpetgeo.2019.104143.

Loma, R., Tritlla, J., Esteban, M., Sanders, C., Carrasco, A., Herra, A., Gerona, M., Mañas, M., & Boix, C. (2018). Hydrothermal flushing and calcite precipitation as main modifiers of a pre-salt reservoir in Kwanza Basin (Angola). In AAPG ACE 2018 Abstracts. American Association of Petroleum Geologists.

Louback, V.S., de Castro Valente, S., de Almeida, C.N., Ross, J., Borghi, L. (2021). Petrogenesis and geodynamics of Eocene alkaline intrusions in the pre-salt sedimentary sequence of Santos Basin, Brazil. Lithos. https://doi.org/10.1016/j.lithos.2021.106400.

Louback, V.S., de Castro Valente, S., de Almeida, C.N. et al., Aptian flood basalts in Bacalhau oil and gas field: petrogenesis and geodynamics of post-rift tholeiites in the pre-salt sequence of Santos Basin, Brazil. Contrib. Mineral. Petrol. 178, 15 (2023). https://doi.org/10.1007/s00410-023-01995-0.

Ludwig, K. R. (1998). On the treatment of concordant uranium-lead ages. Geochimica et Cosmochimica Acta, 62(4), 665-676.

MacDonald, J. M., Faithfull, J. W., Roberts, N. M. W., Davies, A. J., Holdsworth, C. M., Newton, M., Williamson, S., Boyce, A., John, C. M. (2019). Clumped-isotope palaeothermometry and LA-ICP-MS U–Pb dating of lava-pile hydrothermal calcite veins. Contributions to Mineralogy and Petrology, 174, 63, 2019.

Malinverno, A., Erba, E., & Herbert, T. D. (2010). Orbital tuning as an inverse problem: Chronology of the early Aptian oceanic anoxic event 1a (Selli Level) in the Cismon APTICORE. Paleoceanography, 25(2).

Mangenot, X., Gasparrini, M., Gerdes, A., Bonifacie, M. and Rouchon, V. (2018). An emerging thermochronometer for carbonate-bearing rocks: Δ47/(U-Pb). Geology, 46, 1067-1070, 2018.

Mezger, K. and Krogstad, E.J. (1997). Interpretation of discordant U-Pb zircon ages: An evaluation. Journal of Metamorphic Geology, 15, 127-140.

Miyajima, Y. Saito, A., Kagi, H., Yokoyama, T., Takahashi, Y., Hirata, T. (2020). Incorporation of U, Pb and Rare Earth Elements in Calcite through Crystallisation from Amorphous Calcium Carbonate: Simple Preparation of Reference Materials for Microanalysis. Geostandards and Geoanalytical Research. 45(1). Pages 189-205. DOI: 10.1111/ggr.12367.

Mizusaki, A. M. P., Petrini, R., Bellieni, P., Comin-Chiaramonti, P., Dias, J., De Min, A., Piccirillo, E. M. (1992). Basalt magmatism along the passive continental margin of SE Brazil (Campos basin). Contrib. Miner. Petrol 111(2):143–160.

Mohriak, W., Nemčok, M., Enciso, G. (2008). South Atlantic divergent margin evolution: rift-border uplift and salt tectonics in the basins of SE, Brazil, vol 294. Geological Society, London, pp 365–398

Montano, D. (2021). Carbonate U-Pb dating via LA-ICPMS : insights into chronostratigraphy in lacustrine settings. Earth Sciences. Sorbonne Université, 2021.

Moreira, J. L. P.; Esteves, C. A.; Rodrigues, S, J. J. G.; Vasconcelos, C. S. (2006). Magmatismo, sedimentação e estratigrafia da porção norte da Bacia de Santos. Boletim de Geociências da Petrobras, Rio de Janeiro, v. 14, n. 1, p. 161-170, nov. 2005/maio 2006.

Moreira, J. L. P., Madeira, C. V., Gil, J. A., & Machado, M. A. P. (2007). bacia de Santos. Boletim de Geociencias da PETROBRAS, 15(2), 531-549.

Moulin, M., Aslanian, D., Rabineau, M., Patriat, M., Matias, L., 2012. Kinematic keys of the Santos – Namibe basins. In: Mohriak, W.U., Danforth, A., Post, P.J., Brown, D.E., Tari, G.C., Nemcok, M., Sinha, S.T. (Eds.), Conjugate Divergent Margins. London, Geological Society. https://doi.org/10.1144/SP369.3. Special Publications.

Neves, I. A., W. M., Lupinacci, D. J. A., Ferreira, J. P. R., Zambrini, L. O. A., Oliveira, M. O., Azul, A. L., Ferrari, and L. A. P., Gamboa. (2019). Presalt reservoirs of the Santos Basin: Cyclicity, electrofacies, and tectonic-sedimentary evolution: Interpretation, v. 7, no. 4, p. 1–11.

Nuriel, P., Craddock, J., Kylander-Clark, A.R., Uysal, T., Karabacak, V., Dirik, R.K., Hacker, B.R. and Weinberger, R. (2019). Reactivation history of the North Anatolian fault zone based on calcite age-strain analyses. Geology, 47, 465-469, 2019.

Nuriel, P., Wotzlaw, J., Ovtcharova, M., Vaks, A., Stremtan, C., Šala, M., Roberts, N. M. W., Kylander-Clark, A.R.C. (2021). The use of ASH-15 flowstone as a matrix-matched reference material for laser-ablation U − Pb geochronology of calcite. Geochronology, 3, 35–47, DOI: 10.5194/gchron-3-35-2021

Ogg, J. G., Hinnov, L. A., & Huang, C. (2012). Chapter 27, Cretaceous. The geologic time scale, 2012, 793-853.

Oliveira, L. C., Rancan, C. C., Oliveira, M. J. R. (2019). Sill emplacement mechanisms and their relationship with the Pre-Salt stratigraphic framework of the Libra Area (Santos Basin, Brazil). In Abstract. LASI VI Workshop on "The Physical Geology of Subvolcanic Systems: Laccoliths, Sillsvand Dykes", Malargüe, Argentina.

Oliveira, L.C., Penna, R.C., Rancan, C.C., Carmo, I.O., Marins, G.M. (2023). Seismic Interpretation of the Mero Field Igneous Rocks and its Implications for Pre- and Post-Salt Co2 Generation – Santos Basin, Offshore Brazil. Available at SSRN: https://ssrn.com/abstract=4394061 or http://dx.doi.org/10.2139/ssrn.4394061

Oreiro, S.G. (2006). Interpretação sísmica dos eventos magmáticos pós-aptianos no Alto de Cabo Frio, sudeste do Brasil, gênese e relação com os lineamentos pré-Sal Doctoral Thesis. Universidade do Estado do Rio de Janeiro (2006), p. 160.

Paton, C., Hellstrom, J., Paul, B., Woodhead, J., Hergt, J. (2011). Iolite: Freeware for the visualisation and processing of mass spectrometric data. J. Anal. At. Spectrom. 2011, 26, 2508–2518.

Petrus, J. A. and Kamber, B. S. (2012). VizualAge: a novel approach to laser ablation ICP-MS U–Pb geochronology data reduction. Geostand Geoanal Res 36(3):247–270.

Pickering, R., Kramers, J. D., Partridge, T., Kodolanyi, J., Pettke, T. (2010). U–Pb dating of calcite–aragonite layers in speleothems from hominin sites in South Africa by MC1706 ICP-MS. Quaternary Geochronology, 5, 544-558, 2010.

Pietzsch, R., Oliveira, D. M., Tedeschi, L. R., Neto, J. V. Q., Figueiredo, M. F., Vazquez, J. C., & de Souza, R. S. (2018). Palaeohydrology of the Lower Cretaceous pre-salt lacustrine system, from rift to post-rift phase, Santos Basin, Brazil. Palaeogeography, Palaeoclimatology, Palaeoecology, 507, 60-80.

Pietzsch, R., Tedeschi, L. R., Oliveira, D. M., dos Anjos, C. W. D., Vazquez, J. C., & Figueiredo, M. F. (2020). Environmental conditions of deposition of the Lower Cretaceous lacustrine carbonates of the Barra Velha Formation, Santos Basin (Brazil), based on stable carbon and oxygen isotopes: a continental record of pCO2 during the onset of the Oceanic Anoxic Event 1a (OAE 1a) interval?. Chemical Geology, 535, 119457.

Rancan, C. C., Oliveira, L. D., Carmo, I. D. O., Marins, G. M., Pessoa, V. D. O., Andrade, H., ... & Zanatta, A. S. (2018, August). Rochas Ígneas do Bloco de Libra, Bacia de Santos. In Congresso Brasileiro de Geologia (Vol. 49, p. 2012). Rio de Janeiro.

Rangel, H. D., Martins, F. A. L., Esteves, F. R., and Feijo, F. J. (1994). Bacia de Campos: Boletim de Geosiencias da Petrobras, v. 8, p. 203–217.

Rasbury, E.T. and Cole, J.M. (2009). Directly dating geologic events: U‐Pb dating of carbonates. Reviews of Geophysics, 47, 2009.

Rasbury, E.T., Hanson, G.N., Meyers, W.J. and Saller, A.H. (1997). Dating of the time of sedimentation using U-Pb ages for paleosol calcite. Geochimica et Cosmochimica Acta, 61, 1525-1529, 1997.

Rasbury, E. T., Present, M. P., Northrup, P., Tappero, R. V., Lanzirotti, A., Cole, J. M., Wooton., K. M., Hatton, K. (2020). A Sample Characterization Toolkit for Carbonate U-Pb Geochronology. Geochronology Discussions 2020, 1-42..

Rasbury, E.T., Present, T.M., Northrup, P., Tappero, R.V., Lanzirotti, A., Cole, J.M., Wooton, K.M., Hatton K. (2021). Tools for uranium characterization in carbonate samples: case studies of natural U–Pb geochronology reference materials. Geochronology, 3, 103–122, 2021. DOI: 10.5194/gchron-3-103-2021.

Rebelo, T. B., Batezelli, A., Mattos, N. H., & Leite, E. P. (2023). Sedimentary processes and paleoenvironment reconstruction of the Barra Velha formation, Santos Basin, Brazilian pre-salt. Marine and Petroleum Geology, 150, 106141.

Reeder, R.J., Nugent, M., Tait, C.D., Morris, D. E., Heald, S. M., Beck, K.M., W. P., Hess, Lanzirotti, A. (2001). Coprecipitation of Uranium(VI) with Calcite: XAFS, micro-XAS, and luminescence

characterization, Geochimica et Cosmochimica Acta, Volume 65, Issue 20, Pages 3491-3503, DOI: 10.1016/S0016-7037(01)00647-0.

Ren, K., Zhao, J., Liu, Q., Zhao, J. (2020). Hydrocarbons in igneous rock of Brazil: a review. Petrol Res 5(3):265–275. https://doi.org/10.1016/j.ptlrs.2020.06.001.

Richards, D. A., Bottrell, S. H., Cliff, R. A., Ströhle, K. and Rowe, P. J. (1998). U-Pb dating of a speleothem of Quaternary age. Geochimica et Cosmochimica Acta, 62, 3683-3688, 1998.

Rihs, S. Sturchio, N. Orlandini, K. Cheng, L. Teng, H. Fenter, P. Bedzyk, M. (2004). Interaction of uranyl with calcite in the presence of EDTA. Environ. Sci. Technol., 38, pp. 5078-5086.

Roberts, N., Drost, K., Horstwood, M., Condon, D. J., Chew, D., Drake, H., Milodowski, A. E., McLean, N. M., Smye, A., Walker, R. J., Haslam, R., Hodson, K., Imber, J. Beaudoin, N. (2020a). LA-ICP-MS U-Pb carbonate geochronology: strategies, progress, and application to fracture-fill calcite. Geochronology Discussion, Copernicus Gesellschaft mbH. https://doi.org/ 10.5194/gchron-2019-15. In press, 2020.

Roberts, N. M. W., Rasbury, T., Parrish, R. R.., Smith, C. J., Horstwood, M. S. A., Condon, D. J. (2017). A calcite reference material for LA-ICP-MS U-Pb geochronology. Geochem. Geophys. Geosyst. 2017, 18, 2807–2814.

Roberts, N. M. W., Žák, J., Vacek, F., Sláma, J. (2021). No more blind dates with calcite: Fluid-flow vs. fault-slip along the Očkov thrust, Prague Basin, Geoscience Frontiers, Volume 12, Issue 4. DOI: 10.1016/j.gsf.2021.101143

Rochelle-Bates, N., Roberts, N. M. W., Sharp, I., Freitag, U., Verwer, K., Halton, A., Fiordalisi, E., van Dongen, B. E., Swart, R., Ferreira, C.H., Dixon, R., & Schröder, S. (2021). Geochronology of volcanically associated hydrocarbon charge in the pre-salt carbonates of the Namibe Basin, Angola. Geology, 49(3), 335–340. http://dx.doi.org/10.1130/g48019.1.

Rochelle-Bates, N., Wood, R., Schröder, S., & Roberts, N. M. (2022). In situ U–Pb geochronology of Pre-Salt carbonates reveals links between diagenesis and regional tectonics. Terra Nova, 34, 271–277. https://doi.org/10.1111/ter.12586.

Rouff, A. A., E. J. Elzinga, R. J. Reeder, and N. S. Fisher (2004). X-ray absorption spectroscopic evidence for the formation of Pb (II) inner-sphere adsorption complexes and precipitates at the calcite-water interface, Environ. Sci. Technol., 38, 1700– 1707. DOI: 10.1021/es0345625

Sanjinés, A. E. S., Viviers, M. C., Costa, D. S., Zerfass, G. S. A., Beurlen, G., Strohschoen, O. (2022). Planktonic foraminifera from the Aptian section of the southeastern Brazilian Atlantic margin: Cretaceous Research, v. 134, https://doi.org/10.1016/j.cretres.2022.105141.

Sartorato, A. C. L. (2018). Caracterização faciológica, estratigráfica e diagenética dos reservatórios carbonáticos da Formação Barra Velha, Bacia de Santos (Dissertação de Mestrado).

Schoene, B. (2014). U-Th-Pb Geochronology. Refererence Module in Earth Systems and Enviromental Sciences in 'Treatise on Geochemistry', Second edition. Editor(s): Heinrich D. Holland, Karl K. Turekian, Elsevier.Vol 4. Pages 341-378. DOI: 10.1016/B978-0-08-095975- 7.00310-7.

Seder-Colomina, M, Mangeret, A, Stetten, L, Merrot, P, Diez, O, Julien, A, Barker, E, Thouvenot, A, Bargar, J, Cazala, C, Morin, G. (2018). Carbonate Facilitated Mobilization of Uranium from Lacustrine Sediments under Anoxic Conditions. Environ Sci Technol. 2018 Sep 4;52(17):9615-9624. DOI: 10.1021/acs.est.8b01255.

Shannon, R. D. (1976). Revised effective ionic radii and systematic studies of interatomic distances in halides and chalcogenides, Acta Crystallogr., Sect. A Cryst. Phys. Diffr. Theor. Gen. Crystallogr., 32, 751–767.

Sibley, D.F & Gregg, J. M. (1987). Classification of dolomite rock textures. *Journal of Sedimentary Research* 1987; 57(6):967–975.doi: https://doi.org/10.1306/212F8CBA-2B24-11D7-8648000102C1865D.

Smith, P.E. and Farquhar, R.M. (1989). Direct dating of Phanerozoic sediments by the ^{238}U–^{206}Pb method. Nature, 341, 518, 1989.

Souza, R. S., Arienti, L. M., Viana, S. M., Falcao, L. C., Cuglieri, M. A., Silva, R. P., Leite, C. O., Oliveira, V.C., Oliveira, D. M., Anjos, C., et al., (2018). Petrology of the hydrothermal and evaporitic continental

Cretaceous (Aptian) pre- salt carbonates and associated rocks, South Atlantic Santos basin, offshore Brazil. In Proceedings of the AAPG/ACE Annual Convention & Exhibition, Salt Lake City, UT, USA, 19–22 May 2018.

Spötl, C.; Pitman, J. K. (1998). Saddle (baroque) dolomite in carbonates and sandstones: a reappraisal of a burial-diagenetic concept. Carbonate Cementation in Sandstones. Special Publication, n. 26, p. 437-460, 1998.

Sturchio, N.C., Antonio, M.R., Sederholm, L. Sutton, S.R., Brannon, J.C. (1998). Tetravalent Uranium in Calcite. Science. Vol 281 (5379) 971- 3. DOI: 10.1126/science.281.5379.971.

Sumner, D. Y., & Bowring, S. A. (1996). U-Pb geochronologic constraints on deposition of the Campbellrand Subgroup, Transvaal Supergroup, South Africa. Precambrian Research, 79(1-2), 25-35.

Szatmari, P. (2001). Datação de amostras de rochas ígneas do bloco 500 da Bacia de Santos pelo método 40Ar-39Ar. Rio de Janeiro : PETROBRAS. CENPES. PDEP. TEGG, 2001. 5 f. Comunicação técnica.

Szatmari, P., de Lima, C. M., Fontaneta, G., Lima, N. de M., Zambonato, E., Menezes, M.R., Bahniuk, J., Coelho, S.L., Figueiredo, M., Florencio, C.P., and Gontijo, R. (2021). Petrography, geochemistry and origin of South Atlantic evaporites: The Brazilian side: Marine and Petroleum Geology, v. 127, https://doi.org/10.1016/j .marpetgeo.2020.104805.

Szatmari, P., Milani, E.J. (2016). Tectonic control of the oil-rich large igneous-carbonate salt province of the South Atlantic rift. Mar. Petrol. Geol. 77, 567–596.

Tedeschi, L. R., Jenkyns, H. C., Robinson, S. A., Sanjinés, A. E., Viviers, M. C., Quintaes, C. M., & Vazquez, J. C. (2017). New age constraints on Aptian evaporites and carbonates from the South Atlantic: Implications for Oceanic Anoxic Event 1a. Geology, 45(6), 543-546.

Tera, F., & Wasserburg, G. J. (1972). U-Th-Pb systematics in lunar highland samples from the Luna 20 and Apollo 16 missions. Earth and Planetary Science Letters, 17(1), 36-51.

Tera, F., & Wasserburg, G. J. (1972). U-Th-Pb systematics in three Apollo 14 basalts and the problem of initial Pb in lunar rocks. Earth and Planetary Science Letters, 14(3), 281-304.

Thiede, D. S. & Vasconcelos, P. M. (2010) .Paraná food basalts: rapid extrusion hypothesis confrmed by new $^{40}Ar/^{39}Ar$ results. Geology, 38(8):747–750. https://doi.org/10.1130/G30919.1.

Tonietto, S., Sartorato, A. C., Ferreira Santos, J., & Rezende, M & Pereira, E. (2018). UNUSUAL DOLOMITE FABRICS IN SPHERULITIC AND SHRUBBY BOUNDSTONES OF SANTOS BASIN PRE-SALT DEPOSITS. In Congresso Brasileiro de Geologia (Vol. 49). Rio de Janeiro.

Tritlla, J., Esteban, M., Loma, R., Mattos, A., Sánchez, V., Boix, C., da Luca, P. H .V., Carballo, J., & Levresse, G. (2018). Carbonates That Are No More: Silicified Pre-Salt Oil Reservoirs in Campos Basin (Brazil). In AAPG ACE 2018 Abstracts. American Association of Petroleum Geologists.

Vermeesch, P. (2018). IsoplotR: a free and open toolbox for geochronology. Geoscience Frontiers, v.9, p.1479-1493, doi: 10.1016/j.gsf.2018.04.001.

Wetherill, G.W. (1956). Discordant uranium lead ages. Trans. Amer. Geophys. Union 37, 320-326.

Weyer, S., Anbar, A. D., Gerdes, A., Gordon, G. W., Algeo, T. J., & Boyle, E. A. (2008). Natural fractionation of 238U/235U. Geochimica et Cosmochimica Acta, 72(2):345-359.

Woodhead, J., Hellstrom, J., Maas, R., Drysdale, R., Zanchetta, G., Devine, P. and Taylor, E. (2006). U–Pb geochronology of speleothems by MC-ICPMS. Quaternary Geochronology, 1, 208-221, 2006.

Woodhead, J., Petrus, J. A. (2019). Exploring the advantages and limitations of in situ U-Pb carbonate geochronology using speleothems. Geochronology 1(1):69-84. DOI: 10.5194/gchron1-69-2019

Wray, C.M (2018). "Investigating Uranium incorporation in modern carbonates by sequential extraction: Applied to the Permian - Triassic boundary in Lung Cam, Vietnam" (2018). LSU Master's Theses. 4712.

Wright, V. P., & Barnett, A. J. (2015). An abiotic model for the development of textures in some South Atlantic early cretaceous lacustrine carbonates. Geological Society, London, Special Publications, 418, 209–219. https://doi.org/10.1144/SP418.3.

Zuddas, P., Salvi, S., Lopez, O., DeGiudici, G., & Censi, P. (2018). Rapid migration of CO2-rich micro-fluids in calcite matrices. Scientific Reports, 8(1), 14080.

ANEXO A – Tabela de Idades do sistema do pré-sal publicadas na literatura para eventos de magmatismo, hidrotermalismo, deposição e diagênese. Estes dados foram os utilizados nos histogramas da Figura 4 e da *Figure 1*, e na confecção da *Figure 8*.

Idade Central (Ma)	Evento	Idade (Ma)	Sistema Isotópico	Fase Analisada	Referência
130	Magmatismo	130	Ar-Ar	Basalto	Gomes et al. (2015); Oliveira et al. (2023)
130	Magmatismo	130	Ar-Ar	Basalto	Moreira et al. (2007)
130	Magmatismo	130	Ar-Ar	Basalto	Moreira et al. (2007)
128	Magmatismo	128	Ar-Ar	Basalto	Szatmari & Milani, 2016
127.4	Magmatismo	127.4 ± 2.3	Ar-Ar	Basalto	Loma et al. (2018)
125.5	Magmatismo	125.5 ± 0.7	Ar-Ar	Basalto	Rancan et al. (2018)
124	Magmatismo	124	Ar-Ar	Basalto	Gordon et al. (2023)
124	Magmatismo	124	Ar-Ar	Basalto	Gordon et al. (2023)
124	Magmatismo	124	Ar-Ar	Basalto	Gordon et al. (2023)
122	Magmatismo	122	Ar-Ar	Basalto	Gordon et al. (2023)
121	Magmatismo	121	Ar-Ar	Basalto	Moreira et al. (2007)
121	Magmatismo	121	Ar-Ar	Basalto	Gordon et al. (2023)
120	Magmatismo	120	Ar-Ar	Basalto	Gomes et al. (2015); Oliveira et al. (2023)
120	Magmatismo	120	Ar-Ar	Basalto	Gordon et al. (2023)
119	Magmatismo	119	Ar-Ar	Basalto	Gordon et al. (2023)
118	Magmatismo	118	Ar-Ar	Basalto	Moreira et al. (2007)
118	Magmatismo	118	Ar-Ar	Basalto	Gordon et al. (2023)
117	Magmatismo	117	Ar-Ar	Basalto	Gordon et al. (2023)
117	Magmatismo	117	Ar-Ar	Basalto	Gordon et al. (2023)
116.93	Magmatismo	116.93 ± 0.22	Ar-Ar	Basalto	Louback et al. (2023)
116.16	Magmatismo	116.16 ± 0.10	Ar-Ar	Basalto	Louback et al. (2023)
116	Magmatismo	116	Ar-Ar	Basalto	Gordon et al. (2023)
115.21	Magmatismo	115.21 ± 0.13	Ar-Ar	Basalto	Louback et al. (2023)

Idade Central (Ma)	Evento	Idade (Ma)	Sistema Isotópico	Fase Analisada	Referência
115	Magmatismo	115	Ar-Ar	Basalto	Gomes et al. (2015); Oliveira et al. (2023)
115	Magmatismo	115	Ar-Ar	Basalto	Gordon et al. (2023)
113	Magmatismo	113	Ar-Ar	Basalto	Gomes et al. (2015); Oliveira et al. (2023)
110	Magmatismo	110	Ar-Ar	Basalto	Gordon et al. (2023)
109.95	Magmatismo	109.95 ± 0.20	Ar-Ar	Basalto	Louback et al. (2023)
107	Magmatismo	107	Ar-Ar	Basalto	Gordon et al. (2023)
107	Magmatismo	107	K-Ar	Basalto	Gordon et al. (2023)
90	Magmatismo	90 ± 6	K-Ar	Basalto	Gordon et al. (2023)
87	Magmatismo	87 ± 12	K-Ar	Basalto	Gordon et al. (2023)
83.3	Magmatismo	83.3 ± 0.66	Ar-Ar	Basalto	Rancan et al. (2018)
82	Magmatismo	82 ± 1	Ar-Ar	Basalto	Gordon et al. (2023)
77	Magmatismo	77 ± 3	K-Ar	Basalto	Gordon et al. (2023)
75	Magmatismo	75 ± 2	K-Ar	Basalto	Gordon et al. (2023)
72.4	Magmatismo	72.4 ± 4.9	Ar-Ar	Basalto	Rancan et al. (2018)
67.3	Magmatismo	67.3	K-Ar	Basalto	Gordon et al. (2023)
49.9	Magmatismo	49.9 ± 0.45	Ar-Ar	Basalto	Gordon et al. (2023)
48.9	Magmatismo	48.9	Ar-Ar	Basalto	Szatmari, (2001)
48.1	Magmatismo	48.1	Ar-Ar	Basalto	Gordon et al. (2023)
41.06	Magmatismo	41.06±0.02	Ar-Ar	Basalto	Louback et al. (2021)
38.62	Magmatismo	38.62 ± 0.02	Ar-Ar	Basalto	Louback et al. (2021)
50	Magmatismo	50 ± 7	K-Ar	Plagioclásio	Gordon et al. (2023)
114.5	Hidrotermalismo	114.5 ±2.9	Ar-Ar	Basalto	Loma et al. (2018)
114.3	Hidrotermalismo	114.3 ± 1.1	Ar-Ar	Basalto	Rancan et al. (2018)
107	Hidrotermalismo	107.0 ± 1.0	Ar-Ar	Adulária	Trittla et al. (2018)
106.9	Hidrotermalismo	106.9 ± 1.6	Ar-Ar	Basalto	Loma et al. (2018)
104.3	Hidrotermalismo	104.3 ± 0.8	Ar-Ar	Adulária	Trittla et al. (2018)
49.9	Hidrotermalismo	49.9 ± 0.45	Ar-Ar	Basalto	Rancan et al. (2018)

Idade Central (Ma)	Evento	Idade (Ma)	Sistema Isotópico	Fase Analisada	Referência
115.83	Deposição/Diagênese	115.83 ± 1.56	U-Pb	Calcita	Lawson et al. (2022)
115	Deposição/Diagênese	115	U-Pb	Dolomita	Godeau et al. (2021)
114.46	Deposição/Diagênese	114.46 ± 4.72	U-Pb	Calcita	Lawson et al. (2022)
114	Deposição/Diagênese	114.0 ± 13.4	U-Pb	Calcita	Rochelle-Bates et al. (2022)
113	Deposição/Diagênese	113.0 ± 15.3	U-Pb	Calcita	Rochelle-Bates et al. (2022)
112.5	Deposição/Diagênese	112.5 ± 2.8	U-Pb	Calcita	Godeau et al. (2021)
110.2	Deposição/Diagênese	110.2 ± 2.1	Th-Pb	Calcita	Godeau et al. (2021)
109.73	Deposição/Diagênese	109.73 ± 9.26	U-Pb	Calcita	Lawson et al. (2022)
107.6	Deposição/Diagênese	107.6 ± 5.1	U-Pb	Calcita	Rochelle-Bates et al. (2022)
107	Deposição/Diagênese	107.0 ± 27.2 Ma	U-Pb	Calcita	Rochelle-Bates et al. (2022)
106.9	Deposição/Diagênese	106.9 ± 4.3	U-Pb	Calcita	Rochelle-Bates et al. (2022)
103.8	Deposição/Diagênese	103.8 ± 3.0	U-Pb	Dolomita	Godeau et al. (2021)
92	Deposição/Diagênese	92 ± 3 Ma	U-Pb	Calcedônia	Godeau et al. (2021)
90	Deposição/Diagênese	90	U-Pb	Dolomita	Godeau et al. (2021)
86.2	Deposição/Diagênese	86.2 ± 2.4	U-Pb	Calcita	Rochelle-Bates et al. (2021)
85.5	Deposição/Diagênese	85.5 ± 9.5	U-Pb	Calcita	Godeau et al. (2021)
77	Deposição/Diagênese	77.0 ± 11.2	U-Pb	Calcita	Rochelle-Bates et al. (2022)
59.2	Deposição/Diagênese	59.2 ± 5.3	U-Pb	Dolomita	Rochelle-Bates et al. (2022)
58	Deposição/Diagênese	58.0 ± 4.6	U-Pb	Dolomita	Rochelle-Bates et al. (2022)
56.8	Deposição/Diagênese	56.8 ± 4.8	U-Pb	Dolomita	Rochelle-Bates et al. (2021)
124	Deposição/Diagênese	124 ± 5	U-Pb	Dolomita	Este trabalho
123	Deposição/Diagênese	123 ± 4	U-Pb	Dolomita	Este trabalho
122	Deposição/Diagênese	122 ± 5	U-Pb	Dolomita	Este trabalho
117	Deposição/Diagênese	117 ± 3	U-Pb	Dolomita	Este trabalho
116	Deposição/Diagênese	116 ± 4	U-Pb	Calcita	Este trabalho
115	Deposição/Diagênese	115 ± 5	U-Pb	Calcita	Este trabalho
114	Deposição/Diagênese	114 ± 3	U-Pb	Calcita	Este trabalho

Idade Central (Ma)	Evento	Idade (Ma)	Sistema Isotópico	Fase Analisada	Referência
113	Deposição/Diagênese	113 ± 3	U-Pb	Calcita	Este trabalho
112	Deposição/Diagênese	112 ± 7	U-Pb	Dolomita	Este trabalho
112	Deposição/Diagênese	112 ± 3	U-Pb	Calcita	Este trabalho
110	Deposição/Diagênese	110 ± 4	U-Pb	Calcita	Este trabalho
109	Deposição/Diagênese	109 ± 4	U-Pb	Dolomita	Este trabalho
109	Deposição/Diagênese	109 ± 3	U-Pb	Dolomita	Este trabalho
108	Deposição/Diagênese	108 ± 5	U-Pb	Dolomita	Este trabalho
105	Deposição/Diagênese	105 ± 3	U-Pb	Calcita	Este trabalho
104	Deposição/Diagênese	104 ± 5	U-Pb	Dolomita	Este trabalho
100	Deposição/Diagênese	100 ± 5	U-Pb	Calcita	Este trabalho
100	Deposição/Diagênese	100 ± 3	U-Pb	Calcita	Este trabalho
100	Deposição/Diagênese	103 ± 7	U-Pb	Calcita	Este trabalho
99	Deposição/Diagênese	99 ± 7	U-Pb	Calcita	Este trabalho
99	Deposição/Diagênese	99 ± 6	U-Pb	Dolomita	Este trabalho
99	Deposição/Diagênese	99 ± 4	U-Pb	Dolomita	Este trabalho
97	Deposição/Diagênese	97 ± 4	U-Pb	Dolomita	Este trabalho
97	Deposição/Diagênese	97 ± 5	U-Pb	Dolomita	Este trabalho
95	Deposição/Diagênese	95 ± 4	U-Pb	Dolomita	Este trabalho
82	Deposição/Diagênese	82 ± 6	U-Pb	Calcita	Este trabalho

ANEXO B – Tabelas de dados U-Pb

Identificador	f206c	^{206}Pb	Uppm	Th/U	$^{206}Pb/^{204}Pb$	1s%	$^{238}U/^{206}Pb$	1s%	$^{207}Pb/^{206}Pb$	1s%
C_Walnut	318	3078	5.6	0.0048	4.9	2.4	20.4	0.7	0.2	1.7
C_Walnut	341	2665	4.7	0.0008	4.5	2.2	20.0	0.8	0.2	2.0
C_Walnut	348	2232	4.1	0.0014	4.7	2.3	21.1	0.9	0.1	2.4
C_Walnut	482	1697	2.8	0.0056	2.9	2.0	18.9	1.0	0.2	2.0
C_Walnut	258	4393	8.5	0.0138	6.1	1.8	21.8	0.8	0.1	1.4
C_Walnut	321	2701	5.2	0.0259	4.8	2.1	21.8	0.6	0.2	1.9
C_Walnut	293	3626	6.7	0.0003	5.3	2.3	20.4	0.7	0.2	1.8
C_Walnut	588	923	1.6	0.0112	2.5	2.5	19.1	1.3	0.2	3.1
C_Walnut	406	1451	2.7	0.0021	3.7	2.4	20.3	1.1	0.2	2.1
C_Walnut	241	3764	7.6	0.0005	6.5	2.1	21.4	0.7	0.1	1.6
C_Walnut	319	2258	4.8	0.0009	4.9	2.6	22.6	0.9	0.2	2.0
C_Walnut	234	3696	7.8	0.0003	6.8	1.9	22.1	0.9	0.1	1.3
C_Walnut	370	2007	4.1	0.0009	4.0	1.8	21.4	0.9	0.2	1.8
C_Walnut	535	969	1.7	0.0026	2.7	2.8	18.9	1.2	0.2	2.6
C_Walnut	240	3767	8.5	0.0003	6.6	1.7	22.6	0.8	0.1	1.5
C_Walnut	364	1957	3.9	0.0004	4.1	2.4	20.1	1.4	0.2	2.1
C_Walnut	333	2556	5.5	0.0001	4.4	1.8	21.8	1.0	0.2	1.6
C_Walnut	412	1759	3.5	0.0001	3.4	2.3	19.7	1.0	0.2	2.0
C_Walnut	374	1571	3.5	0.0005	4.3	3.3	22.1	0.9	0.2	2.4
C_Walnut	312	2651	5.4	0.0001	4.7	2.1	19.9	0.8	0.2	1.9
C_Walnut	366	1979	4.3	0.0054	4.1	2.6	20.5	0.9	0.2	2.4
C_Walnut	285	2414	6.3	0.0009	5.8	2.9	24.7	0.7	0.1	2.0
C_Walnut	440	1671	3.3	0.0009	3.1	2.1	18.8	1.0	0.2	2.1
C_Walnut	428	1617	3.7	0.0023	3.4	2.1	20.9	1.1	0.2	1.7
C_Walnut	486	1568	3.3	0.0026	2.8	2.1	19.2	0.8	0.3	2.0
C_Walnut	396	2132	4.7	0.0016	3.6	2.5	20.4	0.8	0.2	2.7

Identificador	f206c	^{206}Pb	Uppm	Th/U	$^{206}Pb/^{204}Pb$	1s%	$^{238}U/^{206}Pb$	1s%	$^{207}Pb/^{206}Pb$	1s%
C_Walnut	460	1428	3.1	0.0020	3.0	2.3	19.9	1.0	0.2	2.2
C_Walnut	383	1843	4.3	0.0040	3.8	2.6	21.2	1.0	0.2	2.3
(928)5144.00_CalcEsf	497	4088	10.4	0.0002	2.2	1.3	27.1	1.1	0.4	1.4
(928)5144.00_CalcEsf	565	4157	10.3	0.0020	1.8	1.0	26.5	0.9	0.5	1.0
(928)5144.00_CalcEsf	576	4335	10.6	0.0001	1.7	1.0	25.8	1.3	0.6	0.7
(928)5144.00_CalcEsf	521	3777	12.1	0.0004	2.0	1.0	34.2	0.9	0.5	1.0
(928)5144.00_CalcEsf	565	3470	8.6	0.0008	1.8	1.7	27.2	2.4	0.5	1.7
(928)5144.00_CalcEsf	621	6743	2.9	0.0034	1.5	1.3	4.2	2.1	0.6	1.4
(928)5144.00_CalcEsf	814	555	1.4	0.0021	1.6	4.3	28.0	2.7	0.3	5.0
(928)5144.00_CalcEsf	660	1846	2.1	0.0068	1.5	1.7	12.0	2.6	0.6	2.0
(928)5144.00_CalcEsf	1664	242	0.9	0.3552	0.9	5.4	46.5	3.8	0.3	8.9
(928)5144.00_CalcEsf	557	2058	5.2	0.0030	1.9	2.4	27.0	2.8	0.5	2.8
(928)5144.00_CalcEsf	685	2020	3.8	0.0012	1.4	1.5	19.8	2.5	0.6	1.6
(928)5144.00_CalcEsf	488	2492	9.1	0.0008	2.4	2.4	38.5	1.6	0.4	2.8
(928)5144.00_CalcEsf	603	1731	4.3	0.0002	1.7	1.9	27.1	2.3	0.5	2.2
(928)5144.00_CalcEsf	702	1820	2.8	0.0021	1.3	1.4	16.9	2.4	0.7	1.4
(928)5144.00_CalcEsf	686	1286	2.4	0.0044	1.5	3.2	18.8	1.8	0.5	2.4
(928)5144.00_CalcEsf	714	1651	1.9	0.0027	1.2	1.4	13.1	3.1	0.7	1.5
(928)5144.00_CalcEsf	725	9508	2.3	0.0011	1.1	0.5	3.1	3.4	0.9	0.4
(928)5144.00_CalcEsf	710	4049	2.8	0.0019	1.2	1.0	8.8	3.2	0.8	0.9
(928)5144.00_CalcEsf	717	1772	2.4	0.0020	1.3	1.6	17.1	3.3	0.6	2.1
(928)5144.00_CalcEsf	670	2191	2.8	0.0005	1.4	1.9	17.3	4.0	0.6	2.4
(928)5144.00_DolRomb	570	1506	4.9	0.0002	2.0	2.1	33.9	1.0	0.4	2.4
(928)5144.00_DolRomb	647	1089	3.4	0.0044	1.8	2.8	31.1	1.6	0.4	3.2
(928)5144.00_DolRomb	707	1016	3.3	0.0008	1.7	2.8	37.2	2.1	0.4	3.7
(928)5144.00_DolRomb	640	1462	3.8	0.0011	1.6	1.4	26.6	1.3	0.5	2.0
(928)5144.00_DolRomb	658	1589	3.5	0.0008	1.5	1.5	23.3	1.7	0.5	1.9
(928)5144.00_DolRomb	581	1025	4.5	0.0008	2.5	3.4	45.8	1.7	0.2	4.9

Identificador	f206c	^{206}Pb	Uppm	Th/U	$^{206}Pb/^{204}Pb$	1s%	$^{238}U/^{206}Pb$	1s%	$^{207}Pb/^{206}Pb$	1s%
(928)5144.00_DolRomb	668	1896	4.3	0.0003	1.4	1.1	22.8	1.1	0.6	1.4
(928)5144.00_DolRomb	585	1645	4.8	0.0004	1.9	1.8	30.9	1.5	0.4	2.0
(928)5144.00_DolRomb	663	2146	4.2	0.0005	1.4	1.1	21.0	2.2	0.6	1.5
(928)5144.00_DolRomb	454	1046	5.5	0.0004	4.0	5.2	53.1	0.9	0.1	4.1
(928)5144.00_DolRomb	691	4608	4.2	0.0178	1.2	1.1	9.2	2.0	0.7	1.2
(928)5144.00_DolRomb	652	1018	3.7	0.0036	1.8	2.5	36.5	1.4	0.4	2.5
(928)5144.00_DolRomb	711	1525	2.7	0.0001	1.3	1.2	17.6	1.3	0.6	1.1
(928)5144.00_DolRomb	683	1530	3.7	0.0004	1.5	1.5	24.9	1.2	0.5	1.6
(928)5144.00_DolRomb	586	1093	4.4	0.0001	2.3	2.8	40.1	1.4	0.3	2.8
(928)5144.00_DolRomb	699	976	3.1	0.0003	1.6	2.3	31.4	1.3	0.5	2.3
(928)5144.00_DolRomb	573	1280	4.5	0.0214	2.1	2.4	36.0	1.3	0.4	2.4
(928)5144.00_DolRomb	619	1648	4.1	0.0001	1.7	1.8	24.7	1.9	0.5	2.1
(928)5144.00_DolRomb	682	851	3.0	0.0003	1.7	2.8	35.6	1.4	0.4	2.5
(928)5144.00_DolRomb	625	920	3.4	0.0001	2.0	3.1	37.1	1.2	0.4	2.8
(928)5194.50_DolMicro	640	13703	13.0	0.0001	1.5	1.7	10.7	2.6	0.6	0.6
(928)5194.50_DolMicro	533	3919	9.3	0.0010	2.0	1.1	26.0	1.1	0.4	1.2
(928)5194.50_DolMicro	655	3560	6.6	0.0003	1.5	1.2	22.1	2.9	0.6	1.3
(928)5194.50_DolMicro	351	3213	10.3	0.0002	4.0	4.6	38.2	1.9	0.2	5.4
(928)5194.50_DolMicro	671	16135	7.3	0.0005	1.3	0.4	4.7	1.2	0.7	0.4
(928)5194.50_DolMicro	566	3172	6.7	0.0086	1.9	1.8	24.6	2.2	0.5	1.9
(928)5194.50_DolMicro	678	4400	4.4	0.0043	1.3	1.3	10.7	5.9	0.6	2.0
(928)5194.50_DolMicro	-2660	-3	0.1	0.0570	0.0	-71.7	-13.9	-136.8	0.1	791.7
(928)5194.50_DolMicro	677	4182	4.3	0.0004	1.3	1.2	12.0	2.7	0.7	1.0
(928)5194.50_DolMicro	597	3635	5.7	0.0005	1.6	1.2	17.4	2.8	0.5	1.3
(928)5194.50_DolMicro	707	30473	9.5	0.0003	1.2	0.4	3.1	2.4	0.7	0.4
(928)5194.50_DolMicro	563	4024	8.3	0.0114	1.9	1.5	23.0	2.8	0.5	1.6
(928)5194.50_DolMicro	337	6038	27.0	0.0001	4.1	2.4	46.1	0.9	0.2	2.2
(928)5194.50_DolMicro	628	4550	5.7	0.0178	1.5	1.3	15.3	3.5	0.6	1.4

Identificador	f206c	^{206}Pb	Uppm	Th/U	$^{206}Pb/^{204}Pb$	1s%	$^{238}U/^{206}Pb$	1s%	$^{207}Pb/^{206}Pb$	1s%
(928)5194.50_DolMicro	622	1195	3.4	0.0009	2.0	2.8	29.8	1.9	0.3	2.7
(928)5194.50_DolMicro	634	3298	3.4	0.0050	1.6	3.4	14.5	4.7	0.5	2.8
(928)5194.50_DolMicro	350	2462	8.8	0.0004	4.3	3.0	38.9	1.5	0.2	3.8
(928)5194.50_DolMicro	324	2252	8.7	0.0005	5.0	3.2	41.7	1.0	0.2	4.3
(928)5194.50_DolMicro	404	2465	8.3	0.0004	3.2	2.1	36.0	1.0	0.3	2.4
(928)5194.50_DolMicro	371	2046	7.5	0.0003	3.9	2.6	38.7	0.9	0.2	2.9
(928)5194.50_DolRomb	733	2148	3.6	0.0026	1.4	1.7	22.6	3.6	0.5	2.4
(928)5194.50_DolRomb	694	3036	3.4	0.0224	1.4	1.2	13.1	1.9	0.6	1.0
(928)5194.50_DolRomb	621	1115	3.9	0.0015	2.2	2.6	40.1	1.6	0.3	4.8
(928)5194.50_DolRomb	728	1838	2.6	0.0113	1.4	1.4	17.4	3.0	0.5	1.8
(928)5194.50_DolRomb	676	12096	14.3	0.0003	1.3	0.7	13.8	2.7	0.6	0.7
(928)5194.50_DolRomb	740	5129	2.5	0.0023	1.2	0.7	6.0	3.3	0.7	0.7
(928)5194.50_DolRomb	742	17491	2.4	0.0028	1.2	0.7	4.0	8.2	0.7	0.9
(928)5194.50_DolRomb	742	4437	2.5	0.0035	1.2	3.6	8.7	4.7	0.7	1.1
(928)5194.50_DolRomb	672	1485	3.5	0.0102	1.7	2.2	28.2	3.0	0.4	3.3
(928)5194.50_DolRomb	737	6515	3.2	0.0010	1.3	1.3	12.0	4.3	0.6	1.8
(928)5194.50_DolRomb	683	1404	3.5	0.0029	1.6	1.7	28.1	2.0	0.4	2.3
(928)5194.50_DolRomb	687	1210	2.9	0.0009	1.6	1.8	25.9	1.0	0.4	2.0
(928)5194.50_DolRomb	660	1624	3.3	0.0052	1.6	1.9	23.5	2.5	0.5	2.1
(928)5194.50_DolRomb	653	2153	3.5	0.0006	1.6	2.4	22.9	4.7	0.5	2.7
(928)5194.50_DolRomb	689	1577	2.7	0.0112	1.5	1.9	20.5	2.9	0.5	2.1
(928)5194.50_DolRomb	682	5097	3.1	0.0019	1.3	0.8	8.0	3.8	0.7	0.9
(928)5194.50_DolRomb	606	1413	4.8	0.0011	2.0	2.2	39.0	1.7	0.4	2.1
(928)5194.50_DolRomb	720	939	2.6	0.0016	1.7	2.6	31.6	2.0	0.4	3.2
(928)5194.50_DolRomb	673	2160	3.2	0.0017	1.5	2.0	17.9	2.6	0.6	1.6
(928)5194.50_DolRomb	680	989	2.9	0.0080	1.9	2.8	33.0	2.2	0.3	3.6
(SPH-6)5124.60_CalcPart	256	3226	16.7	0.0003	6.0	1.8	48.4	0.7	0.2	1.5
(SPH-6)5124.60_CalcPart	352	2396	12.0	0.0002	4.1	2.4	45.8	1.2	0.2	1.9

Identificador	f206c	^{206}Pb	Uppm	Th/U	$^{206}Pb/^{204}Pb$	1s%	$^{238}U/^{206}Pb$	1s%	$^{207}Pb/^{206}Pb$	1s%
(SPH-6)5124.60_CalcPart	288	3057	15.7	0.0006	5.3	2.5	47.2	0.8	0.2	2.3
(SPH-6)5124.60_CalcPart	299	3073	15.4	0.0005	4.8	1.7	46.4	0.9	0.2	1.3
(SPH-6)5124.60_CalcPart	227	3327	18.6	0.0003	7.3	2.2	52.2	0.8	0.1	1.5
(SPH-6)5124.60_CalcPart	326	3134	15.1	0.0002	4.3	1.5	44.8	0.9	0.2	1.1
(SPH-6)5124.60_CalcPart	271	3274	16.9	0.0003	5.7	2.0	48.1	0.8	0.2	1.4
(SPH-6)5124.60_CalcPart	330	2882	15.3	0.0004	4.3	1.6	48.7	0.7	0.2	1.5
(SPH-6)5124.60_CalcPart	349	3126	14.5	0.0009	3.9	1.5	42.7	0.9	0.2	1.3
(SPH-6)5124.60_CalcPart	301	3049	15.3	0.0002	4.9	2.1	46.1	1.0	0.2	1.8
(SPH-6)5124.60_CalcPart	297	2960	15.5	0.0004	5.1	2.2	48.1	0.9	0.2	1.7
(SPH-6)5124.60_CalcPart	246	4907	25.7	0.0002	6.1	1.4	47.8	0.8	0.2	1.3
(SPH-6)5124.60_CalcPart	274	3563	18.9	0.0017	5.5	2.3	48.8	0.9	0.2	1.8
(SPH-6)5124.60_CalcPart	268	3193	17.3	0.0002	6.0	3.8	50.1	0.8	0.2	1.9
(SPH-6)5124.60_CalcPart	418	2611	11.3	0.0003	3.0	1.4	39.5	0.7	0.3	1.5
(SPH-6)5124.60_CalcPart	368	2850	13.6	0.0003	3.6	1.6	43.8	0.8	0.3	1.5
(SPH-6)5124.60_CalcPart	275	3459	18.2	0.0001	5.4	1.6	47.9	0.7	0.2	1.5
(SPH-6)5124.60_CalcPart	283	2772	14.9	0.0006	5.4	2.1	48.6	0.9	0.2	1.6
(SPH-6)5124.60_CalcPart	294	3267	16.3	0.0008	4.9	1.6	45.1	0.9	0.2	1.4
(SPH-6)5124.60_CalcPart	285	2690	14.7	0.0003	5.5	2.7	49.7	0.8	0.2	2.2
(SPH-6)5124.60_DolRomb	655	4708	4.1	0.0018	1.3	0.7	8.5	0.8	0.7	0.5
(SPH-6)5124.60_DolRomb	660	11047	6.5	0.0003	1.3	0.5	6.3	2.8	0.7	0.5
(SPH-6)5124.60_DolRomb	659	4033	4.2	0.0003	1.3	0.8	10.0	0.8	0.7	0.7
(SPH-6)5124.60_DolRomb	664	2689	2.8	0.0014	1.3	0.9	10.2	1.0	0.7	0.8
(SPH-6)5124.60_DolRomb	658	2828	3.4	0.0014	1.4	0.8	11.7	0.8	0.7	0.9
(SPH-6)5124.60_DolRomb	651	4288	3.9	0.0023	1.3	0.7	8.9	0.9	0.7	0.7
(SPH-6)5124.60_DolRomb	663	4275	3.9	0.0005	1.3	0.6	8.7	0.9	0.7	0.6
(SPH-6)5124.60_DolRomb	657	4553	4.2	0.0002	1.3	0.6	8.9	1.1	0.7	0.6
(SPH-6)5124.60_DolRomb	650	5864	5.3	0.0026	1.3	0.5	8.7	0.7	0.7	0.5
(SPH-6)5124.60_DolRomb	664	3364	3.5	0.0039	1.3	0.8	10.1	1.5	0.7	0.8

Identificador	f206c	^{206}Pb	Uppm	Th/U	$^{206}Pb/^{204}Pb$	1s%	$^{238}U/^{206}Pb$	1s%	$^{207}Pb/^{206}Pb$	1s%
(SPH-6)5124.60_DolRomb	708	1996	1.4	0.0043	1.2	1.0	6.9	2.6	0.7	0.9
(SPH-6)5124.60_DolRomb	664	4646	3.3	0.0004	1.3	0.6	7.0	1.6	0.8	0.6
(SPH-6)5124.60_DolRomb	657	5026	4.1	0.0008	1.3	0.6	8.2	2.3	0.7	0.7
(SPH-6)5124.60_DolRomb	658	5698	4.8	0.0005	1.3	0.6	8.0	0.6	0.7	0.5
(SPH-6)5124.60_DolRomb	658	3839	3.8	0.0109	1.3	0.7	9.4	0.9	0.7	0.7
(SPH-6)5124.60_DolRomb	655	5074	4.1	0.0004	1.3	0.5	7.7	0.6	0.7	0.6
(SPH-6)5124.60_DolRomb	662	5545	4.4	0.0036	1.3	0.6	7.5	1.0	0.7	0.6
(SPH-6)5124.60_DolRomb	657	4155	4.2	0.1361	1.3	0.7	9.6	1.7	0.7	0.8
(SPH-6)5124.60_DolRomb	650	3585	3.9	0.0031	1.3	0.7	10.2	1.1	0.7	0.7
(SPH-6)5124.60_DolRomb	645	2479	3.4	0.0015	1.4	0.9	13.0	1.1	0.7	0.8
(SPH-6)5124.60_DolSel	879	716	1.0	0.0001	1.1	1.9	14.8	1.5	0.6	1.8
(SPH-6)5124.60_DolSel	920	705	0.6	0.0005	0.9	1.6	10.9	1.7	0.8	1.4
(SPH-6)5124.60_DolSel	894	752	0.6	0.0004	1.0	1.8	9.6	2.0	0.7	1.6
(SPH-6)5124.60_DolSel	879	771	0.2	0.0001	0.9	1.6	3.6	5.3	0.8	1.6
(SPH-6)5124.60_DolSel	891	759	0.5	0.0002	1.0	1.7	8.4	2.1	0.8	1.6
(SPH-6)5124.60_DolSel	812	792	1.5	0.0025	1.2	2.0	19.6	1.4	0.6	1.6
(SPH-6)5124.60_DolSel	804	999	1.3	0.0000	1.1	1.5	13.8	1.9	0.7	1.6
(SPH-6)5124.60_DolSel	867	725	0.4	0.0011	1.0	1.8	7.7	2.3	0.8	1.5
(SPH-6)5124.60_DolSel	888	745	0.3	0.0014	1.0	1.8	4.6	3.9	0.8	1.8
(SPH-6)5124.60_DolSel	855	777	0.3	0.0006	1.0	1.8	4.5	4.4	0.8	1.8
(SPH-6)5124.60_DolSel	873	788	0.3	0.0041	1.0	1.7	5.0	3.7	0.8	1.6
(SPH-6)5124.60_DolSel	814	758	0.7	0.0012	1.1	1.9	11.1	1.8	0.7	1.8
(SPH-6)5124.60_DolSel	847	743	0.9	0.0010	1.1	1.8	12.6	1.5	0.7	1.5
(SPH-6)5124.60_DolSel	887	752	0.5	0.0004	1.0	1.5	8.5	2.5	0.8	1.6
(SPH-6)5124.60_DolSel	942	713	0.3	0.0034	0.9	1.8	4.5	4.2	0.8	1.7
(SPH-6)5124.60_DolSel	891	657	0.6	0.0012	1.0	1.8	11.9	1.7	0.7	1.7
(SPH-6)5124.60_DolSel	984	543	0.7	0.0037	0.9	2.2	15.3	1.7	0.7	1.7
(SPH-6)5124.60_DolSel	968	649	0.3	0.0064	0.9	1.9	5.6	3.9	0.8	1.8

Identificador	f206c	^{206}Pb	Uppm	Th/U	$^{206}Pb/^{204}Pb$	1s%	$^{238}U/^{206}Pb$	1s%	$^{207}Pb/^{206}Pb$	1s%
(SPH-6)5124.60_DolSel	902	572	0.7	0.0073	1.0	2.1	13.9	1.9	0.7	2.0
(SPH-6)5124.60_DolSel	906	608	0.6	0.0054	1.0	1.8	11.5	1.8	0.7	1.9
Barstow	468	5854	141.8	0.0000	2.6	0.8	270.0	0.9	0.3	0.9
Barstow	472	5048	124.9	0.0000	2.6	0.9	274.5	0.7	0.3	0.9
Barstow	603	5691	101.9	0.0001	1.8	0.8	195.9	0.6	0.4	0.9
Barstow	598	7576	111.9	0.0001	1.6	0.7	157.3	0.7	0.5	0.7
Barstow	518	5039	111.7	0.0000	2.2	0.9	239.0	0.6	0.4	0.8
Barstow	515	5523	123.8	0.0000	2.2	1.0	240.9	1.0	0.4	0.9
Barstow	622	8828	100.9	0.0000	1.5	0.8	119.9	1.7	0.6	0.6
Barstow	529	4109	94.0	0.0000	2.2	1.1	238.8	0.6	0.4	0.9
Barstow	426	4233	117.6	0.0000	3.0	0.9	290.4	0.7	0.3	0.9
Barstow	304	7499	237.4	0.0000	4.6	1.7	323.5	0.5	0.2	1.6
Barstow	474	3780	103.2	0.0000	2.6	1.0	278.1	0.8	0.3	1.1
Barstow	421	2903	90.3	0.0001	3.2	1.4	317.5	0.8	0.2	1.3
Barstow	523	5311	125.2	0.0000	2.1	1.0	233.6	0.8	0.4	0.9
Barstow	615	7547	108.0	0.0000	1.5	0.7	143.4	1.1	0.6	0.8
Barstow	545	4720	104.2	0.0000	2.0	0.8	220.3	0.8	0.4	0.8
Barstow	514	3870	104.3	0.0000	2.3	1.0	260.9	0.8	0.4	0.9
Barstow	466	4404	126.4	0.0000	2.6	1.0	276.2	0.7	0.3	1.0
Barstow	514	5088	126.4	0.0000	2.2	1.0	239.1	0.6	0.4	0.9
Barstow	555	5987	109.6	0.0000	1.8	0.7	171.4	0.7	0.5	0.7
Barstow	581	5774	103.2	0.0000	1.7	0.6	167.5	0.6	0.5	0.7
Barstow	584	5167	86.6	0.0000	1.7	0.6	155.9	0.6	0.5	0.8
Barstow	608	7148	102.0	0.0001	1.5	0.5	129.2	0.9	0.6	0.6
Barstow	512	5443	128.5	0.0000	2.1	0.9	212.3	0.8	0.4	0.8
Barstow	533	3971	112.0	0.0000	2.2	1.0	255.1	0.7	0.4	1.1

Identificador	f206c	^{206}Pb	Uppm	Th/U	$^{206}Pb/^{204}Pb$	1s%	$^{238}U/^{206}Pb$	1s%	$^{207}Pb/^{206}Pb$	1s%
C_Walnut	314	4272	2.89	0.0077	4.6	2.3	21.5	0.8	0.2	1.9
C_Walnut	311	5172	3.54	73.0597	4.7	1.4	21.6	0.6	0.2	1.1
C_Walnut	284	6210	4.22	0.0012	5.2	1.4	21.4	0.5	0.2	1.0
C_Walnut	252	6673	4.79	0.0007	6.0	1.5	22.6	0.5	0.2	1.2
C_Walnut	331	4965	3.33	0.0042	4.4	1.9	21.1	0.7	0.2	1.7
C_Walnut	271	6079	4.12	0.0006	5.3	1.8	20.3	1.6	0.2	1.9
C_Walnut	295	6691	4.01	0.0002	4.8	2.2	18.8	2.5	0.2	2.8
C_Walnut	283	9820	4.95	0.0016	4.7	1.3	14.9	0.7	0.2	1.0
C_Walnut	244	4115	3.28	0.0005	6.2	2.0	22.3	0.5	0.2	1.4
C_Walnut	263	3527	2.70	0.0006	5.8	2.1	21.3	0.6	0.2	1.5
C_Walnut	241	4950	3.82	0.0001	6.1	1.3	21.4	0.5	0.2	1.2
C_Walnut	222	5871	4.90	0.0003	6.8	1.4	21.9	0.6	0.2	1.0
C_Walnut	233	4897	3.95	0.0001	6.3	1.4	21.1	0.5	0.2	1.0
C_Walnut	251	4488	3.57	0.0005	5.9	1.7	20.8	0.5	0.2	1.2
C_Walnut	297	3523	2.67	0.0158	4.9	2.5	18.8	0.9	0.2	1.7
C_Walnut	199	5076	4.64	0.0002	7.9	1.9	22.4	0.5	0.1	1.4
C_Walnut	216	4667	4.11	0.0004	7.1	1.7	21.5	0.5	0.2	1.3
C_Walnut	209	4447	4.02	0.0001	7.4	2.0	20.8	0.5	0.2	1.3
C_Walnut	228	4586	3.98	0.0005	6.5	1.5	19.8	0.7	0.2	1.1
C_Walnut	275	4560	3.42	0.0002	5.0	2.4	17.3	1.2	0.2	1.9
C_Walnut	194	4562	4.31	0.0017	8.2	2.1	21.6	0.5	0.1	1.3
C_Walnut	212	4461	4.10	0.0005	7.3	2.0	20.9	0.7	0.2	1.2
(923A)5100.75_CalcPart	746	1224	0.03	0.0207	1.1	1.2	0.6	15.9	0.8	1.1
(923A)5100.75_CalcPart	829	842	0.08	0.0061	1.0	1.5	2.2	6.0	0.8	1.4
(923A)5100.75_CalcPart	961	461	0.13	0.0268	1.0	2.4	6.9	4.1	0.7	2.1
(923A)5100.75_CalcPart	752	1297	0.07	1.1613	1.1	1.2	1.4	6.2	0.8	1.3
(923A)5100.75_CalcPart	869	650	0.02	0.2791	1.0	2.1	0.6	29.9	0.8	1.9
(923A)5100.75_CalcPart	764	1210	0.06	0.0575	1.1	1.4	1.3	7.7	0.8	1.5

Identificador	f206c	^{206}Pb	Uppm	Th/U	$^{206}Pb/^{204}Pb$	1s%	$^{238}U/^{206}Pb$	1s%	$^{207}Pb/^{206}Pb$	1s%
(923A)5100.75_CalcPart	703	2070	0.06	0.0158	1.2	0.9	0.6	7.7	0.9	0.8
(923A)5100.75_CalcPart	729	1301	0.01	0.0880	1.1	1.4	0.3	36.7	0.9	1.2
(923A)5100.75_CalcPart	701	1744	0.04	0.0131	1.2	1.2	0.5	11.7	0.8	0.9
(923A)5100.75_CalcPart	715	1641	0.05	0.0934	1.1	1.1	0.6	9.2	0.8	0.9
(923A)5100.75_CalcPart	729	1120	0.15	0.0044	1.2	1.4	3.3	3.6	0.8	1.3
(923A)5100.75_CalcPart	665	2153	0.19	0.0039	1.2	1.0	2.1	2.2	0.8	0.8
(923A)5100.75_CalcPart	769	846	0.08	0.0666	1.1	1.7	2.3	5.5	0.8	1.5
(923A)5100.75_CalcPart	768	784	0.15	0.0082	1.1	1.8	4.4	2.7	0.7	1.3
(923A)5100.75_CalcPart	730	871	0.18	0.0106	1.2	1.7	4.8	2.6	0.7	1.4
(923A)5100.75_CalcPart	792	676	0.14	0.0031	1.1	2.1	5.0	4.1	0.7	1.8
(923A)5100.75_CalcPart	779	872	0.14	0.0108	1.1	1.7	3.9	3.6	0.8	1.3
(923A)5100.75_CalcPart	756	1053	0.11	0.0150	1.1	1.6	2.6	4.3	0.8	1.1
(923A)5100.75_CalcPart	729	1174	0.16	0.0104	1.2	1.2	3.1	3.1	0.8	1.0
(923A)5100.75_CalcPart	798	670	0.14	0.0663	1.1	2.1	5.0	3.6	0.7	1.6
(923A)5100.75_DolBloc	1676	192	0.03	0.0035	0.6	5.0	4.6	15.9	0.8	4.2
(923A)5100.75_DolBloc	2254	162	0.01	0.0020	0.4	37.0	1.0	69.1	0.9	4.5
(923A)5100.75_DolBloc	3925	40	0.00	0.0036	0.2	16.7	-1.9	-413.8	0.5	53.3
(923A)5100.75_DolBloc	1688	186	0.01	0.0032	0.6	4.3	1.3	50.3	1.0	3.8
(923A)5100.75_DolBloc	1309	262	0.01	0.0063	0.7	3.5	1.1	40.1	0.8	2.6
(923A)5100.75_DolBloc	4023	72	0.01	0.0099	0.4	13.7	-2.8	-132.8	1.1	22.3
(923A)5100.75_DolBloc	6871	69	0.00	0.0018	0.3	10.1	-3.8	-123.5	0.7	28.2
(923A)5100.75_DolBloc	3636	102	0.00	0.0022	0.4	8.4	-0.1	-5421.2	0.3	334.9
(923A)5100.75_DolBloc	3763	90	0.00	0.0292	0.4	9.9	9.2	52.4	1.6	11.3
(923A)5100.75_DolBloc	3748	65	0.01	0.0007	0.3	14.9	-3.5	-300.8	0.7	43.3
(923A)5100.75_DolBloc	3117	106	0.01	0.0113	0.4	6.3	1.0	152.2	1.1	8.1
(923A)5100.75_DolBloc	4181	91	0.00	0.0054	0.3	8.2	-4.8	-158.4	0.2	130.6
(923A)5100.75_DolBloc	4202	101	0.00	0.0138	0.4	18.2	-1.9	-224.3	0.2	143.5
(923A)5100.75_DolBloc	4348	96	0.01	0.0271	0.1	216.8	1.2	512.6	0.5	48.3

Identificador	f206c	^{206}Pb	Uppm	Th/U	$^{206}Pb/^{204}Pb$	1s%	$^{238}U/^{206}Pb$	1s%	$^{207}Pb/^{206}Pb$	1s%
(923A)5100.75_DolBloc	2509	144	0.01	0.0377	0.5	5.7	-0.1	-914.6	1.0	8.9
(923A)5100.75_DolBloc	2054	146	0.01	0.0374	0.5	5.2	1.3	76.2	0.9	6.7
(923A)5100.75_DolBloc	3996	82	0.01	0.0089	0.3	7.1	3.9	81.0	1.0	18.4
(923A)5100.75_DolBloc	1685	212	0.01	0.0045	0.6	4.4	0.9	64.4	0.9	3.8
(923A)5100.75_DolBloc	1175	339	0.01	0.0124	0.8	3.3	0.8	43.8	0.8	2.3
(923A)5100.75_DolBloc	2724	100	0.00	0.0121	0.6	22.6	1.5	105.8	0.9	7.4
(923A)5100.75_DolRomb	801	1098	0.11	0.0241	1.0	1.3	2.9	3.5	0.8	1.3
(923A)5100.75_DolRomb	896	761	0.10	0.0212	1.0	2.0	3.7	4.5	0.8	1.6
(923A)5100.75_DolRomb	715	2276	0.11	0.0072	1.2	1.1	1.4	4.6	0.8	0.9
(923A)5100.75_DolRomb	1040	427	0.15	0.0085	0.9	2.9	9.6	3.8	0.8	2.3
(923A)5100.75_DolRomb	943	562	0.35	0.0020	1.1	2.5	17.7	2.1	0.6	1.9
(923A)5100.75_DolRomb	715	1859	0.13	0.0832	1.1	1.1	1.9	3.1	0.8	1.1
(923A)5100.75_DolRomb	779	962	0.28	0.0022	1.1	1.7	8.1	2.0	0.8	1.4
(923A)5100.75_DolRomb	821	954	0.09	0.0563	1.0	2.0	2.9	6.1	0.8	1.6
(923A)5100.75_DolRomb	817	874	0.20	0.0058	1.1	1.7	6.7	3.4	0.8	1.4
(923A)5100.75_DolRomb	834	746	0.29	0.0014	1.1	5.8	10.6	1.9	0.7	1.7
(923A)5100.75_DolRomb	920	678	0.13	0.0238	1.0	1.9	5.8	4.2	0.8	1.7
(923A)5100.75_DolRomb	893	684	0.34	0.0037	1.1	2.4	13.3	2.6	0.7	1.8
(923A)5100.75_DolRomb	1001	900	0.16	0.0204	1.0	3.8	6.7	7.7	0.8	2.6
(923A)5100.75_DolRomb	1216	334	0.15	0.0105	0.8	2.9	11.9	3.2	0.7	2.8
(923A)5100.75_DolRomb	772	1179	0.15	0.0059	1.1	1.4	3.6	3.7	0.8	1.1
(923A)5100.75_DolRomb	1078	373	0.01	0.2969	0.8	2.8	1.0	26.6	0.8	2.1
(923A)5100.75_DolRomb	833	623	0.57	0.0017	1.3	2.2	24.8	1.5	0.5	1.9
(923A)5100.75_DolRomb	983	522	0.49	0.0010	1.1	2.5	25.4	1.8	0.5	2.5
(923A)5100.75_DolRomb	787	888	0.43	0.0009	1.2	1.8	12.9	1.3	0.7	1.6
(923A)5100.75_DolRomb	764	743	0.50	0.0016	1.3	2.0	17.7	1.2	0.6	1.8
(928)5015.10.1_CalcShrub	906	1305	0.23	0.0038	0.9	1.2	5.7	2.6	0.8	1.2
(928)5015.10.1_CalcShrub	928	1228	0.13	0.1257	0.9	2.0	3.8	4.6	0.9	1.4

Identificador	f206c	^{206}Pb	Uppm	Th/U	$^{206}Pb/^{204}Pb$	1s%	$^{238}U/^{206}Pb$	1s%	$^{207}Pb/^{206}Pb$	1s%
(928)5015.10.1_CalcShrub	1020	852	0.12	0.2598	0.8	1.6	4.6	3.2	0.8	1.6
(928)5015.10.1_CalcShrub	778	4381	0.11	0.0160	1.0	0.7	1.0	4.8	0.9	0.6
(928)5015.10.1_CalcShrub	911	1491	0.09	0.0264	0.9	1.4	2.1	5.7	0.9	1.3
(928)5015.10.1_CalcShrub	973	1040	0.36	0.1832	1.0	2.1	12.7	3.6	0.7	1.8
(928)5015.10.1_CalcShrub	757	3697	0.12	0.0433	1.0	0.7	1.1	4.6	0.9	0.7
(928)5015.10.1_CalcShrub	807	3324	0.45	0.0162	1.0	1.3	9.4	4.2	0.8	1.1
(928)5015.10.1_CalcShrub	788	1543	0.47	0.0529	1.1	1.2	9.6	2.0	0.8	1.1
(928)5015.10.1_CalcShrub	946	1018	0.18	0.0269	0.9	1.6	6.3	3.8	0.8	1.5
(928)5015.10.1_CalcShrub	970	988	0.13	0.0614	0.9	1.8	4.4	3.8	0.9	1.5
(928)5015.10.1_CalcShrub	1120	753	0.20	0.0163	0.8	2.4	9.3	3.5	0.8	2.1
(928)5015.10.1_CalcShrub	1168	609	0.10	0.0845	0.8	2.6	6.0	5.8	0.9	2.1
(928)5015.10.1_CalcShrub	980	986	0.19	0.0083	0.9	1.7	6.6	3.5	0.8	1.6
(928)5015.10.1_CalcShrub	871	1216	0.18	0.0043	1.0	1.6	5.6	4.6	0.9	1.4
(928)5015.10.1_CalcShrub	899	1129	0.35	0.0114	1.0	1.6	11.8	4.3	0.8	1.7
(928)5015.10.1_CalcShrub	743	2416	0.25	0.0342	1.1	1.4	3.4	3.5	0.9	1.0
(928)5015.10.1_CalcShrub	718	3045	0.15	0.0250	1.1	0.7	1.4	2.7	0.9	0.7
(928)5015.10.1_CalcShrub	774	1458	0.37	0.0027	1.1	1.1	7.4	2.2	0.8	1.0
(928)5015.10.1_CalcShrub	1028	730	0.17	0.0166	0.9	2.3	8.5	4.6	0.8	1.8
(928)5015.10.1_DolInt	642	2019	1.29	0.0035	1.5	1.1	18.9	1.6	0.6	1.3
(928)5015.10.1_DolInt	631	3008	1.57	0.0021	1.4	1.1	15.4	1.1	0.7	0.8
(928)5015.10.1_DolInt	688	4361	0.37	0.0061	1.2	1.7	3.0	3.8	0.8	0.7
(928)5015.10.1_DolInt	672	2453	0.94	0.0041	1.3	1.1	11.9	2.1	0.7	1.0
(928)5015.10.1_DolInt	825	1176	0.04	0.3892	1.0	1.3	1.0	9.3	0.9	1.2
(928)5015.10.1_DolInt	631	1625	1.14	0.0077	1.6	3.2	21.3	1.9	0.6	1.4
(928)5015.10.1_DolInt	642	1888	1.12	0.0018	1.4	1.1	17.2	1.6	0.7	1.1
(928)5015.10.1_DolInt	822	952	0.21	0.0067	1.0	2.1	6.6	3.5	0.8	2.2
(928)5015.10.1_DolInt	577	3166	2.04	0.0026	1.6	0.9	18.9	1.5	0.6	1.0
(928)5015.10.1_DolInt	601	1454	1.51	0.0003	1.8	1.8	30.9	1.7	0.5	1.8

Identificador	f206c	^{206}Pb	Uppm	Th/U	^{206}Pb/^{204}Pb	1s%	^{238}U/^{206}Pb	1s%	^{207}Pb/^{206}Pb	1s%
(928)5015.10.1_DolInt	683	1417	0.78	0.0376	1.4	1.6	16.8	2.7	0.6	1.5
(928)5015.10.1_DolInt	619	1810	1.31	0.0027	1.6	1.4	21.4	1.8	0.6	1.3
(928)5015.10.1_DolInt	553	1712	1.73	0.0009	2.0	2.2	29.3	2.0	0.5	2.9
(928)5015.10.1_DolInt	693	1427	0.68	0.0012	1.3	1.3	13.7	1.4	0.7	1.3
(928)5015.10.1_DolInt	685	6826	0.24	0.0182	1.2	0.8	1.2	3.9	0.9	0.5
(928)5015.10.1_DolInt	695	2536	0.34	0.0057	1.2	0.9	3.8	1.9	0.8	0.7
(928)5015.10.1_DolInt	723	1540	0.40	0.0018	1.2	1.2	7.5	2.2	0.8	1.1
(928)5015.10.1_DolInt	659	3846	0.37	0.0051	1.2	0.6	2.7	1.9	0.8	0.6
Barstow	494	10092	85.52	0.0000	2.3	0.8	266.2	0.7	0.4	0.9
Barstow	459	9504	89.43	0.0000	2.6	0.7	295.6	0.5	0.3	0.7
Barstow	476	9282	85.93	0.0000	2.5	0.7	288.6	0.5	0.3	0.9
Barstow	502	8716	62.22	0.0000	2.1	1.3	221.0	2.0	0.4	1.8
Barstow	490	5148	47.39	0.0000	2.4	0.9	272.9	0.8	0.3	1.2
Barstow	492	4131	41.71	0.0000	2.5	1.0	296.7	0.6	0.3	1.0
Barstow	514	3689	32.61	0.0000	2.2	1.1	251.5	0.9	0.4	1.3
Barstow	504	6235	52.03	0.0000	2.2	0.8	230.8	0.4	0.4	0.7
Barstow	533	6584	49.21	0.0000	2.0	0.8	205.6	0.5	0.5	0.7
Barstow	480	6420	54.07	0.0000	2.2	0.8	218.7	0.6	0.4	0.8
Barstow	527	3973	37.06	0.0000	2.1	0.9	242.6	0.8	0.4	1.2
Barstow	470	4196	44.06	0.0000	2.5	1.1	272.5	0.6	0.3	0.9
Barstow	429	5853	62.61	0.0000	2.8	1.3	267.7	1.0	0.3	1.2
Barstow	506	4131	37.08	0.0010	2.2	1.5	251.4	1.3	0.4	1.9
Barstow	485	5117	49.41	0.0000	2.3	0.8	234.6	0.6	0.4	0.8
Barstow	422	4927	55.89	0.0000	2.7	0.8	257.6	0.6	0.4	0.9
Barstow	488	3857	44.01	0.0000	2.4	1.0	258.2	0.6	0.4	0.9
Barstow	470	4724	51.77	0.0000	2.4	0.9	248.8	0.8	0.4	1.1

Identificador	f206c	^{206}Pb	Uppm	Th/U	$^{206}Pb/^{204}Pb$	1s%	$^{238}U/^{206}Pb$	1s%	$^{207}Pb/^{206}Pb$	1s%
C_Walnut	302	5093	3.02	0.0021	4.7	1.3	20.7	0.7	0.2	1.4
C_Walnut	283	6862	4.27	0.0004	5.1	1.1	20.1	0.5	0.2	1.1
C_Walnut	272	6935	4.36	0.0006	5.4	1.2	20.3	0.5	0.2	1.1
C_Walnut	271	7112	4.53	0.0023	5.5	1.1	20.4	0.6	0.2	1.1
C_Walnut	267	6102	3.99	0.0008	5.7	1.3	20.9	0.5	0.2	1.4
C_Walnut	257	5464	3.87	0.0003	5.7	1.2	21.4	0.7	0.2	1.0
C_Walnut	224	6570	4.63	0.0006	6.7	1.4	21.2	0.6	0.2	1.2
C_Walnut	251	5731	3.84	0.0003	5.9	1.3	20.1	0.7	0.2	1.2
C_Walnut	219	5387	3.97	0.0005	6.8	1.3	21.0	0.8	0.2	1.2
C_Walnut	221	5201	3.95	0.0003	6.9	1.4	21.3	0.7	0.2	1.6
C_Walnut	246	4552	3.41	0.0007	6.1	1.5	21.1	0.6	0.2	1.3
C_Walnut	215	4858	4.12	0.0007	7.2	1.5	22.4	0.6	0.1	1.4
C_Walnut	225	4399	3.59	0.0003	6.8	1.8	21.6	0.8	0.2	1.4
C_Walnut	221	4455	3.65	0.0016	7.0	1.5	21.7	0.7	0.2	1.4
C_Walnut	207	4526	3.94	0.0001	7.5	1.7	21.2	0.9	0.1	1.4
C_Walnut	242	3693	3.08	0.0001	6.3	1.7	20.7	0.7	0.2	1.7
C_Walnut	208	4490	3.92	0.0000	7.5	2.1	21.1	0.8	0.1	1.4
C_Walnut	234	3298	2.96	0.0001	6.6	1.8	20.6	0.8	0.2	1.4
C_Walnut	232	3321	3.01	0.0000	6.6	1.8	20.9	0.8	0.2	1.4
C_Walnut	224	3523	3.27	0.0001	6.8	1.6	21.1	0.6	0.2	1.5
C_Walnut	228	3953	3.81	0.0003	6.6	1.5	20.7	0.6	0.2	1.4
C_Walnut	228	3350	3.34	0.0003	6.7	1.7	21.2	0.6	0.2	1.4
C_Walnut	242	3036	2.93	0.0004	6.3	1.6	20.6	0.7	0.2	1.8
C_Walnut	239	3011	3.16	0.0005	6.5	2.0	20.7	0.7	0.2	1.7
C_Walnut	226	3321	3.55	0.0005	6.9	2.0	21.1	0.7	0.2	1.5
C_Walnut	234	3963	4.02	0.0025	6.4	1.7	19.8	0.8	0.2	1.5
C_Walnut	218	4452	5.08	0.0013	7.0	1.4	20.4	0.6	0.2	1.4
C_Walnut	239	3077	3.55	0.0012	6.7	1.9	20.8	0.7	0.1	1.7

Identificador	f206c	^{206}Pb	Uppm	Th/U	$^{206}Pb/^{204}Pb$	1s%	$^{238}U/^{206}Pb$	1s%	$^{207}Pb/^{206}Pb$	1s%
C_Walnut	226	4087	4.65	0.0067	6.7	1.9	20.4	0.6	0.2	1.8
C_Walnut	229	2961	3.48	0.0004	7.2	2.8	21.0	0.7	0.1	2.0
C_Walnut	212	4524	5.30	0.0003	7.2	1.3	20.8	0.6	0.2	1.2
(928)5049.95_DolOstra	644	1651	1.36	0.0002	1.5	1.5	23.1	2.1	0.6	1.6
(928)5049.95_DolOstra	709	1419	0.58	0.0003	1.2	1.5	11.2	2.2	0.7	1.3
(928)5049.95_DolOstra	839	677	0.28	0.0023	1.0	2.0	11.0	2.3	0.7	2.0
(928)5049.95_DolOstra	659	1341	1.00	0.0004	1.4	1.7	20.1	2.5	0.6	1.8
(928)5049.95_DolOstra	736	1079	0.39	0.0030	1.2	1.5	9.7	2.0	0.7	1.6
(928)5049.95_DolOstra	940	759	0.02	0.0110	0.9	2.2	0.9	22.7	0.9	2.0
(928)5049.95_DolOstra	887	755	0.13	0.0087	1.0	2.2	5.0	5.7	0.8	2.0
(928)5049.95_DolOstra	769	1213	0.06	0.0164	1.1	4.2	1.3	10.5	0.9	1.5
(928)5049.95_DolOstra	839	888	0.03	0.0191	1.0	1.8	1.1	15.5	0.9	1.7
(928)5049.95_DolOstra	784	1046	0.20	0.0113	1.1	1.7	5.3	3.7	0.8	1.7
(928)5049.95_DolOstra	909	826	0.17	0.1267	1.0	4.6	6.9	5.4	0.8	2.1
(928)5049.95_DolOstra	873	719	0.17	0.0331	1.0	2.7	6.8	4.7	0.8	2.1
(928)5049.95_DolOstra	849	836	0.14	0.0038	1.0	1.9	4.5	4.0	0.8	1.8
(928)5049.95_DolOstra	908	753	0.13	0.0071	1.0	2.2	4.8	4.7	0.8	1.9
(928)5049.95_DolOstra	840	823	0.14	0.0035	1.0	1.8	4.6	4.8	0.8	1.9
(928)5049.95_DolOstra	1151	352	0.04	0.0087	0.8	3.7	3.1	12.8	0.9	3.2
(928)5049.95_DolOstra	1128	364	0.04	0.0070	0.8	3.8	3.0	14.4	0.9	3.2
(928)5049.95_DolOstra	1129	383	0.05	0.0060	0.8	3.9	3.7	12.4	0.8	3.4
(928)5049.95_DolOstra	1251	327	0.05	0.0062	0.7	3.5	3.7	10.9	0.9	3.1
(928)5049.95_DolOstra	1173	395	0.03	0.0225	0.8	3.5	2.1	17.2	0.8	2.5
(928)5049.95_DolPonte	684	2027	0.43	0.0012	1.3	1.2	7.0	4.2	0.7	1.3
(928)5049.95_DolPonte	730	1132	0.51	0.0014	1.2	2.0	11.6	2.3	0.7	1.6
(928)5049.95_DolPonte	703	76169	0.47	0.0017	1.1	0.2	0.2	3.0	0.8	0.2
(928)5049.95_DolPonte	941	488	0.07	0.0054	0.9	2.6	3.5	7.9	0.9	2.5
(928)5049.95_DolPonte	2757	122	0.01	0.0052	0.5	7.2	1.7	103.7	0.9	9.8

Identificador	f206c	^{206}Pb	Uppm	Th/U	$^{206}Pb/^{204}Pb$	1s%	$^{238}U/^{206}Pb$	1s%	$^{207}Pb/^{206}Pb$	1s%
(928)5049.95_DolPonte	772	940	0.31	0.0005	1.1	1.8	7.9	2.5	0.8	1.8
(928)5049.95_DolPonte	776	774	0.36	0.0008	1.1	1.9	12.2	3.4	0.7	1.9
(928)5049.95_DolPonte	679	2135	0.47	0.0003	1.2	1.0	5.5	2.6	0.8	1.0
(928)5049.95_DolPonte	835	683	0.19	0.0029	1.1	2.0	7.4	4.0	0.8	1.9
(928)5049.95_DolPonte	772	853	0.50	0.0002	1.2	2.0	14.6	2.6	0.7	1.8
(928)5049.95_DolPonte	737	856	0.47	0.0007	1.3	2.0	13.1	1.7	0.6	1.7
(928)5049.95_DolPonte	711	962	0.62	0.0001	1.3	1.8	15.6	2.0	0.7	1.7
(928)5049.95_DolPonte	693	1163	0.72	0.0002	1.3	1.6	14.8	1.6	0.7	1.5
(928)5049.95_DolPonte	714	1175	0.45	0.0000	1.2	1.5	9.3	2.4	0.7	1.5
(928)5049.95_DolPonte	747	1026	0.28	0.0001	1.1	1.5	6.6	2.4	0.8	1.6
(928)5049.95_DolPonte	654	1050	0.90	0.0000	1.5	2.4	20.0	1.1	0.6	1.9
(928)5049.95_DolPonte	686	1812	0.30	0.0034	1.2	1.1	4.0	2.6	0.8	1.0
(928)5049.95_DolPonte	812	602	0.26	0.0004	1.1	2.7	10.3	3.6	0.7	2.2
(928)5049.95_DolPonte	1062	305	0.06	0.0052	0.8	4.4	4.9	8.4	0.8	3.2
(928)5049.95_DolPonte	778	756	0.28	0.0002	1.1	2.0	8.4	3.5	0.8	1.7
(SPH-6)5113.00_CalcOstra	665	2320	1.68	0.0073	1.5	1.2	23.0	1.0	0.5	1.1
(SPH-6)5113.00_CalcOstra	697	1983	1.30	0.0010	1.4	1.7	20.5	1.2	0.6	1.6
(SPH-6)5113.00_CalcOstra	676	2691	1.58	0.0010	1.4	1.2	19.2	2.2	0.6	1.5
(SPH-6)5113.00_CalcOstra	736	44895	2.25	0.0042	1.1	0.9	1.7	3.5	0.8	0.2
(SPH-6)5113.00_CalcOstra	600	2791	2.47	0.0007	1.8	1.5	27.6	0.9	0.5	1.6
(SPH-6)5113.00_CalcOstra	552	3560	3.17	0.0003	2.0	1.3	27.7	0.9	0.4	1.3
(SPH-6)5113.00_CalcOstra	526	3576	3.54	0.0120	2.1	1.2	31.0	0.6	0.4	0.9
(SPH-6)5113.00_CalcOstra	335	3348	5.16	0.0008	4.5	1.9	47.9	0.7	0.2	1.6
(SPH-6)5113.00_CalcOstra	436	2764	3.91	0.0006	3.1	1.8	44.1	0.8	0.2	1.5
(SPH-6)5113.00_CalcOstra	538	2032	2.30	0.0004	2.2	1.9	35.3	1.2	0.3	1.5
(SPH-6)5113.00_CalcOstra	471	3211	3.70	0.0003	2.5	1.2	35.7	0.9	0.3	1.2
(SPH-6)5113.00_CalcOstra	429	2991	3.92	0.0018	3.0	1.5	40.7	0.8	0.3	1.5
(SPH-6)5113.00_CalcOstra	687	2525	1.08	0.0041	1.3	1.2	13.3	0.8	0.7	1.0

Identificador	f206c	^{206}Pb	Uppm	Th/U	$^{206}Pb/^{204}Pb$	1s%	$^{238}U/^{206}Pb$	1s%	$^{207}Pb/^{206}Pb$	1s%
(SPH-6)5113.00_CalcOstra	725	2039	0.96	0.0034	1.3	1.1	14.7	0.9	0.6	1.0
(SPH-6)5113.00_CalcOstra	716	1931	0.85	0.0015	1.2	1.2	13.6	1.2	0.7	1.2
(SPH-6)5113.00_CalcOstra	709	2195	0.90	0.0011	1.3	1.2	12.6	1.2	0.7	1.0
(SPH-6)5113.00_CalcOstra	705	2077	0.90	0.0034	1.3	1.3	13.2	1.2	0.7	1.1
(SPH-6)5113.00_CalcOstra	724	1870	0.85	0.0073	1.2	1.2	13.9	1.2	0.7	1.1
(SPH-6)5113.00_CalcOstra	692	2277	0.92	0.0019	1.3	1.2	12.4	0.9	0.7	1.0
(SPH-6)5113.00_CalcOstra	688	2272	1.08	0.0302	1.3	1.1	14.4	1.0	0.7	1.1
(SPH-6)5113.00_CalcPart	602	3122	2.07	0.0004	1.6	1.1	18.5	1.3	0.6	1.1
(SPH-6)5113.00_CalcPart	449	2937	3.83	0.0002	2.7	1.5	36.5	0.9	0.3	1.4
(SPH-6)5113.00_CalcPart	602	2112	1.55	0.0017	1.6	1.4	20.6	0.8	0.5	1.2
(SPH-6)5113.00_CalcPart	314	3934	6.43	0.0001	4.4	1.7	45.5	0.8	0.2	1.5
(SPH-6)5113.00_CalcPart	462	3730	3.98	0.0003	2.4	1.3	29.5	0.7	0.4	1.2
(SPH-6)5113.00_CalcPart	558	2666	2.26	0.0004	1.8	1.0	23.4	0.7	0.5	1.0
(SPH-6)5113.00_CalcPart	444	2957	3.88	0.0002	2.7	1.2	36.0	0.8	0.3	1.2
(SPH-6)5113.00_CalcPart	550	2062	1.73	0.0003	1.9	1.3	23.4	0.9	0.5	1.2
(SPH-6)5113.00_CalcPart	502	1632	2.12	0.0079	2.4	2.0	35.7	0.9	0.3	2.0
(SPH-6)5113.00_CalcPart	568	1808	1.73	0.0006	1.8	1.3	26.3	0.9	0.5	1.3
(SPH-6)5113.00_CalcPart	537	2643	2.47	0.0002	2.0	2.4	25.7	1.5	0.5	1.6
(SPH-6)5113.00_CalcPart	452	2817	3.39	0.0003	2.6	1.3	33.0	1.0	0.4	1.2
(SPH-6)5113.00_CalcPart	491	2212	2.75	0.0002	2.3	1.5	33.7	0.7	0.4	1.4
(SPH-6)5113.00_CalcPart	488	2058	2.50	0.0003	2.4	1.7	33.0	0.8	0.4	1.4
(SPH-6)5113.00_CalcPart	470	2424	3.07	0.0004	2.5	1.7	34.0	0.7	0.4	1.5
(SPH-6)5113.00_CalcPart	557	1535	1.71	0.0008	2.0	1.8	30.0	1.0	0.4	1.4
(SPH-6)5113.00_CalcPart	546	1530	1.91	0.0008	2.1	1.9	33.7	1.1	0.4	1.4
(SPH-6)5113.00_CalcPart	574	2083	1.82	0.0007	1.8	1.3	23.4	1.0	0.5	1.4
(SPH-6)5113.00_CalcPart	496	3308	3.57	0.0003	2.2	1.1	28.7	0.7	0.4	1.0
(SPH-6)5113.00_CalcPart	590	2616	1.78	0.0019	1.6	1.0	18.2	0.8	0.6	1.1
(SPH-6)5113.00_DolBloc	1942	233	0.32	0.0039	0.8	9.7	43.6	3.4	0.3	7.0

Identificador	f206c	^{206}Pb	Uppm	Th/U	$^{206}Pb/^{204}Pb$	1s%	$^{238}U/^{206}Pb$	1s%	$^{207}Pb/^{206}Pb$	1s%
(SPH-6)5113.00_DolBloc	1587	281	0.34	0.0085	0.8	4.9	38.3	2.6	0.4	7.0
(SPH-6)5113.00_DolBloc	1324	381	0.50	0.0111	1.0	4.0	40.2	2.1	0.3	5.5
(SPH-6)5113.00_DolBloc	1238	363	0.37	0.0073	0.9	3.5	31.1	2.2	0.5	4.0
(SPH-6)5113.00_DolBloc	1073	479	0.57	0.0025	1.2	4.9	35.8	2.0	0.4	3.6
(SPH-6)5113.00_DolBloc	1112	445	0.53	0.0024	1.1	3.4	36.4	2.4	0.4	4.2
(SPH-6)5113.00_DolBloc	1081	429	0.61	0.0013	1.4	9.5	43.3	2.4	0.3	6.1
(SPH-6)5113.00_DolBloc	1734	261	0.31	0.0011	0.8	4.3	36.9	3.2	0.4	5.5
(SPH-6)5113.00_DolBloc	1413	289	0.39	0.0031	1.0	5.8	40.3	2.7	0.4	6.3
(SPH-6)5113.00_DolBloc	1074	453	0.39	0.0038	1.0	3.4	25.8	1.9	0.6	3.3
(SPH-6)5113.00_DolBloc	1769	248	0.26	0.0052	0.7	4.5	33.1	3.5	0.4	6.4
(SPH-6)5113.00_DolBloc	1626	261	0.13	0.0063	0.6	3.5	16.3	4.1	0.7	4.1
(SPH-6)5113.00_DolBloc	1417	308	0.24	0.0180	0.8	3.6	23.2	3.0	0.6	3.3
(SPH-6)5113.00_DolBloc	1240	353	0.24	0.0056	0.9	3.1	20.5	2.8	0.6	3.7
(SPH-6)5113.00_DolBloc	1342	270	0.17	0.0087	0.8	4.6	18.7	4.3	0.6	3.6
(SPH-6)5113.00_DolBloc	1196	388	0.29	0.0074	0.9	3.8	22.1	2.7	0.6	3.6
(SPH-6)5113.00_DolBloc	1147	418	0.25	0.0568	1.1	18.4	18.3	2.8	0.6	3.4
(SPH-6)5113.00_DolBloc	904	703	0.30	0.0359	1.0	2.4	12.1	1.9	0.7	2.1
(SPH-6)5113.00_DolBloc	1372	343	0.16	0.0295	0.8	6.2	14.2	3.5	0.6	3.6
(SPH-6)5113.00_DolBloc	1679	226	0.21	0.0057	0.7	9.3	27.1	5.0	0.6	6.5
(SPH-6)5127.90_CalcPart	649	4452	0.39	0.0072	1.2	0.7	1.7	2.6	0.8	0.6
(SPH-6)5127.90_CalcPart	628	2620	1.22	0.0010	1.4	0.9	8.9	1.4	0.7	1.0
(SPH-6)5127.90_CalcPart	630	2392	1.20	0.0013	1.4	1.0	9.9	1.3	0.7	1.0
(SPH-6)5127.90_CalcPart	631	3711	0.78	0.0016	1.3	0.8	4.0	1.1	0.8	0.7
(SPH-6)5127.90_CalcPart	581	2383	2.18	0.0016	1.6	1.1	17.6	1.3	0.6	1.2
(SPH-6)5127.90_CalcPart	612	5280	1.52	0.0011	1.4	0.6	5.5	0.9	0.8	0.6
(SPH-6)5127.90_CalcPart	596	3451	1.75	0.0004	1.5	0.9	9.7	0.9	0.7	0.8
(SPH-6)5127.90_CalcPart	597	2120	1.78	0.0008	1.5	1.1	15.9	1.4	0.6	0.9
(SPH-6)5127.90_CalcPart	581	2351	2.09	0.0010	1.6	1.6	16.8	1.4	0.6	1.2

Identificador	f206c	^{206}Pb	Uppm	Th/U	$^{206}Pb/^{204}Pb$	1s%	$^{238}U/^{206}Pb$	1s%	$^{207}Pb/^{206}Pb$	1s%
(SPH-6)5127.90_CalcPart	576	2139	1.88	0.0007	1.6	1.1	16.8	1.1	0.6	1.3
(SPH-6)5127.90_CalcPart	644	3182	0.78	0.0020	1.3	0.8	4.6	1.1	0.8	0.8
(SPH-6)5127.90_CalcPart	633	4562	1.00	0.0018	1.3	0.7	4.1	1.3	0.8	0.7
(SPH-6)5127.90_CalcPart	612	3985	1.46	0.0011	1.4	0.8	6.8	1.0	0.8	0.7
(SPH-6)5127.90_CalcPart	615	4131	1.54	0.0014	1.4	0.7	6.9	0.9	0.8	0.7
(SPH-6)5127.90_CalcPart	617	4627	1.37	0.0031	1.3	0.8	5.3	0.8	0.8	0.6
(SPH-6)5127.90_CalcPart	642	4651	0.61	0.0036	1.3	0.6	2.4	1.0	0.8	0.5
(SPH-6)5127.90_CalcPart	620	3034	1.18	0.0022	1.4	0.8	7.1	1.1	0.8	0.8
(SPH-6)5127.90_CalcPart	629	4102	1.21	0.0021	1.3	0.7	5.4	0.8	0.8	0.6
(SPH-6)5127.90_CalcPart	633	4566	0.64	0.0033	1.3	0.7	2.5	1.7	0.8	0.6
(SPH-6)5127.90_CalcPart	630	3618	1.10	0.0017	1.3	0.8	5.5	1.1	0.8	0.8
(928)5049.95_DolPooled	640	1667	1.36	0.0002	1.5	1.5	22.7	2.3	0.6	1.6
(928)5049.95_DolPooled	700	1526	0.59	0.0046	1.2	1.4	10.6	2.9	0.8	1.3
(928)5049.95_DolPooled	829	746	0.28	0.0022	1.0	1.8	10.3	3.0	0.8	1.9
(928)5049.95_DolPooled	662	1230	1.02	0.0004	1.4	2.0	21.6	1.6	0.6	1.8
(928)5049.95_DolPooled	732	1107	0.39	0.0026	1.2	1.4	9.5	2.2	0.7	1.5
(928)5049.95_DolPooled	962	528	0.02	0.0306	0.9	2.9	1.2	23.1	0.8	2.6
(928)5049.95_DolPooled	888	807	0.13	0.0058	1.0	2.0	4.7	6.1	0.8	2.0
(928)5049.95_DolPooled	741	1346	0.06	0.0216	1.1	4.1	1.3	9.3	0.9	1.4
(928)5049.95_DolPooled	834	739	0.03	0.0208	1.0	2.1	1.2	17.4	0.8	2.0
(928)5049.95_DolPooled	788	948	0.20	3.8689	1.1	1.8	5.6	3.2	0.8	1.8
(928)5049.95_DolPooled	915	691	0.17	0.0058	1.0	5.1	7.3	5.3	0.8	2.3
(928)5049.95_DolPooled	868	760	0.17	0.0130	1.0	2.4	6.6	4.9	0.8	2.1
(928)5049.95_DolPooled	848	780	0.14	0.0049	1.0	2.0	4.6	4.1	0.8	1.9
(928)5049.95_DolPooled	918	551	0.11	0.0175	1.0	2.8	5.1	4.9	0.8	2.4
(928)5049.95_DolPooled	833	771	0.14	0.0035	1.0	1.9	4.8	4.8	0.8	1.9
(928)5049.95_DolPooled	1167	301	0.04	0.0083	0.8	4.2	3.3	13.9	0.8	3.6
(928)5049.95_DolPooled	1198	257	0.04	0.0044	0.7	4.8	3.5	17.2	0.9	4.4

Identificador	f206c	^{206}Pb	Uppm	Th/U	$^{206}Pb/^{204}Pb$	1s%	$^{238}U/^{206}Pb$	1s%	$^{207}Pb/^{206}Pb$	1s%
(928)5049.95_DolPooled	1189	321	0.05	0.0049	0.7	4.4	4.3	11.8	0.9	4.1
(928)5049.95_DolPooled	1287	268	0.04	0.0048	0.7	4.3	4.1	15.2	0.9	4.1
(928)5049.95_DolPooled	1255	299	0.03	0.0026	0.7	4.2	2.6	19.2	0.8	3.1
(928)5049.95_DolPooled	689	1555	0.42	0.0013	1.2	1.5	7.8	3.6	0.7	1.5
(928)5049.95_DolPooled	731	1104	0.51	0.0009	1.2	2.1	11.7	2.2	0.7	1.6
(928)5049.95_DolPooled	705	65211	0.46	0.0021	1.1	0.2	0.2	2.7	0.8	0.2
(928)5049.95_DolPooled	996	384	0.07	0.0021	0.9	3.2	4.2	8.6	0.9	3.1
(928)5049.95_DolPooled	3038	91	0.01	0.0063	0.4	8.5	1.5	139.6	0.9	11.3
(928)5049.95_DolPooled	786	875	0.30	0.0005	1.1	2.1	8.3	2.5	0.8	2.1
(928)5049.95_DolPooled	779	694	0.35	0.0008	1.1	2.1	12.5	2.9	0.7	2.0
(928)5049.95_DolPooled	675	2102	0.48	0.0003	1.2	1.1	5.6	2.7	0.8	1.0
(928)5049.95_DolPooled	845	608	0.19	0.0017	1.0	2.2	7.9	3.7	0.8	2.1
(928)5049.95_DolPooled	777	788	0.50	0.0002	1.2	2.2	15.3	2.3	0.7	2.0
(928)5049.95_DolPooled	735	861	0.47	0.0005	1.3	2.1	13.0	1.8	0.6	1.8
(928)5049.95_DolPooled	710	953	0.62	0.0001	1.3	2.0	15.5	1.8	0.7	1.8
(928)5049.95_DolPooled	699	1118	0.72	0.0001	1.3	1.8	15.1	1.5	0.7	1.5
(928)5049.95_DolPooled	709	1294	0.46	0.0000	1.2	1.5	8.9	3.1	0.7	1.5
(928)5049.95_DolPooled	745	1011	0.28	0.0001	1.1	1.5	6.6	2.4	0.8	1.7
(928)5049.95_DolPooled	656	1041	0.90	0.0000	1.5	2.3	19.9	1.1	0.6	1.8
(928)5049.95_DolPooled	682	1947	0.30	0.0022	1.2	1.0	3.7	3.2	0.8	1.0
(928)5049.95_DolPooled	799	624	0.25	0.0043	1.1	2.9	9.5	3.1	0.7	2.4
(928)5049.95_DolPooled	1046	317	0.06	0.0032	0.8	3.7	4.5	8.7	0.8	2.9
(928)5049.95_DolPooled	777	762	0.28	0.0003	1.1	2.0	8.4	3.4	0.8	1.7
Barstow	544	14798	102.97	0.0000	2.0	0.6	221.0	0.8	0.4	0.6
Barstow	508	12711	98.74	0.0000	2.2	0.5	246.3	0.6	0.4	0.6
Barstow	584	14748	88.31	0.0000	1.7	0.6	190.3	1.1	0.5	0.6
Barstow	437	9220	83.71	0.0000	2.7	0.8	271.2	0.6	0.3	0.7
Barstow	479	9936	76.04	0.0000	2.3	0.8	228.9	0.6	0.4	0.8

Identificador	f206c	^{206}Pb	Uppm	Th/U	$^{206}Pb/^{204}Pb$	1s%	$^{238}U/^{206}Pb$	1s%	$^{207}Pb/^{206}Pb$	1s%
Barstow	519	9547	66.41	0.0000	2.0	0.6	206.7	0.5	0.5	0.7
Barstow	507	8417	59.18	0.0000	2.0	0.5	196.6	0.6	0.5	0.6
Barstow	408	9358	91.13	0.0000	2.9	0.8	273.2	0.9	0.3	1.0
Barstow	425	10419	93.98	0.0000	2.7	1.0	252.3	0.6	0.4	1.1
Barstow	474	3895	40.06	0.0000	2.5	1.1	270.2	0.7	0.3	1.0
Barstow	438	6052	61.33	0.0000	2.7	0.8	264.3	0.5	0.3	0.8
Barstow	420	9193	92.40	0.0000	2.8	0.7	262.6	0.6	0.3	1.2
Barstow	418	7465	79.51	0.0000	2.8	0.8	259.7	0.5	0.3	0.9
Barstow	436	5491	57.53	0.0000	2.7	0.9	255.4	0.7	0.3	0.8
Barstow	451	7462	71.30	0.0000	2.5	0.7	232.4	0.7	0.4	0.7
Barstow	480	4083	41.84	0.0000	2.3	0.9	232.0	0.7	0.4	0.9
Barstow	386	5185	63.23	0.0000	3.2	0.8	274.0	0.7	0.3	1.3
Barstow	416	6442	75.74	0.0000	2.8	0.9	264.6	0.5	0.3	0.9
Barstow	492	11637	80.26	0.0000	2.1	1.7	160.5	3.2	0.5	2.0
Barstow	402	5167	66.59	0.0000	3.0	0.9	269.8	0.6	0.3	1.1
Barstow	550	6503	41.61	0.0000	1.7	0.6	134.0	0.7	0.6	0.6
Barstow	438	3373	46.53	0.0000	2.8	1.0	266.8	0.7	0.3	1.1
Barstow	474	7814	79.29	0.0000	2.2	0.7	195.0	0.6	0.5	0.7
Barstow	380	5524	80.51	0.0001	3.3	1.0	279.9	0.7	0.3	1.1
Barstow	417	6297	88.22	0.0000	2.8	0.8	249.0	0.7	0.3	0.8
Barstow	400	5420	86.59	0.0000	3.1	1.0	280.2	0.5	0.3	1.0
Barstow	453	7824	96.12	0.0000	2.4	1.0	216.3	1.1	0.4	1.3

Identificador	f206c	^{206}Pb	Uppm	Th/U	$^{206}Pb/^{204}Pb$	1s%	$^{238}U/^{206}Pb$	1s%	$^{207}Pb/^{206}Pb$	1s%
C_Walnut	232	3098	5.99	0.0031	6.8	1.3	21.8	2.0	0.1	9.5
C_Walnut	314	2931	5.55	0.0181	4.8	1.8	21.0	0.8	0.2	1.8
C_Walnut	354	2575	4.72	0.0011	4.2	1.9	20.7	1.4	0.2	2.2
C_Walnut	498	1815	3.15	0.0040	3.0	2.9	19.4	0.9	0.2	2.5
C_Walnut	345	2597	4.98	0.0042	4.4	1.8	21.5	0.8	0.2	1.8
C_Walnut	284	3317	5.48	0.0021	5.4	2.4	19.8	0.7	0.2	1.6
C_Walnut	320	2237	3.80	0.0010	4.8	2.4	20.4	0.8	0.2	2.2
C_Walnut	305	2471	4.34	0.0563	5.1	2.5	21.1	0.8	0.2	2.0
C_Walnut	297	2338	4.01	0.0020	5.4	2.7	22.0	1.0	0.1	2.3
C_Walnut	330	1874	3.02	0.0032	4.7	2.8	20.8	0.9	0.2	2.1
C_Walnut	229	3695	6.01	0.0004	6.8	1.7	20.9	0.7	0.1	1.4
C_Walnut	258	2146	3.38	0.0001	6.6	3.1	21.5	1.0	0.1	2.4
C_Walnut	197	3507	5.75	0.0000	8.2	2.1	22.4	0.7	0.1	1.7
C_Walnut	205	3320	5.36	0.0000	8.1	2.7	22.1	0.9	0.1	2.1
C_Walnut	246	3684	5.07	0.0009	6.3	1.9	19.9	0.9	0.2	2.3
C_Walnut	186	4082	6.22	0.0010	8.8	1.7	22.0	0.7	0.1	1.6
C_Walnut	503	932	1.22	0.0026	3.0	3.3	18.9	1.2	0.2	3.4
C_Walnut	314	2225	2.96	0.0069	4.8	2.2	20.2	0.9	0.2	1.9
C_Walnut	199	3765	5.35	0.0018	8.2	2.5	21.6	0.6	0.1	1.9
C_Walnut	206	3652	4.80	0.0032	7.9	2.1	20.0	0.8	0.1	1.7
C_Walnut	299	2335	3.05	0.0040	5.1	2.3	19.9	0.7	0.2	1.7
C_Walnut	199	4133	5.60	0.0013	8.1	2.2	20.7	0.8	0.1	1.9
(928)5020.10_DolRomb	735	1424	1.07	0.0057	1.2	1.5	9.6	2.5	0.7	1.4
(928)5020.10_DolRomb	837	1131	0.29	0.0289	1.0	1.8	3.3	4.4	0.8	1.8
(928)5020.10_DolRomb	878	674	0.67	0.0060	1.0	2.2	13.2	3.4	0.8	2.5
(928)5020.10_DolRomb	679	1953	1.24	0.0028	1.2	1.2	7.9	2.2	0.8	1.1
(928)5020.10_DolRomb	1044	527	0.14	0.1333	0.8	3.4	3.3	10.3	0.9	2.8
(928)5020.10_DolRomb	3364	118	0.01	0.0316	0.4	6.6	7.7	70.8	0.7	19.2

Identificador	f206c	^{206}Pb	Uppm	Th/U	$^{206}Pb/^{204}Pb$	1s%	$^{238}U/^{206}Pb$	1s%	$^{207}Pb/^{206}Pb$	1s%
(928)5020.10_DolRomb	1063	455	0.26	0.0545	0.9	3.4	7.7	5.0	0.8	2.5
(928)5020.10_DolRomb	3108	79	0.02	0.0703	0.3	6.4	7.1	63.9	2.0	31.9
(928)5020.10_DolRomb	938	500	0.76	1.8917	1.2	6.4	19.5	2.9	0.6	3.1
(928)5020.10_DolRomb	642	5255	0.89	0.0052	1.2	0.6	2.2	2.3	0.8	0.6
(928)5020.10_DolRomb	664	2123	1.51	0.0012	1.3	1.3	9.0	1.3	0.8	1.2
(928)5020.10_DolRomb	625	2974	1.93	0.0019	1.4	1.0	8.3	1.7	0.7	1.2
(928)5020.10_DolRomb	648	2197	1.73	0.0026	1.3	1.1	10.1	1.7	0.8	1.4
(928)5020.10_DolRomb	697	1230	1.05	0.0070	1.3	1.6	11.3	3.2	0.7	1.7
(928)5020.10_DolRomb	639	2114	1.58	0.0055	1.4	1.3	9.6	1.8	0.7	1.2
(928)5020.10_DolRomb	607	2993	2.43	0.0037	1.4	1.0	10.4	1.1	0.7	1.0
(928)5020.10_DolRomb	661	1935	1.02	0.0315	1.3	1.3	6.7	1.5	0.7	1.2
(928)5020.10_DolRomb	628	4337	1.76	0.0026	1.3	0.9	5.7	3.8	0.8	0.9
(928)5020.10_DolRomb	634	1651	1.51	0.0031	1.4	1.5	11.7	1.6	0.7	1.4
(928)5020.10_DolRomb	641	2166	1.65	0.0015	1.3	1.2	9.9	1.7	0.7	1.2
(928)5020.10_DolSel	857	957	0.88	0.0162	1.0	2.0	11.3	3.3	0.8	2.0
(928)5020.10_DolSel	776	1574	0.82	0.1326	1.0	1.3	6.1	2.7	0.9	1.3
(928)5020.10_DolSel	737	1811	0.89	0.1057	1.1	1.3	5.9	3.0	0.9	1.2
(928)5020.10_DolSel	843	1389	0.72	0.0270	1.0	1.3	6.5	3.7	0.9	1.5
(928)5020.10_DolSel	1101	1463	-0.01	0.1434	1.0	12.6	-0.2	-196.2	0.9	2.1
(928)5020.10_DolSel	1089	756	0.90	0.0668	1.0	3.1	19.9	5.0	0.7	3.4
(928)5020.10_DolSel	1202	569	0.79	0.0943	0.9	2.8	20.8	5.2	0.7	3.6
(928)5020.10_DolSel	3304	306	-0.01	0.0751	0.4	12.1	-0.2	-1864.5	1.1	16.1
(928)5020.10_DolSel	1008	567	0.92	0.0401	1.0	3.3	20.6	3.5	0.7	2.6
(928)5020.10_DolSel	918	855	0.47	0.0096	0.9	2.0	6.4	2.9	0.8	1.6
(928)5020.10_DolSel	793	1231	0.64	0.0301	1.0	1.8	6.8	4.0	0.8	1.4
(928)5020.10_DolSel	699	3769	0.33	0.0238	1.1	1.0	1.1	5.0	0.9	0.8
(928)5020.10_DolSel	697	1436	2.12	0.0103	1.3	1.4	17.8	2.6	0.7	1.6
(928)5020.10_DolSel	723	1139	1.64	0.0113	1.3	2.2	17.8	2.7	0.7	1.7

Identificador	f206c	^{206}Pb	Uppm	Th/U	$^{206}Pb/^{204}Pb$	1s%	$^{238}U/^{206}Pb$	1s%	$^{207}Pb/^{206}Pb$	1s%
(928)5020.10_DolSel	682	1350	2.28	0.0054	1.4	1.6	21.6	3.0	0.6	2.0
(928)5020.10_DolSel	734	1020	1.34	0.0264	1.3	1.8	15.8	2.0	0.7	1.6
(928)5020.10_DolSel	624	1610	2.67	0.0154	1.5	1.4	20.4	2.5	0.6	1.5
(928)5020.10_DolSel	671	1780	2.53	0.0523	1.3	1.6	17.2	2.2	0.7	1.3
(928)5020.10_DolSel	684	1308	2.05	0.0040	1.3	1.5	19.7	2.7	0.7	1.5
(928)5020.10_DolSel	702	1612	1.25	0.1020	1.2	1.2	10.0	3.2	0.8	1.3
(928)5020.10_Peloid	652	1920	0.95	0.0013	1.3	1.2	6.7	2.6	0.8	1.2
(928)5020.10_Peloid	634	1565	1.83	0.0024	1.5	1.5	15.7	2.5	0.6	1.6
(928)5020.10_Peloid	561	3743	3.94	0.0039	1.7	1.7	14.3	3.1	0.6	1.5
(928)5020.10_Peloid	687	1700	0.73	0.0304	1.2	1.2	5.7	2.5	0.8	1.2
(928)5020.10_Peloid	632	1403	1.48	0.0042	1.5	1.6	14.0	1.5	0.6	1.5
(928)5020.10_Peloid	668	1549	1.08	0.0013	1.3	1.4	9.3	1.8	0.7	1.4
(928)5020.10_Peloid	627	1615	1.87	0.0140	1.5	1.5	15.6	1.9	0.6	1.4
(928)5020.10_Peloid	708	1254	0.32	0.0060	1.1	1.7	3.4	3.4	0.8	1.3
(928)5020.10_Peloid	654	1468	1.26	0.0010	1.4	1.4	11.4	1.9	0.7	1.5
(928)5020.10_Peloid	508	2737	4.56	0.0002	2.0	2.1	23.5	2.8	0.5	2.6
(928)5020.10_Peloid	698	1267	0.82	0.0078	1.2	1.2	9.1	2.5	0.8	1.5
(928)5020.10_Peloid	625	2125	1.61	0.0012	1.4	1.1	10.2	1.6	0.7	1.2
(928)5020.10_Peloid	645	1868	1.00	0.0009	1.3	1.5	7.5	2.7	0.8	1.4
(928)5020.10_Peloid	617	1408	1.74	0.0014	1.5	1.9	17.4	2.1	0.6	1.5
(928)5020.10_Peloid	736	1091	0.67	0.0040	1.2	1.9	8.3	2.2	0.8	1.4
(928)5020.10_Peloid	668	1531	0.63	0.0007	1.2	1.2	5.6	1.9	0.8	1.2
(928)5020.10_Peloid	606	1668	1.82	0.0006	1.5	1.6	15.0	1.8	0.6	1.5
(928)5020.10_Peloid	711	1181	0.54	0.0029	1.2	1.6	6.5	2.6	0.8	1.4
(928)5020.10_Peloid	699	1042	0.51	0.0008	1.2	1.8	6.7	2.4	0.8	1.5
(928)5020.10_Peloid	654	1342	1.20	0.0003	1.4	1.7	12.2	1.5	0.7	1.5
(SPH-6)5132.50_DolSel	983	887	0.11	0.0013	0.9	2.8	3.7	12.3	0.9	2.2
(SPH-6)5132.50_DolSel	2310	182	0.01	0.0065	0.5	5.3	-0.7	-124.3	0.9	5.6

Identificador	f206c	^{206}Pb	Uppm	Th/U	$^{206}Pb/^{204}Pb$	1s%	$^{238}U/^{206}Pb$	1s%	$^{207}Pb/^{206}Pb$	1s%
(SPH-6)5132.50_DolSel	960	826	0.02	0.0032	0.9	2.6	0.3	61.4	0.9	2.0
(SPH-6)5132.50_DolSel	633	4886	0.91	0.0003	1.3	0.6	2.6	1.5	0.8	0.6
(SPH-6)5132.50_DolSel	633	11573	1.50	0.0003	1.3	1.2	1.9	2.5	0.9	0.5
(SPH-6)5132.50_DolSel	699	1785	0.10	0.2424	1.2	1.2	0.8	7.1	0.8	1.0
(SPH-6)5132.50_DolSel	1150	367	0.26	0.0010	0.9	3.9	11.5	4.7	0.7	3.0
(SPH-6)5132.50_DolSel	1049	455	0.23	0.0035	0.9	3.2	8.4	5.5	0.7	2.4
(SPH-6)5132.50_DolSel	925	556	0.03	0.0103	0.9	2.6	0.8	28.0	0.9	2.2
(SPH-6)5132.50_DolSel	1213	284	0.20	0.0045	0.8	3.3	10.9	5.4	0.8	3.4
(SPH-6)5132.50_DolSel	-723	6	-0.01	0.1354	0.0	89.3	2.3	429.3	0.3	75.0
(SPH-6)5132.50_DolSel	2164	238	-0.01	0.0188	0.6	6.5	-1.6	-57.3	0.9	4.6
(SPH-6)5132.50_DolSel	936	441	0.05	0.1377	0.9	2.9	1.3	18.4	0.9	2.6
(SPH-6)5132.50_DolSel	819	583	0.05	0.1553	1.0	3.5	1.1	17.1	0.9	1.8
(SPH-6)5132.50_DolSel	822	754	0.03	0.0184	1.0	2.1	0.6	29.7	0.8	1.8
(SPH-6)5132.50_DolSel	709	1108	0.03	0.0391	1.1	1.7	0.4	24.5	0.9	1.4
(SPH-6)5132.50_DolSel	1160	401	0.27	0.0150	0.9	3.7	11.2	5.8	0.7	2.7
(SPH-6)5132.50_DolSel	1573	267	0.07	0.0239	0.7	4.2	3.9	13.5	0.9	4.0
(SPH-6)5132.50_DolSel	1155	269	0.30	0.3104	1.0	6.1	18.0	4.5	0.7	4.0
(SPH-6)5132.50_DolSel	3643	17	0.00	0.0856	0.1	22.7	-0.4	-1951.3	0.3	73.2
(SPH-6)5132.50_Peloid	480	3360	5.81	0.0003	2.2	1.4	25.6	2.1	0.5	1.7
(SPH-6)5132.50_Peloid	604	9792	1.91	0.0007	1.3	0.5	2.9	1.8	0.8	0.5
(SPH-6)5132.50_Peloid	580	6618	3.71	0.0004	1.5	0.6	8.2	1.2	0.7	0.5
(SPH-6)5132.50_Peloid	468	1534	2.98	0.0006	2.7	2.1	29.3	1.9	0.3	2.6
(SPH-6)5132.50_Peloid	489	3249	5.05	0.0025	2.1	1.6	24.0	2.2	0.5	1.8
(SPH-6)5132.50_Peloid	507	2171	3.94	0.0008	2.1	1.5	27.1	1.2	0.5	1.2
(SPH-6)5132.50_Peloid	413	3307	7.43	0.0003	2.8	1.5	33.3	1.4	0.4	1.7
(SPH-6)5132.50_Peloid	565	5525	4.06	0.0009	1.6	0.7	10.9	0.9	0.7	0.7
(SPH-6)5132.50_Peloid	595	7960	2.75	0.0025	1.4	0.5	5.1	1.0	0.8	0.5
(SPH-6)5132.50_Peloid	592	3641	1.86	0.0031	1.5	0.9	7.7	2.0	0.7	0.8

Identificador	f206c	^{206}Pb	Uppm	Th/U	$^{206}Pb/^{204}Pb$	1s%	$^{238}U/^{206}Pb$	1s%	$^{207}Pb/^{206}Pb$	1s%
(SPH-6)5132.50_Peloid	1156	255	0.20	0.2609	0.9	5.2	12.2	4.0	0.7	3.4
(SPH-6)5132.50_Peloid	577	4386	2.35	0.0022	1.5	1.2	8.6	2.9	0.7	1.0
(SPH-6)5132.50_Peloid	472	2554	4.75	0.0004	2.3	1.2	28.4	1.2	0.4	1.4
(SPH-6)5132.50_Peloid	501	2241	3.63	0.0005	2.1	1.1	24.5	1.1	0.5	1.0
(SPH-6)5132.50_Peloid	587	8960	3.37	0.0008	1.4	0.5	5.7	0.8	0.8	0.5
(SPH-6)5132.50_Peloid	540	1452	2.14	0.0122	2.0	1.7	22.4	1.1	0.5	1.8
(SPH-6)5132.50_Peloid	619	2652	0.86	0.0068	1.4	1.0	5.0	2.3	0.8	0.9
(SPH-6)5132.50_Peloid	514	2945	3.14	0.0052	1.9	1.6	16.7	2.0	0.5	1.6
(SPH-6)5132.50_Peloid	565	7077	3.82	0.0008	1.5	0.8	8.5	2.4	0.7	0.8
(SPH-6)5132.50_Peloid	519	2647	3.67	0.0013	2.0	1.6	21.7	2.9	0.5	2.0
Barstow	473	8498	192.12	0.0001	2.4	0.8	253.3	0.5	0.4	0.8
Barstow	491	7812	163.26	0.0001	2.3	0.7	235.8	0.7	0.4	0.7
Barstow	565	8882	132.41	0.0001	1.7	0.6	169.0	1.0	0.5	0.7
Barstow	450	10428	196.69	0.0000	2.4	0.6	227.2	0.6	0.4	0.7
Barstow	410	8201	173.52	0.0000	2.8	0.7	256.0	0.6	0.4	0.8
Barstow	428	8797	181.97	0.0001	2.7	0.6	250.6	0.4	0.4	0.7
Barstow	463	6963	114.47	0.0000	2.3	0.9	212.1	1.1	0.4	1.1
Barstow	442	7532	133.90	0.0000	2.5	0.8	229.3	0.6	0.4	0.9
Barstow	408	7958	157.70	0.0000	2.8	0.8	256.7	0.5	0.4	0.8
Barstow	352	6620	140.18	0.0000	3.6	1.1	288.9	0.7	0.3	1.2
Barstow	474	7082	107.36	0.0000	2.2	0.7	208.3	0.6	0.4	0.8
Barstow	404	7080	130.50	0.0000	2.9	0.8	253.6	0.6	0.4	1.0
Barstow	413	7445	119.54	0.0001	2.7	0.7	232.6	0.5	0.4	0.7
Barstow	466	7295	101.07	0.0000	2.3	0.7	200.7	0.7	0.4	0.8
Barstow	445	6451	97.84	0.0000	2.5	0.8	221.1	0.7	0.4	0.7
Barstow	389	7380	119.50	0.0001	3.0	0.7	247.1	0.6	0.3	0.9
Barstow	410	7640	115.77	0.0000	2.8	0.8	232.5	0.6	0.4	1.0
Barstow	401	7749	120.95	0.0000	2.9	0.7	239.6	0.5	0.4	0.8

Identificador	f206c	^{206}Pb	Uppm	Th/U	$^{206}Pb/^{204}Pb$	1s%	$^{238}U/^{206}Pb$	1s%	$^{207}Pb/^{206}Pb$	1s%
C_Walnut	288	2707	3.47	0.0003	5.6	1.8	30.1	5.8	0.1	8.4
C_Walnut	298	2784	3.21	0.0040	5.5	2.8	20.8	1.1	0.1	2.1
C_Walnut	248	3262	3.94	0.0030	6.5	2.3	20.9	1.4	0.1	1.9
C_Walnut	283	3136	3.49	0.0079	5.7	2.5	19.5	1.3	0.1	1.7
C_Walnut	250	4463	5.18	0.0028	7.0	3.3	21.7	1.3	0.1	3.6
C_Walnut	204	4127	5.16	0.0106	8.1	1.9	21.5	1.2	0.1	1.8
C_Walnut	209	4428	5.35	0.0078	7.8	2.1	20.7	1.0	0.1	1.7
C_Walnut	200	4226	5.36	0.0037	8.2	2.1	21.7	1.2	0.1	1.9
C_Walnut	237	2560	3.20	0.0008	7.0	2.7	21.6	1.2	0.1	2.2
C_Walnut	298	2138	2.57	0.0054	5.1	2.4	19.6	1.2	0.2	2.3
C_Walnut	242	2982	3.59	0.0046	6.5	1.8	20.9	1.3	0.2	1.7
C_Walnut	195	3552	4.67	0.1212	8.5	2.1	21.6	1.3	0.1	1.6
C_Walnut	267	2400	3.01	0.0045	5.8	2.6	20.2	1.2	0.2	2.4
C_Walnut	234	2829	3.70	0.0018	6.9	2.2	22.2	1.2	0.1	1.7
C_Walnut	264	2948	3.62	0.0010	5.8	2.3	20.3	1.2	0.2	1.7
C_Walnut	216	3578	4.50	0.0005	7.3	2.0	20.7	1.1	0.1	1.6
C_Walnut	281	2979	3.57	0.0011	5.4	2.3	19.4	1.2	0.2	2.2
C_Walnut	245	3050	3.86	0.0267	6.3	2.4	20.3	1.2	0.2	1.6
C_Walnut	174	3661	5.42	0.0005	9.9	2.4	23.2	1.2	0.1	1.9
C_Walnut	227	3394	4.35	0.0023	7.0	2.2	20.2	1.1	0.1	2.0
C_Walnut	255	2469	3.57	0.0001	6.3	2.1	22.9	1.2	0.1	1.9
C_Walnut	242	3088	4.00	0.0000	6.3	1.9	20.4	1.1	0.2	1.8
C_Walnut	279	2228	2.96	0.0000	5.7	3.3	19.7	1.3	0.2	2.0
C_Walnut	245	2483	3.42	0.0002	6.5	2.7	20.0	1.5	0.2	2.2
C_Walnut	243	2652	3.68	0.0036	6.5	2.4	20.9	1.7	0.1	2.8
C_Walnut	202	3332	4.80	0.0003	8.0	2.1	21.4	1.1	0.1	1.8
C_Walnut	203	3205	4.60	0.0010	8.1	2.5	21.1	1.1	0.1	1.6

Identificador	f206c	^{206}Pb	Uppm	Th/U	$^{206}Pb/^{204}Pb$	1s%	$^{238}U/^{206}Pb$	1s%	$^{207}Pb/^{206}Pb$	1s%
C_Walnut	264	2292	3.17	0.0013	6.1	2.9	21.0	1.3	0.1	2.1
(923A)5090.95_DolBloc	2120	155	0.14	1.2194	0.6	7.1	19.5	6.8	0.7	7.0
(923A)5090.95_DolBloc	1869	195	0.14	0.0461	0.6	4.7	13.6	5.9	0.6	4.3
(923A)5090.95_DolBloc	2244	153	0.11	0.0638	0.5	6.0	15.2	7.3	0.7	6.4
(923A)5090.95_DolBloc	3280	99	0.12	0.0500	0.4	6.2	26.3	7.9	0.6	10.9
(923A)5090.95_DolBloc	2745	107	0.11	2.1402	0.4	9.6	26.5	8.7	0.7	13.9
(923A)5090.95_DolBloc	2222	160	0.04	0.0829	0.5	4.6	4.9	20.4	0.8	5.4
(923A)5090.95_DolBloc	2106	164	0.14	0.3818	0.5	6.1	16.6	6.0	0.7	5.7
(923A)5090.95_DolBloc	1242	268	0.12	0.0669	0.7	3.3	8.1	6.8	0.8	3.6
(923A)5090.95_DolBloc	1774	200	0.07	0.1919	0.5	4.5	7.0	13.2	0.9	5.8
(923A)5090.95_DolBloc	2195	127	0.04	0.2057	0.5	5.1	6.0	19.3	0.8	8.8
(923A)5090.95_DolBloc	1443	220	0.09	0.2529	0.7	6.7	7.1	8.7	0.8	4.8
(923A)5090.95_DolBloc	4352	90	0.13	0.0880	0.4	6.2	33.1	10.6	0.5	17.5
(923A)5090.95_DolBloc	3027	128	0.09	0.2782	0.5	6.5	20.8	13.2	0.9	14.3
(923A)5090.95_DolBloc	3438	89	0.10	0.0426	0.5	14.0	25.4	11.8	0.8	12.3
(923A)5090.95_DolBloc	1079	409	0.07	0.2956	0.8	2.5	2.9	9.5	0.8	2.7
(923A)5090.95_DolBloc	1165	397	0.08	0.0857	0.8	3.2	3.7	8.4	0.8	3.1
(923A)5090.95_DolBloc	1635	218	0.07	0.1256	0.6	4.7	7.1	10.5	0.8	4.4
(923A)5090.95_DolBloc	3126	113	0.02	0.0648	0.4	5.4	4.3	29.7	0.9	8.3
(923A)5090.95_DolBloc	1941	164	0.04	0.1084	0.6	5.4	4.8	17.1	0.8	5.7
(923A)5090.95_DolBloc	2198	127	0.05	0.1238	0.5	5.6	7.8	15.1	0.8	8.0
(923A)5090.95_DolRomb	744	686	0.84	0.0029	1.5	3.6	20.6	3.0	0.5	2.8
(923A)5090.95_DolRomb	867	454	0.98	0.0005	1.5	4.2	34.6	1.8	0.3	4.9
(923A)5090.95_DolRomb	592	721	1.75	0.0009	2.5	3.3	39.2	1.2	0.2	3.8
(923A)5090.95_DolRomb	589	978	1.54	0.0013	2.0	2.7	28.5	3.7	0.4	3.4
(923A)5090.95_DolRomb	591	2522	1.22	0.0013	1.6	1.8	10.5	4.9	0.6	2.1
(923A)5090.95_DolRomb	605	1089	1.14	0.0007	1.6	2.0	16.7	2.2	0.6	1.6

Identificador	f206c	^{206}Pb	Uppm	Th/U	$^{206}Pb/^{204}Pb$	1s%	$^{238}U/^{206}Pb$	1s%	$^{207}Pb/^{206}Pb$	1s%
(923A)5090.95_DolRomb	799	499	0.91	0.0010	1.6	4.0	32.2	2.2	0.4	3.8
(923A)5090.95_DolRomb	743	536	0.84	0.0013	1.7	4.0	25.9	2.7	0.4	3.6
(923A)5090.95_DolRomb	689	687	0.95	0.0014	1.6	2.5	22.3	1.9	0.5	2.4
(923A)5090.95_DolRomb	636	1301	0.85	0.0009	1.5	5.8	11.4	2.7	0.7	1.8
(923A)5090.95_DolRomb	658	1363	0.47	0.0006	1.3	1.9	5.7	3.6	0.7	1.4
(923A)5090.95_DolRomb	627	10019	0.82	0.0010	1.3	0.6	1.6	7.9	0.8	0.7
(923A)5090.95_DolRomb	756	591	1.21	0.0012	1.7	4.4	33.3	1.7	0.3	3.6
(923A)5090.95_DolRomb	689	935	0.95	0.0015	1.4	1.6	16.9	3.1	0.6	2.3
(923A)5090.95_DolRomb	637	9900	0.85	0.0003	1.3	0.8	1.4	6.7	0.8	0.9
(923A)5090.95_DolRomb	709	1061	0.50	0.0003	1.3	2.0	8.5	3.9	0.7	1.5
(923A)5090.95_DolRomb	695	731	0.90	0.0006	1.6	3.6	20.3	3.0	0.5	2.6
(923A)5090.95_DolRomb	869	417	0.53	0.0013	1.3	6.6	21.4	2.4	0.5	3.1
(923A)5090.95_DolRomb	831	443	0.74	0.0005	1.5	3.1	28.0	2.2	0.4	4.1
(923A)5090.95_DolRomb	765	466	0.97	0.0032	1.7	4.0	33.4	2.0	0.4	3.3
(923A)5090.95_Esf	1018	377	0.38	0.0005	1.1	3.4	17.0	2.9	0.6	2.8
(923A)5090.95_Esf	734	564	0.46	0.1170	1.3	3.0	13.7	3.0	0.7	2.3
(923A)5090.95_Esf	1450	235	0.48	0.0005	1.0	6.4	33.8	3.1	0.4	5.7
(923A)5090.95_Esf	1013	362	0.43	0.0004	1.1	3.9	20.5	3.4	0.6	3.3
(923A)5090.95_Esf	874	501	0.40	0.0010	1.1	2.5	12.9	2.8	0.7	2.2
(923A)5090.95_Esf	1367	240	0.39	0.0043	1.1	6.4	25.8	3.1	0.4	5.3
(923A)5090.95_Esf	822	648	0.31	0.0032	1.1	2.3	8.3	3.8	0.7	1.9
(923A)5090.95_Esf	977	374	0.41	0.0057	1.1	3.2	17.9	3.4	0.6	3.7
(923A)5090.95_Esf	1161	257	0.45	0.0024	1.0	4.1	28.4	3.1	0.5	3.8
(923A)5090.95_Esf	1384	221	0.28	0.0046	0.8	4.6	22.5	4.3	0.6	3.6
(923A)5090.95_Esf	752	749	0.30	0.0554	1.1	1.9	6.5	2.9	0.8	1.7
(923A)5090.95_Esf	850	518	0.42	0.0017	1.1	3.0	13.0	2.7	0.7	2.1
(923A)5090.95_Esf	1057	297	0.53	0.0232	1.2	4.8	29.6	2.9	0.5	4.2

Identificador	f206c	^{206}Pb	Uppm	Th/U	$^{206}Pb/^{204}Pb$	1s%	$^{238}U/^{206}Pb$	1s%	$^{207}Pb/^{206}Pb$	1s%
(923A)5090.95_Esf	973	325	0.27	0.0205	1.0	3.8	13.4	3.9	0.7	3.0
(923A)5090.95_Esf	825	586	0.22	0.0130	1.1	2.6	6.2	4.7	0.8	2.0
(923A)5090.95_Esf	517	5441	1.50	0.0008	1.8	0.7	4.4	1.3	0.6	0.7
(923A)5090.95_Esf	595	4191	0.31	0.0035	1.4	1.0	1.4	4.6	0.8	1.0
(923A)5090.95_Esf	793	536	0.43	0.0026	1.2	2.6	12.7	3.1	0.6	2.8
(923A)5090.95_Esf	1007	335	0.52	0.0181	1.2	3.9	26.5	3.5	0.5	4.0
(923A)5090.95_Esf	975	342	0.54	0.0120	1.3	5.2	25.5	2.5	0.4	3.8
(923A)5099.05_CalcPart	694	2783	0.20	0.0598	1.2	0.9	1.3	2.6	0.8	0.8
(923A)5099.05_CalcPart	682	3596	0.19	0.0661	1.2	0.7	1.0	3.4	0.8	0.7
(923A)5099.05_CalcPart	719	1934	0.38	0.2324	1.1	1.2	3.5	1.9	0.8	1.0
(923A)5099.05_CalcPart	725	1621	0.59	0.0445	1.2	1.4	6.8	1.7	0.8	1.2
(923A)5099.05_CalcPart	687	2072	0.66	0.0045	1.2	1.1	5.7	1.3	0.8	1.0
(923A)5099.05_CalcPart	695	1917	0.25	0.0410	1.2	1.0	2.3	2.7	0.8	1.2
(923A)5099.05_CalcPart	828	687	0.22	0.0406	1.0	2.6	5.9	3.7	0.8	2.0
(923A)5099.05_CalcPart	732	1133	0.49	0.0085	1.1	1.6	7.8	1.8	0.8	1.5
(923A)5099.05_CalcPart	690	1638	0.47	0.0800	1.2	1.1	5.3	1.9	0.8	1.1
(923A)5099.05_CalcPart	565	4820	6.14	0.0022	1.7	1.2	26.6	3.0	0.6	1.6
(923A)5099.05_CalcPart	1126	438	0.15	0.0557	0.8	3.6	6.5	4.9	0.8	2.6
(923A)5099.05_CalcPart	790	727	0.25	0.0225	1.1	2.4	6.3	3.5	0.8	1.9
(923A)5099.05_CalcPart	688	1492	0.41	0.0216	1.2	1.5	5.0	2.1	0.8	1.3
(923A)5099.05_CalcPart	756	883	0.33	0.1750	1.1	2.1	6.8	2.7	0.8	1.7
(923A)5099.05_CalcPart	679	2191	0.11	0.0838	1.2	1.0	0.9	7.1	0.8	1.0
(923A)5099.05_CalcPart	688	1682	0.26	0.0501	1.2	1.4	2.8	2.4	0.8	1.0
(923A)5099.05_CalcPart	819	736	0.23	0.0362	1.0	2.1	5.9	3.5	0.8	1.8
(923A)5099.05_CalcPart	1666	294	0.10	0.1037	0.7	4.5	7.0	9.9	0.8	4.1
(923A)5099.05_CalcPart	699	1603	0.42	0.0209	1.2	1.4	4.8	2.3	0.8	1.1
(923A)5099.05_CalcPart	659	2358	0.21	0.0608	1.2	1.0	1.6	4.0	0.8	0.9

Identificador	f206c	^{206}Pb	Uppm	Th/U	$^{206}Pb/^{204}Pb$	1s%	$^{238}U/^{206}Pb$	1s%	$^{207}Pb/^{206}Pb$	1s%
(923A)5099.05_DolInt	651	2708	0.26	0.0661	1.2	0.9	1.7	2.7	0.8	0.9
(923A)5099.05_DolInt	668	2890	0.09	0.1401	1.2	0.9	0.5	6.6	0.8	0.8
(923A)5099.05_DolInt	671	1956	0.08	0.0348	1.2	1.2	0.7	7.5	0.9	0.9
(923A)5099.05_DolInt	624	8589	0.32	0.0130	1.3	0.5	0.7	2.6	0.9	0.4
(923A)5099.05_DolInt	664	2359	0.16	0.1098	1.2	1.0	1.2	4.3	0.9	1.0
(923A)5099.05_DolInt	685	1998	0.27	0.0342	1.2	1.1	2.4	2.4	0.8	1.0
(923A)5099.05_DolInt	673	1524	0.35	0.0289	1.2	1.3	4.0	2.1	0.8	1.1
(923A)5099.05_DolInt	627	2766	0.42	1.9519	1.3	1.0	2.6	2.3	0.8	0.8
(923A)5099.05_DolInt	670	2050	0.17	0.0589	1.2	1.1	1.4	3.9	0.9	0.9
(923A)5099.05_DolInt	645	3312	0.57	1.8299	1.3	0.9	2.9	1.8	0.8	0.7
(923A)5099.05_DolInt	669	2429	0.46	0.0254	1.2	1.2	3.2	2.5	0.8	0.9
(923A)5099.05_DolInt	649	2895	0.40	0.0064	1.3	0.8	2.3	1.9	0.8	0.8
(923A)5099.05_DolInt	651	2795	0.30	0.0625	1.2	0.8	1.8	2.6	0.8	0.9
(923A)5099.05_DolInt	664	2393	0.24	0.0340	1.2	0.9	1.8	3.5	0.8	0.8
(923A)5099.05_DolInt	636	3530	0.87	0.0177	1.3	0.8	3.5	6.0	0.8	0.7
(923A)5099.05_DolInt	647	2688	0.22	0.0488	1.2	0.8	1.4	3.2	0.8	0.8
(923A)5099.05_DolInt	659	2168	0.17	0.0754	1.2	1.0	1.4	3.7	0.8	0.9
(923A)5099.05_DolInt	644	2609	0.30	0.0237	1.3	0.9	2.0	2.4	0.8	0.8
(923A)5099.05_DolInt	646	2344	0.27	0.0082	1.3	0.9	2.0	2.6	0.8	0.8
(923A)5099.05_DolInt	644	2634	0.28	0.0188	1.3	0.9	1.8	2.8	0.8	0.8
(SPH-6)5118.95_DolRomb	596	3534	2.07	0.0017	1.4	0.8	9.7	1.0	0.7	0.7
(SPH-6)5118.95_DolRomb	586	2517	1.68	0.0012	1.5	1.1	11.4	2.0	0.7	1.0
(SPH-6)5118.95_DolRomb	579	5688	2.47	0.0005	1.5	0.7	7.3	1.4	0.8	0.5
(SPH-6)5118.95_DolRomb	560	3944	2.78	0.0074	1.6	0.8	11.8	1.1	0.7	0.7
(SPH-6)5118.95_DolRomb	592	2412	1.61	0.0067	1.5	1.0	10.9	0.9	0.7	1.1
(SPH-6)5118.95_DolRomb	590	4472	2.02	0.0011	1.4	0.7	7.4	1.5	0.7	0.7
(SPH-6)5118.95_DolRomb	586	4470	2.11	0.0114	1.5	0.7	7.8	1.5	0.7	0.7

Identificador	f206c	^{206}Pb	Uppm	Th/U	$^{206}Pb/^{204}Pb$	1s%	$^{238}U/^{206}Pb$	1s%	$^{207}Pb/^{206}Pb$	1s%
(SPH-6)5118.95_DolRomb	579	2758	2.22	0.0004	1.5	0.9	13.2	1.3	0.7	0.9
(SPH-6)5118.95_DolRomb	581	5893	2.52	0.0020	1.5	0.6	7.0	0.8	0.7	0.6
(SPH-6)5118.95_DolRomb	577	5677	2.80	0.0021	1.5	0.7	8.2	1.4	0.7	0.7
(SPH-6)5118.95_DolRomb	578	7982	3.49	0.0004	1.5	0.8	6.6	1.3	0.7	0.7
(SPH-6)5118.95_DolRomb	583	5480	2.23	0.0021	1.4	0.6	6.7	1.3	0.8	0.7
(SPH-6)5118.95_DolRomb	596	3689	2.01	0.0008	1.4	0.9	8.6	1.2	0.7	0.9
(SPH-6)5118.95_DolRomb	586	3199	2.07	0.0006	1.5	0.9	10.7	1.2	0.7	0.8
(SPH-6)5118.95_DolRomb	578	4471	2.60	0.0004	1.5	0.7	9.5	0.7	0.7	0.8
(SPH-6)5118.95_DolRomb	583	2515	1.73	0.0005	1.5	1.0	11.1	1.4	0.7	1.0
(SPH-6)5118.95_DolRomb	590	2745	1.82	0.0004	1.5	0.9	10.9	1.0	0.7	0.9
(SPH-6)5118.95_DolRomb	592	3072	1.73	0.0173	1.5	1.1	9.1	1.1	0.7	0.8
(SPH-6)5118.95_DolRomb	581	3768	2.20	0.0148	1.5	0.8	9.5	1.3	0.7	0.7
(SPH-6)5118.95_DolRomb	583	5973	2.78	0.0024	1.4	0.7	7.7	1.7	0.8	0.6
(SPH-6)5118.95_Shrub	705	761	0.91	0.0369	1.5	2.2	20.4	1.8	0.5	2.2
(SPH-6)5118.95_Shrub	710	852	0.88	0.0053	1.3	1.9	17.9	1.6	0.6	1.9
(SPH-6)5118.95_Shrub	696	891	0.88	0.0055	1.4	2.1	16.9	1.6	0.6	1.5
(SPH-6)5118.95_Shrub	703	771	0.92	0.0036	1.4	2.3	20.4	1.5	0.6	2.0
(SPH-6)5118.95_Shrub	770	765	0.80	0.0042	1.3	1.9	17.6	1.5	0.6	2.1
(SPH-6)5118.95_Shrub	711	813	0.91	0.0048	1.4	2.1	19.0	1.7	0.6	1.7
(SPH-6)5118.95_Shrub	650	1314	0.97	0.0014	1.4	1.5	12.5	1.9	0.7	1.5
(SPH-6)5118.95_Shrub	685	835	0.91	0.0128	1.4	2.0	18.7	1.6	0.6	1.8
(SPH-6)5118.95_Shrub	659	918	1.22	0.0049	1.5	2.0	22.7	1.4	0.5	1.7
(SPH-6)5118.95_Shrub	719	858	0.88	0.0251	1.3	2.2	17.7	1.6	0.6	1.9
(SPH-6)5118.95_Shrub	664	909	1.17	0.0042	1.5	2.1	22.3	1.6	0.6	1.8
(SPH-6)5118.95_Shrub	617	979	1.79	0.0013	1.8	2.1	30.9	1.4	0.4	1.9
(SPH-6)5118.95_Shrub	679	1087	0.97	0.0021	1.4	1.8	15.2	1.4	0.7	1.5
(SPH-6)5118.95_Shrub	650	1220	1.12	0.0009	1.4	1.6	15.5	1.2	0.6	1.3

Identificador	f206c	^{206}Pb	Uppm	Th/U	$^{206}Pb/^{204}Pb$	1s%	$^{238}U/^{206}Pb$	1s%	$^{207}Pb/^{206}Pb$	1s%
(SPH-6)5118.95_Shrub	628	1425	1.37	0.0015	1.5	1.3	16.2	1.5	0.6	1.2
(SPH-6)5118.95_Shrub	627	1653	1.42	0.0051	1.5	1.4	14.0	1.4	0.7	1.3
(SPH-6)5118.95_Shrub	642	1242	1.10	0.0026	1.5	1.9	14.9	1.2	0.6	1.4
(SPH-6)5118.95_Shrub	641	1010	1.55	0.0010	1.7	2.0	26.0	1.3	0.5	2.0
(SPH-6)5118.95_Shrub	689	933	1.15	0.0050	1.4	1.8	20.9	1.4	0.5	1.5
(SPH-6)5118.95_Shrub	702	789	1.21	0.0033	1.5	2.4	25.9	1.6	0.5	2.1
Barstow	540	8672	96.63	0.0001	2.0	0.6	193.0	1.1	0.4	0.7
Barstow	395	9277	147.15	0.0000	3.2	0.7	277.3	1.2	0.3	0.8
Barstow	440	10237	140.82	0.0001	2.7	0.7	239.9	1.0	0.3	1.0
Barstow	414	8480	122.59	0.0001	2.9	0.8	247.4	1.1	0.3	1.0
Barstow	473	11062	133.33	0.0001	2.3	0.7	208.3	0.6	0.4	0.7
Barstow	488	11057	124.54	0.0001	2.1	0.5	192.6	1.3	0.5	0.6
Barstow	406	8227	115.33	0.0002	2.8	0.8	235.5	1.5	0.4	0.8
Barstow	402	6138	97.00	0.0001	3.0	0.8	264.7	1.4	0.3	1.0
Barstow	381	5711	93.30	0.0002	3.3	0.8	272.9	1.0	0.3	1.1
Barstow	415	7352	106.26	0.0001	2.8	0.8	235.7	0.9	0.4	1.0
Barstow	360	6325	104.88	0.0001	3.5	1.3	272.1	1.3	0.3	1.9
Barstow	515	6483	61.23	0.0001	1.9	0.7	154.5	1.1	0.5	0.7
Barstow	382	5972	100.73	0.0000	3.2	0.9	269.8	1.2	0.3	0.9
Barstow	362	8232	136.03	0.0000	3.3	0.8	263.8	1.0	0.3	0.7
Barstow	422	8447	113.97	0.0000	2.6	0.8	215.1	0.9	0.4	0.8
Barstow	402	7063	107.82	0.0000	2.9	0.6	237.2	1.1	0.4	0.9
Barstow	332	7303	132.05	0.0000	3.8	0.9	281.4	1.0	0.3	1.2
Barstow	481	6877	80.37	0.0000	2.1	0.6	182.4	1.3	0.5	0.7
Barstow	409	7781	116.48	0.0000	2.7	0.6	228.0	1.2	0.4	0.8
Barstow	398	8743	127.39	0.0000	2.8	0.7	221.6	1.1	0.4	0.7
Barstow	457	6719	89.25	0.0000	2.4	0.8	201.8	1.4	0.4	0.9

Identificador	f206c	^{206}Pb	Uppm	Th/U	$^{206}Pb/^{204}Pb$	1s%	$^{238}U/^{206}Pb$	1s%	$^{207}Pb/^{206}Pb$	1s%
Barstow	387	5695	97.49	0.0000	3.0	0.8	253.6	1.3	0.3	0.9
Barstow	454	7105	97.29	0.0000	2.3	0.7	202.7	1.3	0.4	0.7
Barstow	510	4556	48.85	0.0000	1.9	0.8	158.4	0.9	0.5	0.8

Identificador	f206c	^{206}Pb	Uppm	Th/U	$^{206}Pb/^{204}Pb$	1s%	$^{238}U/^{206}Pb$	1s%	$^{207}Pb/^{206}Pb$	1s%
C_Walnut	182	13448	5.0	0.00560	8.3	1.0	20.9	0.5	0.1	0.9
C_Walnut	194	12580	4.6	0.00128	7.7	1.1	20.4	0.5	0.2	1.0
C_Walnut	222	11757	4.0	0.00081	6.5	1.8	19.4	1.1	0.2	2.1
C_Walnut	190	13427	5.0	0.00079	7.8	1.3	20.6	0.7	0.2	1.0
C_Walnut	176	12571	4.8	0.00017	8.6	1.0	21.2	0.4	0.2	0.7
C_Walnut	182	5990	2.4	0.00042	8.3	1.5	20.6	0.5	0.2	1.0
C_Walnut	143	8425	3.6	0.00039	11.2	1.6	21.6	0.5	0.1	1.0
C_Walnut	174	9745	3.7	0.00030	8.3	1.1	18.7	0.8	0.2	0.9
C_Walnut	151	6051	2.9	0.00087	10.3	1.5	21.5	0.5	0.1	1.2
C_Walnut	142	7106	3.5	0.00036	11.2	1.5	21.9	0.5	0.1	1.2
C_Walnut	156	5690	2.7	0.00012	10.1	1.7	20.7	0.5	0.1	1.2
C_Walnut	138	6086	3.7	0.00002	11.7	3.2	23.4	0.7	0.1	1.4
C_Walnut	152	6535	3.7	0.00000	10.1	1.8	21.8	0.5	0.2	1.3
C_Walnut	147	7067	3.7	0.00001	10.4	1.5	20.0	0.5	0.2	1.0
C_Walnut	161	6335	4.1	0.00096	9.3	1.7	21.3	0.6	0.2	1.0
C_Walnut	157	7560	4.5	0.00015	9.2	1.4	19.6	0.6	0.2	0.9
C_Walnut	180	5677	3.5	0.00213	8.1	1.3	20.3	0.5	0.2	1.0
C_Walnut	157	6466	4.2	0.00039	9.5	1.5	21.0	0.5	0.2	1.0
C_Walnut	172	5511	3.5	0.00141	8.5	1.5	20.6	0.6	0.2	1.1
(928)5016.90_DolLamtTDS	514	3022	1.4	0.00032	2.0	1.3	26.5	1.7	0.5	1.3
(928)5016.90_DolLamtTDS	754	1222	0.6	0.00250	1.4	2.2	28.8	1.9	0.5	1.9
(928)5016.90_DolLamtTDS	849	884	0.5	0.00274	1.3	2.7	30.2	2.0	0.5	2.4
(928)5016.90_DolLamtTDS	565	2803	0.6	0.00363	1.6	1.4	14.6	3.4	0.7	1.2
(928)5016.90_DolLamtTDS	509	4332	0.6	0.00336	1.7	1.1	8.0	3.6	0.7	1.0
(928)5016.90_DolLamtTDS	823	885	0.4	0.02136	1.2	2.7	24.3	2.1	0.6	2.1
(928)5016.90_DolLamtTDS	651	1382	0.6	0.00729	1.6	2.0	26.8	3.0	0.5	2.0
(928)5016.90_DolLamtTDS	473	2914	1.0	0.00088	2.0	1.2	19.7	2.3	0.6	1.3
(928)5016.90_DolLamtTDS	426	2816	1.6	0.00027	2.6	1.4	31.4	1.7	0.4	1.5

Identificador	f206c	^{206}Pb	Uppm	Th/U	$^{206}Pb/^{204}Pb$	1s%	$^{238}U/^{206}Pb$	1s%	$^{207}Pb/^{206}Pb$	1s%
(928)5016.90_DolLamtTDS	528	1936	0.8	0.00124	1.9	1.6	23.4	2.5	0.5	1.6
(928)5016.90_DolLamtTDS	434	2458	1.4	0.12559	2.5	1.6	29.6	1.0	0.4	1.5
(928)5016.90_DolLamtTDS	407	3182	1.5	0.00209	2.6	1.5	26.5	2.1	0.5	1.4
(928)5016.90_DolLamtTDS	421	2603	1.5	0.00029	2.6	1.3	30.2	1.1	0.4	1.3
(928)5016.90_DolLamtTDS	396	2887	1.8	0.00104	2.9	1.3	32.7	1.0	0.4	1.5
(928)5016.90_DolLamtTDS	378	3673	2.0	0.00060	2.9	1.3	29.4	1.3	0.4	1.2
(928)5016.90_DolLamtTDS	383	2867	1.7	0.00032	2.9	1.3	30.9	0.9	0.4	1.4
(928)5016.90_DolLamtTDS	400	3219	1.5	0.00039	2.6	1.2	24.9	1.7	0.5	1.2
(928)5016.90_DolLamtTDS	411	1976	1.2	0.00176	2.8	1.7	32.0	1.2	0.4	1.6
(928)5016.90_DolLamtTDS	426	3571	1.4	0.00357	2.4	1.3	27.3	3.7	0.5	2.1
(928)5016.90_DolLamtTDS	372	2651	1.6	0.00039	3.0	1.4	31.1	0.9	0.4	1.4
(928)5016.90_DolLamtTDS	364	6545	2.1	0.00040	2.7	1.0	16.1	1.9	0.5	1.0
(928)5016.90_DolLamtTDS	374	7914	2.1	0.00045	2.5	1.0	13.9	3.1	0.6	1.3
(928)5016.90_DolLamtTDS	366	3645	2.1	0.00035	2.9	1.5	27.9	1.3	0.4	1.3
(928)5016.90_DolLamtTDS	362	8580	2.6	0.00050	2.6	1.0	15.2	2.8	0.6	1.1
(928)5016.90_DolLamtTDS	365	3684	2.0	0.00042	2.9	1.2	27.1	1.9	0.5	1.5
(928)5016.90_DolLamtTDS	406	3796	1.5	0.00351	2.4	1.3	21.2	3.1	0.6	1.6
(928)5016.90_DolLamtTDS	379	3692	1.8	0.00033	2.7	1.3	23.7	1.3	0.5	1.4
(928)5016.90_DolLamtTDS	358	3024	1.9	0.00031	3.1	1.5	30.3	1.2	0.4	1.7
(928)5016.90_DolLamtTDS	342	5360	2.8	0.00030	3.0	1.2	25.0	2.1	0.5	1.3
(928)5016.90_DolLamtTDS	337	5123	2.8	0.00039	3.1	1.2	25.5	1.5	0.5	1.5
(928)5016.90_DolLamtTDS	406	3472	1.4	0.00043	2.3	1.3	18.7	1.9	0.6	1.1
(928)5016.90_DolLamtTDS	388	4130	1.8	0.00024	2.5	1.1	20.5	1.9	0.6	1.0
(928)5016.90_DolLamtTDS	392	8567	1.5	0.00042	2.2	0.8	8.6	3.1	0.7	0.8
(928)5016.90_DolLamtTDS	398	3939	1.5	0.00041	2.4	1.1	19.4	3.3	0.6	1.1
(928)5016.90_DolLamtTDS	395	3053	1.3	0.00076	2.5	2.2	19.7	1.5	0.6	1.1
(928)5016.90_DolLamtTDS	404	2980	1.4	0.00031	2.4	1.2	22.5	1.6	0.6	1.1
(928)5016.90_DolLamtTDS	407	9894	1.1	0.00035	2.1	0.5	7.1	4.6	0.8	0.6

Identificador	f206c	^{206}Pb	Uppm	Th/U	$^{206}Pb/^{204}Pb$	1s%	$^{238}U/^{206}Pb$	1s%	$^{207}Pb/^{206}Pb$	1s%
(928)5016.90_DolLamtTDS	399	3345	1.2	0.00032	2.3	1.1	17.4	1.6	0.6	0.9
(928)5016.90_DolLamtTDS	433	3645	0.9	0.00075	2.1	2.7	12.9	2.9	0.7	0.9
(928)5016.90_DolLamtTDS	409	3915	0.9	0.00073	2.2	1.0	10.7	1.5	0.6	0.8
(928)5133.95_Shrub	338	2936	2.1	0.00005	3.1	1.5	27.6	1.4	0.5	1.3
(928)5133.95_Shrub	360	3139	1.7	0.00009	2.7	1.4	20.1	1.2	0.6	1.1
(928)5133.95_Shrub	370	2445	1.5	0.00011	2.7	1.4	23.9	1.1	0.5	1.3
(928)5133.95_Shrub	337	1851	1.9	0.00008	3.7	2.9	38.8	1.3	0.3	2.8
(928)5133.95_Shrub	424	1354	1.4	0.00033	2.9	2.5	39.3	1.6	0.3	2.7
(928)5133.95_Shrub	364	2005	1.8	0.00014	3.1	1.7	33.3	1.4	0.4	1.8
(928)5133.95_Shrub	435	1384	1.4	0.00018	2.8	2.2	36.9	1.6	0.4	3.1
(928)5133.95_Shrub	382	2265	1.4	0.01200	2.8	1.6	27.3	4.0	0.4	2.1
(928)5133.95_Shrub	379	1558	1.6	0.00011	3.2	2.3	38.3	1.7	0.4	2.9
(928)5133.95_Shrub	351	1908	2.3	0.00014	3.7	2.6	42.9	1.2	0.3	2.9
(928)5133.95_Shrub	405	1511	1.8	0.00020	3.2	2.3	42.7	1.6	0.3	3.0
(928)5133.95_Shrub	360	2134	2.2	0.00024	3.2	1.9	35.3	1.0	0.4	1.8
(928)5133.95_Shrub	344	2062	2.3	0.00025	3.6	1.9	39.6	1.2	0.3	2.3
(928)5133.95_Shrub	330	2715	2.5	0.00023	3.4	1.7	32.7	1.3	0.4	1.4
(928)5133.95_Shrub	401	1937	1.4	0.00037	2.5	1.4	25.2	1.2	0.6	1.2
(928)5133.95_Shrub	352	2356	2.1	0.00022	3.1	1.5	31.2	1.6	0.4	1.9
(928)5133.95_Shrub	375	4004	1.7	0.00031	2.4	1.0	14.4	1.4	0.7	0.9
(928)5133.95_Shrub	373	4950	1.7	0.00037	2.3	0.8	11.7	1.2	0.7	0.7
(928)5133.95_Shrub	381	3061	1.5	0.00054	2.4	1.0	16.5	0.9	0.6	0.7
(928)5133.95_Shrub	396	2122	1.5	0.00044	2.5	1.5	24.5	1.2	0.6	1.4
Barstow	457	17744	43.5	0.00018	2.1	0.4	136.0	0.6	0.6	0.4
Barstow	440	15610	46.4	0.00014	2.3	0.5	163.3	0.7	0.5	0.5
Barstow	375	16291	65.9	0.00011	2.9	0.6	220.2	0.6	0.4	0.4
Barstow	361	11447	39.1	0.00013	2.8	0.6	169.5	0.6	0.5	0.5
Barstow	378	10336	36.8	0.00010	2.7	0.5	176.7	0.8	0.5	0.7

Identificador	f206c	^{206}Pb	Uppm	Th/U	$^{206}Pb/^{204}Pb$	1s%	$^{238}U/^{206}Pb$	1s%	$^{207}Pb/^{206}Pb$	1s%
Barstow	381	10476	33.5	0.00011	2.6	0.6	158.4	0.7	0.5	0.6
Barstow	365	8004	33.7	0.00005	2.8	0.8	185.9	0.8	0.5	0.7
Barstow	346	7471	34.1	0.00005	3.0	0.7	200.2	0.5	0.5	0.6
Barstow	376	9429	29.3	0.00007	2.5	0.6	136.4	0.9	0.6	0.6
Barstow	262	12820	87.9	0.00000	4.5	0.7	262.9	0.6	0.3	0.6
Barstow	338	10712	44.5	0.00001	2.9	0.6	158.0	0.7	0.5	0.6
Barstow	247	16209	113.4	0.00001	4.7	0.6	263.8	0.5	0.3	0.6
Barstow	362	9731	38.9	0.00009	2.6	0.7	128.0	0.9	0.6	0.6
Barstow	338	7530	44.0	0.00009	3.0	0.8	186.0	0.8	0.5	0.8
Barstow	343	7253	44.8	0.00009	3.0	0.7	193.9	0.5	0.5	0.6

ANEXO C – Imagens de Petrografia, QEMSCAN e os respectivos diagramas da concórdia de cada fase analisada

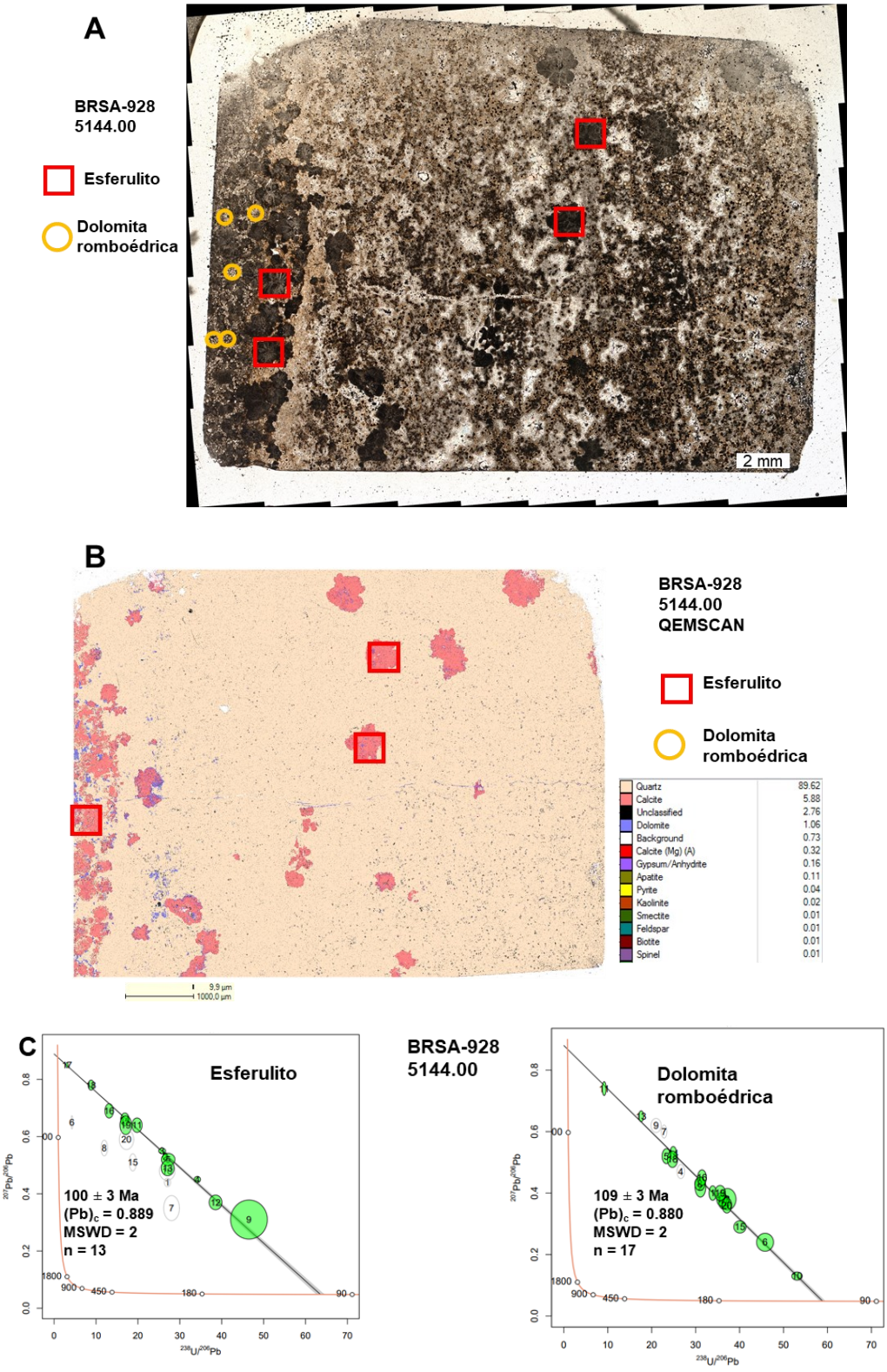

Figura 1. (A) Vista da amostra 5144.00 do testemunho BRSA-928 em microsópio petrográfico. (B) Imagem de QEMSCAN da amostra A. (C) Diagramas da concordia de Tera-Wasserburg das respectivas fases analisadas.

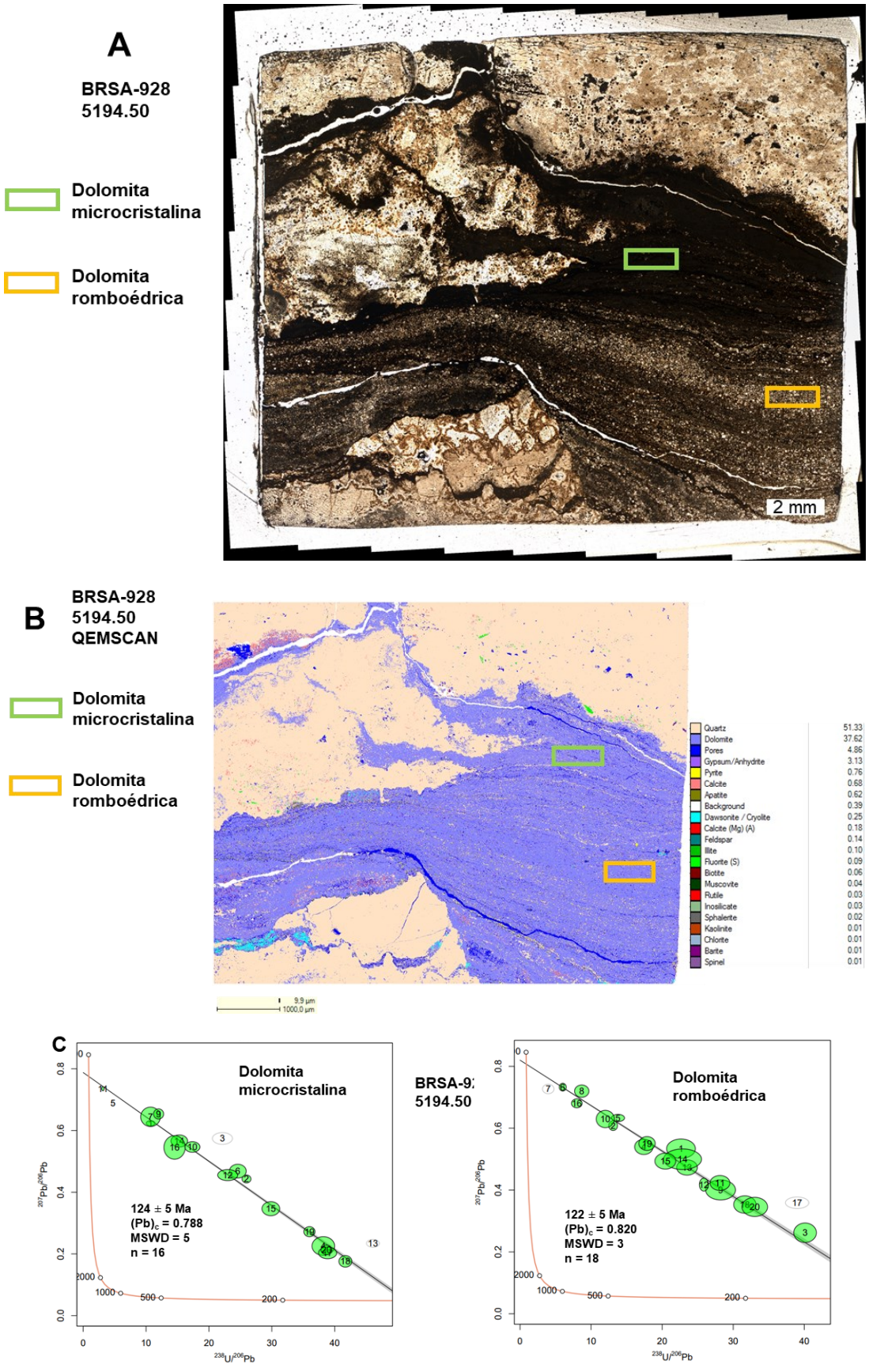

Figura 2. (A) Vista da amostra 5194.50 do testemunho BRSA-928 em microsópio petrográfico. (B) Imagem de QEMSCAN da amostra A. (C) Diagramas da concordia de Tera-Wasserburg das respectivas fases analisadas.

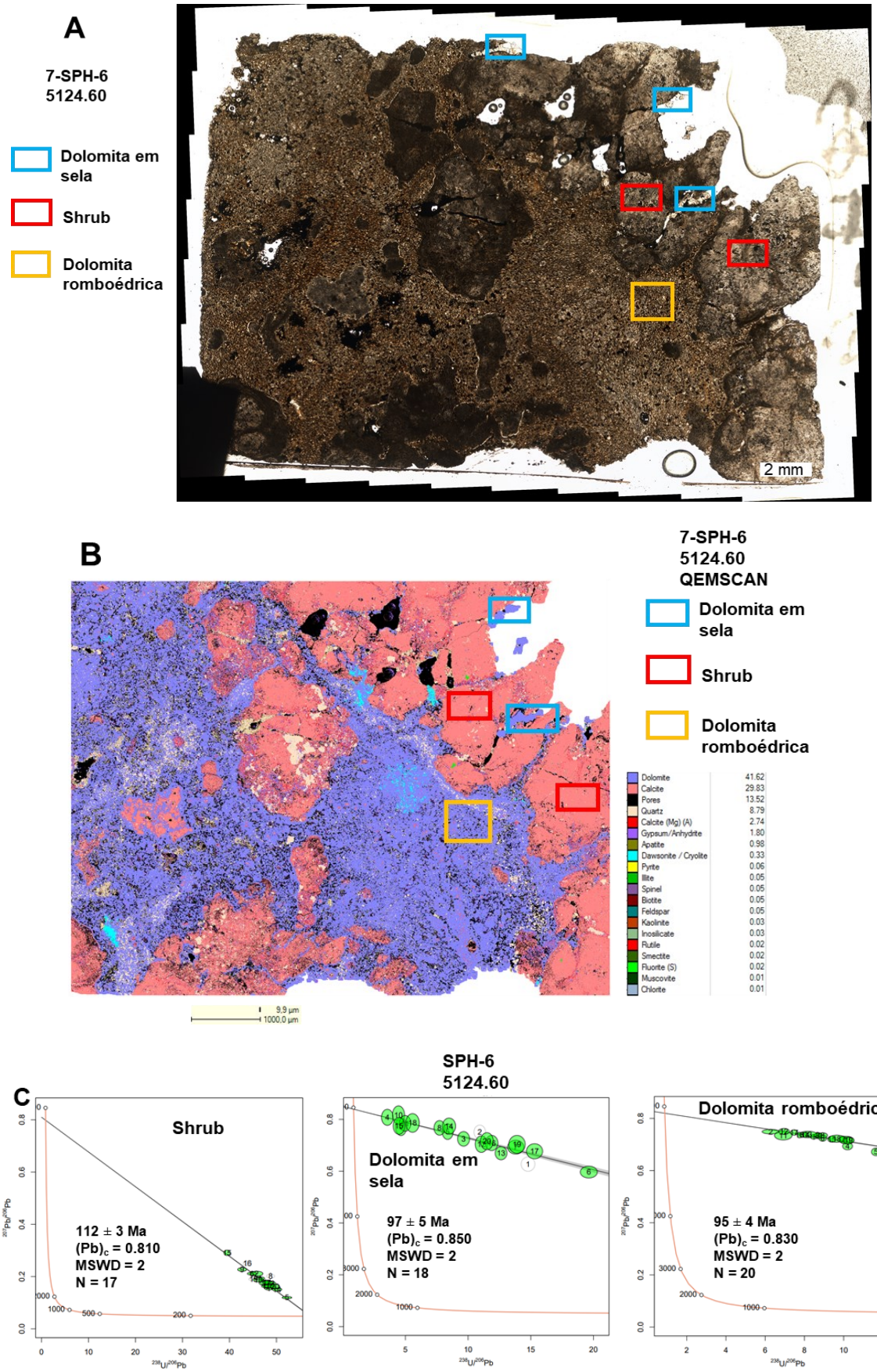

Figura 3. (A) Vista da amostra 5127.60 do testemunho 7-SPH-6 em microsópio petrográfico. (B) Imagem de QEMSCAN da amostra A. (C) Diagramas da concordia de Tera-Wasserburg das respectivas fases analisadas.

Materiais de referência

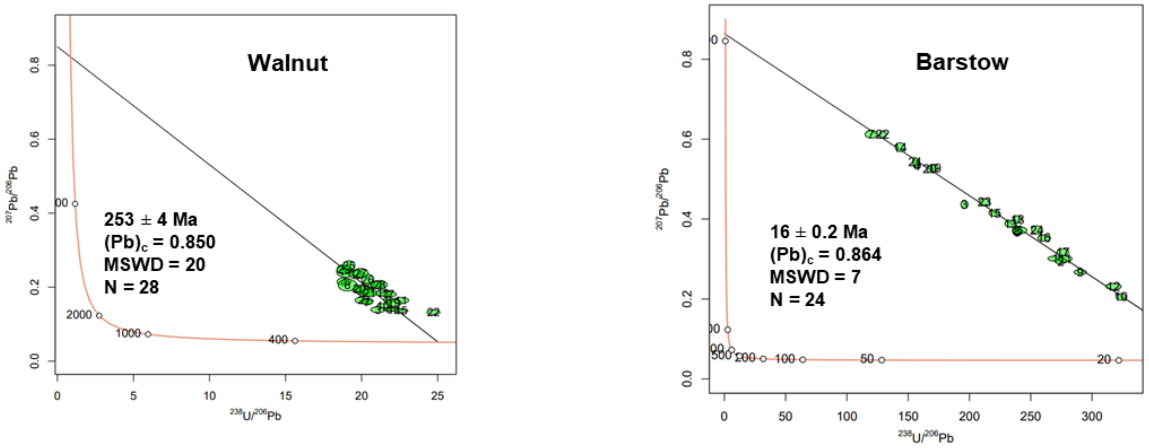

Figura 4. Diagramas da concordia de Tera-Wasserburg dos materiais de referência analisados durante a rodada analítica na qual as amostras 5144.00 5194.50, e 5124.60 foram analisadas.

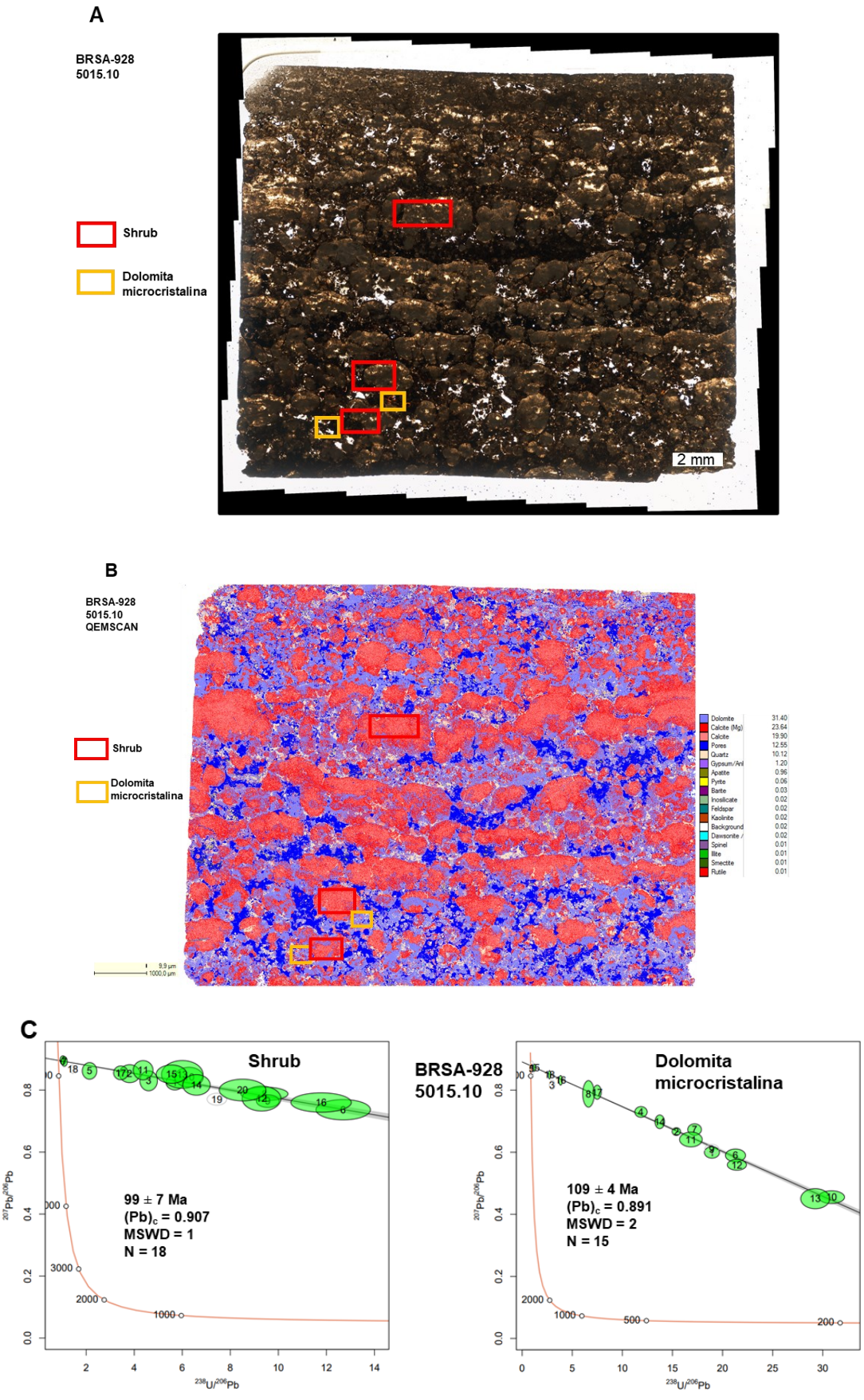

Figura 5. (A) Vista da amostra 5015.10 do testemunho BRSA-928 em microsópio petrográfico. (B) Imagem de QEMSCAN da amostra A. (C) Diagramas da concordia de Tera-Wasserburg das respectivas fases analisadas.

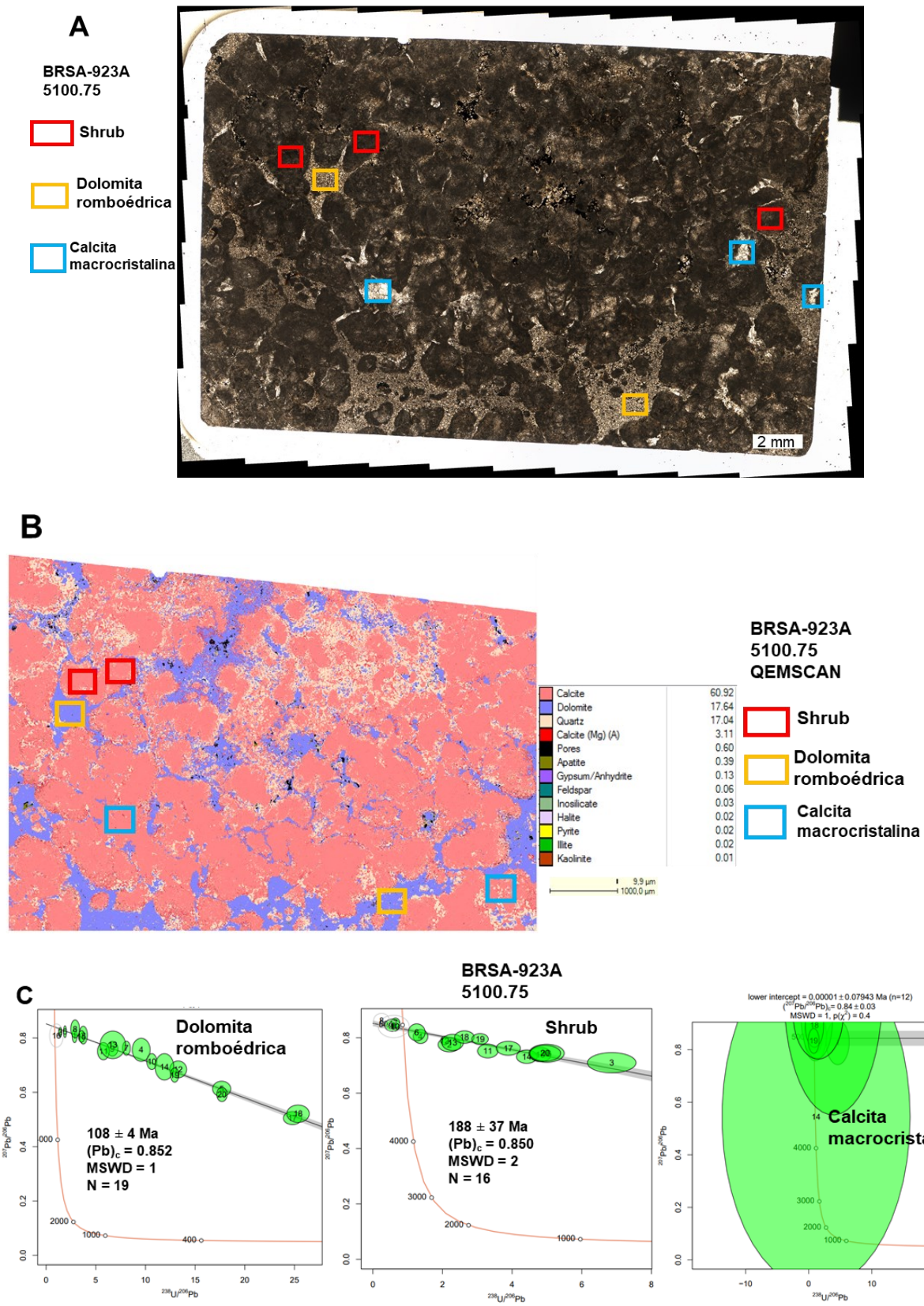

Figura 6. (A) Vista da amostra 5100.75 do testemunho BRSA-923A em microsópio petrográfico. (B) Imagem de QEMSCAN da amostra A. (C) Diagramas da concordia de Tera-Wasserburg das respectivas fases analisadas.

Materiais de referência

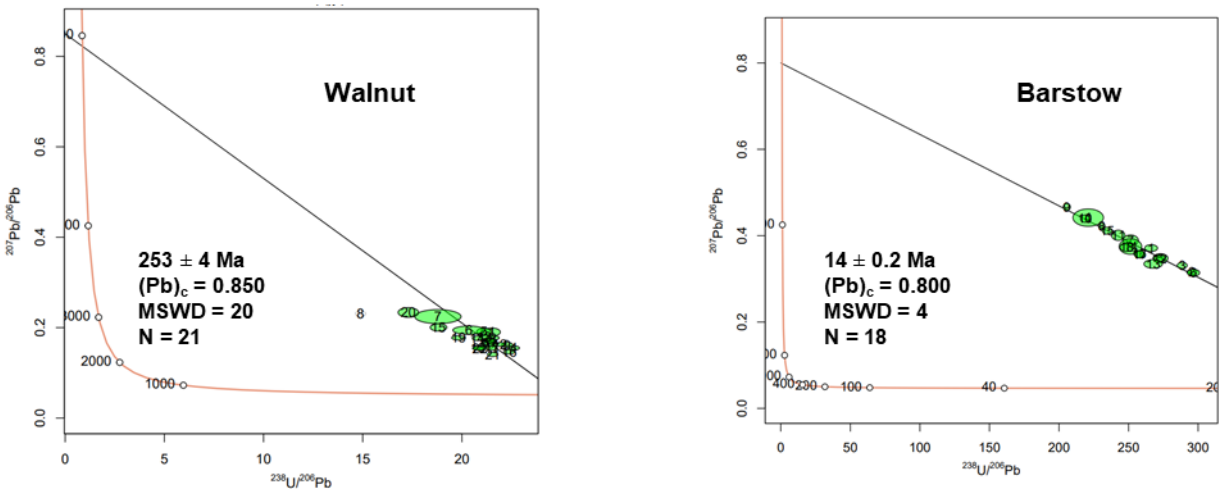

Figura 7. Diagramas da concordia de Tera-Wasserburg dos materiais de referência analisados durante a rodada analítica na qual as amostras 5015.10 e 5100.75 foram analisadas.

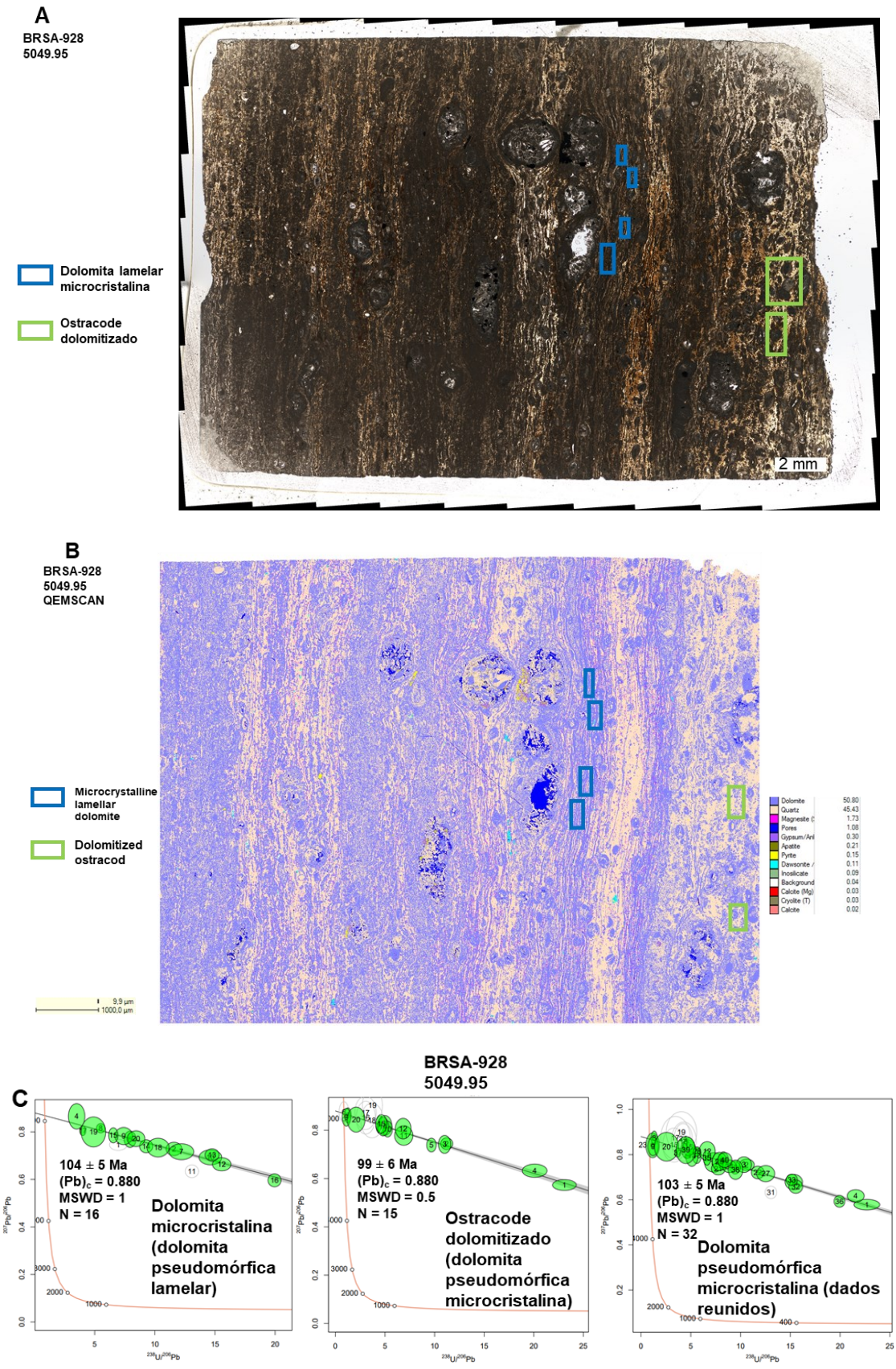

Figura 8. (A) Vista da amostra 5049.95 do testemunho BRSA-928 em microsópio petrográfico. (B) Imagem de QEMSCAN da amostra A. (C) Diagramas da concordia de Tera-Wasserburg das respectivas fases analisadas. (D) Diagramas da concordia de Tera-Wasserburg dos dados reunidos das análises da dolomita microcristalina pseudomórfica.

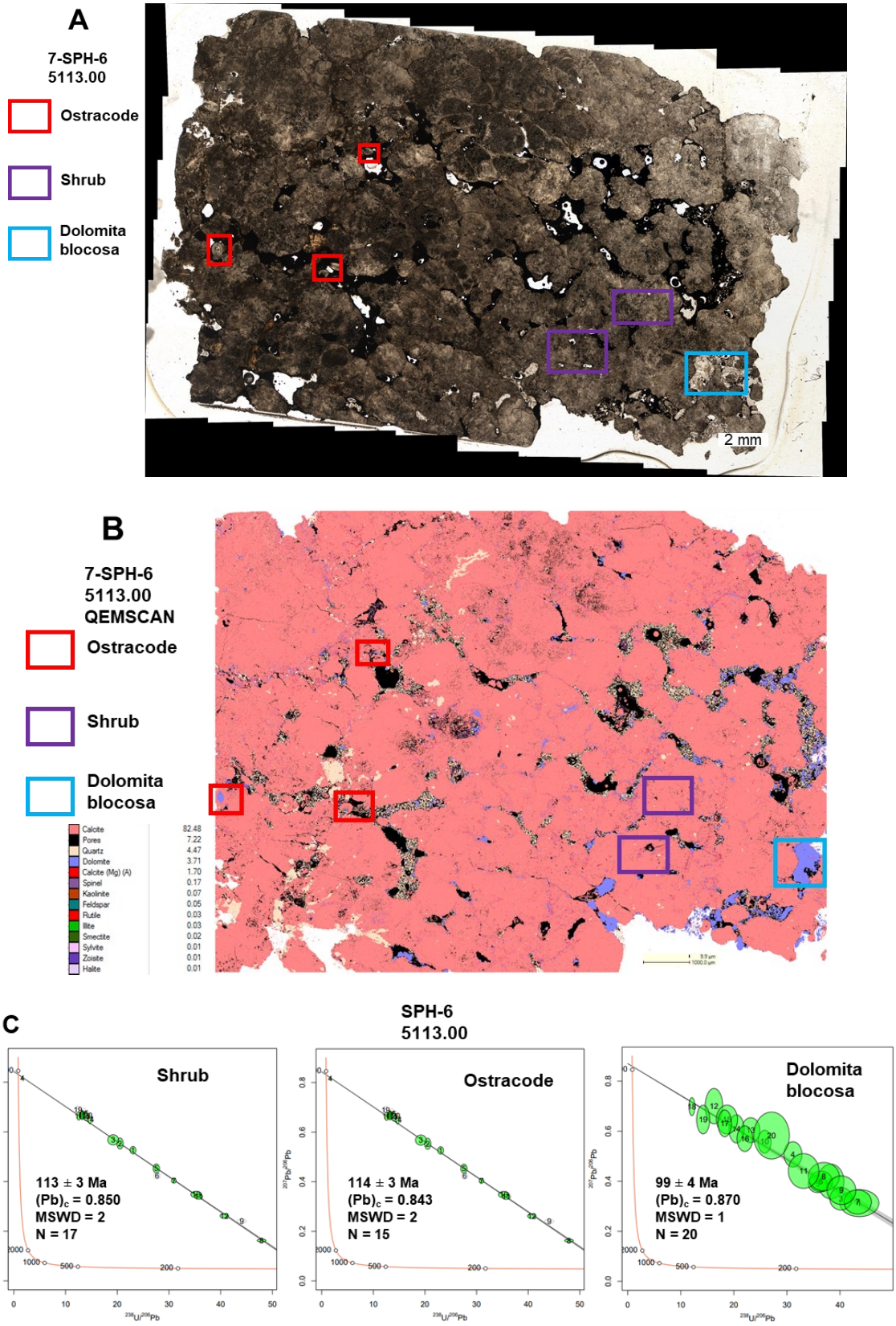

Figura 9. (A) Vista da amostra 5113.00 do testemunho 7-SPH-6 em microsópio petrográfico. (B) Imagem de QEMSCAN da amostra A. (C) Diagramas da concordia de Tera-Wasserburg das respectivas fases analisadas.

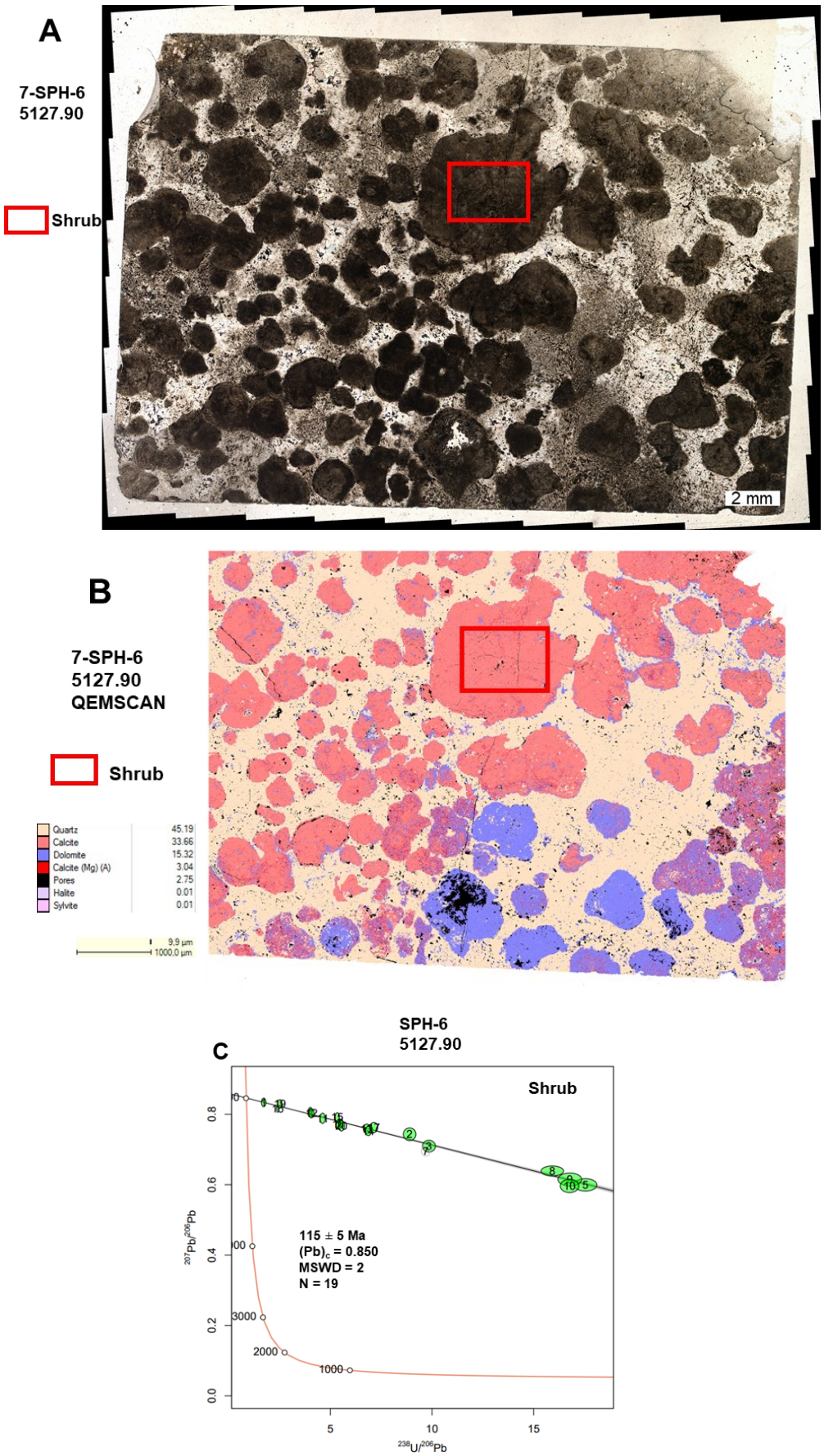

Figura 10. (A) Vista da amostra 5127.90 do testemunho 7-SPH-6 em microsópio petrográfico. (B) Imagem de QEMSCAN da amostra A. (C) Diagramas da concordia de Tera-Wasserburg das respectivas fases analisadas.

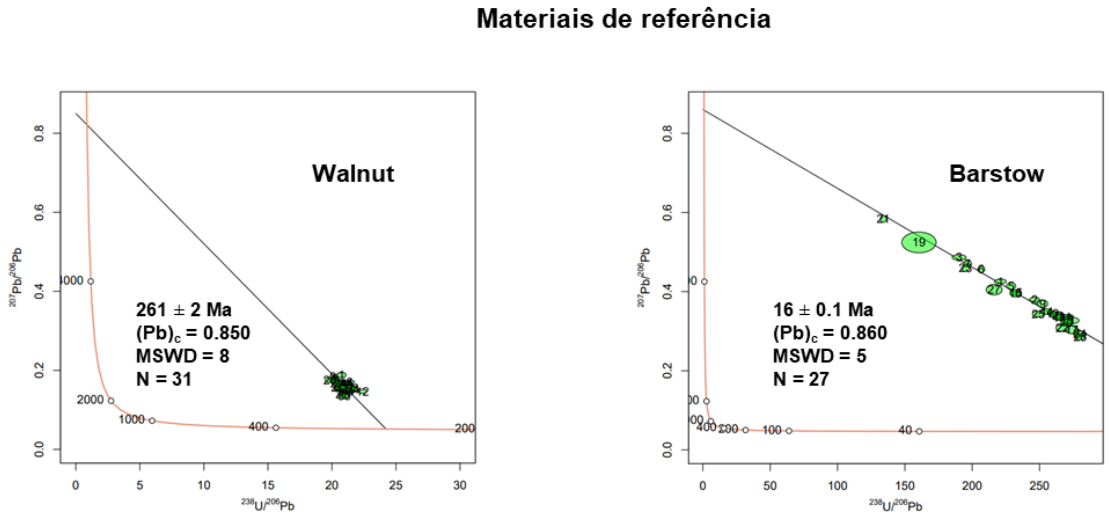

Figura 11. Diagramas da concordia de Tera-Wasserburg dos materiais de referência analisados durante a rodada analítica na qual as amostras 5049.95, 5113.00 e 5127.90 foram analisadas.

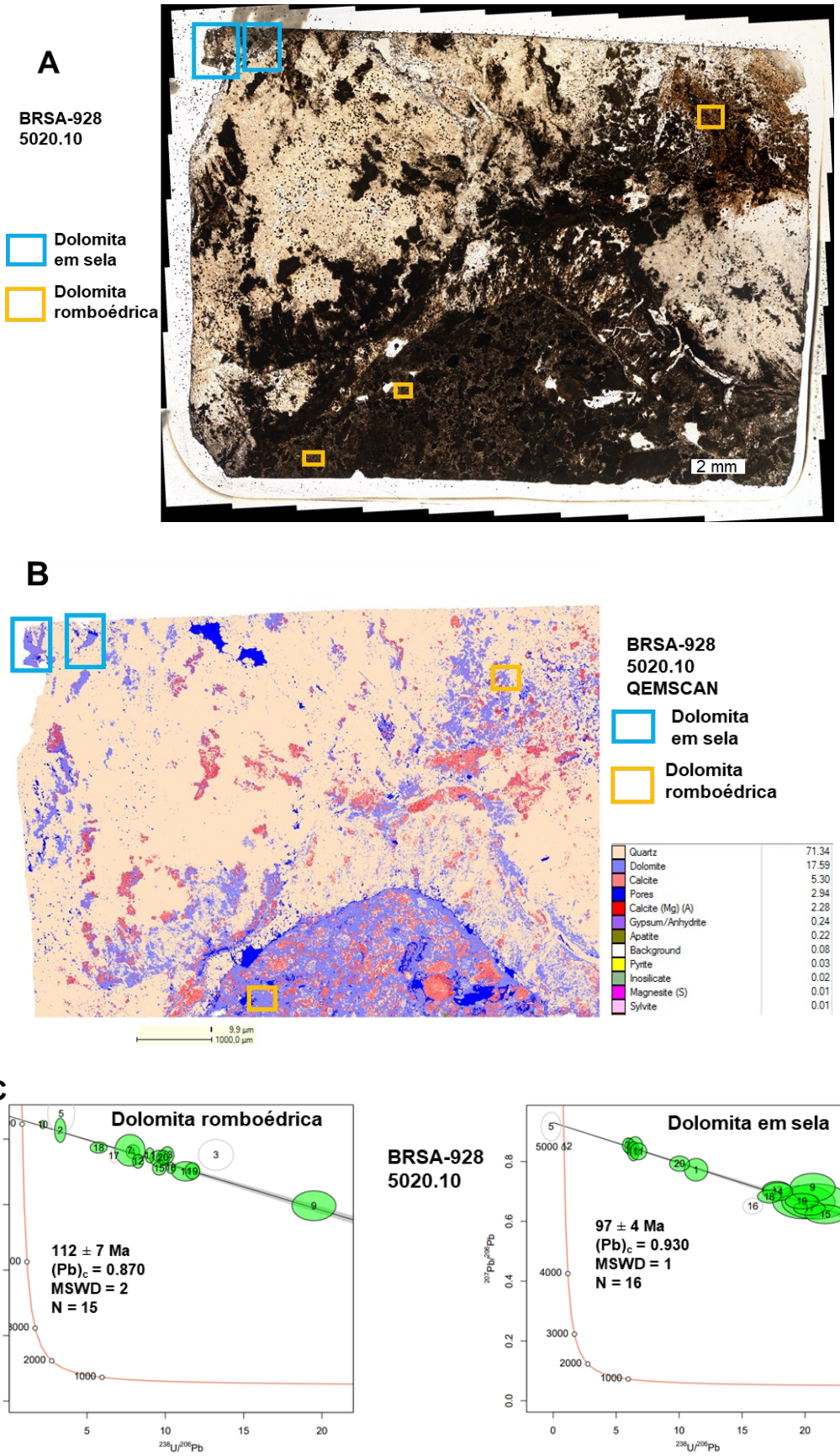

Figura 12. (A) Vista da amostra 5020.10 do testemunho BRSA-928 em microsópio petrográfico. (B) Imagem de QEMSCAN da amostra A. (C) Diagramas da concordia de Tera-Wasserburg das respectivas fases analisadas.

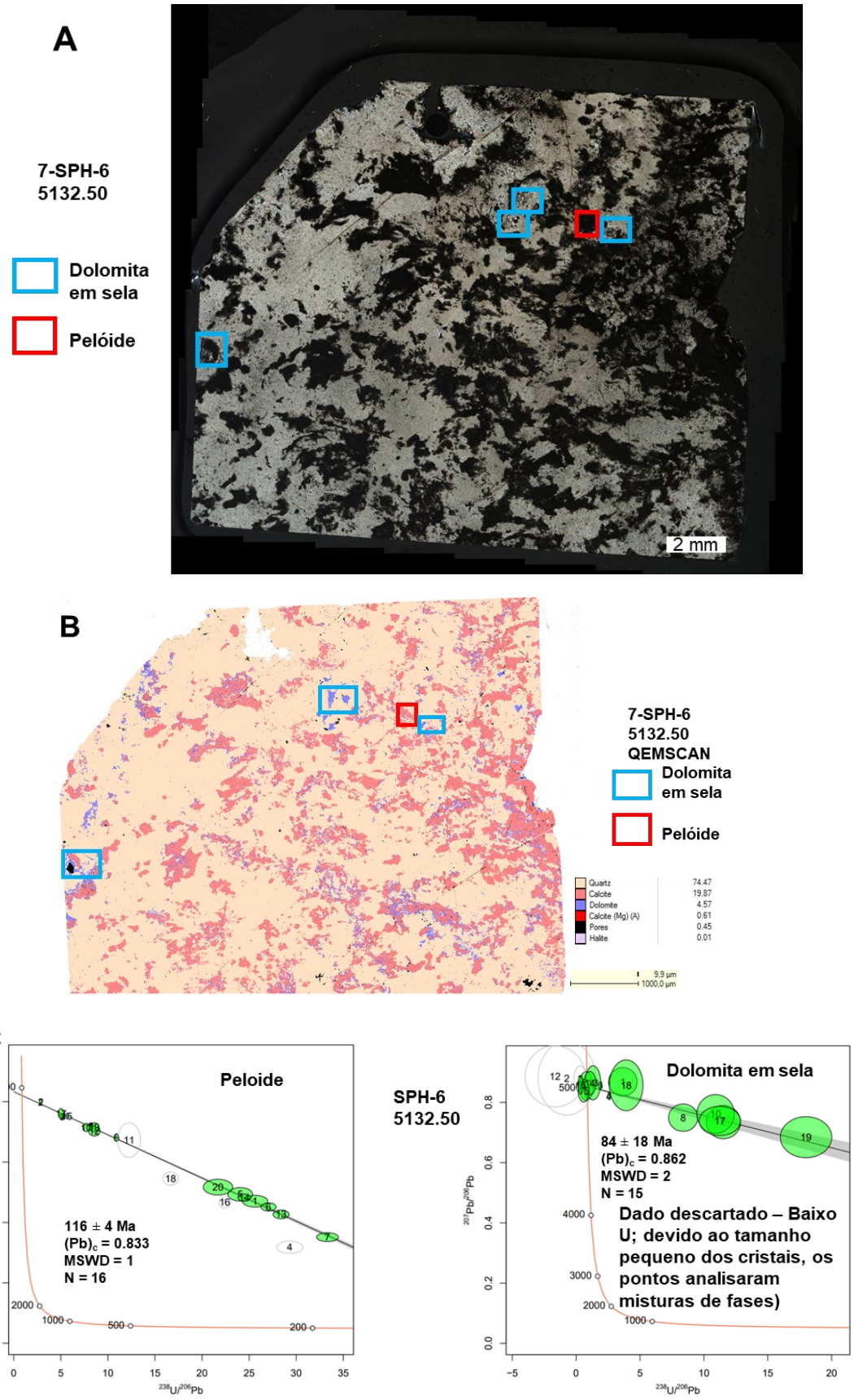

Figura 13. (A) Vista da amostra 5132.50 do testemunho 7-SPH-6 em microsópio petrográfico. (B) Imagem de QEMSCAN da amostra A. (C) Diagramas da concordia de Tera-Wasserburg das respectivas fases analisadas.

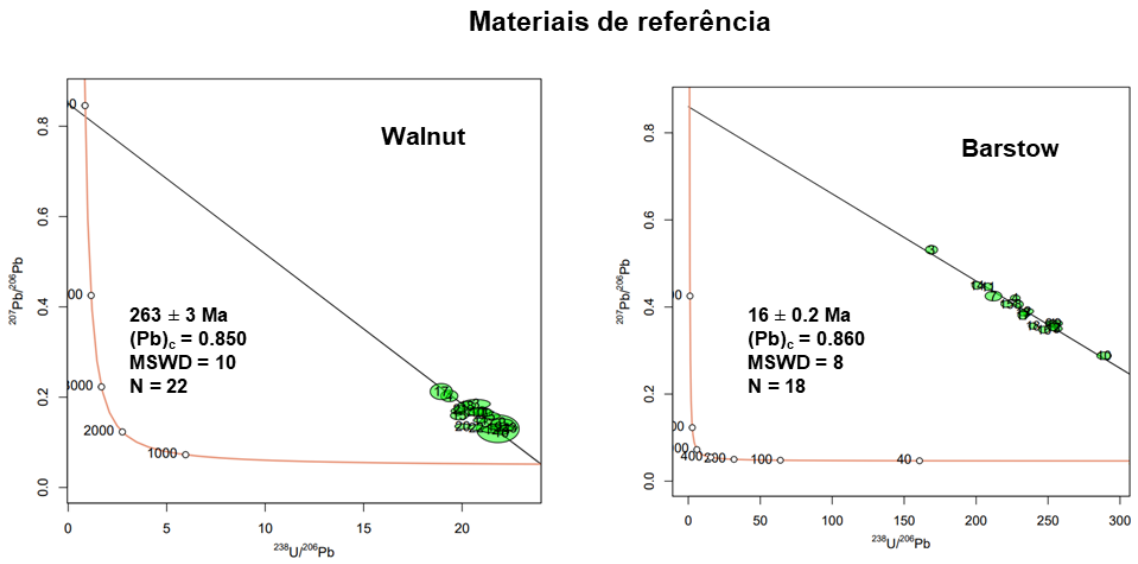

Figura 14. Diagramas da concordia de Tera-Wasserburg dos materiais de referência analisados durante a rodada analítica na qual as amostras 5020.10 e 5132.50 foram analisadas.

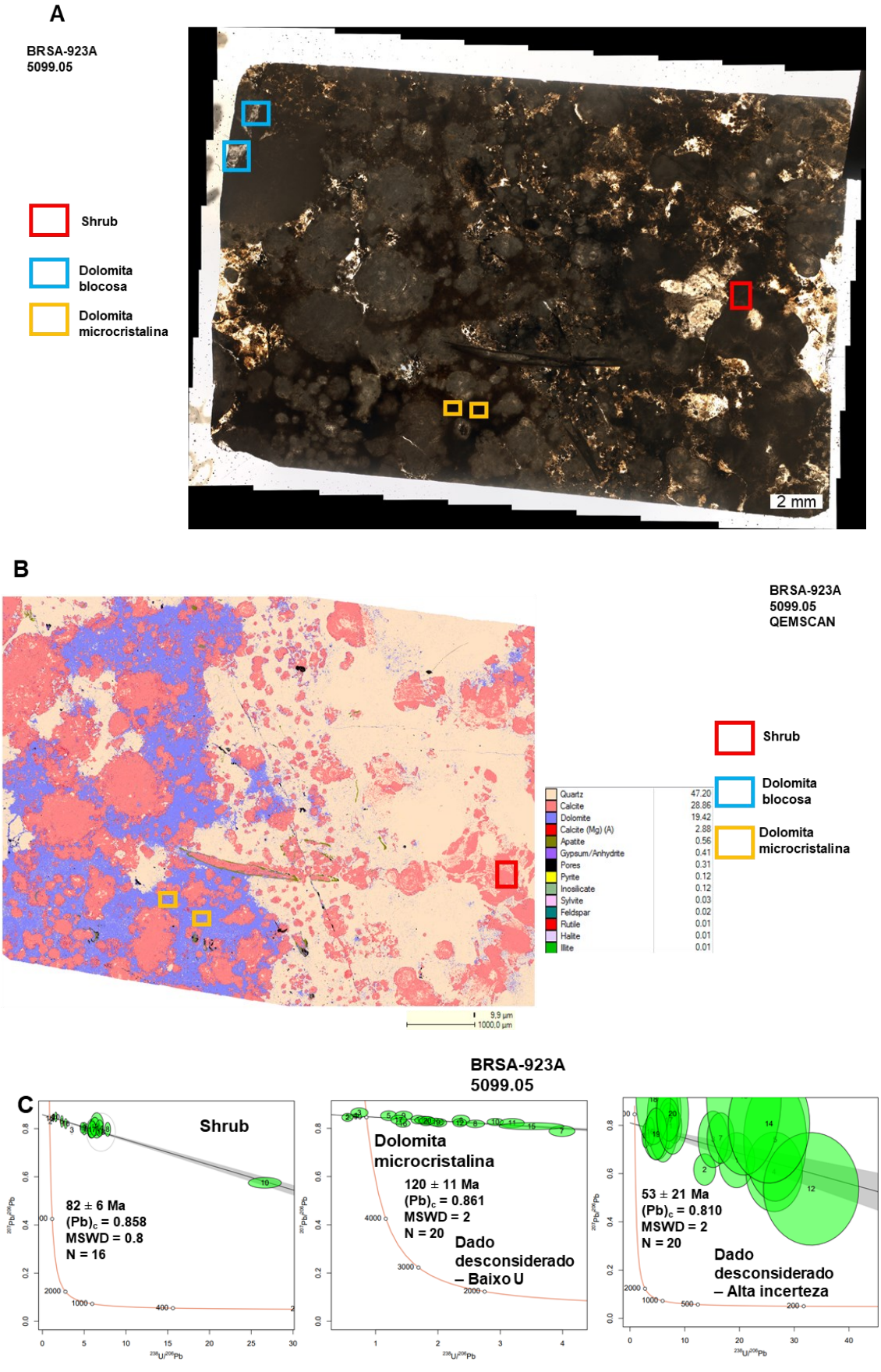

Figura 15. (A) Vista da amostra 5099.05 do testemunho BRSA-923A em microsópio petrográfico. (B) Imagem de QEMSCAN da amostra A. (C) Diagramas da concordia de Tera-Wasserburg das respectivas fases analisadas.

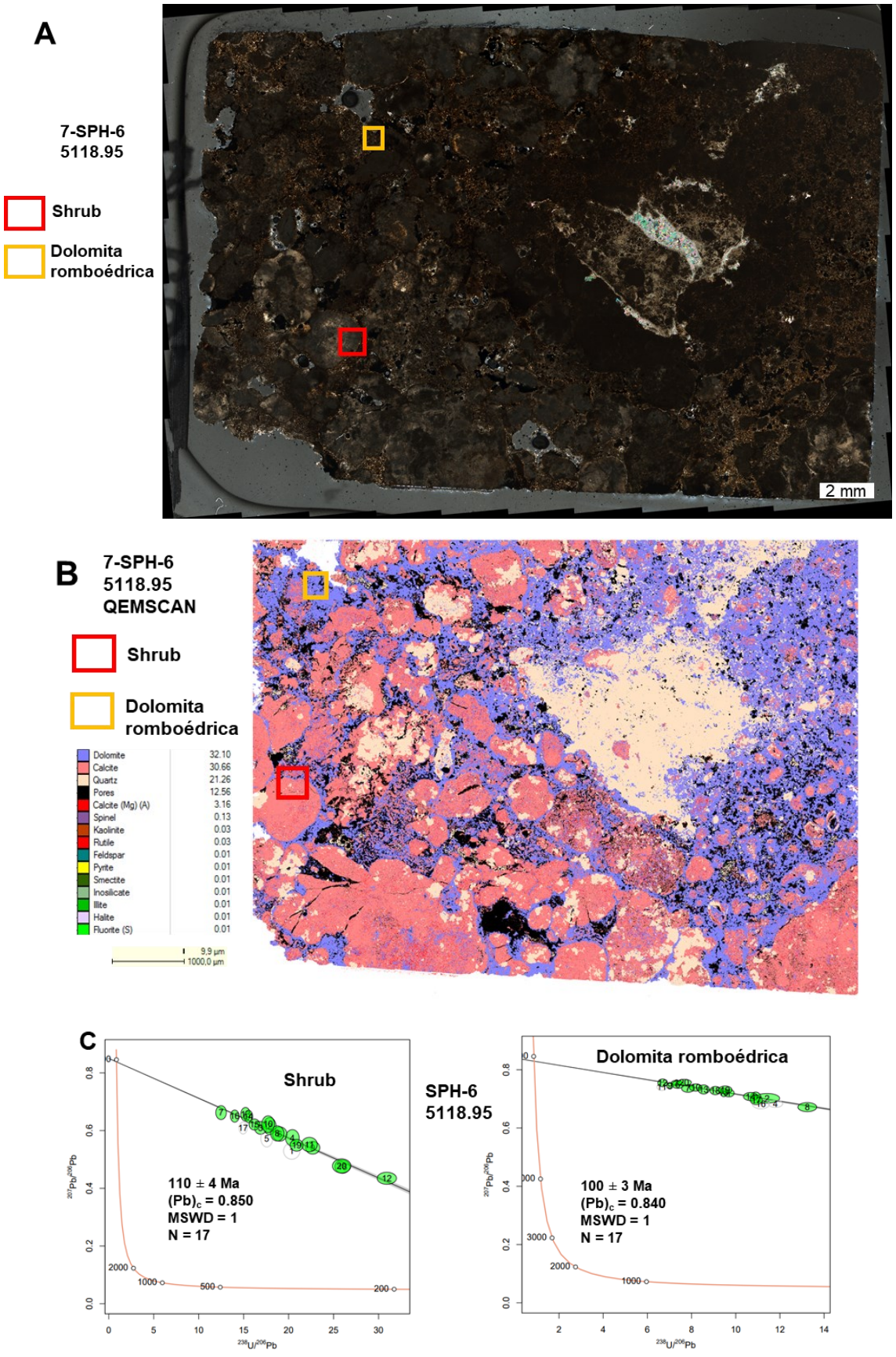

Figura 16. (A) Vista da amostra 5118.95 do testemunho 7-SPH-6 em microsópio petrográfico. (B) Imagem de QEMSCAN da amostra A. (C) Diagramas da concordia de Tera-Wasserburg das respectivas fases analisadas.

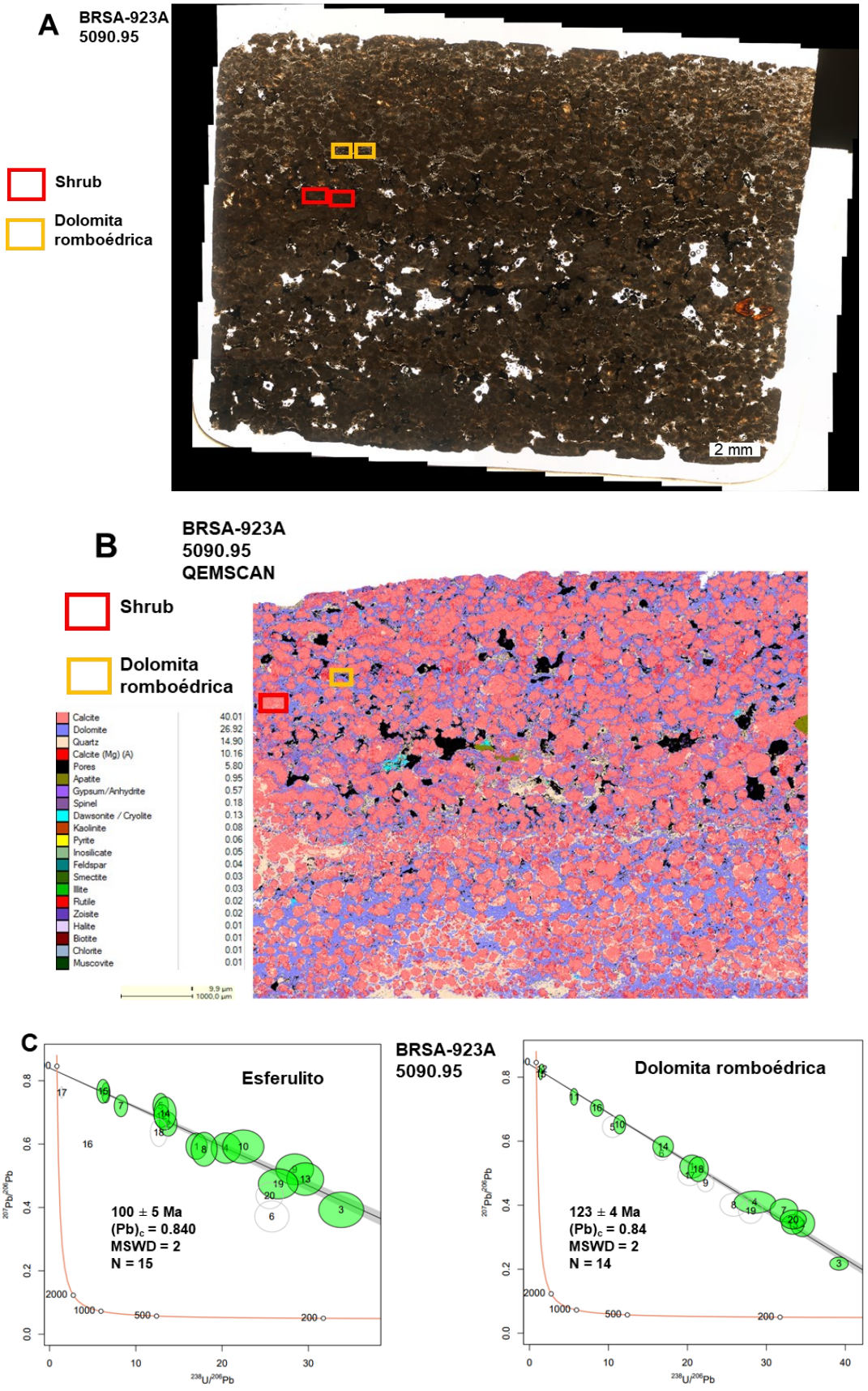

Figura 17. (A) Vista da amostra 5090.95 do testemunho BRSA-923A em microsópio petrográfico. (B) Imagem de QEMSCAN da amostra A. (C) Diagramas da concordia de Tera-Wasserburg das respectivas fases analisadas.

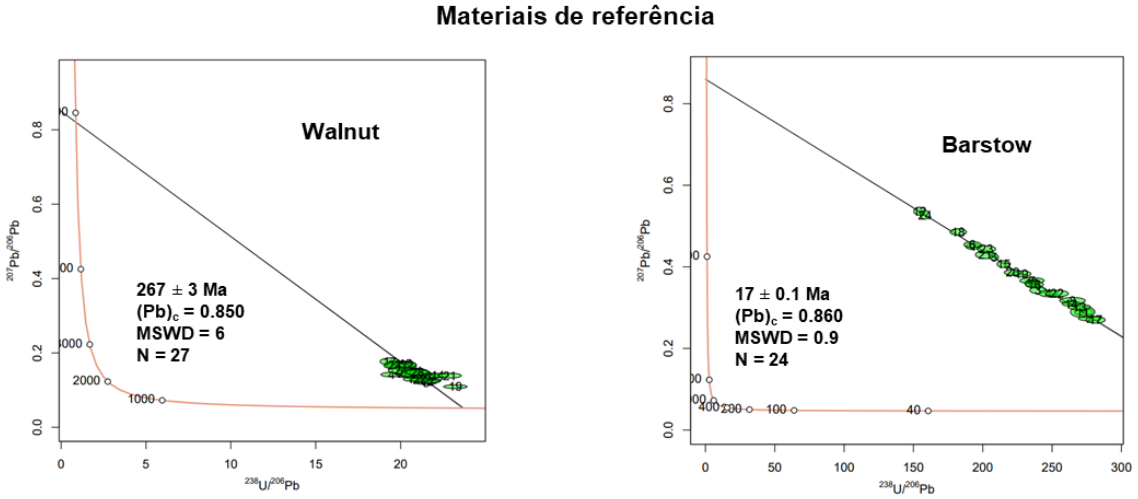

Figura 18. Diagramas da concordia de Tera-Wasserburg dos materiais de referência analisados durante a rodada analítica na qual as amostras 5099.05, 5118.95, e 5090.95 foram analisadas.

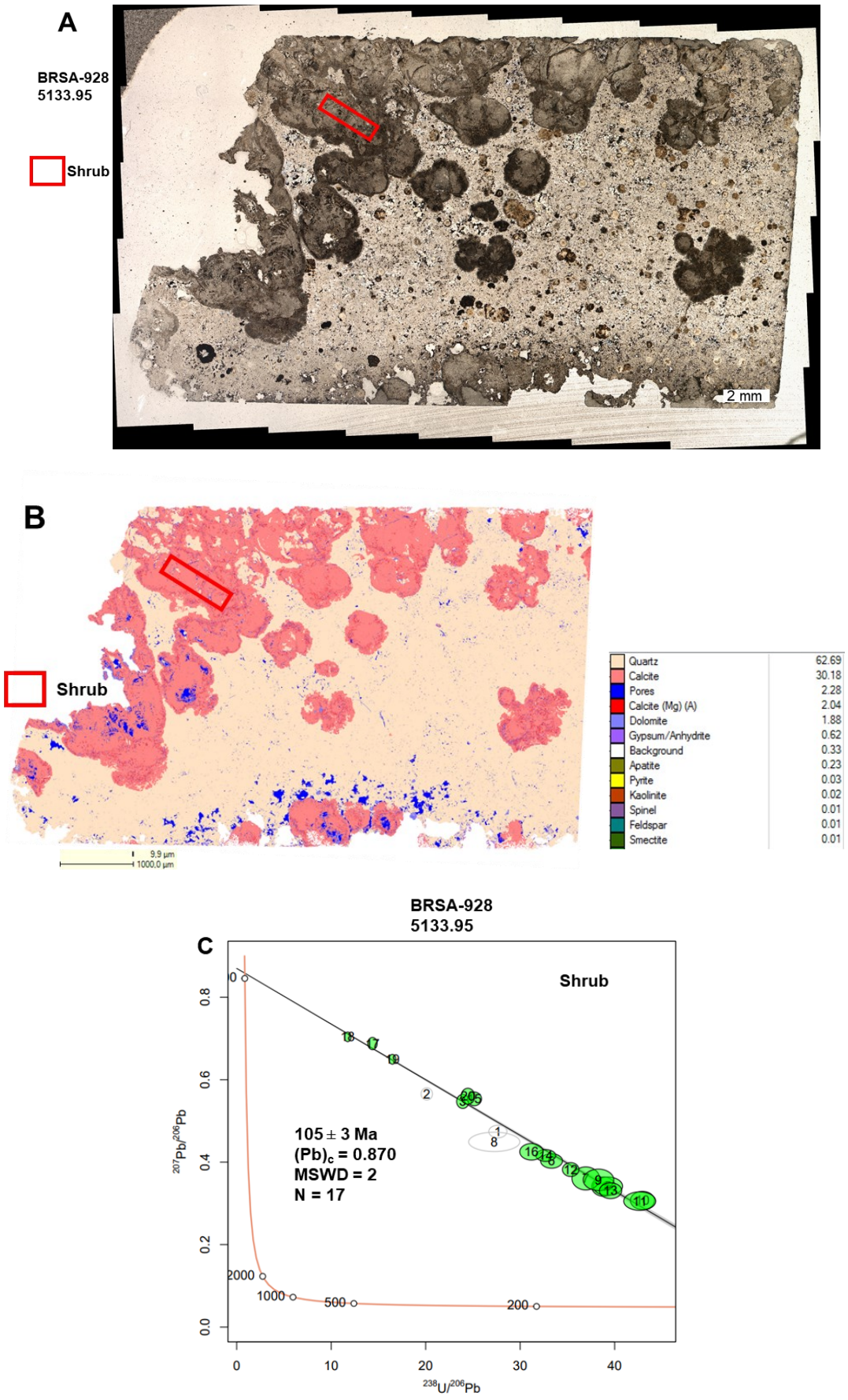

Figura 19. (A) Vista da amostra 5133.95 do testemunho BRSA-928 em microsópio petrográfico. (B) Imagem de QEMSCAN da amostra A. (C) Diagramas da concordia de Tera-Wasserburg das respectivas fases analisadas.

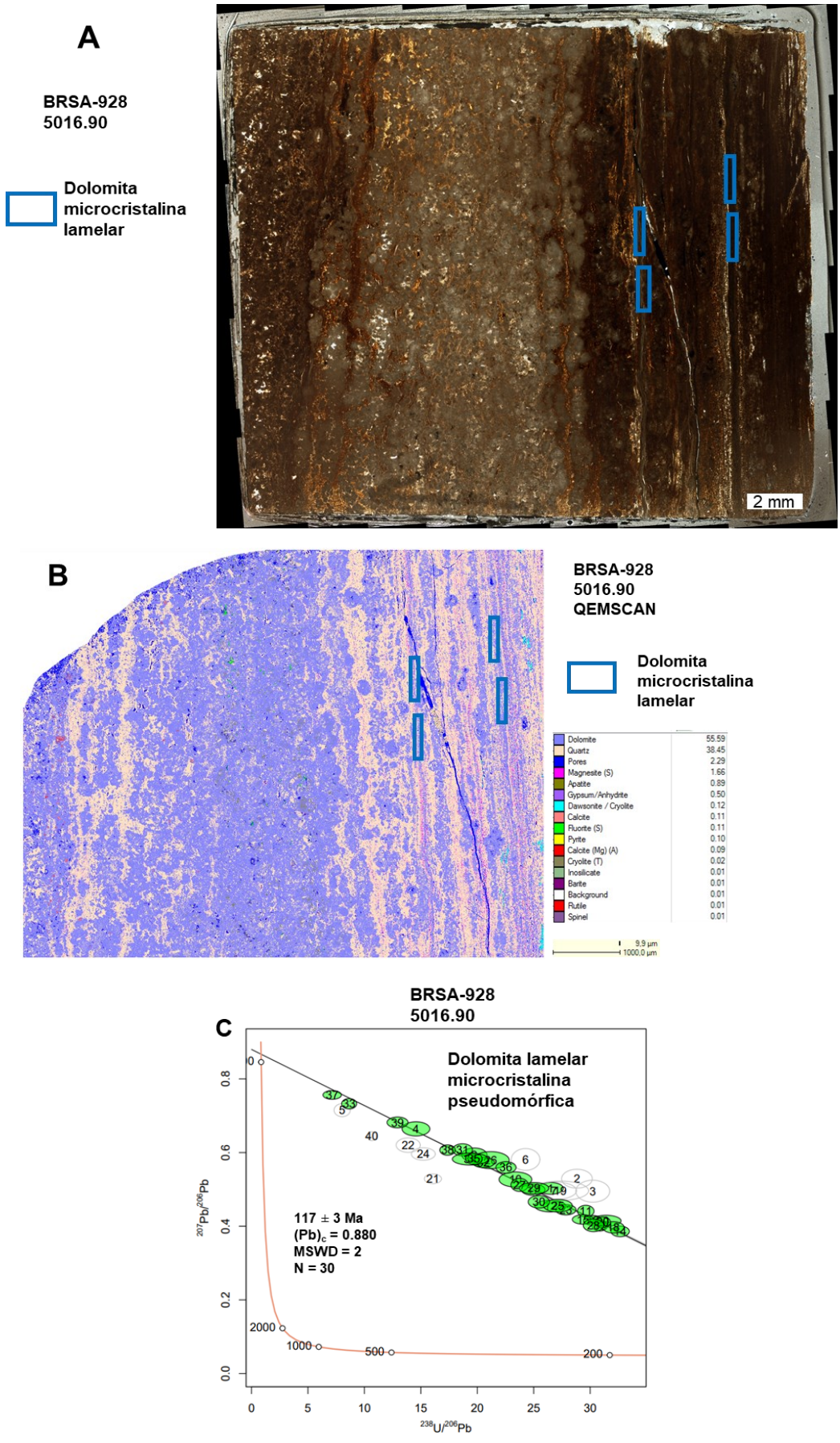

Figura 20. (A) Vista da amostra 5016.90 do testemunho BRSA-928 em microsópio petrográfico. (B) Imagem de QEMSCAN da amostra A. (C) Diagramas da concordia de Tera-Wasserburg das respectivas fases analisadas.

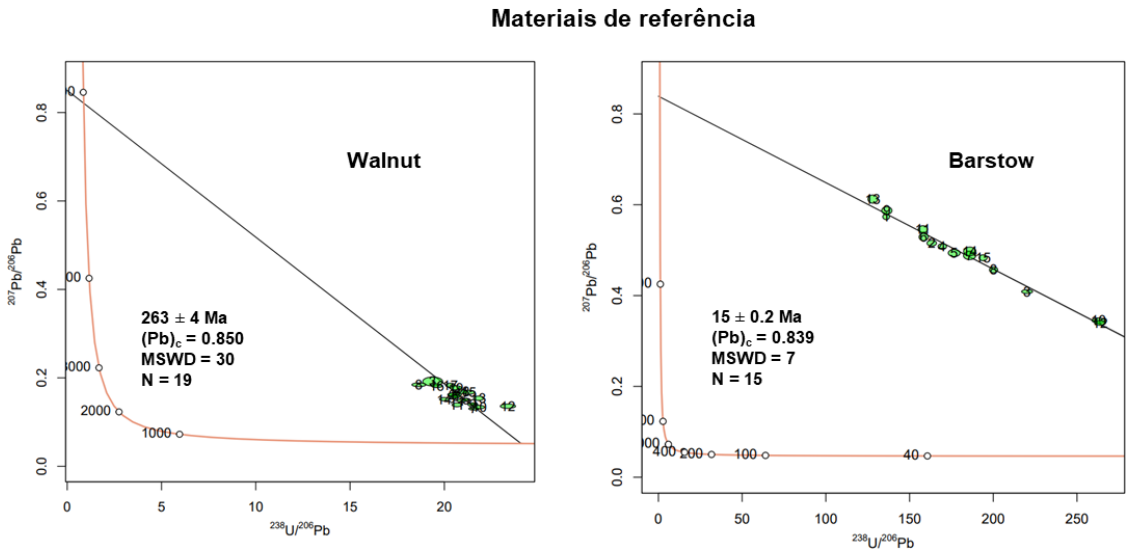

Figura 21. Diagramas da concordia de Tera-Wasserburg dos materiais de referência analisados durante a rodada analítica na qual as amostras 5133.95 e 5016.90 foram analisadas.